# Synthesis, characterisation, and diffusive properties of functionalised nanomaterials

Edward Douglas Hugh Mansfield

*Submitted as partial fulfilment for the degree of Doctor of Philosophy*

School of Pharmacy

October 2016

"If we knew what it was we were doing, it would not be called research, would it?"

Albert Einstein

# **Acknowledgements**

*Declaration of original authorship*

I confirm that this is my own work and the use of all material from other sources has been properly and fully acknowledged

Edward Mansfield

June 2016

# Abstract

The aim of this thesis was to assess the diffusive properties of functionalised and unfunctionalised nanomaterials in a variety of different media. The main goal was to gain an insight into the fundamental mechanisms underpinning nanoparticle diffusion and how the surface properties of nanoparticles alter their net movement through different environments. Initially a library of polymer-functionalised silica nanoparticles were synthesised and characterised. The polymers chosen were; poly(ethylene glycol) (PEG), poly(2-oxazolines) (POZ) and poly(n-isopropyl acrylamide) (PNIPAM).

Firstly, the diffusion of different sized gold nanoparticles was assessed in concentrations of Pluronic F-127, in order to determine how the solution properties affected diffusion. It was found that as the solution undergoes a transition in response to environmental stimuli, there is an increase in diffusion coefficient; however the area they move in becomes more confined (assessed using a bespoke python script written for use with NTA).

PNIPAM- and PNPOZ-silica nanoparticles were assessed for their aggregation and diffusion using DLS, NTA, and SANS. It was found that the position of a nitrogen atom in the amide group, present in both polymers, plays a key role in governing how the particles aggregate in solution, which in turn affects how they diffuse through solvents of varying polarities.

POZ-silica nanoparticles were assessed for mucus penetration against a positive control of PEGylated nanoparticles. It was found that POZ-silica was effective at enhancing nanoparticle mucus penetration, and the hydrophilicity of these polymers plays a key role in determining the degree of permeation (with methylated POZ significantly more diffusive than propylated POZ).

These finding provide valuable insight into some of the molecular mechanisms governing nanoparticle diffusion and how surface chemistry governs these effects.

# List of Publications

**Original research articles**

E. D. H. Mansfield, K. Sillence, P. Hole, A. C. Williams and V. V Khutoryanskiy, POZylation: a new approach to enhance nanoparticle diffusion through mucosal barriers. *Nanoscale*, 2015, **7**, 13671–9.

E. D. H. Mansfield, V. R. de la Rosa, R. M. Kowalczyk, I. Grillo, R. Hoogenboom, K. Sillence, P. Hole, A. C. Williams, V. V. .Khutoryanskiy.  Minor polymer modifications radically alter the diffusion of poly(2-alkyl-2-oxazolines) functionalised      nanoparticles through a mucosal barrier. *Biomaterials Science*, 2016, **4**, 1318-1327.

**Book chapters**

"Temperature-responsive polymers functionalised to solid-core nanoparticles" to be published in Temperature-responsive polymers: chemistry, properties and plications.  To be published by Wiley & Sons, December 2016.

# List of oral presentations

**UKICRS:** (University of Cardiff, April 2016). *Does the nature of a poly(2-oxazoline) coat affect the rate of nanoparticle diffusion through mucus?*

**ISIS student meeting:** (Rutherford Appleton Laboratories, Harwell. October 2015). *Phase transition and diffusive properties of temperature responsive silica nanoparticles*

**M4 Colloids:** (University of Bristol. June 2015). *POZylation; a new approach to enhance nanoparticle diffusion through mucosal barriers*

**School of Pharmacy Research Day:** (University of Reading. January 2015). *Rapid mucopenetration of poly(2-oxazoline) functionalised nanoparticles through gastric mucus: A diffusion study*

**ISIS student meeting:** (Rutherford Appleton Laboratories, Harwell. October 2014) *Probing the thermo-sensitive nature of poly(N-isopropyl acrylamide) functionalised nanoparticles, and its effect on particle size and diffusion*

**M4 Colloids:** (University of Cardiff. June 2014). *Probing the diffusion of polymer functionalised nanoparticles through gastric mucus*

**UKICRS:** (University of Cork, April 2014). *Diffusion of polymer-coated nanoparticles through gastric mucin*

## List of poster presentations

**ISIS student meeting:** (Rutherford Appleton Laboratories, Harwell. October 2015). *Phase transition and diffusive properties of temperature responsive silica nanoparticles*

**42nd Annual meeting for the Controlled Release Society:** (Edenborough. July 2015). *Probing the diffusive characteristics of silica nanoparticles functionalized with pharmaceutically relevant polymers through gastric mucus*

**UKICRS:** (University of Nottingham. April 2015). *Altering the diffusive properties of mucoadhesive silica nanoparticles by functionalising them with poly(ethylene glycol) and poly(2-ethyl-2-oxaqzoline)*

**ISIS student meeting:** (Rutherford Appleton Laboratories, Harwell. October 2014) *Probing the thermo-sensitive nature of poly(N-isopropyl acrylamide) functionalised nanoparticles, and its effect on particle size and diffusion*

**ISIS new-users meeting:** (Rutherford Appleton Laboratories, Harwell. February 2014). *Diffusion of polymer-coated nanoparticles through gastric mucin*

**M4 Colloids:** (University of Bath. July 2013). *Measuring the pore size of hydrogels using various sizes of gold nanoparticle*

# Table of contents

## Chapter 1- Introduction: Functionalised nanomaterials and principles of diffusion

### Chapter 2- Synthesis and characterisation of  functionalised and unfunctionalised amorphous silica nanoparticles

### Chapter 3- Diffusion of gold nanoparticles in solutions of Pluronic F-127 at different concentrations

## Chapter 4- Temperature responsive silica nanoparticles – particle solvation and diffusion

## Chapter 5- Diffusion and penetration of PEGylated and POZylated nanoparticles though gastric mucus

# List of figures

## Chapter 3

## Chapter 4

## Chapter 5

# Chapter 6

# List of tables

## Chapter 6

# List of abbreviations

| | |
|---|---|
| ATRP | Atom transfer radical polymerisation |
| ANOVA | Analysis of variance |
| AU | Arbitrary units |
| AuNP's | Gold nanoparticles |
| BBB | Blood-brain barrier |
| CMT | Critical micelle temperature |
| CP | Cross-polarisation |
| CPMAS | Cross-polarisation magic angle spinning |
| CROP | Cationic ring opening polymerisation |
| DLS | Dynamic light scattering |
| DMAPS | 3-dimethyl(methacryloyloxyethyl)ammonium propanesulphonate |
| DMSO | Dimethyl sulphoxide |
| DNA | Deoxyribose nucleic acid |
| DOSY | Diffusion-ordered spectroscopy |
| DSC | Differential scanning calorimetry |
| EC | European Commission |
| EPR | Enhanced permeability and retention effect |
| EU | European Union |
| FDA | Food and Drug Administration |
| FT-IR | Fourier transformed infrared spectroscopy |
| FT-Raman | Fourier transformed Raman spectroscopy |
| GABA | *gamma*-Aminobutyric acid |
| HIV | human immunodeficiency virus |
| HPLC | High performance liquid chromatography |
| HUGO | Human Gene Nomenclature Committee |
| IR | Infra-red |
| LCST | Lower critical solution temperature |
| MAS | magic angle spinning |
| MNP's | Magnetic nanoparticles |
| MPT | Multiple particle tracking |
| MPTS | (3-Mercaptopropyl)trimethoxysilane |
| MRI | Magnetic resonance imaging |
| MSD | Mean squared displacement |
| NMR | Nuclear magnetic resonance |
| NTA | Nanoparticle tracking analysis |
| OCT | Optimum cutting temperature |
| OECD | Organisation for Economic Cooperation and Development |
| PAA | Poly(acrylic acid) |
| PDI | Polydispersity index |
| PDMAEMA | poly(2-dimethylamino)ethyl methacrylate |
| PEG | poly(ethylene glycol) |
| PEO | poly(ethylene oxide) |
| PEOZ | poly(2-ethyl-2-oxazoline) |
| PEOZ (Sigma) | poly(2-ethyl-2-oxazoline), Sigma |

| | |
|---|---|
| PIPOZ | poly(2-isopropyl-2-oxazoline) |
| PLGA | poly(lactic-co-glycolic acid) |
| PMOZ | poly(2-methyl-2-oxazoline) |
| PNIPAM | poly(n-isopropyl acrylamide) |
| PNPOZ | poly(2-n-propyl-2-oxazoline) |
| PNPOZ | poly(2-n-propyl-2-oxazoline) |
| POZ | poly(2-oxazolines) |
| POZ | poly(2-oxazolines) |
| PPO | poly(propylene oxide) |
| QDs | Quantum dots |
| RAFT | Reversible addition-fragmentation chain transfer |
| Rg | Radius of gyration |
| Rh | Hydrodynamic radius |
| RNA | Ribose nucleic acid |
| SANS | Small angle neutron scattering |
| SAXS | Small angle X-ray scattering |
| SLD | Scattering length density |
| SNP | Silica nanoparticles |
| SOP | Standard operating procedure |
| SPMAS | Single pulse magic angle spinning |
| SPT | Single particle tracking |
| TEA | Triethylamine |
| TEM | Transmission electron microscopy |
| Tg | Glass transition temperature |
| TGA | Thermal gravimetric analysis |
| TRP's | Temperature responsive polymers |
| UCST | Upper critical solution temperature |
| UV | Ultra violet |
| VLPs | Virus-like particles |
| WAXS | Wide angle X-ray scattering |

# Chapter 1

## Introduction:

## Functionalised nanomaterials and principles of diffusion

### 1.1 Introduction

Over the past few decades there has been an increase in research into functionalised nanomaterials. Due to their small size and large surface area, they carry unique physical and chemical properties not present in larger bulk materials.[1] These quantum-like properties are dependent on size, morphology, and elemental composition of the material. By altering these parameters, it is possible to tune and engineer nanoparticles to have specific properties designed for bespoke applications. Nanoparticles can have unique magnetic,[2] optical,[3] and surface properties[4] making them ideal for use in a wide range of industries and scientific disciplines including drug delivery,[5] diagnostics,[6] cosmetics,[7] environmental sciences,[8] energy applications,[9] and manufacturing industries,[10] amongst others.

Nanoparticles are defined by the European Union as "*A natural, incidental or manufactured material containing particles, in an unbound state, as an aggregate, or as an agglomerate where, for 50 % or more of the particles in the number size distribution, one or more external dimensions is in the size range 1 nm - 100 nm.*"[11] The nanoscale, defined in Fig 1.1, exists between 1 and 100 nm and ranges from the size of a glucose molecule (~1 nm) up to a virus (~100 nm).
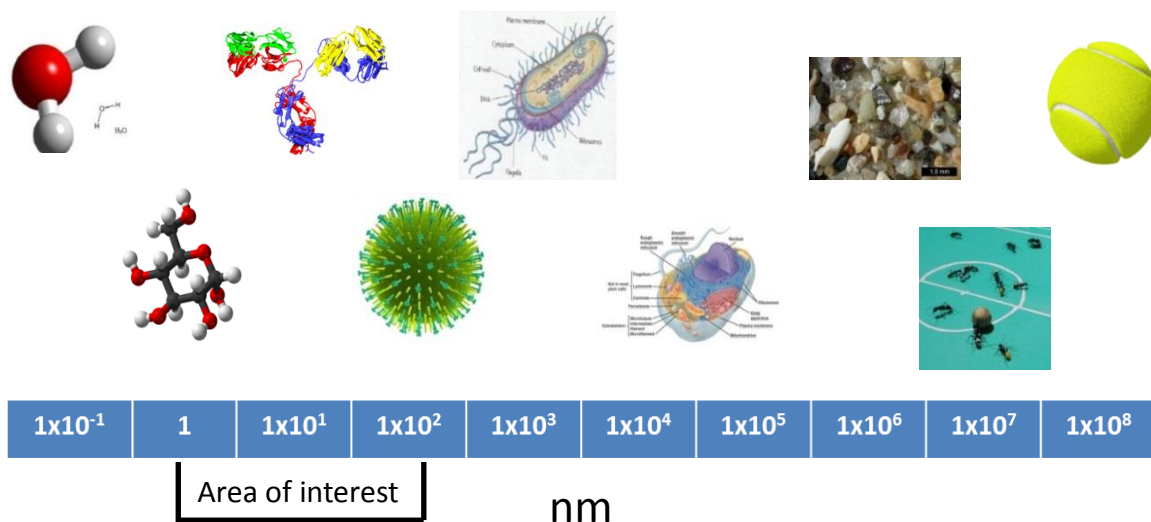
**Fig 1.1 The nanoscale in perspective, with a size-bar showing the area of interest in this project**

Under recent legislation (Regulation (EC) no 1223/2009, 2013), all nanomaterials used for cosmetic and pharmaceutical applications need to be fully characterised for size. Despite this, there are many properties of nanoparticles which are not considered during their design, manufacture and regulation, such as their interactions with the local environment and how they behave in different systems.

With the increased interest in nanomaterials in the scientific community, especially those which have been further modified with small molecules or polymers, there is an increased importance to understand how their surface properties affect their behaviour in different environments, particularly with regards to their diffusion. This is especially true for nanoparticles used in drug delivery applications, when considering how they will cross biological barriers such as mucus.

Diffusion is one of the most important transport phenomena in nature, and is relevant to all fields of science from the atomic level out into the wider universe. Diffusion was first described in the 1830's by Thomas Graham,[12] who noted that gasses of different densities diffused through each other and remained as a mixture rather than separating out. Later in 1855, Adolf Fick studied diffusion by measuring the movement of gas through a

permeable membrane, and founded the Fick equations governing diffusion, known as Fick's laws.[13] This is where the classic definition of diffusion arises; the net movement of particles/molecules from a region of high concentration to a region of low concentration.

An expansion on Fick's principles of diffusion was described by Albert Einstein during work on his PhD thesis looking at the kinetic mobility or "random walk" of particles in solution.[14] The same connection was made independently by Marian Smoluchowski in 1906.[15] It was found that Brownian motion (a process where particles/molecules travel by continuous bombardment from the media they are suspended in)[16] was the mechanism by which diffusion was occurring, explaining Ficks observations. By taking the diffusion principles described by Einstein and Smoluchowski and combining them with Stokes law of fluid dynamics (which measures the friction on a particle in a continuous environment), it is possible to calculate the diffusion coefficient for a spherical particle in a given medium. This is known as the Stokes-Einstein equation (Equation 1.1).[17]

$$Dc = \frac{k_B T}{3\pi\eta d}$$
Equation 1.1,

where $Dc$ is the diffusion coefficient, $k_B$ is the Boltzmann constant, $T$ is the absolute temperature (in Kelvin), $\eta$ is the viscosity of the system, and $d$ is the particle radius. The Stokes-Einstein equation is highly important in the field of nanoscience, as it provides a direct method for determining particle size based on their diffusion coefficient. As already discussed, the size of nanoparticles can govern their quantum-like properties and is also required for regulatory reasons, highlighting the importance of this equation.

Although the primary use of the Stokes-Einstein equation in current technologies is for particle sizing, it can still be used to measure the diffusion coefficient of particles in a viscous environment.

## 1.2 Stokes-Einstein equation

The Stokes-Einstein equation combines Stokes law, describing the frictional force exerted on a spherical object in a continuous viscous environment, and the Einstein-Smoluchowski relation on the kinetic mobility of particles undergoing Brownian motion. By combining these two relationships it is possible to calculate the diffusion coefficient of a particle, based on its movement in a non-turbulent liquid of known viscosity. How this equation is constructed will briefly be discussed in this section.

### 1.2.1 Stokes law

George Stokes, a pioneer of fluid dynamics, identified that it was possible to determine information on the frictional or drag force, exerted on a spherical object in a fluid of sheer viscosity, moving under a continuous velocity, defined by Equation 1.2.[18]

$$F = 3\pi\eta dv$$

Equation 1.2,

where $F$ is the frictional force, $\eta$ is the sheer viscosity, $d$ is the particle diameter, and $v$ is the velocity.[18] This equation, one of the Navier-Stokes equations describing fluid mechanics, assumes a small Reynolds number (a dimensionless number which helps predict similar flow patterns in different fluid flow situations) and as such can only be used under these conditions.[19]

Reynolds number is the ratio of the inertial forces to the viscous forces in a solution, and quantifies how a solution will flow by determining the solutions specific flow conditions, such as laminar or turbulent flow. At low Reynolds numbers, the viscous forces are dominant, resulting in laminar flow (which is required for Stokes law), and a continuous, smooth fluid motion is achieved. At high Reynolds numbers, the inertial forces are dominant, resulting in turbulent flow.[19]

Looking at Equation 2, the frictional force ($F$) can be determined assuming the viscosity and particle diameter are known. The frictional force expressed by this equation refers to the force at the interface between particle and the fluid (known as the solvation shell).

From the frictional force, the friction coefficient can be determined using Equation 1.3, where $f$ is the friction coefficient.[20]

$$F = vf$$  Equation 1.3

It is the relationship between the friction and friction coefficient which allows Stokes law which Einstein theorised could be used to define rotational diffusion.[21]

**1.2.2 Einstein-Smoluchowski relation**

During their work on Brownian motion, both Albert Einstein and Marian Smoluchowski derived independently a relationship between the diffusion coefficient of a particle and its movement caused by Brownian motion (described by Equation 1.4).[14,15]

$$Dc = \mu k_B T$$  Equation 1.4,

where $Dc$ is the diffusion coefficient, $\mu$ is the ratio of the particle's drift velocity to an applied force, $k_B$ is the Boltzmann constant, and $T$ is the absolute temperature (in Kelvin). Einstein theorised that the diffusion coefficient could be linked to the friction coefficient by equation 1.5.

$$Dc = \frac{k_B T}{vf}$$  Equation 1.5

Giving (Equation 1.6)

$$Dc = \frac{k_B T}{F}$$  Equation 1.6

By using Stokes law (Equation 1.2) to calculate $F$; the Stokes-Einstein equation is generated (Equation 1.1), allowing for a calculation of a diffusion coefficient for different sized particles.

**1.2.5 The Stokes-Einstein equation and its relevance to nanoscience**

Besides determining the diffusion coefficient, the Stokes-Einstein equation has another very important use in the field of nanoparticle science. By rearranging the equation, it is possible to determine a particle size (Equation 1.7).

$$Rh = \frac{k_B T}{6\pi\eta D}$$
<div align="right">Equation 1.7</div>

By using techniques which can determine the diffusion coefficient independently of the Stokes-Einstein equation (such as particle tracking technologies, NMR, and scattering techniques), it is possible to rearrange the Stokes-Einstein equation to generate a particle size. With the advancement of technology this process is becoming more accurate, provided the particles are suspended in a solution with a well-known and constant viscosity, such as water. Techniques such as dynamic light scattering (DLS),[22] particle tracking (e.g. Nanoparticle Tracking Analysis, NTA),[23] and Nuclear Magnetic Resonance (NMR)[24] can be used to determine particle size, making it easily accessible for many labs. This rearranged equation is arguably the most common use of the Stokes-Einstein equation, and demonstrates the importance of its use in modern nanoscience.

**1.2.4 Limitations of the Stokes-Einstein equation**

Although the Stokes-Einstein equation is widely used, it has some limitations. Several authors have noted that there are deviations between the experimentally determined diffusion coefficient and those predicted using this equation.[25–27] These can be related to the several factors, including; size of the particle/solute, dynamics of the solvent, and shape of the particle.[28]

Stokes law makes several assumptions of the system being tested (mainly: laminar flow, spherical particles with smooth surfaces, homogenous material, and non-interacting particles). Therefore deviations from this norm can cause variations in the resulting diffusion coefficient. The equation also assumes constant, non-changing sheer viscosity, therefore non-Newtonian fluids can lead to unexpected results.[29] Despite this, attempts have been made to correct for these changes. A study by Achuthan *et al*,[30] proposes a modified Stokes-Einstein equation which takes into account the effective viscosity of the solvent, and also deviations from non-spherical particles. This revised equation has been shown to effectively model the diffusion coefficients of proteins and aggregates in

<div align="right">6</div>

solutions of varying viscosities. However, this equation adds more components, making calculations more challenging and potentially more ambiguous.

In addition to viscosity, the particle size can also alter the calculated diffusion coefficient. If the particle size is too large (or has a non-spherical morphology) then there is reduced Brownian motion exhorted on the particle (causing very little movement), and also the risk of inappropriate flow conditions. This means the diffusion coefficient of larger particles cannot necessarily be easily predicted by the equation.

In addition, if the solute (particle) size is significantly smaller (more than 5 times smaller) than the radius of gyration (Rg) of the solvent molecules, or any macromolecules dissolved in the suspension, then the equation is not valid.[31] The general principle is that where the polymers interact in a solution, the viscosity between the fibres will be smaller. Therefore, if the polymer Rg is higher than the Rh of the particle, then they can potentially move in between the mesh fibres of the polymer, where they will be exposed to a different microenvironment than particles larger than the Rg, and will appear to diffuse quicker than predicted. However, if the particles are larger than the polymer's Rg they will be subjected to movement around the polymer chains as they will not fit in the gaps. Therefore they will be subjected to the viscosity of the polymer solution, meaning they will conform to the Stokes-Einstein equation.[32]

Despite its limitations, the Stokes-Einstein equation remains relatively accurate in determining the diffusion coefficient for particles in certain environments, and has been used widely in the literature.[33–35] However, given the above, the results need to be analysed with the limitations in mind and not treated as absolute, a factor commonly overlooked. Other limitations of this equation has been observed by several authors,[36–39] and are assumed to be due to viscosity, temperature and particle size.

### 1.2.5 Techniques

There are several key techniques which can be used to measure nanoparticle diffusion. These will briefly be discussed, highlighting their strengths and limitations.

### 1.2.5.1 Franz diffusion cells

Franz diffusion cells are commonly used in the pharmaceutical industry to measure the net movement of small molecules,[40] proteins/peptides,[41] or particles[42] through a physiological barrier such as the skin,[43] ocular tissue,[44] or mucosa.[45] Use of a Franz diffusion cell makes it possible to measure the permeability and flux of a molecule through a barrier, which can then be used to estimate bioavailability and calculate the dosage of a drug molecule, in addition to predicting whether it can be delivered by that specific route.

Franz diffusion cells are most commonly used in the development of topical and transdermal formulations and assessing *in vitro* permeation through the skin.[46] An image showing the basic set-up of a Franz diffusion cell can be found in Fig 1.2.
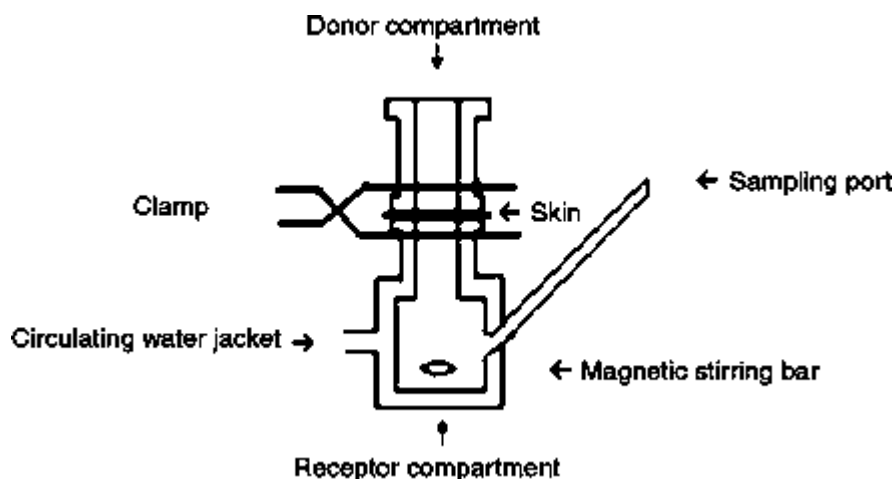


**Fig 1.2 The set-up of a Franz-diffusion cell, taken from Karpanen *et al*.**[47]

Simply, a solution containing the drug, protein, or particle to be studied is placed in the donor compartment, and left to diffuse through the barrier (in this case skin). By taking samples at given time-points and measuring the concentration of molecules/particles in the receptor compartment, it is possible to determine the rate of permeation, lag-time of

the molecule, and when it has reached a steady-state. From this it is possible to calculate the flux and diffusion coefficient of the molecules.

Although a very widely used technique in the pharmaceutical industry and academia with numerous publications, the biggest problem with Franz diffusion cells is time. In order to run an effective experiment, samples should ideally be taken over a minimum of 24 hours, which can result in long experiments, especially when measuring numerous different samples. In addition, following collection samples need to be measured to determine the concentration permeating through the tissue. As such, techniques such as HPLC, UV/vis or fluorescence spectroscopy are used. This requires the use of a calibration curve, and adds further time extensions to data analysis.

### 1.2.5.2 Particle tracking techniques

Particle tracking technologies, such as Nanoparticle Tracking Analysis (NTA), Multiple-Particle Tracking (MPT), and Single Particle Tracking (SPT), allow a diffusion coefficient to be measured by analysing the movement of individual particles in a specific environment.

By tracking individual particles, undergoing random Brownian motion from frame to frame, the average spatial displacement of the particles per unit time can be calculated, and this displacement can be related to the hydrodynamic diameter of the particles through the Stokes-Einstein equation (Equation 1.1). Although translational Brownian motion is a three-dimensional process, it is possible to use a one, two, or three dimensional diffusion coefficient to determine a particles hydrodynamic diameter as described by Equation 1.8:

$$\frac{4}{(x,y)^2} = D_{xy}t = \frac{4k_BTt}{3\pi\eta d} \qquad \text{Equation 1.8}$$

It should be noted that there is no assumption of 2-dimensional movement of particles. All particles are assumed to be moving freely in all 3 dimensions while the measurement is

sampling the projection of each x, y and z component of that movement onto the xy observation plane.

NTA and MPT provide information on particles both in and out of the nanoscale, up to sizes of 2000 nm. However, generally the technology works best at smaller sizes, and optimum conditions are between 20 and 1000 nm, depending on refractive index of the particle and solvent, and system set-up.[48] Because of this, particle tracking techniques are well refined for the study of nanoparticle diffusion, and can show the effects caused by the quantum properties of nanoparticles on diffusion. One major limitation however is hard-drive space. As high-resolution videos need to be recorded, a single 60 s video is around 0.5 GB, therefore a whole sizing experiment (including repeats etc) can generate up to 10 GB of data. This number increases for more complex experiments, which require a larger number of replicates.

Although the use of NTA as a technique to measure diffusion has received less attention compared to MPT (with very few papers reported in the literature), it is possible to measure diffusion directly based on the Brownian motion of the particles,[49] in a similar manner to MPT. The primary difference between MPT and NTA is the fact that NTA is a closed system, whereas MPT involves the use of independent techniques and equipment to determine diffusion coefficients.

Single particle tracking is a similar technique to those already mentioned, however focuses more on tracking particles through biological systems, such as cells.[50] Again, it identifies particle movement through a three dimensional environment, and tracks the particles undergoing Brownian motion over a given time period. From this, a mean squared displacement is calculated, followed by a diffusion coefficient. This technology is commonly used in imaging studies to investigate diseases such as cancer.[51] By tracking particles in a biological system, it is possible to determine protein interactions, and has been used to evaluate cell surface receptor interactions,[52] DNA monitoring,[53] and vesicle movements.[54] Despite its wide use, SPT does carry some limitations compared to NTA

and MPT. It provides less information on the diffusion of particle through liquids and focuses more on the tracking of individual particles in a complex system such as cells, meaning it is hard to measure whether functionalization of particles alters the diffusion and assign quantitative data. These values can be determined using the other two techniques.

Despite the strengths and weaknesses of each technique, particle tracking is becoming increasingly used in the literature, primarily for particle sizing; however it holds great potential in the evaluation of diffusion through a multitude of different systems.

### 1.2.5.3 Diffusion-ordered spectroscopy

Diffusion-ordered spectroscopy (DOSY) is a nuclear magnetic resonance (NMR) technique used to measure the diffusion of molecules in a given environment. In a DOSY experiment a series of pulse-field gradients of different strengths are applied to a sample, producing a series of spin-echo spectra. By using a gradient, it is possible to specifically label individual molecules in their environment. By application of a second gradient (i.e. from a second pulse), it is possible to measure the diffusion time and ultimately a diffusion coefficient for that molecule based on how it moves. Application of different gradient strengths allows for a more accurate determination of the diffusion coefficient.[55] In addition to determining a diffusion coefficient, there are reports on using DOSY to determine other properties about a molecule, such as molecular weight (with use of external calibration curves and normalised diffusion coefficients),[56] particle size (by rearranging the Stokes-Einstein equation),[24] and structure assessment/particle interactions (by assessing how diffusion coefficients change in the presence of different species in the mixture).[57]

Regarding nanoparticle diffusion, DOSY has been extensively studied to examine the diffusion coefficient of particles in numerous sample environments, and of multiple different make-ups,[58] including polymer functionalised nanoparticles.[59] This helps provide insight into how the particles are behaving on a molecular basis (generating information

on their shape, structure, and interactions). It is therefore useful in several fields, such as catalysis where nanomaterials are becoming of increased interest due to an enhanced surface area.[60,61]

Although DOSY is a highly accurate technique for measuring diffusion and will allow for easy determination of any contaminants in the sample (i.e. starting materials), its major limitation is cost. NMR experiments can be expensive to perform, limiting their accessibility. They can also be very lengthy, depending on the number of samples and temperatures being measured at, and require specialist expertise for both running the experiment and analysing the data.

With the advancement in technology over the past several decades, the ability to measure nanoparticle diffusion at higher resolutions and more accurately makes it possible to further probe the interactions between particle and environment, and also makes it possible to develop systems with a manipulated diffusion coefficient, making them more efficient for their application.

## 1.3 Why use nanoparticles?

As already described, nanoparticles are very small, and therefore have a large surface area and can exhibit quantum-like properties (dependent on the size and elemental composition of the material). As such, they carry significant advantages over larger bulk-materials. There are many examples in the literature of different nanomaterial formulations including metallic nanoparticles,[62] organic nanoparticles,[63] and silica nanoparticles.[64] By further functionalising these particles with small molecules, biomolecules or polymers, it is possible to further expand upon their physicochemical properties whilst still maintaining all the advantages of using a nanomaterial. Thus, combining specific moieties to a particle surface allows for numerous applications such as targeted drug delivery,[65] or controlled/triggered drug release.[66,67]

**1.3.1 Effect of nanoparticle core**

Due to their small size, nanoparticles offer several advantages over larger particles of similar compositions, and are currently being used in various formulations available on the market in a variety of industries. Table 1.1 provides some examples on the use of nanoparticles in consumer products, their composition and reason for use.

**Table 1.1 Nanoparticles found in different consumer products, and why they are used.**

| Nanoparticle | Application | Reason for use | Reference |
|---|---|---|---|
| Copper nanoparticles | Deodorant | Odour elimination | 68 |
| Titanium dioxide and zinc oxide | Sun-cream | Block the sun's rays through reflection, and leave no noticeable residue on the skin | 69 |
| Iron nanoparticles | Environmental remediation | Transformation and detoxification of environmental contaminants | 70 |
| Silver nanoparticles | Clothing | Antimicrobial activities | 71 |
| Quantum dots | Electronic displays and light emitting technologies | High luminescence efficiency, tuneable colour spectrum, and very energy efficient | 72 |
| Liposomes/polymeric nanoparticles | Drug delivery | Small, highly penetrating, and low toxicity | 73 |

These are just some of the applications nanoparticles are currently being used in; however there are numerous other applications presented in the literature. Despite their versatility across numerous industries, one of their biggest applications is in the pharmaceutical industry, mainly as drug delivery systems.

### 1.3.2 Nanoparticles in the pharmaceutical industry

There are many examples in the literature of different applications of core-nanoparticles made from different composites. Some of the most widely studied nanoparticles will be discussed here.

### 1.3.2.1 Gold nanoparticles

Gold nanoparticles (AuNPs) have been in use since ancient Roman times, where they were used in the manufacture of stained-glass windows. Due to their rapid and facile synthesis,[74] ease of functionalisation allowing for a large array of surface moieties,[75] and wide range of morphologies (such as spheres, rods, stars, and rings)[76,77] they are very attractive for biological and pharmaceutical applications, especially in bioimaging and drug delivery.

There are numerous reports on the optical properties of gold nanoparticles with various morphologies. These optical properties stem from a surface-plasmon resonance effect, a phenomenon which is size dependent.[78] Smaller particles (<20 nm) appear red in colour, however as the particles get larger, their colour changes to purple, blue, and (in larger sizes) exist in the near-IR region. This is because when light interacts with the electrons on the surface of the particles, it causes them to oscillate. For larger particles, there is a denser cloud of electrons around the particle, causing them to oscillate at a different frequency, thus emit light at a lower wavelength, and so appear different in colour.[79] These changes are clearly detectible using UV-Vis spectroscopy, giving a clear sharp absorbance peak.[80,81] By changing the morphology and surface chemistries of the particles, it is possible to tune their optical properties making them ideal for bespoke applications in the bio-imaging field, phototherapy and other novel applications.[82]

The optical properties of gold nanoparticles combined with their ease in synthesis, large array of surface functionalities, and good biocompatibility make them of particular interest to the pharmaceutical industry, especially in the field of diagnostics.[83]

### 1.3.2.2 Silica nanoparticles

Silica nanoparticles (SNPs) are another popular system. Their interest to the pharmaceutical industry stems from the fact that they can be synthesised to contain pores on their surface. These so-called mesoporous SNPs can allow for easy loading of a small molecule, and controlled release by using environmentally-sensitive polymers.[84] As with gold nanoparticles, they can be easily synthesised using cost-effective methods, and can be readily functionalised with a variety of surface moieties, allowing for further modifications.

Traditionally SNP's are made from $SiO_2$ in the presence of a rod-like structure or surfactant, allowing for the formation of pores.[85] The strong silica-oxygen bonds make the particles very stable in harsh environments, such as the stomach or endosomes. Despite this, their biocompatibility is disputed by several factors, including; size, method of synthesis, and surface functionality, and there is much debate in the literature concerning their toxicity.[86] In general, these particles appear to be safe at low concentrations, thus making them an ideal model particle to study. SNP's will be covered in more detail in Chapter 2.

### 1.3.2.3 Quantum dots

Quantum dots (QDs) are semiconductor devices, which exhibit bright fluorescence (and narrow fluorescence emission bands), very long Stokes shifts, good resistance to photobleaching, and tuneable emissions at a single excitation wavelength.[87] Traditionally, QDs are composed of a semiconductor core (usually CdSe) surrounded by a shell composed of another semiconductor (such as ZnS). By controlling the size, shape, and/or chemical composition of the core and shell, it is possible to tune the emission wavelength over a wider range than the individual semiconductors themselves.[88]

Typically, QDs exist in sizes <10 nm as larger particles start to emit light outside the visible range. Although their size is not necessarily a problem in some applications, it

limits their application as potential fluorophores and in electronic devices. It is possible to functionalise them with various surface ligands[87] or polymers[89] allowing them to be used as fluorophores for cell labelling, and *in vivo* imaging.[90] Indeed, they have been referred to as the next-generation of fluorophore.

QDs have applications in several industries. They have an emerging interest in the electronics industry for applications in technologies such as quantum computing,[91] and light emitting devices (such as televisions, mobile phones, and monitors).[92] However, one of their most widely reported applications is in the field of biology, as next-generation fluorophores.

Due to their sub 10 nm size and wide versatility of their surface chemistry, QDs can be functionalised to interact with specific targets, allowing DNA, RNA, and protein conjugation for use in bioimaging;[93] there are examples in the literature of QDs used for both *in vitro* and *in vivo* labelling.[94] Despite their popularity, a question does remain over their cytotoxicity and there is much debate in the literature over this subject.[95,96] This unknown cytotoxicity is the major draw-back of QDs, and despite attempts to minimise their toxic nature[97] *in vivo* applications of QDs are very limited. As such their main application lies in *in vitro* cell labelling, and as encapsulated fluorophores.

### 1.3.2.4 Magnetic nanoparticles

Magnetic nanoparticles (MNPs) are nanoparticles which can be manipulated by application of a magnetic field. There are several reported synthetic techniques used in the literature, including; the co-precipitation of metal salts composed of the magnetic elements (iron, cobalt, or nickel), the thermal decomposition of organometallic compounds, or using reverse-micelles in a microemulsion.[98] Different routes of synthesis produce particles with different compositions, which allow them to have a wide-range of properties suitable for multiple applications, including cancer treatment (using a technique called magnetic hyperthermia, where a magnetic field is applied to magnetic nanoparticles

*in vivo*, which produces heat and kills local cancer cells),[28] targeted drug delivery[99], MRI contrast agents[100], bioimaging[101], and energy storage[102]

Due to their magnetic nature, MNP's have been broadly investigated for targeted drug delivery. By encapsulating the particles in a shell allowing for sustained circulation, it is possible to target these so called "smart nanoparticles" to a specific area of the body by applying a magnetic field to said area.[103] In addition to targeted delivery, there are studies exploring the application of MNP's in thermotherapy. When exposed to an alternating magnetic field, MNP's generate heat due to oscillations in the magnetic elements which make-up the core. By taking advantage of the enhanced permeability and retention effect (EPR), which is the localisation and bioaccumulation of nanoparticles in tumour tissue, it is possible to localise nanoparticles in tumour tissue, and produce a localised increase in temperature, which causes the cells to die.[104]

Although a highly promising therapy, there are concerns over the safely and removal of MNP's from the body after treatment is complete. As with other nanomaterials, MNP toxicity is centred on several key parameters, namely; composition, size, surface chemistry, and physical properties (charge, solubility etc.). The disadvantage MNP's have over other nanoparticle formulations is that, by definition, they have to be made up of magnetic elements, which can lead to leaching of free metal ions causing a large increase in reactive oxygen species leading to systemic toxicity.[105] In addition to this risk, there is a large volume of evidence suggesting MNP's will accumulate in the body and not be removed, thus extending the risk of toxicity.[106] As such, MNP's need to be extensively modified making them more biocompatible which could have detrimental effects to their magnetic properties, rendering them less effective.

In addition to targeted drug delivery and thermal therapy, MNP's have also been used as MRI contrast agents. Superparamagnetic iron oxide nanoparticles have been investigated in this regard, as they can increase the signal intensity detected by MRI by shortening the longitudinal and transverse relaxation of nearby protons.[107] Given their tuneable magnetic

properties, and versatile surface chemistries, MNP's carry significant advantages over other MRI contrast agents,[108] and indeed some formulations are available on the market, such as Feridex IV, Sinerem, and Ferumoxsil.[109]

**1.3.2.5 Polymersomes, liposomes, and micelles**

From a biological and pharmaceutical perspective, one of the most interesting nanoparticle types are polymersomes, liposomes, and micelles.  Indeed current nanoparticle formulations available on the market (Doxil)[110] fit into this category.  Although all three are either monolayered or bilayered vesicles, there are some key differences between them.

Polymersomes are artificial vesicles composed of synthetic block-polymers.  Traditionally they are hollow, allowing for the easy encapsulation of a drug.[111]  These block polymers are composed of a hydrophobic core, surrounded by hydrophilic blocks (or *vice versa*), and assemble in solution to form bilayered particles,  Due to their synthetic nature, polymersomes are highly versatile in nature and can be designed to show specific properties, allowing for a more controllable release.  Although they can be tailored much more readily to specific applications, the down-side is that the potential for polymersomes to be cytotoxic is greater due to their synthetic origin.

Liposomes are particles made-up of lipids or surfactants which comprise a polar head group and a non-polar body.  In solution, a liposome will exist as a bilayer, similar to a polymersome.  The difference is that they are from natural origin rather than synthetic and are comprised of lipid bilayers which self-assemble to form vesicles.  In contrast to polymersomes, they are less toxic in nature, exhibit good biocompatibility and offer a long circulation time.  However, they have a high start-up cost, are poorly soluble in water, and can exhibit leakage of materials which have been loaded inside the particle.[112]

Micelles are different in that they are monolayered in nature, and can be comprised of either polymers (such as surfactants) or lipids.  Because of this, they are generally much

smaller in size and can therefore penetrate into tissues and cells via more passive mechanisms than their larger counterparts and exhibit good vascular permeability.[113] Due to their smaller size, they have a much larger surface area, and therefore allow for a greater degree of drug-loading. However, they are relatively unstable in suspension, and will readily leak encapsulated molecules with ease, leading to unwanted premature release.[114]

For drug delivery applications, micelles and micelle-type nanoparticles are one of the most heavily studied due to good biocompatibility, easy and cost effective production, and ease of loading. Polymers and lipids are also used in combination to make these formulations, which will further enhance their stability and biocompatibility. This combination can be used to minimise the disadvantages of using polymersomes and liposomes.[115] There are many types of polymer used in such cases such as poly(ethylene glycol),[116] and poly(lactic-co-glycolic acid).[117] These nanoparticles are most promising as drug carriers, and are being widely studied for such applications.

### 1.3.2.6 Virus-like particles

Virus-like particles (VLPs) are empty (non-pathogenic) virus particles, which have been engineered to remove any genetic information, inhibiting their ability to replicate and reproduce. VLPs are produced by transducing prokaryotic or eukaryotic cells with viral DNA or plasmids, in order to create the protein coat, or envelope.

The main application for VLPs is in the production of vaccines, as they provide safer alternatives to attenuated viruses (due to their inability to replicate).[118] Two good examples are the hepatitis B vaccine, and human papilloma virus vaccine,[119] and there are many others in development or undergoing clinical trials.[120]

Although the bulk of the literature looks at the vaccine potential of VLPs, there are examples of VLPs being studied as drug delivery vehicles.[121] As they can be mass produced at cost-effective prices, alongside good biocompatibility, they are very attractive

to pharmaceutical companies as delivery vectors.[122]  As they are protein-structures, it is also possible to modify the surface amino acids, allowing for more facile control over the particle, and its drug release parameters, making them potentially a very robust particle.

## 1.3.3 Surface modifications

Nanoparticle surface coatings are primarily used to maintain the stability of the particle itself and limit aggregation.  In addition, by using specific pharmaceutically-relevant molecules, it is possible to: target the particle to specific proteins,[123] target specific cells/bacteria,[124] or increase the bioactivity of drug complexes and alter bio-distribution.[125] With the addition of these surface modifications there is the potential for altered diffusion. This is due to factors such as size, shape, hydrophobicity, and charge changing the interactions between the particle and the surrounding environment.  This makes surface modifications a very promising strategy for manipulating the diffusion coefficient of nanoparticles.

### 1.3.3.1 Polymer coatings

In addition to their core chemistry, it is common practice to functionalise nanoparticles with polymers in order to improve their colloidal stability.  In addition, it is possible to further expand their application, by manipulating the particles physico-chemical properties.  By combining these with the novel properties of the core nanoparticle itself, it is possible to create diverse systems suitable for multiple applications.  Table 1.2 provides some examples of polymer functionalised nanomaterials, with their reported applications.

**Table 1.2 Core-shell composition and applications to the pharmaceutical industry of polymer functionalised nanomaterials**

| Polymer | Core | Application | Reference |
|---|---|---|---|
| Poly(vinyl pyrrolidone) | Silver | Anti-viral, specifically HIV | [126] |
| Poly(ethylene glycol) | Polystyrene | Increases rate of diffusion through mucus | [127] |
| Poloxamer | Polystyrene | Drug delivery, low phagocytic uptake | [128] |
| Poly(vinyl benzyllactonamide) | Polystyrene | High affinity for hepatocytes, targeted hepatocyte delivery | [129] |
| poly(methyl methacrylate) | Polymersome | Increased uptake of particles in endothelial cells of the blood brain barrier | [130] |
| Dextran | Polymersome | Hemaglutinating and targeted oral delivery | [131] |
| Chitosan | Liposome | Insulin delivery | [132] |
| poly(*N*-isopropylacrylamide) | Superparamagnetic Iron Oxide | Enhanced MRI imaging | [133] |
| poly(2-methyl-2-oxazoline) | Polymersome | Delivery of non-viral DNA. | [134] |
| poly(hydroxyethyl-L-asparagine) | Liposome | Longer blood circulation time than PEG | [135] |
| N-(2-hydroxypropyl)methacrylamide | Polymersome | Intracellular drug delivery | [136] |
| poly(vinyl alcohol) | Polymersome | Oral delivery of anticancer drugs | [137] |

From Table 1.2, it is clear that the potential application of polymer-functionalised nanoparticles is vast and diverse. As such, there is continuing research into this area, using several different grafting techniques; grafting from, grafting too, and during synthesis.[138]

The "grafting from" approach is where polymers are synthesised off the surface of nanoparticles using living radical polymerisation reactions. This method allows the nanoparticles to be functionalised in a controlled manner, using techniques such as atom transfer radical polymerisation (ATRP) or reversible addition-fragmentation chain transfer (RAFT).[139] For this to be successful however, the nanoparticles need to carry a specific surface moiety. This varies depending on the type of reaction; e.g. a RAFT agent for RAFT polymerisation (such as trithiocarbonates, or dithiocarbamates), or a halide ion in ATRP reactions. By controlling the mass of monomer units, and the choice of catalyst/initiator, it is possible to generate polymers with a well-defined molecular mass and low polydispersity (a measure of how heterogeneous a polymer/particle size is). This is highly advantageous for polymer-nanoparticle composites as it ensures even coverage on all nanoparticles in the suspension, each with a well-defined, monomodal polymer distribution functionalised onto its surface. This technique also allows nanoparticles of a different elemental make-up to be functionalised without the risk of adverse reactions. Indeed, there are numerous examples of different core nanoparticles functionalised using the "grafting from" approach, such as CdSe nanocrystals functionalised with polystyrene, poly(methacrylate) and poly(butyl acetate),[140] silica nanoparticles functionalised with polystyrene,[141] and cellulose nanocrystals functionalised with poly($\varepsilon$-caprolactone).[142]

Although this technique is very useful for functionalising nanoparticles with a well-defined structure and even coverage of polymer, it does carry some drawbacks; it can only be used to generate polymers of low molecular weight, it requires specific reaction conditions which could affect the core nanoparticle itself, and it requires very specific surface

moieties in order for the monomer to initially bind to the particle surface, which must be taken into consideration during the synthesis of the particle itself.[143]

The "grafting too" approach on the other hand, allows polymers to be added onto the surface, rather than grown off the surface. This technique involves polymers with specific end-group functionalities to be attached covalently to specific surface moieties of the nanoparticles. As such, there is much more versatility compared to the "grafting from" approach, meaning core particle synthesis can be more varied. It also allows attachment of commercially available polymers, eliminating the polymerisation step.[144] Again, this technique does not discriminate against the composition of the core, however does require the polymer to be synthesised separately before grafting, and thus can take longer (unless a commercially available polymer is used). In addition, when using commercially available polymers, this process can be more costly than the "grafting from" approach.

There are numerous examples in the literature of polymer coated nanoparticles using the "grafting too" approach, including; silica nanoparticles functionalised with poly(oxazolines),[145,146] gold nanoparticles functionalised with poly(2- vinylpyridine),[147] and superparamagnetic iron oxide nanoparticles functionalised with PEG.[148] Due to the more versatile nature and ability to use commercially available polymers, the "grafting to" approach appears more popular in the literature, as more varied chemistries available.

Another popular form of synthesising polymer functionalised nanomaterials is to add the polymer into the reaction mixture during nanoparticle synthesis, or used to drive the synthesis itself. This method provides a more rapid synthesis, and can be more cost-effective as all the reagents and starting materials are used in the first instance and there are no subsequent synthetic steps. However, it can lead to more polydisperse nanoparticles, as there is little chance of an even coverage on each nanoparticle. In addition, depending on the size of the polymer, they can be harder to purify to obtain a pure sample. There are fewer examples of this technique in the literature, as its limitations out-weigh the benefits of a one-pot reaction.[149]

As discussed here, there are numerous applications and synthetic strategies in the design of polymer functionalised nanoparticles. Not only do the polymers act as stabilising agents to the colloidal dispersion, making them less prone to aggregation, but they also enhance their applications; making the particles more versatile in nature, adding to their unique properties.

### 1.3.3.2 Protein/antibody functionalised nanoparticles

In addition to polymer functionalised nanoparticles, there are examples in the literature of nanoparticles functionalised with proteins or antibodies. Indeed, a commercially available protein-bound nanoparticle formulation is already on the market for treatment of breast, lung and pancreatic cancer (Abraxane).[150,151]

Due to their charged surfaces in conjunction with large surface area, unfunctionalised nanoparticles exhibit strong interactions with proteins *in vivo* and is a major concern regarding their safety as drug delivery vectors.[152] This can be overcome with further modification, using small molecules/polymers. However, it is also possible to covalently bind proteins or antibodies to the surface of nanoparticles. By doing so, it is possible to enhance the colloidal stability of the particles (where the proteins act in a similar structural manor to polymers, as already discussed), and also enhance their biocompatibility due to the biological origin of proteins. In addition (certainly in the case of antibodies), it is possible to target the nanoparticle to specific cell types and tissues by taking advantage of protein-receptor interactions on the cell surface. This is a popular strategy for use in combination with magnetic nanoparticles which can induce hyperthermia conditions when exposed to a magnetic field. By functionalising the nanoparticles with proteins which have an affinity to cancer cells, and applying a magnetic field, the nanoparticles will cause the cancer cells to die, leaving healthy cells alive.[153–155]

In addition to protein functionalised nanoparticles, examples of antibody functionalised nanoparticles can be found in the literature.[156,157] Given that antibodies bind to specific epitopes, they can be used to target specific cells, and are often used in fluorescent

imaging techniques. Based on this, some researchers[158] have grafted antibodies to nanoparticles to achieve more potent targeted drug delivery systems. Antibody based treatments are becoming more common as pharmaceutical agents and are available as marketed therapeutic drugs, for example Herceptin. It has been shown that by functionalising silica nanoparticles with Herceptin, the drug has greater specificity and can be readily internalised into cells via endocytosis. This is due to the enhanced surface area of the nanoparticles and high degree of antibody binding on the surface. This is not the only example of using antibody functionalised nanoparticles for enhanced therapeutic effects. Other examples include; antibody functionalised superparamagnetic nanoparticles for enhanced MRI visualisation of specific targets,[159] antibody functionalised calcium phosphate nanoparticles as intracellular targeting for gene delivery,[160] and antibody functionalised gold nanoparticles for drug detection via fingerprint analysis in forensic investigations.[161] This method also has potential in the visualisation of cancerous tissues both *in vitro* and *in vivo*.[162]

Although protein and antibody functionalised nanoparticles show potential in the field of drug delivery, they do contain some inherent weaknesses. Due to the complex nature of proteins, and their highly conserved structure, binding molecules to them could initiate conformational changes, thus rendering them inactive. The chemistry involved (such as high/low temperatures, solvents and harsh chemicals), could also affect the protein structure, rendering it ineffective. In addition, it is possible that this conformational change could invoke an immune-response from the body, making the treatment ineffective and potentially causing adverse reactions for the patient.

Despite these weaknesses, protein and antibody functionalised nanoparticles show good potential, especially in cancer research and gene delivery.[163]

### 1.3.3.3 Small molecule functionalised nanoparticles

Another method of nanoparticle functionalisation is the attachment of small molecules. By functionalising nanoparticles with small molecules, such as sugar residues, amino acids or

drug molecules, it is possible to alter their surface chemistry and allow them to interact with specific cellular targets, such as membrane protein receptors.

One of the most common small-molecule functionalities grafted to nanoparticles is fluorophores. By fluorescently labelling a nanoparticle it is possible to monitor their transit in biological tissues either *in vitro* or *in vivo*.[164] This allows information to be generated on specific tissue interactions of the nanoparticles, or if they are localising in specific organelles or tissues. It also allows for the detection of particles in more complex systems, making it possible to assess their interactions with the surrounding environment, such as in diffusion studies across mucus barriers, or across the cornea.[52,165] The limitation to this however, is that the fluorophores can quench at a faster rate than normal due to their large surface area and small point of detection.

As an alternative to fluorophores, it is possible to label nanoparticles with a radioactive tag. This makes it possible to track nanoparticles in a living system, whereas *in vivo* fluorescent imaging requires the organism to be dead as the fluorescent emission will not penetrate out of the organism. Radioactive isotopes can either be included in the synthesis of the particle itself, or used as labels, functionalising the surface allowing for detection.[166] This technique is regularly used to assess the EPR effect of nanoparticles, and measure their localisation in the body and tumour cells.[167,168] Although this technique is very useful for tracking and mapping the locations of nanoparticles in real-time in an *in vivo* system, it is very expensive, can be dangerous due to the radioactive nature of the samples, and requires specific handling and safety assessments. Therefore it is rarely used for *in vitro* imaging.

In addition to labelling moieties, such as radio labelled and fluorescent probes, there are also reports of nanoparticles functionalised with biomolecules, such as amino acids,[169] nucleic acids,[170] and sugar residues.[171] The addition of biomolecules to the surface of a nanoparticle will not only enhance its biocompatibility, but also allow it to interact with specific cellular targets, allowing for a targeted delivery mechanism on the nanoparticle.

The attachment of small molecules to a nanoparticle surface allows for many different features, especially in bioimaging and tracking technologies. Small molecule functionalisations are often used in combination with polymer or protein additions, making it possible to track the movements of these particles, or enhance their potential to interact with specific cell types.

## 1.3.3.4 Stimuli-responsive nanoparticles

Nanoparticles with stimuli-responsive polymers, such as poly(N-isopropyl acrylamide) (PNIPAM), or poly(acrylic acid) (PAA), allow for novel surface properties of a nanoparticle which gives them unique properties not expressed by other functionalised nanoparticles. These so-called "smart" nanoparticles, are being extensively studied, in part for controlled release studies, controlled biodegradation, wound-healing, environmental remediation, and energy storage.[172]

PNIPAM is a commonly used temperature responsive polymer (TRP). As PNIPAM undergoes coil-globule phase transition, it is an ideal surface modifier for porous silica nanoparticles, as (below the lower critical solution temperature (LCST) of 32 $^{o}$C) it allows the pores to open up and release their contents.[173] By using targeted cooling techniques, it is possible to initiate the release of a drug molecule this way. Several authors have found that it is possible to reach a level of controlled uptake and release of a drug using this technique. For example, You *et al*[174] reported that fluorescein uptake was retarded when PNIPAM was in its globule conformation, however when in its coil conformation (below the LCST), the molecules are free to diffuse out through the pores of the silica and through the polymer. It was found that around 80% of the fluorescein was released over 48 hours at 25 $^{o}$C, as opposed to <20% release at 38 $^{o}$C. This is useful in terms of loading (as drug molecules can be readily trapped inside the particles by a change in temperature), however, in terms of systemic release, as the LCST exists below physiological temperature, the release mechanisms need to be further enhanced. However for use as a local subcutaneous release, this could be of great interest, as the

local temperature of the skin can be decreased easily without the addition of long-term adverse effects.

By combining the coil to globule phase transition of PNIPAM to the surface of porous nanoparticles, it is possible to trap molecules inside. This is because the polymer (in its hydrophobic globule state) will block the pores in the particle, thus not allowing molecules to escape. However, below the LCST in its coil conformation, molecules are free to diffuse out the pores, and into the external environment. This is depicted in Fig 1.3.[173]



T < LCST          T > LCST
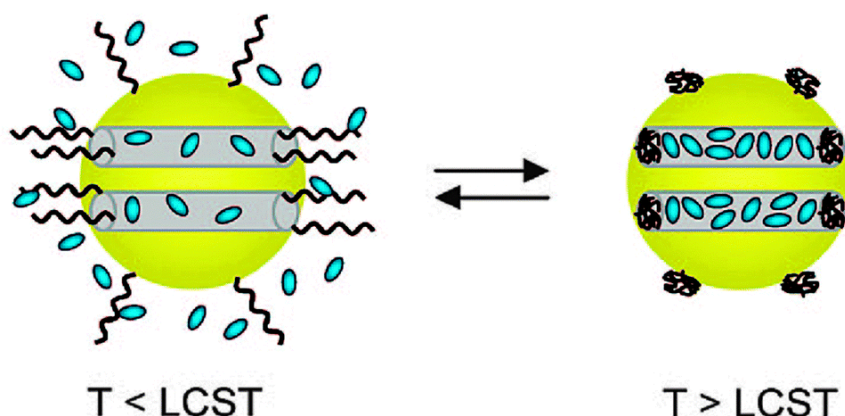
**Fig 1.3 Porous silica nanoparticles functionalised with PNIPAM can undergo phase transition allowing the globular hydrophobic form of PNIPAM (above the LCST) to block the pores, thus not allowing release of any encapsulated molecules.** Below the LCST (in its hydrophilic coil conformation), PNIPAM allows molecules to be readily released from the pores[173]

However, this in itself can cause problems in some areas, for example drug delivery. With an LCST 32 $^{o}$C, the polymer will undergo phase transition prematurely in a physiological system, where the temperature is 37 $^{o}$C. Therefore using PNIPAM in this respect will be of little use, as no drugs can be released systemically. However by combining this polymer with other polymers (for example pH responsive polymers such as poly(acrylic acid)), it is possible to overcome this obstacle and obtain a dual-responsive, switchable nanoparticle that can effectively release a drug compound[175].

Although silica functionalised-PNIPAM nanoparticles show some limitations with regards to drug delivery, there are methods to overcome this. Baeza *et al*[176] reported on the use

of poly(ethyleneimine)-b-poly(N-isopropylacrylamide) grafted to porous silica nanoparticles which contain magnetic iron core. By loading drug molecules into the hydrophilic PNIPAM shell, and a protein into the silica pores, it was found that upon heating by an alternating magnetic field, these two components would release separately, where the drug molecule being released instantly as the PNIPAM undergoes phase transition followed by a slow release of the protein. This illustrates that multiple drugs can be released from a single nanoparticle composite, and that release can be remotely controlled by use of an alternating magnetic field. However, the severe limitation of this study remains that the LCST of PNIPAM is around 32 $^{o}$C, where physiological temperature is 37 $^{o}$C. Therefore the polymer will undergo phase transition before it can reach its target, so the components will release prematurely, a fact overlooked by the authors in this study. Despite this, the particle designed in this study offers potential in the field of drug delivery, as it shows the remote controlled release of two compounds from one particle.

Another useful TRP grafted to silica nanoparticles was described by Sun *et al,*[177] who created a biocompatible zwitterionic sulphobetaine copolymer, functionalised onto the surface of a silica nanoparticle. Poly(2-dimethylamino)ethyl methacrylate (PDMAEMA) was initially grown off the surface of the silica nanoparticles by RAFT polymerisation, followed by further functionalisation of the tertiary amine groups in the polymer by 3-dimethyl(methacryloyloxyethyl)ammonium propanesulphonate (DMAPS). Upon functionalisation with the DMAPS, no phase transition was seen and the particle size remained constant at temperatures between 25 and 65 $^{o}$C. However, when the particles were in an ionic solution of either 0.1 or 0.2 M NaCl, the particles underwent phase transition between these two temperatures. The zwitterionic DMAPS enhances the particles biocompatibility, and indeed they exhibited little toxicity in the MTT assay, whereas the PDMAEMA defines the particles temperature-responsive nature.

To test drug release behaviour, the particles were loaded with rhodamine B. The release kinetics greatly improved at temperatures above 45 $^{\circ}$C, at pH 7, 0.2 M NaCl. However release was severely impaired at 30 $^{\circ}$C under the same conditions. With the LCST of the system being 45 $^{\circ}$C, this explains the release profile demonstrated, making the particles potentially suitable for thermal therapy. Therefore, due to the presence of ions, these particles will undergo a phase-transition in physiological systems, whilst remaining stable in pure water; making them ideal vehicles for drug delivery.

A further study with PDMAEMA grafted onto $SiO_2$ nanoparticles examined the phase transition using two variables; temperature and pH.[178] As PDMAEMA is both temperature and pH responsive, it offers potential for drug delivery, despite its high LCST (>45 $^{\circ}$C). Although no release studies were performed in this specific study, the lack of toxicity of reducible PDMAEMA[179] means that this polymer is attracting a lot of attention in terms of drug delivery.

## **1.4 Biological barriers and how to overcome them**

As nanoparticles are so small, they can cross membranes and barriers designed to stop foreign objects entering systemic circulation, and causing harm to the body. Encapsulated poorly water soluble drugs may benefit from this, as they could be administered orally whilst reducing their typically poor bioavailability. Therefore understanding how nanoparticles diffuse through biological barriers is of key importance, in order to maximise effectiveness of the encapsulated drug.

As nanoparticles can act as either drug carriers or as drugs themselves (with the drug conjugated to the particle surface), understanding how they diffuse through biological barriers, such as mucus membranes, and whether the rate of diffusion can be manipulated to speed up diffusion, is gaining interest in the literature.[180]

### 1.4.1 Mucosal barriers

In the body there are numerous barriers a drug or nanoparticle will need to cross in order to reach its therapeutic target. Mucosal membranes are one such example and coat parts of the body exposed to the harsh external environment, such as the lung airways, nasal cavity, and gastro-intestinal tract. Mucosal barriers consist of five distinct layers; a layer of mucus, the mucosa, the submucosa, and the muscularis externia and serosa.

### 1.4.1.1 Mucus

Mucus is a complex mixture of glycoproteins, salts, lipids and cellular debris which form a hydrogel protecting mucosal cells from the harsh external environment. Apart from water (which makes up 95-99.5% of mucus)[181] the primary components are mucin proteins, heavily glycosylated proteins which are secreted by goblet cells located in the epithelium. According to HUGO (the Human Gene Nomenclature Committee), there are currently 21 known mucin genes in the human genome,[182] of which there are two distinct types; the secretory mucins, and adherent mucins; both of which are between 0.5 and 20 MDa in size.

Secretory mucins have two distinct regions; a central block containing tandem repeats of serine, threonine, and proline residues which are heavily modified by glycosylation, and two cysteine rich domains at the N and C termini, respectively. These cysteine-rich domains allow the protein to cross-link with other mucins by the formation of disulphide-bridges, creating a mesh-like structure.[183] Typically, each oligosaccharide unit contains 8-10 sugar residues, of which the main constituents are galactose, fructose, N-acetylglucosamine, N-acetylgalactosamine and sialic acid.[184] These are bound to the amino acid backbone by O-linked glycosylation. Adherent mucins differ in that they contain a hydrophobic terminus, allowing it to anchor into the cell membrane.[185] They are smaller than secretory mucins and are secreted by foveolar cells rather than goblet cells, and is around 100-200 μm thick.[186]

Both the adherent and secretory mucins form a gel which lines surface epithelial cells exposed to the external environment, such as the GI tract, airways, vagina, and ocular tissue. This gel traps foreign bodies and molecules, preventing them from reaching the underlying cells thus causing damage. This is a significant barrier to overcome in terms of drug delivery, as it prevents lipophilic compounds from entering systemic circulation. In addition, large particles (>300 nm) cannot penetrate through the mucin fibres and will become trapped.[183] However, there are examples of mucoadhesive systems which have been specifically engineered to allow sustained release over a period of time for the treatment of certain forms of cancer, fungal infections, anti-inflammatory drugs and ulcers.[187] However, the limitation to these kinds of formulation is mucus clearance.

Mucus clearance is where the mucus layer is stripped away, and replaced with a fresh one, allowing removal of any trapped compounds. The rate of clearance depends on the location. For example, the intestinal mucosa is estimated to be replaced every 47–270 min,[188] whereas in ocular tissue it is between 15–20 h.[189] This adds another barrier, as the rate of mucus clearance needs to be considered as to allow the formulation sufficient time to achieve its therapeutic effect.

In addition to protective roles, mucus also serves to lubricate certain tissues, allowing easy passage of food and other compounds to their destination. This is especially important in tissues such as the oesophagus and airways.

**1.4.1.2 Mucosa**

Underneath the mucus layer, lies the mucosa. The mucosa consists of a layer of epithelial cells, the lamina propria ( a loose layer of connective tissue which keeps the epithelium rigid and in place), and the muscularis mucosae (a thin layer of smooth muscle).[190]

The mucosa epithelia also contains specific cells allowing the normal function of the organ in which it is located. For example, the gastric mucosa contains parietal cells which control the pH balance of the stomach and secretes HCl and chief cells which secrete

digestive enzymes such as pepsin and gastrin.[191]  The intestinal epithelia on the other hand, contains a large number of enterocytes, which enhance the absorption of nutrients.[192]  In addition to changes in cell type, the general histology of the epithelia also changes depending on location.  The stomach contains gastric pits, whereas the small intestine contains villi and microvilli which enhance absorption.

Underlying the epithelia is the lamina propria.  The lamina propria is a layer of loose connective tissue, comprised mainly of fibroblasts, fibrocytes, and endothelial cells.  It also contains capillaries and lymphatic tissue, providing the epithelial cells with a blood supply.[193]  The lamina propria contains a large number of cells from the immune system, including B-cells, T-cells, and dendritic cells.[194]  As the mucosa protects the body from the external environment, the immune cells are needed to remove any pathogens that cross the mucus and epithelial cells, before they reach systemic circulation.  Indeed, the mucosa contains many lymph nodes such as the Payer's patch in the small intestine.[195]

The final layer of the mucosa is the muscularis mucosae, a thin layer of smooth muscle which allows the tissue to contract and move depending on its biological function.

### 1.4.1.3 Submucosa, muscularis externia and serosa

The submucosa is a dense layer of connective tissue which contains larger blood and lymph vessels and also nervous tissue.[196]  The submucosa of the stomach and intestine contains the submucosal plexus, one of the major sets of neurons in the enteric nervous system and controls digestion.  The primary role of the submucosa is to connect the mucosa to the muscularis externa, and provide a blood and lymphatic supply to the mucosa.

Depending on the location in the body, the muscularis externa is made of either smooth or skeletal muscle.  The tissue has two layers of muscle and controls movement of the tissue, such as peristalsis.  The final layer is the serosa, which is a final layer of connective tissue, containing more blood vessels, lymphatics, and nervous tissue. [197]

## 1.4.2 Other physiological barriers to drug delivery

As already discussed, the primary role of the mucosa is to protect parts of the body exposed to the external environment. However there are other physiological barriers which are designed to protect specific organs, such as the brain, the immune system, and also metabolic pathways which will breakdown molecules making them safe to remove from the body before a physiological effect can be achieved.

### 1.4.2.1 The blood-brain barrier

The blood-brain barrier (BBB), a complex network of highly selectively permeable capillaries, protects the brain from damage by molecules and pathogens. The endothelial cells which make up the walls of the capillaries are held together by very strong tight-junctions, which restricts the movement of molecules, particles and bacteria so as not to cause adverse effects to the brain.[198] In addition to the tight junctions, the capillary network also contains several specific cell types, including pericytes (contractile cells which wrap around the capillaries and aid in the regulation of the permeability of the BBB),[199] astrocytes (brain-specific cells which control homeostasis, aid in repair, and control extracellular ion balance and help maintain biochemical processes in and around the endothelial cells),[200] and microglial cells (brain specific macrophages, maintaining the immune system and removing pathogens passing through the BBB).[201]

There are several key properties for a molecule to cross the BBB, namely size, charge, hydrogen-bonding potential and lipophilicity. Apart from biomolecules essential for normal cell growth and control (amino acids, proteins, carbohydrates etc.), only small lipophilic compounds less than 500 Da can cross the BBB.[202] This is a major limiting factor in the development of a pharmaceutical agent for delivery to the brain, and one that must be considered for the treatment of brain-specific diseases. Drug delivery to the brain is of increasing concern due to age-related diseases and neurodegenerative diseases such as Alzheimer's disease.

### 1.4.2.2 Immune system

Another biological barrier which needs to be considered in the development of pharmaceutical formulations is the immune system. The immune system protects organisms from damage by microbes, viruses, and toxic agents.

The immune system consists of highly specialised cells which can provide rapid defence (the innate immune system), or long-term protection (adaptive immune system) from pathogens and other harmful compounds, especially those of biological origin. Cells of the innate immune system (such as macrophages, dendritic cells, and natural killer cells) provide immediate response to a pathogen or potentially toxic compound, removing them before they can cause harm to the body.[203]

Immunogenicity mainly affects drugs of a biological origin, such as proteins, or antibodies. This is because the protein is recognised as foreign by the immune system, and therefore attacked to be removed from the body. Over the past few decades, there has been an increase in the number of biotherapeutics on the market (such as Herceptin)[204] which are of biological origin, and can therefore generate an immune response. Due to the power of the immune system, this can lead to complete removal of the drug before it can achieve its therapeutic effect and can be a big hurdle to overcome, due to the adaptive nature of the immune system.[205]

### 1.4.3 Ways of overcoming physiological barriers

Given the wide variety of defence mechanisms in humans and other organisms against foreign bodies, there is a great deal of interest in developing formulations that can bypass these barriers.

### 1.4.3.1 Pro-drugs, precursors and analogues

Prodrugs are compounds which can be administered to a patient in an inactive form and become active upon enzyme or chemical activation. Reasons for using prodrugs are multiple; enhanced absorption through the GI tract or other membranes, reduce the

adverse effects caused by the active compound, provide greater chemical stability thus improving the efficacy of the drug, penetration across the BBB or protection against rapid metabolism allowing the drug to have a longer systemic circulation.[206]

A prodrug is made by attaching a small molecule (designed to improve bioavailability, stability, etc.) to an active drug via a biodegradable link, such as an ester bond. This will allow enzymes to attack this bond, releasing the small molecule and creating the active drug. It is also possible to attach a targeting molecule to a prodrug, allowing the prodrug to interact with specific cellular targets in specific organs, where they can become the active drug. This strategy is especially useful in chemotherapeutics, as drugs can be targeted to cancer cells where they can be metabolised and become active, destroying the cancer cells avoiding adverse effects to healthy cells.[207,208]

There are numerous examples of FDA/OECD approved prodrugs on the market, for example Capecitabine, used in the treatment of some cancers. The active drug, 5-fluorouracil, is modified to the prodrug Capecitabine, to modulate the adverse effects caused by the potent anti-metabolite drug, and enhance oral absorption. Upon ingestion it is converted to 5′-deoxy-5-fluorouridine in the liver by enzymatic action from two enzymes; carboxylesterase and cytidine deaminase. This is then further metabolised into the active compound by thymidine phosphorylase and/or uridine phosphorylase, both of which are enzymes overly expressed in cancerous tissue.[209] The addition of small molecules to 5-fluorouracil thus provides enhanced oral bioavailability (improving patient compliance), and also controls the action of the drug.

Precursor biomolecules are small molecules which are converted to different molecules through metabolic pathways. For example, amino acids are used in the body as precursor molecules to various bioactive compounds such as glutathione (a detoxifying molecule), nitric oxide (a cell signalling molecule), porphyrins (used in the synthesis of haemoglobin), and GABA (neurotransmitter).[210] As they have good biocompatibility, precursor biomolecules can be used as drugs, especially in the case of neurological orders, for

example L-dopa (the precursor for dopamine). The dopamine molecule itself cannot cross the BBB, whereas its precursor (L-dopa) can, allowing it to be converted into dopamine in the brain.[211] This strategy is used in the treatment of Parkinson's disease.

An analogue is a compound which is structurally similar to an active biomolecule, which either exhibits a pharmaceutical effect itself, or becomes metabolised into an active form. Analogues have the same mechanism of action as the biocompound, however, they can have either diminished or enhanced effects depending on their potency, for example codeine. Codeine is an analogue of morphine, and follows the same metabolic pathway, however at a reduced potency. In addition, a small amount of codeine is metabolised into morphine in the liver by the cytochrome P450 CYP2D6.[212] Codeine mimics morphine, allowing it to be used as a potent pain medication, and also helps to reduce the side-effects associated with morphine. Further, codeine can be delivered by the oral route, due to enhanced absorption through the GI tract, whereas morphine needs to be delivered intravenously as it cannot cross the mucosa into systemic circulation.

The use of prodrugs, analogues and precursors are strategies to avoid the bodies defence mechanisms, however they can still be prone to premature degradation and reduced efficacy, and a strong understanding of their mechanism of action needs to be understood in order to make an effective formulation.

**1.4.3.2 PEGylation**

Poly(ethylene glycol) (PEG) is a polyether compound synthesised by the ring-opening polymerisation of ethylene oxide. It is non-toxic, non-immunogenic, non-antigenic, and highly soluble in water making it suitable for use in pharmaceutical applications. By functionalising molecules, proteins/peptides, or drug delivery vehicles with PEG (PEGylation), it is possible to enhance solubility, increase circulation time in the blood stream, enhance stability, decrease enzymatic degradation, and avoid detection by the immune system.[213] There are numerous examples of PEGylated formulations which have gained regulatory approval in the EU and USA, such as; Pegaptanib (used for age-related

muscular degeneration),[214] Certolizumab Pegol (used in the treatment of Chrone's disease),[215] and Pegylated interferon alfa-2a (used in chronic Hepatitis B patients).[216]

Despite its wide range of applications in the pharmaceutical industry; PEG has some significant drawbacks. These include lack of biodegradation, *in vivo* fate of PEG, and bioaccumulation in vacuoles for small molecular-weight polymers.[217] Despite this, PEG is actively used in formulations, and extensively studied in the literature.

There are several reported ways in which PEG can avoid the bodies defence mechanisms. The development of mucus-penetrating nanoparticles, (particles functionalised with PEG) provides a vehicle for drugs to be delivered by the oral route. This is especially useful for the delivery of hydrophobic drugs which need to be given via subcutaneous or intravenous injection.[218] By modifying the surface of nanoparticles with polymers, such as PEG, it is possible to reduce the surface properties of that particle, minimising the mucoadhesive interactions between the particle and the mucus environment due to its uncharged, hydrophilic nature. By doing so, it is possible to enhance the penetration of larger particles (larger than the mesh-size of mucin, ~300 nm). Particles up to 500 nm have been reported to show enhanced mucus penetration through PEGylation.[183,218,219] This has paved the way in the development of other mucus penetrating particles, nanoparticles functionalised with other polymers including poly(vinyl alcohol),[220] and poly(2-oxazolines).[145]

Another application of PEG is using its so-called "stealth" properties. By functionalising peptides or proteins with PEG, it is possible to reduce their non-specific binding to cells of the immune system, thus avoiding an immune response raised against them.[221] In addition, PEG will help stabilise the system, and allow a longer circulation time. The stealth properties of PEG are very popular in the literature, and there are numerous examples of PEGylated proteins,[222] nanoparticles,[223] and viruses.[224]

The pharmaceutical usefulness of PEG cannot be overlooked, and it is one of the most studied polymers for applications in drug delivery and dosage formulation. Due to its

unique abilities, it is being increasingly used in formulations, and they are readily used to evade the bodies defence mechanisms.

### 1. 4.3.3 Nanoparticles

Nanoparticles, due to their sub-micron size, can penetrate through barriers more readily than larger particles.  As discussed previously, PEGylated nanoparticles are mucus penetrating, allowing them to diffuse rapidly across a mucin network.  Although the addition of PEG does play an important role in this phenomenon, the particles size also plays a significant role.  Smaller nanoparticles were more diffusive than larger ones,[219] and indeed, particles larger than 500 nm were found not to penetrate at all, clearly showing the size does matter.

In addition to their mucus penetrating effects, nanoparticles have also been utilised for delivery across the BBB.  There are many studies in this area, as drug delivery to the brain is a major challenge to the pharmaceutical industry.  As such, nanocarriers are being designed and engineered with specific surface properties allowing them to permeate across the BBB.  Again, this process appears to be size dependent, and it has been found that particles >70 nm will not cross the BBB.[225]

As with drug permeability across the BBB, the composition and surface properties of the nanoparticle will dictate its ability to permeate into the brain.  Neutral, uncharged species more readily cross the BBB and allow delivery into the brain.  For example, PEG nanogels have been developed to deliver of oligonucleotides into the brain.[226]  Given that oligonucleotides are promising candidates for gene[227] and cancer[228] therapy and they do not naturally cross the BBB, this is a promising therapy.[229]  This is but one example of nanoparticles which have been engineered to allow for delivery of molecules through the BBB, overcoming the body's defences.

In addition to the BBB, another strong physical barrier to drug delivery is the skin and indeed, the skin is one of the major routes of drug delivery either by subcutaneous

injection or the use of dermal patches/hydrogels.[230] The subject of nanoparticle permeation across the skin is highly debated in the literature, and indeed remains inconclusive. Generally it is understood that nanoparticles will permeate across the skin, dependent on several key parameters, namely; size, charge, hydrophilicity, isoelectric point, how the particles are being administered, exposure times, location of the skin (i.e. thickness) etc.[231] Due to all these confounding factors, it is hard to accurately assess the degree of nanoparticle penetration.

Despite this, nanoparticles are being developed for transdermal drug delivery, specifically those targeted to specific layers of the skin. For example, solid-lipid nanoparticles delivering encapsulated vitamin A to the upper layers of the skin,[42] delivery of highly lipophilic drugs encapsulated in biodegradable poly(caprolactone) nanoparticles,[232] and nanoemulsions containing paclitaxel for use in the treatment of psoriasis (an auto-immune disease which leaves patchy, itchy rashes on the skin).[233] An area of specific interest is the use of silver nanoparticles for use as anti-fungal and anti-microbial formulations in skin lesions.[234] Indeed, silver nanoparticles have also been shown to aid in wound healing,[235] giving rise to new applications for silver nanoparticles with regards to dermal treatment.

As already discussed, one of the major advantages of using nanoparticles is the ability to functionalise them with small molecules or polymers, further expanding their characteristics and enabling more varied applications. Based on the advantages PEG has to the pharmaceutical industry, there are multiple examples in the literature of PEGylated nanoparticles as drug delivery vectors. In addition to the enhanced diffusion of nanoparticles through a mucus gel, PEG also helps nanoparticles avoid the immune system,[236,237] and prolong circulation time of the functionalised nanoparticle.[238] In addition, PEG (along with poly(lactic-co-glycolic acid) (PLGA)), are regularly used in the synthesis of polymeric nanoparticles, due to their good biocompatibility, good circulation times, and reduced toxicity, and further modified with targeting molecules allowing for targeted drug delivery.[239]

As well as PEGylated nanoparticles, there are also examples of nanoparticles functionalised to form a pro-drug.[240–242] By taking advantage of the high surface-area of nanoparticles, along with their small size (allowing them to enter cells more readily than larger molecules), and wide versatility in chemistry, the use of nanoparticles as either carriers of prodrugs, or surface-modified with prodrugs is very interesting. Functionalising or incorporating a prodrug into a nanoparticle system allows for a more controlled delivery/release, and also provides stability to the drug complex itself.[243]

## 1.5 Nanoparticle diffusion

In the pharmaceutical industry, measuring the diffusion of a compound across different barriers is of fundamental importance as it allows the permeability of drug formulations to be assessed. There are numerous reports in the literature on the use of Franz-diffusion cells to measure the diffusion of small molecules,[244] polymers,[245] nanoparticles[43] and peptides[41] across different tissue types including skin,[246] ocular tissue,[44] buccal mucosa,[45] and the bladder.[40]

However, with the advancement of nanotechnology, there is a need to understand the diffusive properties of nanomaterials through different biological systems, such as mucus gels and blood. Due to continuous environmental exposure to nanomaterials, their biological fate needs to be studied, which includes their route of exposure. Given that environmental nanoparticles are likely to be either inhaled, or ingested, their diffusion is the first barrier they need to overcome.[247] Therefore, from a safety stand point, understanding the diffusive properties of nanoparticles, and how size, shape, and surface modification affect these properties is of fundamental importance.

In addition to the risk-factors associated with exposure to engineered nanoparticles along with their increasing popularity of as drug delivery systems, the need to understand how particles are interacting and diffusing in physiological systems is becoming increasingly important, and an area which is generally lacking in the literature.

To date, nanoparticle diffusion through several different mucosal tissues has been studied as a potential for drug delivery, namely; cervicovaginal mucus,[218] intestinal mucus,[248] sputum,[249] gastric mucus,[145] and mucus from chronic rhinosinusitis patients.[250] Due to the complex nature of the physicochemical characteristics of nanoparticles and that of biological systems, nanoparticle diffusion for pharmaceutical applications is exceedingly complex and much is still to be learned.

Nanoparticle diffusion is also highly important in other areas of science, not just the pharmaceutical industry. In the physical sciences, nanoparticle diffusion is important in providing insights into how the particles are behaving in different solutions and systems, and indeed provides the ground-work in the development of nanoparticle formulations for use in drug delivery. As diffusion is caused by particles undergoing Brownian motion, understanding this process can be of importance in diverse fields, such as printing,[251] agrochemicals,[252] and energy storage.[253]

This chapter has highlighted the process of nanoparticle diffusion, different techniques used to measure diffusion, and why nanoparticles are important in different industries, particularly the pharmaceutical industry, and how this relates to diffusion. To conclude, understanding diffusion processes and the diffusion coefficients of different nanomaterials, and different functionalities in a variety of different media is of fundamental importance in generating the next-generation medicines, storage devices and many other state-of-the-art technologies.

## 1.6 Aims and objectives

Previous work in this area has shown that nanoparticle modification via PEGylation significantly enhanced particle diffusion through a range of mucosal tissues; however the mechanisms of mucus penetration, and how the properties of the particle/polymer corona can affect this permeation, have not been studied in depth. It is thought that the surface charge/ζ-potential plays an important role in permeation but the work in this thesis shows

that other factors also need to be considered.[254]    Given that the physicochemical properties of  mucosa vary, depending on factors such as diet, geography, and disease states, the physicochemical properties of the environment around the particles also needs to be studied.

The **aim** of this thesis was to design, synthesise and characterise a series of functionalised nanomaterials, and assess how their diffusion can be manipulated in a variety of different media, primarily focused on the development of novel nanomaterials for enhanced transmucosal delivery by the oral route.  By using diverse analytical tools, such as scattering techniques, NMR, microscopy, and particle tracking analysis, it was possible to further assess how the structure and functionality of these particles related to their diffusion, based on surface chemistry/composition of the particle, or solution properties of the surrounding media.

To meet this overall aim, the following **objectives** were met:

- Develop the nanoparticle tracking methodology.
- Synthesise and characterise a library of polymer-functionalised silica nanoparticles.
- Study the diffusion of inert gold nanoparticles in a solution of biocompatible polymers (Pluronics F-127) in order to gain insights into how nanoparticles behave in a complex mixture of polymer networks, and micelles.
- Study the effects of temperature on the diffusion of temperature-responsive silica nanoparticles in a range of organic solvents with different polarities.
- Finally, study the diffusion of mucus penetrating nanoparticles in mucin dispersions and asses their permeation through a gastric mucosa, using PEG as a standard.

# References

(1)     Roduner, E. Size Matters: Why Nanomaterials Are Different. *Chem. Soc. Rev.* **2006**, *35* (7), 583–592.

(2)     Akbarzadeh, A.; Samiei, M.; Davaran, S. Magnetic Nanoparticles: Preparation, Physical Properties, and Applications in Biomedicine. *Nanoscale Res. Lett.* **2012**, *7* (1), 144.

(3)     Iskandar, F. Nanoparticle Processing for Optical Applications – A Review. *Adv. Powder Technol.* **2009**, *20* (4), 283–292.

(4)     Albanese, A.; Tang, P. S.; Chan, W. C. W. The Effect of Nanoparticle Size, Shape, and Surface Chemistry on Biological Systems. *Annu. Rev. Biomed. Eng.* **2012**, *14*, 1–16.

(5)     Farokhzad, O. C.; Langer, R. Impact of Nanotechnology on Drug Delivery. *ACS Nano* **2009**, *3* (1), 16–20.

(6)     Parveen, S.; Misra, R.; Sahoo, S. K. Nanoparticles: A Boon to Drug Delivery, Therapeutics, Diagnostics and Imaging. *Nanomedicine* **2012**, *8* (2), 147–166.

(7)     Wiechers, J. W.; Musee, N. Engineered Inorganic Nanoparticles and Cosmetics: Facts, Issues, Knowledge Gaps and Challenges. *J. Biomed. Nanotechnol.* **2010**, *6* (5), 408–431.

(8)     Masciangioli, T.; Zhang, W.-X. Peer Reviewed: Environmental Technologies at the Nanoscale. *Environ. Sci. Technol.* **2003**, *37* (5), 102A–108A.

(9)     Raimondi, F.; Scherer, G. G.; Kötz, R.; Wokaun, A. Nanoparticles in Energy Technology: Examples from Electrochemistry and Catalysis. *Angew. Chem. Int. Ed. Engl.* **2005**, *44* (15), 2190–2209.

(10)    Aitken, R. J.; Chaudhry, M. Q.; Boxall, A. B. A.; Hull, M. Manufacture and Use of Nanomaterials: Current Status in the UK and Global Trends. *Occup. Med. (Lond).* **2006**, *56* (5), 300–306.

(11)    European Commission, "COMMISSION RECOMMENDATION of 18 October 2011 on the definition of nanomaterial (2011/696/EU)," 2011 http://eur-lex.europa.eu/LexUriServ/LexUriServ.do?uri=OJ:L:2013:114:0001:0059:EN:PDF (accessed May 9, 2014).

(12)    Graham, T. XXVII. On the Law of the Diffusion of Gases. *Philos. Mag. Ser. 3* **1833**, *2* (9), 175–190.

(13)    Fick, A. V. On Liquid Diffusion. *Philos. Mag. Ser. 4* **1855**, *10* (63), 30–39.

(14)    Einstein, A. Zur Theorie Der Brownschen Bewegung. *Ann. Phys.* **1906**, *324* (2), 371–381.

(15)    von Smoluchowski, M. Zur Kinetischen Theorie Der Brownschen Molekularbewegung Und Der Suspensionen. *Ann. Phys.* **1906**, *326* (14), 756–780.

(16)    Brown, R. A Brief Account of Microscopical Observations Made in the Months of June, July and August 1827, on the Particles Contained in the Pollen of Plants; and on the General Existence of Active Molecules in Organic and Inorganic Bodies. *Philos. Mag. Ser. 2* **1828**, *4* (21), 161–173.

(17)    Cruickshank Miller, C. The Stokes-Einstein Law for Diffusion in Solution. *R. Soc. London Proc. Ser. A* **1924**, *106*, 724–749.

(18)    Stokes, G. G. *On the Effect of the Internal Friction of Fluids on the Motion of Pendulums*; 1851.

(19)    Reynolds, O. An Experimental Investigation of the Circumstances Which Determine

Whether the Motion of Water Shall Be Direct or Sinuous, and of the Law of Resistance in Parallel Channels. *Philos. Trans. R. Soc. London* **1883**, *174*, 935–982.

(20)   Dattagupta, S. *Diffusion: Formalism and Applications*; Taylor & Francis, 2013; Vol. 2013.

(21)   Festa, R.; d'Agliano, E. G. Diffusion Coefficient for a Brownian Particle in a Periodic Field of Force. *Phys. A Stat. Mech. its Appl.* **1978**, *90* (2), 229–244.

(22)   Pecora, R. Dynamic Light Scattering Measurement of Nanometer Particles in Liquids. *J. Nanoparticle Res.* **2000**, *2* (2), 123–131.

(23)   Dragovic, R. A.; Gardiner, C.; Brooks, A. S.; Tannetta, D. S.; Ferguson, D. J. P.; Hole, P.; Carr, B.; Redman, C. W. G.; Harris, A. L.; Dobson, P. J.; et al. Sizing and Phenotyping of Cellular Vesicles Using Nanoparticle Tracking Analysis. *Nanomedicine* **2011**, *7* (6), 780–788.

(24)   Canzi, G.; Mrse, A. A.; Kubiak, C. P. Diffusion-Ordered NMR Spectroscopy as a Reliable Alternative to TEM for Determining the Size of Gold Nanoparticles in Organic Solutions. *J. Phys. Chem. C* **2011**, *115* (16), 7972–7978.

(25)   Swallen, S. F.; Ediger, M. D. Self-Diffusion of the Amorphous Pharmaceutical Indomethacin near Tg. *Soft Matter* **2011**, *7* (21), 10339.

(26)   Matthiesen, J.; Scott Smith, R.; Kay, B. D. Probing the Mobility of Supercooled Liquid 3-Methylpentane at Temperatures near the Glass Transition Using Rare Gas Permeation. *J. Chem. Phys.* **2012**, *137* (6), 64509.

(27)   Abade, G. C.; Cichocki, B.; Ekiel-Jeżewska, M. L.; Nägele, G.; Wajnryb, E. High-Frequency Viscosity and Generalized Stokes-Einstein Relations in Dense Suspensions of Porous Particles. *J. Phys. Condens. Matter* **2010**, *22* (32), 322101.

(28)   Kumar, C. S. S. R.; Mohammad, F. Magnetic Nanomaterials for Hyperthermia-Based Therapy and Controlled Drug Delivery. *Adv. Drug Deliv. Rev.* **2011**, *63* (9), 789–808.

(29)   Squires, T. M.; Mason, T. G. Fluid Mechanics of Microrheology. **2009**.

(30)   Achuthan, S.; Chung, B. J.; Ghosh, P.; Rangachari, V.; Vaidya, A. A Modified Stokes-Einstein Equation for Aβ Aggregation. *BMC Bioinformatics* **2011**, *12 Suppl 1* (Suppl 10), S13.

(31)   Yashonath, S.; Ghorai, P. K. Diffusion in Nanoporous Phases: Size Dependence and Levitation Effect. *J. Phys. Chem. B* **2008**, *112* (3), 665–686.

(32)   Liu, J.; Cao, D.; Zhang, L. Molecular Dynamics Study on Nanoparticle Diffusion in Polymer Melts: A Test of the Stokes-Einstein Law. *J. Phys. Chem. C* **2008**, *112* (17), 6653–6661.

(33)   Gaskell, T. Self-Diffusion in Liquid Metals: A Generalized Stokes-Einstein Equation. *J. Non. Cryst. Solids* **1984**, *61–62*, 913–918.

(34)   Silvester, D. S.; Uprety, S.; Wright, P. J.; Massi, M.; Stagni, S.; Muzzioli, S. Redox Properties of a Rhenium Tetrazolato Complex in Room Temperature Ionic Liquids: Assessing the Applicability of the Stokes–Einstein Equation for a Metal Complex in Ionic Liquids. *J. Phys. Chem. C* **2012**, *116* (13), 7327–7333.

(35)   Harris, J. M.; Chess, R. B. Effect of Pegylation on Pharmaceuticals. *Nat. Rev. Drug Discov.* **2003**, *2* (3), 214–221.

(36)   Mackay, M. E.; Dao, T. T.; Tuteja, A.; Ho, D. L.; van Horn, B.; Kim, H.-C.; Hawker, C. J. Nanoscale Effects Leading to Non-Einstein-like Decrease in Viscosity. *Nat. Mater.* **2003**, *2* (11), 762–766.

(37) Mondiot, F.; Loudet, J.-C.; Mondain-Monval, O.; Snabre, P.; Vilquin, A.; Würger, A. Stokes-Einstein Diffusion of Colloids in Nematics. *Phys. Rev. E* **2012**, *86* (1), 10401.

(38) Mauro, J. C.; Ellison, A. J. Breakdown of the Fractional Stokes–Einstein Relation in Silicate Liquids. *J. Non. Cryst. Solids* **2011**, *357* (24), 3924–3927.

(39) Sosso, G. C.; Behler, J.; Bernasconi, M. Breakdown of Stokes-Einstein Relation in the Supercooled Liquid State of Phase Change Materials. *Phys. status solidi* **2012**, *249* (10), 1880–1885.

(40) Moch, C.; Salmon, D.; Rodríguez Armesto, L.; Colombel, M.; Pivot, C.; Pirot, F. Bladder Tissue Permeability and Transport Modelling of Intravesical Alum, Lidocaine Hydrochloride, Methylprednisolone Hemisuccinate and Mitomycin C. *Int. J. Pharm.* **2014**, *464* (1–2), 91–103.

(41) Lopes, L. B.; Brophy, C. M.; Furnish, E.; Flynn, C. R.; Sparks, O.; Komalavilas, P.; Joshi, L.; Panitch, A.; Bentley, M. V. L. B. Comparative Study of the Skin Penetration of Protein Transduction Domains and a Conjugated Peptide. *Pharm. Res.* **2005**, *22* (5), 750–757.

(42) Jenning, V.; Gysler, A.; Schäfer-Korting, M.; Gohla, S. H. Vitamin A Loaded Solid Lipid Nanoparticles for Topical Use: Occlusive Properties and Drug Targeting to the Upper Skin. *Eur. J. Pharm. Biopharm.* **2000**, *49* (3), 211–218.

(43) Larese, F. F.; D'Agostin, F.; Crosera, M.; Adami, G.; Renzi, N.; Bovenzi, M.; Maina, G. Human Skin Penetration of Silver Nanoparticles through Intact and Damaged Skin. *Toxicology* **2009**, *255* (1–2), 33–37.

(44) Morrison, P. W. J.; Connon, C. J.; Khutoryanskiy, V. V. Cyclodextrin-Mediated Enhancement of Riboflavin Solubility and Corneal Permeability. *Mol. Pharm.* **2013**, *10* (2), 756–762.

(45) Amores, S.; Domenech, J.; Colom, H.; Calpena, A. C.; Clares, B.; Gimeno, Á.; Lauroba, J. An Improved Cryopreservation Method for Porcine Buccal Mucosa in Ex Vivo Drug Permeation Studies Using Franz Diffusion Cells. *Eur. J. Pharm. Sci.* **2014**, *60*, 49–54.

(46) Bartosova, L.; Bajgar, J. Transdermal Drug Delivery in Vitro Using Diffusion Cells. *Curr. Med. Chem.* **2012**, *19* (27), 4671–4677.

(47) Karpanen, T. J.; Worthington, T.; Conway, B. R.; Hilton, A. C.; Elliott, T. S. J.; Lambert, P. A. Penetration of Chlorhexidine into Human Skin. *Antimicrob. Agents Chemother.* **2008**, *52* (10), 3633–3636.

(48) Malloy, A.; Carr, B. NanoParticle Tracking Analysis - The Halo™ System. *Part. Part. Syst. Charact.* **2006**, *23* (2), 197–204.

(49) Ryu, J. H.; Bang, S. Y.; Yoon, J.-W.; Lim, C. S.; Shim, K. B. Pulsed Laser Induced Synthesis of Scheelite-Type Colloidal Nanoparticles in Liquid and the Size Distribution by Nanoparticle Tracking Analysis. *Appl. Surf. Sci.* **2007**, *253* (20), 8408–8414.

(50) Jaqaman, K.; Loerke, D.; Mettlen, M.; Kuwata, H.; Grinstein, S.; Schmid, S. L.; Danuser, G. Robust Single-Particle Tracking in Live-Cell Time-Lapse Sequences. *Nat. Methods* **2008**, *5* (8), 695–702.

(51) Tada, H.; Higuchi, H.; Wanatabe, T. M.; Ohuchi, N. In Vivo Real-Time Tracking of Single Quantum Dots Conjugated with Monoclonal Anti-HER2 Antibody in Tumors of Mice. *Cancer Res.* **2007**, *67* (3), 1138–1144.

(52) Morrison, I. E. G.; Karakikes, I.; Barber, R. E.; Fernández, N.; Cherry, R. J. Detecting and Quantifying Colocalization of Cell Surface Molecules by Single

Particle Fluorescence Imaging. *Biophys. J.* **2003**, *85* (6), 4110–4121.

(53) Pouget, N.; Dennis, C.; Turlan, C.; Grigoriev, M.; Chandler, M.; Salomé, L. Single-Particle Tracking for DNA Tether Length Monitoring. *Nucleic Acids Res.* **2004**, *32* (9), e73.

(54) Hao, X.; Shang, X.; Wu, J.; Shan, Y.; Cai, M.; Jiang, J.; Huang, Z.; Tang, Z.; Wang, H. Single-Particle Tracking of Hepatitis B Virus-like Vesicle Entry into Cells. *Small* **2011**, *7* (9), 1212–1218.

(55) Johnson, C. S. Diffusion Ordered Nuclear Magnetic Resonance Spectroscopy: Principles and Applications. *Prog. Nucl. Magn. Reson. Spectrosc.* **1999**, *34* (3–4), 203–256.

(56) Neufeld, R.; Stalke, D. Accurate Molecular Weight Determination of Small Molecules via DOSY-NMR by Using External Calibration Curves with Normalized Diffusion Coefficients. *Chem. Sci.* **2015**, *6* (6), 3354–3364.

(57) Shastry, T. A.; Morris-Cohen, A. J.; Weiss, E. A.; Hersam, M. C. Probing Carbon Nanotube-Surfactant Interactions with Two-Dimensional DOSY NMR. *J. Am. Chem. Soc.* **2013**, *135* (18), 6750–6753.

(58) Durand, J.; Fernández, F.; Barrière, C.; Teuma, E.; Gómez, K.; González, G.; Gómez, M. DOSY Technique Applied to Palladium Nanoparticles in Ionic Liquids. *Magn. Reson. Chem.* **2008**, *46* (8), 739–743.

(59) Valentini, M.; Vaccaro, A.; Rehor, A.; Napoli, A.; Hubbell, J. A.; Tirelli, N. Diffusion NMR Spectroscopy for the Characterization of the Size and Interactions of Colloidal Matter: The Case of Vesicles and Nanoparticles. *J. Am. Chem. Soc.* **2004**, *126* (7), 2142–2147.

(60) Stevens, P. D.; Fan, J.; Gardimalla, H. M. R.; Yen, M.; Gao, Y. Superparamagnetic Nanoparticle-Supported Catalysis of Suzuki Cross-Coupling Reactions. *Org. Lett.* **2005**, *7* (11), 2085–2088.

(61) Huang, R.; Wen, Y.-H.; Zhu, Z.-Z.; Sun, S.-G. Pt–Pd Bimetallic Catalysts: Structural and Thermal Stabilities of Core–Shell and Alloyed Nanoparticles. *J. Phys. Chem. C* **2012**, *116* (15), 8664–8671.

(62) Mody, V. V; Siwale, R.; Singh, A.; Mody, H. R. Introduction to Metallic Nanoparticles. *J. Pharm. Bioallied Sci.* **2010**, *2* (4), 282–289.

(63) Horn, D.; Rieger, J. Organic Nanoparticles in the Aqueous Phase—Theory, Experiment, and Use. *Angew. Chemie Int. Ed.* **2001**, *40* (23), 4330.

(64) Tang, F.; Li, L.; Chen, D. Mesoporous Silica Nanoparticles: Synthesis, Biocompatibility and Drug Delivery. *Adv. Mater.* **2012**, *24* (12), 1504–1534.

(65) Singh, R.; Lillard, J. W. Nanoparticle-Based Targeted Drug Delivery. *Exp. Mol. Pathol.* **2009**, *86* (3), 215–223.

(66) Natarajan, J. V.; Nugraha, C.; Ng, X. W.; Venkatraman, S. Sustained-Release from Nanocarriers: A Review. *J. Control. Release* **2014**, *193*, 122–138.

(67) Kim, C. S.; Duncan, B.; Creran, B.; Rotello, V. M. Triggered Nanoparticles as Therapeutics. *Nano Today* **2013**, *8* (4), 439–447.

(68) Singh, A.; Krishna, V.; Angerhofer, A.; Do, B.; MacDonald, G.; Moudgil, B. Copper Coated Silica Nanoparticles for Odor Removal. *Langmuir* **2010**, *26* (20), 15837–15844.

(69) Osmond, M. J.; Mccall, M. J. Zinc Oxide Nanoparticles in Modern Sunscreens: An Analysis of Potential Exposure and Hazard. **2010**.

(70) Zhang, W. Nanoscale Iron Particles for Environmental Remediation: An Overview. *J. Nanoparticle Res.* **2003**, *5* (3–4), 323–332.

(71) Rai, M.; Yadav, A.; Gade, A. Silver Nanoparticles as a New Generation of Antimicrobials. *Biotechnol. Adv.* **2009**, *27* (1), 76–83.

(72) Shirasaki, Y.; Supran, G. J.; Bawendi, M. G.; Bulović, V. Emergence of Colloidal Quantum-Dot Light-Emitting Technologies. *Nat. Photonics* **2012**, *7* (1), 13–23.

(73) Gad, S. C. *Pharmaceutical Sciences Encyclopedia*; John Wiley & Sons, Inc.: Hoboken, NJ, USA, 2010.

(74) Zhao, P.; Li, N.; Astruc, D. State of the Art in Gold Nanoparticle Synthesis. *Coord. Chem. Rev.* **2013**, *257* (3), 638–665.

(75) Zhou, J.; Ralston, J.; Sedev, R.; Beattie, D. A. Functionalized Gold Nanoparticles: Synthesis, Structure and Colloid Stability. *J. Colloid Interface Sci.* **2009**, *331* (2), 251–262.

(76) Grzelczak, M.; Pérez-Juste, J.; Mulvaney, P.; Liz-Marzán, L. M. Shape Control in Gold Nanoparticle Synthesis. *Chem. Soc. Rev.* **2008**, *37* (9), 1783–1791.

(77) Chen, R.; Wu, J.; Li, H.; Cheng, G.; Lu, Z.; Che, C.-M. Fabrication of Gold Nanoparticles with Different Morphologies in HEPES Buffer. *Rare Met.* **2010**, *29* (2), 180–186.

(78) Njoki, P. N.; Lim, I.-I. S.; Mott, D.; Park, H.-Y.; Khan, B.; Mishra, S.; Sujakumar, R.; Luo, J.; Zhong, C.-J. Size Correlation of Optical and Spectroscopic Properties for Gold Nanoparticles. *J. Phys. Chem. C* **2007**, *111* (40), 14664–14669.

(79) Eustis, S.; el-Sayed, M. A. Why Gold Nanoparticles Are More Precious than Pretty Gold: Noble Metal Surface Plasmon Resonance and Its Enhancement of the Radiative and Nonradiative Properties of Nanocrystals of Different Shapes. *Chem. Soc. Rev.* **2006**, *35* (3), 209–217.

(80) Haiss, W.; Thanh, N. T. K.; Aveyard, J.; Fernig, D. G. Determination of Size and Concentration of Gold Nanoparticles from UV-Vis Spectra. *Anal. Chem.* **2007**, *79* (11), 4215–4221.

(81) Amendola, V.; Meneghetti, M. Size Evaluation of Gold Nanoparticles by UV−vis Spectroscopy. *J. Phys. Chem. C* **2009**, *113* (11), 4277–4285.

(82) Huang, X.; El-Sayed, M. A. Gold Nanoparticles: Optical Properties and Implementations in Cancer Diagnosis and Photothermal Therapy. *J. Adv. Res.* **2010**, *1* (1), 13–28.

(83) Giljohann, D. A.; Seferos, D. S.; Daniel, W. L.; Massich, M. D.; Patel, P. C.; Mirkin, C. A. Gold Nanoparticles for Biology and Medicine. *Angew. Chem. Int. Ed. Engl.* **2010**, *49* (19), 3280–3294.

(84) Bharti, C.; Nagaich, U.; Pal, A. K.; Gulati, N. Mesoporous Silica Nanoparticles in Target Drug Delivery System: A Review. *Int. J. Pharm. Investig. 5* (3), 124–133.

(85) Tang, F.; Li, L.; Chen, D. Mesoporous Silica Nanoparticles: Synthesis, Biocompatibility and Drug Delivery. *Adv. Mater.* **2012**, *24* (12), 1504–1534.

(86) Asefa, T.; Tao, Z. Biocompatibility of Mesoporous Silica Nanoparticles. *Chem. Res. Toxicol.* **2012**, *25* (11), 2265–2284.

(87) Michalet, X.; Pinaud, F. F.; Bentolila, L. A.; Tsay, J. M.; Doose, S.; Li, J. J.; Sundaresan, G.; Wu, A. M.; Gambhir, S. S.; Weiss, S. Quantum Dots for Live Cells, in Vivo Imaging, and Diagnostics. *Science* **2005**, *307* (5709), 538–544.

(88) Loukanov, A. R.; Dushkin, C. D.; Papazova, K. I.; Kirov, A. V.; Abrashev, M. V.;

Adachi, E. Photoluminescence Depending on the ZnS Shell Thickness of CdS/ZnS Core-Shell Semiconductor Nanoparticles. *Colloids Surfaces A Physicochem. Eng. Asp.* **2004**, *245* (1–3), 9–14.

(89) Tomczak, N.; Jańczewski, D.; Han, M.; Vancso, G. J. Designer Polymer–quantum Dot Architectures. *Prog. Polym. Sci.* **2009**, *34* (5), 393–430.

(90) Wegner, K. D.; Hildebrandt, N. Quantum Dots: Bright and Versatile in Vitro and in Vivo Fluorescence Imaging Biosensors. *Chem. Soc. Rev.* **2015**, *44* (14), 4792–4834.

(91) Kloeffel, C.; Loss, D. Prospects for Spin-Based Quantum Computing in Quantum Dots. *Annu. Rev. Condens. Matter Phys.* **2013**, *4* (1), 51–81.

(92) Kwak, J.; Bae, W. K.; Lee, D.; Park, I.; Lim, J.; Park, M.; Cho, H.; Woo, H.; Yoon, D. Y.; Char, K.; et al. Bright and Efficient Full-Color Colloidal Quantum Dot Light-Emitting Diodes Using an Inverted Device Structure. *Nano Lett.* **2012**, *12* (5), 2362–2366.

(93) Jamieson, T.; Bakhshi, R.; Petrova, D.; Pocock, R.; Imani, M.; Seifalian, A. M. Biological Applications of Quantum Dots. *Biomaterials* **2007**, *28* (31), 4717–4732.

(94) Kikkeri, R.; Lepenies, B.; Adibekian, A.; Laurino, P.; Seeberger, P. H. In Vitro Imaging and in Vivo Liver Targeting with Carbohydrate Capped Quantum Dots. *J. Am. Chem. Soc.* **2009**, *131* (6), 2110–2112.

(95) Chang, E.; Thekkek, N.; Yu, W. W.; Colvin, V. L.; Drezek, R. Evaluation of Quantum Dot Cytotoxicity Based on Intracellular Uptake. *Small* **2006**, *2* (12), 1412–1417.

(96) Tsay, J. M.; Michalet, X. New Light on Quantum Dot Cytotoxicity. *Chem. Biol.* **2005**, *12* (11), 1159–1161.

(97) Winnik, F. M.; Maysinger, D. Quantum Dot Cytotoxicity and Ways to Reduce It. *Acc. Chem. Res.* **2013**, *46* (3), 672–680.

(98) Lu, A.-H.; Salabas, E. L.; Schüth, F. Magnetic Nanoparticles: Synthesis, Protection, Functionalization, and Application. *Angew. Chem. Int. Ed. Engl.* **2007**, *46* (8), 1222–1244.

(99) Dobson, J. Magnetic Nanoparticles for Drug Delivery. *Drug Dev. Res.* **2006**, *67* (1), 55–60.

(100) Hadjipanayis, C. G.; Bonder, M. J.; Balakrishnan, S.; Wang, X.; Mao, H.; Hadjipanayis, G. C. Metallic Iron Nanoparticles for MRI Contrast Enhancement and Local Hyperthermia. *Small* **2008**, *4* (11), 1925–1929.

(101) Yoon, T.-J.; Yu, K. N.; Kim, E.; Kim, J. S.; Kim, B. G.; Yun, S.-H.; Sohn, B.-H.; Cho, M.-H.; Lee, J.-K.; Park, S. B. Specific Targeting, Cell Sorting, and Bioimaging with Smart Magnetic Silica Core-Shell Nanomaterials. *Small* **2006**, *2* (2), 209–215.

(102) Zhang, H.; Liu, Y.; Sun, S. Synthesis and Assembly of Magnetic Nanoparticles for Information and Energy Storage Applications. *Front. Phys. China* **2010**, *5* (4), 347–356.

(103) Chomoucka, J.; Drbohlavova, J.; Huska, D.; Adam, V.; Kizek, R.; Hubalek, J. Magnetic Nanoparticles and Targeted Drug Delivering. *Pharmacol. Res.* **2010**, *62* (2), 144–149.

(104) Wankhede, M.; Bouras, A.; Kaluzova, M.; Hadjipanayis, C. G. Magnetic Nanoparticles: An Emerging Technology for Malignant Brain Tumor Imaging and Therapy. *Expert Rev. Clin. Pharmacol.* **2012**, *5* (2), 173–186.

(105) Reddy, L. H.; Arias, J. L.; Nicolas, J.; Couvreur, P. Magnetic Nanoparticles: Design

and Characterization, Toxicity and Biocompatibility, Pharmaceutical and Biomedical Applications. *Chem. Rev.* **2012**, *112* (11), 5818–5878.

(106) Xia, Q.; Hwang, H.-M.; Ray, P. C.; Yu, H. Mechanisms of Nanotoxicity: Generation of Reactive Oxygen Species. *J. Food Drug Anal.* **2014**, *22* (1), 64–75.

(107) SUN, C.; LEE, J.; ZHANG, M. Magnetic Nanoparticles in MR Imaging and Drug Delivery☆. *Adv. Drug Deliv. Rev.* **2008**, *60* (11), 1252–1265.

(108) Huang, J.; Zhong, X.; Wang, L.; Yang, L.; Mao, H. Improving the Magnetic Resonance Imaging Contrast and Detection Methods with Engineered Magnetic Nanoparticles. *Theranostics* **2012**, *2* (1), 86–102.

(109) Li, L.; Jiang, W.; Luo, K.; Song, H.; Lan, F.; Wu, Y.; Gu, Z. Superparamagnetic Iron Oxide Nanoparticles as MRI Contrast Agents for Non-Invasive Stem Cell Labeling and Tracking. *Theranostics* **2013**, *3* (8), 595–615.

(110) Barenholz, Y. Doxil®--the First FDA-Approved Nano-Drug: Lessons Learned. *J. Control. Release* **2012**, *160* (2), 117–134.

(111) Lee, J. S.; Feijen, J. Polymersomes for Drug Delivery: Design, Formation and Characterization. *J. Control. Release* **2012**, *161* (2), 473–483.

(112) Akbarzadeh, A.; Rezaei-Sadabady, R.; Davaran, S.; Joo, S. W.; Zarghami, N.; Hanifehpour, Y.; Samiei, M.; Kouhi, M.; Nejati-Koshki, K. Liposome: Classification, Preparation, and Applications. *Nanoscale Res. Lett.* **2013**, *8* (1), 102.

(113) Kwon, G. S.; Okano, T. Polymeric Micelles as New Drug Carriers. *Adv. Drug Deliv. Rev.* **1996**, *21* (2), 107–116.

(114) Yokoyama, M. Polymeric Micelles as Drug Carriers: Their Lights and Shadows. *J. Drug Target.* **2014**, *22* (7), 576–583.

(115) Pattni, B. S.; Chupin, V. V; Torchilin, V. P. New Developments in Liposomal Drug Delivery. *Chem. Rev.* **2015**, *115* (19), 10938–10966.

(116) Immordino, M. L.; Dosio, F.; Cattel, L. Stealth Liposomes: Review of the Basic Science, Rationale, and Clinical Applications, Existing and Potential. *Int. J. Nanomedicine* **2006**, *1* (3), 297–315.

(117) Zou, P.; Stern, S. T.; Sun, D. PLGA/liposome Hybrid Nanoparticles for Short-Chain Ceramide Delivery. *Pharm. Res.* **2014**, *31* (3), 684–693.

(118) Noad, R.; Roy, P. Virus-like Particles as Immunogens. *Trends Microbiol.* **2003**, *11* (9), 438–444.

(119) Wang, J. W.; Roden, R. B. S. Virus-like Particles for the Prevention of Human Papillomavirus-Associated Malignancies. *Expert Rev. Vaccines* **2013**, *12* (2), 129–141.

(120) Roldão, A.; Mellado, M. C. M.; Castilho, L. R.; Carrondo, M. J. T.; Alves, P. M. Virus-like Particles in Vaccine Development. *Expert Rev. Vaccines* **2010**, *9* (10), 1149–1176.

(121) Georgens, C.; Weyermann, J.; Zimmer, A. Recombinant Virus Like Particles as Drug Delivery System. *Curr. Pharm. Biotechnol.* **2005**, *6* (1), 49–55.

(122) Georgens, C.; Weyermann, J.; Zimmer, A. Recombinant Virus like Particles as Drug Delivery System. *Curr. Pharm. Biotechnol.* **2005**, *6* (1), 49–55.

(123) Barrán-Berdón, A. L.; Pozzi, D.; Caracciolo, G.; Capriotti, A. L.; Caruso, G.; Cavaliere, C.; Riccioli, A.; Palchetti, S.; Laganà, A. Time Evolution of Nanoparticle-Protein Corona in Human Plasma: Relevance for Targeted Drug Delivery. *Langmuir* **2013**, *29* (21), 6485–6494.

(124) Mackowiak, S. A.; Schmidt, A.; Weiss, V.; Argyo, C.; von Schirnding, C.; Bein, T.; Bräuchle, C. Targeted Drug Delivery in Cancer Cells with Red-Light Photoactivated Mesoporous Silica Nanoparticles. *Nano Lett.* **2013**, *13* (6), 2576–2583.

(125) El-Shabouri, M. . Positively Charged Nanoparticles for Improving the Oral Bioavailability of Cyclosporin-A. *Int. J. Pharm.* **2002**, *249* (1–2), 101–108.

(126) Lara, H. H.; Garza-Treviño, E. N.; Ixtepan-Turrent, L.; Singh, D. K. Silver Nanoparticles Are Broad-Spectrum Bactericidal and Virucidal Compounds. *J. Nanobiotechnology* **2011**, *9* (1), 30.

(127) Lai, S. K.; O'Hanlon, D. E.; Harrold, S.; Man, S. T.; Wang, Y.-Y.; Cone, R.; Hanes, J. Rapid Transport of Large Polymeric Nanoparticles in Fresh Undiluted Human Mucus. *Proc. Natl. Acad. Sci. U. S. A.* **2007**, *104* (5), 1482–1487.

(128) Illum, L.; Jacobsen, L. O.; Müller, R. H.; Mak, E.; Davis, S. S. Surface Characteristics and the Interaction of Colloidal Particles with Mouse Peritoneal Macrophages. *Biomaterials* **1987**, *8* (2), 113–117.

(129) Tatsuki Shinoda, A. M. S. K. S. K. Y. K. T. S. T. A. Nanosphere Coated with Lactosyl-Polystyrene Polymer as a Targeting Carrier to Hepatocytes. **2008**.

(130) Borchard, G.; Audus, K. L.; Shi, F.; Kreuter, J. Uptake of Surfactant-Coated Poly(methyl Methacrylate)-Nanoparticles by Bovine Brain Microvessel Endothelial Cell Monolayers. *Int. J. Pharm.* **1994**, *110* (1), 29–35.

(131) Rodrigues, J. S.; Santos-Magalhães, N. S.; Coelho, L. C. B. B.; Couvreur, P.; Ponchel, G.; Gref, R. Novel Core(polyester)-Shell(polysaccharide) Nanoparticles: Protein Loading and Surface Modification with Lectins. *J. Control. Release* **2003**, *92* (1–2), 103–112.

(132) Fonte, P.; Andrade, F.; Araújo, F.; Andrade, C.; Neves, J. das; Sarmento, B. Chitosan-Coated Solid Lipid Nanoparticles for Insulin Delivery. *Methods Enzymol.* **2012**, *508*, 295–314.

(133) Balasubramaniam, S.; Pothayee, N.; Lin, Y.; House, M.; Woodward, R. C.; St. Pierre, T. G.; Davis, R. M.; Riffle, J. S. Poly( N -Isopropylacrylamide)-Coated Superparamagnetic Iron Oxide Nanoparticles: Relaxometric and Fluorescence Behavior Correlate to Temperature-Dependent Aggregation. *Chem. Mater.* **2011**, *23* (14), 3348–3356.

(134) von Erlach, T.; Zwicker, S.; Pidhatika, B.; Konradi, R.; Textor, M.; Hall, H.; Lühmann, T. Formation and Characterization of DNA-Polymer-Condensates Based on poly(2-Methyl-2-Oxazoline) Grafted poly(L-Lysine) for Non-Viral Delivery of Therapeutic DNA. *Biomaterials* **2011**, *32* (22), 5291–5303.

(135) Romberg, B.; Oussoren, C.; Snel, C. J.; Carstens, M. G.; Hennink, W. E.; Storm, G. Pharmacokinetics of Poly(hydroxyethyl-L-Asparagine)-Coated Liposomes Is Superior over that of PEG-Coated Liposomes at Low Lipid Dose and upon Repeated Administration. *Biochim. Biophys. Acta* **2007**, *1768* (3), 737–743.

(136) Kopecek, J.; Kopecková, P. HPMA Copolymers: Origins, Early Developments, Present, and Future. *Adv. Drug Deliv. Rev.* **2010**, *62* (2), 122–149.

(137) Win, K. Y.; Feng, S.-S. Effects of Particle Size and Surface Coating on Cellular Uptake of Polymeric Nanoparticles for Oral Delivery of Anticancer Drugs. *Biomaterials* **2005**, *26* (15), 2713–2722.

(138) Balazs, A. C.; Emrick, T.; Russell, T. P. Nanoparticle Polymer Composites: Where Two Small Worlds Meet. *Science (80-. ).* **2006**, *314* (5802), 1107–1110.

(139) Monteiro, M. J.; Cunningham, M. F. Polymer Nanoparticles via Living Radical Polymerization in Aqueous Dispersions: Design and Applications. *Macromolecules*

**2012**, *45* (12), 4939–4957.

(140) Skaff, H.; Emrick, T. Reversible Addition Fragmentation Chain Transfer (RAFT) Polymerization from Unprotected Cadmium Selenide Nanoparticles. *Angew. Chemie* **2004**, *116* (40), 5497–5500.

(141) Bartholome, C.; Beyou, E.; Bourgeat-Lami, E.; Chaumont, P.; Zydowicz, N. Nitroxide-Mediated Polymerizations from Silica Nanoparticle Surfaces: "Graft From" Polymerization of Styrene Using a Triethoxysilyl-Terminated Alkoxyamine Initiator. *Macromolecules* **2003**, *36* (21), 7946–7952.

(142) Habibi, Y.; Goffin, A.-L.; Schiltz, N.; Duquesne, E.; Dubois, P.; Dufresne, A. Bionanocomposites Based on Poly(ε-Caprolactone)-Grafted Cellulose Nanocrystals by Ring-Opening Polymerization. *J. Mater. Chem.* **2008**, *18* (41), 5002.

(143) Greszta, D.; Mardare, D.; Matyjaszewski, K. "Living" radical Polymerization. 1. Possibilities and Limitations. *Macromolecules* **1994**, *27* (3), 638–644.

(144) Gann, J. P.; Yan, M. A Versatile Method for Grafting Polymers on Nanoparticles. *Langmuir* **2008**, *24* (10), 5319–5323.

(145) Mansfield, E. D. H.; Sillence, K.; Hole, P.; Williams, A. C.; Khutoryanskiy, V. V. POZylation: A New Approach to Enhance Nanoparticle Diffusion through Mucosal Barriers. *Nanoscale* **2015**, *7* (32), 13671–13679.

(146) Bissadi, G.; Weberskirch, R. Efficient Synthesis of Polyoxazoline-Silica Hybrid Nanoparticles by Using the "grafting-Onto" Approach. *Polym. Chem.* **2016**, *7* (6), 1271–1280.

(147) Tokareva, I.; Minko, S.; Fendler, J. H.; Hutter, E. Nanosensors Based on Responsive Polymer Brushes and Gold Nanoparticle Enhanced Transmission Surface Plasmon Resonance Spectroscopy. *J. Am. Chem. Soc.* **2004**, *126* (49), 15950–15951.

(148) Nitin, N.; LaConte, L. E. W.; Zurkiya, O.; Hu, X.; Bao, G. Functionalization and Peptide-Based Delivery of Magnetic Nanoparticles as an Intracellular MRI Contrast Agent. *J. Biol. Inorg. Chem.* **2004**, *9* (6), 706–712.

(149) Wan, S.; Huang, J.; Yan, H.; Liu, K. Size-Controlled Preparation of Magnetite Nanoparticles in the Presence of Graft Copolymers. *J. Mater. Chem.* **2006**, *16* (3), 298–303.

(150) Research, C. for D. E. and. Approved Drugs - Paclitaxel (Abraxane). Center for Drug Evaluation and Research.

(151) Green, M. R.; Manikhas, G. M.; Orlov, S.; Afanasyev, B.; Makhson, A. M.; Bhar, P.; Hawkins, M. J. Abraxane, a Novel Cremophor-Free, Albumin-Bound Particle Form of Paclitaxel for the Treatment of Advanced Non-Small-Cell Lung Cancer. *Ann. Oncol.* **2006**, *17* (8), 1263–1268.

(152) Lynch, I.; Dawson, K. A. Protein-Nanoparticle Interactions. *Nano Today* **2008**, *3* (1–2), 40–47.

(153) Shinkai, M.; Le, B.; Honda, H.; Yoshikawa, K.; Shimizu, K.; Saga, S.; Wakabayashi, T.; Yoshida, J.; Kobayashi, T. Targeting Hyperthermia for Renal Cell Carcinoma Using Human MN Antigen-Specific Magnetoliposomes. *Japanese J. Cancer Res.* **2001**, *92* (10), 1138–1145.

(154) LE, B.; SHINKAI, M.; KITADE, T.; HONDA, H.; YOSHIDA, J.; WAKABAYASHI, T.; KOBAYASHI, T. Preparation of Tumor-Specific Magnetoliposomes and Their Application for Hyperthermia. *J. Chem. Eng. Japan* **2001**, *34* (1), 66–72.

(155) Ito, A.; Shinkai, M.; Honda, H.; Kobayashi, T. Medical Application of Functionalized

Magnetic Nanoparticles. *J. Biosci. Bioeng.* **2005**, *100* (1), 1–11.

(156) Marega, R.; Karmani, L.; Flamant, L.; Nageswaran, P. G.; Valembois, V.; Masereel, B.; Feron, O.; Borght, T. Vander; Lucas, S.; Michiels, C.; et al. Antibody-Functionalized Polymer-Coated Gold Nanoparticles Targeting Cancer Cells: An in Vitro and in Vivo Study. *J. Mater. Chem.* **2012**, *22* (39), 21305.

(157) Karmani, L.; Labar, D.; Valembois, V.; Bouchat, V.; Nagaswaran, P. G.; Bol, A.; Gillart, J.; Levêque, P.; Bouzin, C.; Bonifazi, D.; et al. Antibody-Functionalized Nanoparticles for Imaging Cancer: Influence of Conjugation to Gold Nanoparticles on the Biodistribution of 89Zr-Labeled Cetuximab in Mice. *Contrast Media Mol. Imaging 8* (5), 402–408.

(158) Tsai, C.-P.; Chen, C.-Y.; Hung, Y.; Chang, F.-H.; Mou, C.-Y. Monoclonal Antibody-Functionalized Mesoporous Silica Nanoparticles (MSN) for Selective Targeting Breast Cancer Cells. *J. Mater. Chem.* **2009**, *19* (32), 5737.

(159) Arruebo, M.; Fernández-Pacheco, R.; Velasco, B.; Marquina, C.; Arbiol, J.; Irusta, S.; Ibarra, M. R.; Santamaría, J. Antibody-Functionalized Hybrid Superparamagnetic Nanoparticles. *Adv. Funct. Mater.* **2007**, *17* (9), 1473–1479.

(160) Kozlova, D.; Chernousova, S.; Knuschke, T.; Buer, J.; Westendorf, A. M.; Epple, M. Cell Targeting by Antibody-Functionalized Calcium Phosphatenanoparticles. *J. Mater. Chem.* **2012**, *22* (2), 396–404.

(161) Leggett, R.; Lee-Smith, E. E.; Jickells, S. M.; Russell, D. A. "Intelligent" Fingerprinting: Simultaneous Identification of Drug Metabolites and Individuals by Using Antibody-Functionalized Nanoparticles. *Angew. Chemie* **2007**, *119* (22), 4178–4181.

(162) Shirshahi, V.; Shamsipour, F.; Zarnani, A. H.; Verdi, J.; Saber, R. Active Targeting of HER2-Positive Breast Cancer Cells by Herceptin-Functionalized Organically Modified Silica Nanoparticles. *Cancer Nanotechnol.* **2013**, *4* (1–3), 27–37.

(163) Ghosh, P.; Han, G.; De, M.; Kim, C. K.; Rotello, V. M. Gold Nanoparticles in Delivery Applications. *Adv. Drug Deliv. Rev.* **2008**, *60* (11), 1307–1315.

(164) Mulder, W. J. M.; Griffioen, A. W.; Strijkers, G. J.; Cormode, D. P.; Nicolay, K.; Fayad, Z. A. Magnetic and Fluorescent Nanoparticles for Multimodality Imaging. *Nanomedicine* **2007**, *2* (3), 307–324.

(165) Lai, S. K.; Wang, Y.-Y.; Hanes, J. Mucus-Penetrating Nanoparticles for Drug and Gene Delivery to Mucosal Tissues. *Adv. Drug Deliv. Rev.* **2009**, *61* (2), 158–171.

(166) Xing, Y.; Zhao, J.; Conti, P. S.; Chen, K. Radiolabeled Nanoparticles for Multimodality Tumor Imaging. *Theranostics* **2014**, *4* (3), 290–306.

(167) Hwang, D. W.; Ko, H. Y.; Lee, J. H.; Kang, H.; Ryu, S. H.; Song, I. C.; Lee, D. S.; Kim, S. A Nucleolin-Targeted Multimodal Nanoparticle Imaging Probe for Tracking Cancer Cells Using an Aptamer. *J. Nucl. Med.* **2010**, *51* (1), 98–105.

(168) Cheng, S.-H.; Yu, D.; Tsai, H.-M.; Morshed, R. A.; Kanojia, D.; Lo, L.-W.; Leoni, L.; Govind, Y.; Zhang, L.; Aboody, K. S.; et al. Dynamic In Vivo SPECT Imaging of Neural Stem Cells Functionalized with Radiolabeled Nanoparticles for Tracking of Glioblastoma. *J. Nucl. Med.* **2016**, *57* (2), 279–284.

(169) Gonzalez-McQuire, R.; Chane-Ching, J.-Y.; Vignaud, E.; Lebugle, A.; Mann, S. Synthesis and Characterization of Amino Acid-Functionalized Hydroxyapatite Nanorods. *J. Mater. Chem.* **2004**, *14* (14), 2277.

(170) Polsky, R.; Gill, R.; Kaganovsky, L.; Willner, I. Nucleic Acid-Functionalized Pt Nanoparticles: Catalytic Labels for the Amplified Electrochemical Detection of Biomolecules. *Anal. Chem.* **2006**, *78* (7), 2268–2271.

(171) Kouassi, G. K.; Irudayaraj, J.; McCarty, G. Activity of Glucose Oxidase Functionalized onto Magnetic Nanoparticles. *Biomagn. Res. Technol.* **2005**, *3* (1), 1.

(172) Ballauff, M.; Lu, Y. "Smart" Nanoparticles: Preparation, Characterization and Applications. *Polymer (Guildf).* **2007**, *48* (7), 1815–1823.

(173) Alberti, S.; Soler-Illia, G. J. A. A.; Azzaroni, O. Gated Supramolecular Chemistry in Hybrid Mesoporous Silica Nanoarchitectures: Controlled Delivery and Molecular Transport in Response to Chemical, Physical and Biological Stimuli. *Chem. Commun. (Camb).* **2015**, *51* (28), 6050–6075.

(174) You, Y.-Z.; Kalebaila, K. K.; Brock, S. L. Temperature-Controlled Uptake and Release in PNIPAM-Modified Porous Silica Nanoparticles. *Chem. Mater.* **2008**, *20* (10), 3354–3359.

(175) Soppimath, K. S.; Tan, D. C.-W.; Yang, Y.-Y. pH-Triggered Thermally Responsive Polymer Core-Shell Nanoparticles for Drug Delivery. *Adv. Mater.* **2005**, *17* (3), 318–323.

(176) Baeza, A.; Guisasola, E.; Ruiz-Hernández, E.; Vallet-Regí, M. Magnetically Triggered Multidrug Release by Hybrid Mesoporous Silica Nanoparticles. *Chem. Mater.* **2012**, *24* (3), 517–524.

(177) Sun, J.-T.; Yu, Z.-Q.; Hong, C.-Y.; Pan, C.-Y. Biocompatible Zwitterionic Sulfobetaine Copolymer-Coated Mesoporous Silica Nanoparticles for Temperature-Responsive Drug Release. *Macromol. Rapid Commun.* **2012**, *33* (9), 811–818.

(178) Zhou, L.; Yuan, W.; Yuan, J.; Hong, X. Preparation of Double-Responsive SiO2-G-PDMAEMA Nanoparticles via ATRP. *Mater. Lett.* **2008**, *62* (8–9), 1372–1375.

(179) You, Y.-Z.; Manickam, D. S.; Zhou, Q.-H.; Oupický, D. Reducible poly(2-Dimethylaminoethyl Methacrylate): Synthesis, Cytotoxicity, and Gene Delivery Activity. *J. Control. Release* **2007**, *122* (3), 217–225.

(180) Barua, S.; Mitragotri, S. Challenges Associated with Penetration of Nanoparticles across Cell and Tissue Barriers: A Review of Current Status and Future Prospects. *Nano Today* **2014**.

(181) Bansil, R.; Turner, B. S. Mucin Structure, Aggregation, Physiological Functions and Biomedical Applications. *Curr. Opin. Colloid Interface Sci.* **2006**, *11* (2–3), 164–170.

(182) Http://www.genenames.org/cgi-bin/genefamilies/set/. Mucins (MUC) Gene Family | HUGO Gene Nomenclature Committee http://www.genenames.org/cgi-bin/genefamilies/set/648 (accessed Mar 4, 2016).

(183) Lai, S. K.; Wang, Y.-Y.; Wirtz, D.; Hanes, J. Micro- and Macrorheology of Mucus. *Adv. Drug Deliv. Rev.* **2009**, *61* (2), 86–100.

(184) Peppas, N. A.; Huang, Y. Nanoscale Technology of Mucoadhesive Interactions. *Adv. Drug Deliv. Rev.* **2004**, *56* (11), 1675–1687.

(185) Ho, S. B.; Takamura, K.; Anway, R.; Shekels, L. L.; Toribara, N. W.; Ota, H. The Adherent Gastric Mucous Layer Is Composed of Alternating Layers of MUC5AC and MUC6 Mucin Proteins. *Dig. Dis. Sci.* **2004**, *49* (10), 1598–1606.

(186) Dixon, J.; Strugala, V.; Griffin, S. M.; Welfare, M. R.; Dettmar, P. W.; Allen, A.; Pearson, J. P. Esophageal Mucin: An Adherent Mucus Gel Barrier Is Absent in the Normal Esophagus but Present in Columnar-Lined Barrett's Esophagus. *Am. J. Gastroenterol.* **2001**, *96* (9), 2575–2583.

(187) Shaikh, R.; Raj Singh, T. R.; Garland, M. J.; Woolfson, A. D.; Donnelly, R. F. Mucoadhesive Drug Delivery Systems. *J. Pharm. Bioallied Sci.* **2011**, *3* (1), 89–100.

(188) Lehr, C.-M.; Poelma, F. G. J.; Junginger, H. E.; Tukker, J. J. An Estimate of Turnover Time of Intestinal Mucus Gel Layer in the Rat in Situ Loop. *Int. J. Pharm.* **1991**, *70* (3), 235–240.

(189) Robinson, J. R.; Mlynek, G. M. Bioadhesive and Phase-Change Polymers for Ocular Drug Delivery. *Adv. Drug Deliv. Rev.* **1995**, *16* (1), 45–50.

(190) Shojaei, A. H. Buccal Mucosa as a Route for Systemic Drug Delivery: A Review. *J. Pharm. Pharm. Sci. a Publ. Can. Soc. Pharm. Sci. Société Can. des Sci. Pharm. 1* (1), 15–30.

(191) Kopic, S.; Geibel, J. P. Gastric Acid, Calcium Absorption, and Their Impact on Bone Health. *Physiol. Rev.* **2013**, *93* (1), 189–268.

(192) Peterson, L. W.; Artis, D. Intestinal Epithelial Cells: Regulators of Barrier Function and Immune Homeostasis. *Nat. Rev. Immunol.* **2014**, *14* (3), 141–153.

(193) Hunyady, B.; Mezey, E.; Palkovits, M. Gastrointestinal Immunology: Cell Types in the Lamina Propria--a Morphological Review. *Acta Physiol. Hung.* **2000**, *87* (4), 305–328.

(194) Niess, J. H.; Reinecker, H.-C. Lamina Propria Dendritic Cells in the Physiology and Pathology of the Gastrointestinal Tract. *Curr. Opin. Gastroenterol.* **2005**, *21* (6), 687–691.

(195) Mowat, A. M.; Agace, W. W. Regional Specialization within the Intestinal Immune System. *Nat. Rev. Immunol.* **2014**, *14* (10), 667–685.

(196) Andrée, B.; Bär, A.; Haverich, A.; Hilfiker, A. Small Intestinal Submucosa Segments as Matrix for Tissue Engineering: Review. *Tissue Eng. Part B. Rev.* **2013**, *19* (4), 279–291.

(197) Hoshino, M.; Omura, N.; Yano, F.; Tsuboi, K.; Kashiwagi, H.; Yanaga, K. Immunohistochemical Study of the Muscularis Externa of the Esophagus in Achalasia Patients. *Dis. Esophagus* **2013**, *26* (1), 14–21.

(198) Wolburg, H.; Lippoldt, A. Tight Junctions of the Blood–brain Barrier. *Vascul. Pharmacol.* **2002**, *38* (6), 323–337.

(199) Winkler, E. A.; Bell, R. D.; Zlokovic, B. V. Central Nervous System Pericytes in Health and Disease. *Nat. Neurosci.* **2011**, *14* (11), 1398–1405.

(200) Abbott, N. J.; Rönnbäck, L.; Hansson, E. Astrocyte-Endothelial Interactions at the Blood-Brain Barrier. *Nat. Rev. Neurosci.* **2006**, *7* (1), 41–53.

(201) Muldoon, L. L.; Alvarez, J. I.; Begley, D. J.; Boado, R. J.; Del Zoppo, G. J.; Doolittle, N. D.; Engelhardt, B.; Hallenbeck, J. M.; Lonser, R. R.; Ohlfest, J. R.; et al. Immunologic Privilege in the Central Nervous System and the Blood-Brain Barrier. *J. Cereb. Blood Flow Metab.* **2013**, *33* (1), 13–21.

(202) Wohlfart, S.; Gelperina, S.; Kreuter, J. Transport of Drugs across the Blood-Brain Barrier by Nanoparticles. *J. Control. Release* **2012**, *161* (2), 264–273.

(203) Mayo, L.; Quintana, F. J.; Weiner, H. L. The Innate Immune System in Demyelinating Disease. *Immunol. Rev.* **2012**, *248* (1), 170–187.

(204) Stebbing, J.; Copson, E.; O'Reilly, S. Herceptin (Trastuzamab) in Advanced Breast Cancer. *Cancer Treat. Rev.* **2000**, *26* (4), 287–290.

(205) Wadhwa, M.; Thorpe, R. Unwanted Immunogenicity: Lessons Learned and Future Challenges. *Bioanalysis* **2010**, *2* (6), 1073–1084.

(206) Rautio, J.; Kumpulainen, H.; Heimbach, T.; Oliyai, R.; Oh, D.; Järvinen, T.; Savolainen, J. Prodrugs: Design and Clinical Applications. *Nat. Rev. Drug Discov.*

**2008**, *7* (3), 255–270.

(207) Dhar, S.; Kolishetti, N.; Lippard, S. J.; Farokhzad, O. C. Targeted Delivery of a Cisplatin Prodrug for Safer and More Effective Prostate Cancer Therapy in Vivo. *Proc. Natl. Acad. Sci. U. S. A.* **2011**, *108* (5), 1850–1855.

(208) Zhao, Y.; Duan, S.; Zeng, X.; Liu, C.; Davies, N. M.; Li, B.; Forrest, M. L. Prodrug Strategy for PSMA-Targeted Delivery of TGX-221 to Prostate Cancer Cells. *Mol. Pharm.* **2012**, *9* (6), 1705–1716.

(209) Longley, D. B.; Harkin, D. P.; Johnston, P. G. 5-Fluorouracil: Mechanisms of Action and Clinical Strategies. *Nat. Rev. Cancer* **2003**, *3* (5), 330–338.

(210) Berg JM, Tymoczko JL, S. L. *Biochemistry. 5th Edition*, 5th ed.; New York: W H Freeman, 2002.

(211) Pardridge, W. M. The Blood-Brain Barrier: Bottleneck in Brain Drug Development. *NeuroRx* **2005**, *2* (1), 3–14.

(212) Crews, K. R.; Gaedigk, A.; Dunnenberger, H. M.; Leeder, J. S.; Klein, T. E.; Caudle, K. E.; Haidar, C. E.; Shen, D. D.; Callaghan, J. T.; Sadhasivam, S.; et al. Clinical Pharmacogenetics Implementation Consortium Guidelines for Cytochrome P450 2D6 Genotype and Codeine Therapy: 2014 Update. *Clin. Pharmacol. Ther.* **2014**, *95* (4), 376–382.

(213) Veronese, F. M.; Pasut, G. PEGylation, Successful Approach to Drug Delivery. *Drug Discov. Today* **2005**, *10* (21), 1451–1458.

(214) Feucht, N.; Matthias, H.; Lohmann, C. P.; Maier, M. Pegaptanib Sodium Treatment in Neovascular Age-Related Macular Degeneration: Clinical Experience in Germany. *Clin. Ophthalmol.* **2008**, *2* (2), 253–259.

(215) Schreiber, S.; Khaliq-Kareemi, M.; Lawrance, I. C.; Thomsen, O. Ø.; Hanauer, S. B.; McColm, J.; Bloomfield, R.; Sandborn, W. J. Maintenance Therapy with Certolizumab Pegol for Crohn's Disease. *N. Engl. J. Med.* **2007**, *357* (3), 239–250.

(216) Janssen, H. L. A.; van Zonneveld, M.; Senturk, H.; Zeuzem, S.; Akarca, U. S.; Cakaloglu, Y.; Simon, C.; So, T. M. K.; Gerken, G.; de Man, R. A.; et al. Pegylated Interferon Alfa-2b Alone or in Combination with Lamivudine for HBeAg-Positive Chronic Hepatitis B: A Randomised Trial. *Lancet (London, England)* **2005**, *365* (9454), 123–129.

(217) Knop, K.; Hoogenboom, R.; Fischer, D.; Schubert, U. S. Poly(ethylene Glycol) in Drug Delivery: Pros and Cons as Well as Potential Alternatives. *Angew. Chem. Int. Ed. Engl.* **2010**, *49* (36), 6288–6308.

(218) Lai, S. K.; O'Hanlon, D. E.; Harrold, S.; Man, S. T.; Wang, Y.-Y.; Cone, R.; Hanes, J. Rapid Transport of Large Polymeric Nanoparticles in Fresh Undiluted Human Mucus. *Proc. Natl. Acad. Sci. U. S. A.* **2007**, *104* (5), 1482–1487.

(219) Lai, S. K.; Wang, Y.-Y.; Hanes, J. Mucus-Penetrating Nanoparticles for Drug and Gene Delivery to Mucosal Tissues. *Adv. Drug Deliv. Rev.* **2009**, *61* (2), 158–171.

(220) Yang, M.; Lai, S. K.; Yu, T.; Wang, Y.-Y.; Happe, C.; Zhong, W.; Zhang, M.; Anonuevo, A.; Fridley, C.; Hung, A.; et al. Nanoparticle Penetration of Human Cervicovaginal Mucus: The Effect of Polyvinyl Alcohol. *J. Control. Release* **2014**, *192*, 202–208.

(221) Waku, T.; Matsusaki, M.; Kaneko, T.; Akashi, M. PEG Brush Peptide Nanospheres with Stealth Properties and Chemical Functionality. *Macromolecules* **2007**, *40* (17), 6385–6392.

(222) Veronese, F. M. Peptide and Protein PEGylation. *Biomaterials* **2001**, *22* (5), 405–

417.

(223) Salmaso, S.; Caliceti, P. Stealth Properties to Improve Therapeutic Efficacy of Drug Nanocarriers. *J. Drug Deliv.* **2013**, *2013*, 374252.

(224) Lee, K. L.; Shukla, S.; Wu, M.; Ayat, N. R.; El Sanadi, C. E.; Wen, A. M.; Edelbrock, J. F.; Pokorski, J. K.; Commandeur, U.; Dubyak, G. R.; et al. Stealth Filaments: Polymer Chain Length and Conformation Affect the in Vivo Fate of PEGylated Potato Virus X. *Acta Biomater.* **2015**, *19*, 166–179.

(225) Shilo, M.; Sharon, A.; Baranes, K.; Motiei, M.; Lellouche, J.-P. M.; Popovtzer, R. The Effect of Nanoparticle Size on the Probability to Cross the Blood-Brain Barrier: An in-Vitro Endothelial Cell Model. *J. Nanobiotechnology* **2015**, *13* (1), 19.

(226) Vinogradov, S.; Batrakova, E.; Kabanov, A. Poly(ethylene Glycol)–polyethyleneimine NanoGel$^{TM}$ Particles: Novel Drug Delivery Systems for Antisense Oligonucleotides. *Colloids Surfaces B Biointerfaces* **1999**, *16* (1–4), 291–304.

(227) Rosi, N. L.; Giljohann, D. A.; Thaxton, C. S.; Lytton-Jean, A. K. R.; Han, M. S.; Mirkin, C. A. Oligonucleotide-Modified Gold Nanoparticles for Intracellular Gene Regulation. *Science* **2006**, *312* (5776), 1027–1030.

(228) Stahel, R. A.; Zangemeister-Wittke, U. Antisense Oligonucleotides for Cancer Therapy—an Overview. *Lung Cancer* **2003**, *41*, 81–88.

(229) Evers, M. M.; Toonen, L. J. A.; van Roon-Mom, W. M. C. Antisense Oligonucleotides in Therapy for Neurodegenerative Disorders. *Adv. Drug Deliv. Rev.* **2015**, *87*, 90–103.

(230) Schoellhammer, C. M.; Blankschtein, D.; Langer, R. Skin Permeabilization for Transdermal Drug Delivery: Recent Advances and Future Prospects. *Expert Opin. Drug Deliv.* **2014**.

(231) Baroli, B. Penetration of Nanoparticles and Nanomaterials in the Skin: Fiction or Reality? *J. Pharm. Sci.* **2010**, *99* (1), 21–50.

(232) Alvarez-Román, R.; Naik, A.; Kalia, Y. N.; Guy, R. H.; Fessi, H. Enhancement of Topical Delivery from Biodegradable Nanoparticles. *Pharm. Res.* **2004**, *21* (10), 1818–1825.

(233) Khandavilli, S.; Panchagnula, R. Nanoemulsions as Versatile Formulations for Paclitaxel Delivery: Peroral and Dermal Delivery Studies in Rats. *J. Invest. Dermatol.* **2007**, *127* (1), 154–162.

(234) Prow, T. W.; Grice, J. E.; Lin, L. L.; Faye, R.; Butler, M.; Becker, W.; Wurm, E. M. T.; Yoong, C.; Robertson, T. A.; Soyer, H. P.; et al. Nanoparticles and Microparticles for Skin Drug Delivery. *Adv. Drug Deliv. Rev.* **2011**, *63* (6), 470–491.

(235) Tian, J.; Wong, K. K. Y.; Ho, C.-M.; Lok, C.-N.; Yu, W.-Y.; Che, C.-M.; Chiu, J.-F.; Tam, P. K. H. Topical Delivery of Silver Nanoparticles Promotes Wound Healing. *ChemMedChem* **2007**, *2* (1), 129–136.

(236) Li, S.-D.; Huang, L. Stealth Nanoparticles: High Density but Sheddable PEG Is a Key for Tumor Targeting. *J. Control. Release* **2010**, *145* (3), 178–181.

(237) Yang, Q.; Jones, S. W.; Parker, C. L.; Zamboni, W. C.; Bear, J. E.; Lai, S. K. Evading Immune Cell Uptake and Clearance Requires PEG Grafting at Densities Substantially Exceeding the Minimum for Brush Conformation. *Mol. Pharm.* **2014**, *11* (4), 1250–1258.

(238) Jokerst, J. V; Lobovkina, T.; Zare, R. N.; Gambhir, S. S. Nanoparticle PEGylation for Imaging and Therapy. *Nanomedicine* **2011**, *6* (4), 715–728.

(239) Chan, J. M.; Zhang, L.; Yuet, K. P.; Liao, G.; Rhee, J.-W.; Langer, R.; Farokhzad,

O. C. PLGA-Lecithin-PEG Core-Shell Nanoparticles for Controlled Drug Delivery. *Biomaterials* **2009**, *30* (8), 1627–1634.

(240) Parrott, M. C.; Finniss, M.; Luft, J. C.; Pandya, A.; Gullapalli, A.; Napier, M. E.; DeSimone, J. M. Incorporation and Controlled Release of Silyl Ether Prodrugs from PRINT Nanoparticles. *J. Am. Chem. Soc.* **2012**, *134* (18), 7978–7982.

(241) Gu, Y.; Zhong, Y.; Meng, F.; Cheng, R.; Deng, C.; Zhong, Z. Acetal-Linked Paclitaxel Prodrug Micellar Nanoparticles as a Versatile and Potent Platform for Cancer Therapy. *Biomacromolecules* **2013**, *14* (8), 2772–2780.

(242) Sagnella, S. M.; Gong, X.; Moghaddam, M. J.; Conn, C. E.; Kimpton, K.; Waddington, L. J.; Krodkiewska, I.; Drummond, C. J. Nanostructured Nanoparticles of Self-Assembled Lipid pro-Drugs as a Route to Improved Chemotherapeutic Agents. *Nanoscale* **2011**, *3* (3), 919–924.

(243) Fang, J.-Y.; Al-Suwayeh, S. A. Nanoparticles as Delivery Carriers for Anticancer Prodrugs. *Expert Opin. Drug Deliv.* **2012**, *9* (6), 657–669.

(244) Liu, D.; Zhang, C.; Zhang, X.; Zhen, Z.; Wang, P.; Li, J.; Yi, D.; Jin, Y.; Yang, D. Permeation Measurement of Gestodene for Some Biodegradable Materials Using Franz Diffusion Cells. *Saudi Pharm. J.* **2015**, *23* (4), 413–420.

(245) Chakraborti, C. K.; Sahoo, S.; Behera, P. K. Role of Different Biodegradable Polymers on the Permeability of Ciprofloxacin. *J. Adv. Pharm. Technol. Res.* **2014**, *5* (3), 140–146.

(246) Fox, L. T.; Gerber, M.; du Preez, J. L.; du Plessis, J.; Hamman, J. H. Skin Permeation Enhancement Effects of the Gel and Whole-Leaf Materials of Aloe Vera, Aloe Marlothii and Aloe Ferox. *J. Pharm. Pharmacol.* **2015**, *67* (1), 96–106.

(247) Oberdörster, G.; Maynard, A.; Donaldson, K.; Castranova, V.; Fitzpatrick, J.; Ausman, K.; Carter, J.; Karn, B.; Kreyling, W.; Lai, D.; et al. Principles for Characterizing the Potential Human Health Effects from Exposure to Nanomaterials: Elements of a Screening Strategy. *Part. Fibre Toxicol.* **2005**, *2* (1), 8.

(248) Abdulkarim, M.; Agulló, N.; Cattoz, B.; Griffiths, P.; Bernkop-Schnürch, A.; Borros, S. G.; Gumbleton, M. Nanoparticle Diffusion within Intestinal Mucus: Three-Dimensional Response Analysis Dissecting the Impact of Particle Surface Charge, Size and Heterogeneity across Polyelectrolyte, Pegylated and Viral Particles. *Eur. J. Pharm. Biopharm. Off. J. Arbeitsgemeinschaft für Pharm. Verfahrenstechnik e.V* **2015**, *97* (Pt A), 230–238.

(249) Suk, J. S.; Lai, S. K.; Wang, Y.-Y.; Ensign, L. M.; Zeitlin, P. L.; Boyle, M. P.; Hanes, J. The Penetration of Fresh Undiluted Sputum Expectorated by Cystic Fibrosis Patients by Non-Adhesive Polymer Nanoparticles. *Biomaterials* **2009**, *30* (13), 2591–2597.

(250) Lai, S. K.; Suk, J. S.; Pace, A.; Wang, Y.-Y.; Yang, M.; Mert, O.; Chen, J.; Kim, J.; Hanes, J. Drug Carrier Nanoparticles That Penetrate Human Chronic Rhinosinusitis Mucus. *Biomaterials* **2011**, *32* (26), 6285–6290.

(251) Park, J.; Moon, J. Control of Colloidal Particle Deposit Patterns within Picoliter Droplets Ejected by Ink-Jet Printing. *Langmuir* **2006**, *22* (8), 3506–3513.

(252) De, A.; Bose, R.; Kumar, A.; Mozumdar, S. *Targeted Delivery of Pesticides Using Biodegradable Polymeric Nanoparticles*; Springer Science & Business Media, 2013; Vol. 18.

(253) Malik, R.; Burch, D.; Bazant, M.; Ceder, G. Particle Size Dependence of the Ionic Diffusivity. *Nano Lett.* **2010**, *10* (10), 4123–4127.

(254) Abdulkarim, M.; Agulló, N.; Cattoz, B.; Griffiths, P.; Bernkop-Schnürch, A.; Borros, S. G.; Gumbleton, M. Nanoparticle Diffusion within Intestinal Mucus: Three-Dimensional Response Analysis Dissecting the Impact of Particle Surface Charge, Size and Heterogeneity across Polyelectrolyte, Pegylated and Viral Particles. *Eur. J. Pharm. Biopharm.* **2015**, *97*, 230–238.

# Chapter 2

## Synthesis and characterisation of functionalised and unfunctionalised amorphous silica nanoparticles

### 2.1 Introduction

Silica nanoparticles are one of the most studied core-nanoparticle systems and are regularly used in both industry and academia. Silica nanoparticles exist in two forms; crystalline and amorphous. The most common form of crystalline silica is found naturally in the Earth in the form of quartz. Crystalline silica particles (<10 μm) are often formed as by-products of industrial and chemical processes, and also found in soil samples.[1] There have been many studies exploring the toxicity of crystalline silica, and it has been shown to be both toxic[2] and carcinogenic.[3–5] Epidemiological studies have demonstrated a large number of cases where crystalline silica has induced lung cancer *via* industrial exposure in many industries (including mining, work in the diatomaceous earth industry, agriculture and construction).[1,6–8] For this reason it has little application in the food and pharmaceutical industries.

Amorphous silica nanoparticles on the other hand, have a non-crystalline structure, and are used in a variety of applications in many different industries including cosmetics, paints, dental formulations, drug delivery, and bioimaging.[9,10] This wide range in application stems mainly from their ease in synthesis, controllable particle size, tuneable surface moieties (allowing for further modification with other molecules), and reduced toxicity.[11–13]

The first report on the synthesis of silica micro/nanoparticles was by Stöber in 1968,[14] who described the synthesis of silica particles by hydrolysing alkyl silicates followed by the condensation of silicic acid in alcoholic solutions with an ammonium catalyst. It was found that by varying the alkyl chain length and the type of alcohol used, particles of varying sizes could be readily synthesised. However, by producing larger particles, the particle size distribution widens and the particles become more polydisperse in nature. Since then many reports on the synthesis of silica nanoparticles has been published, creating both small and large particles which are highly monodispersed in nature, and ideal for biomedical applications.[15–18]

By changing the progenitor chemical and reaction conditions used to synthesise the silica, it is possible to create particles with a variety of surface groups including; amine,[19] carboxyl,[20] and thiol groups.[21] Different surface functionalities aid in providing a more stable colloidal suspension and also allow for easy and more versatile modification with other molecules such as polymers. In addition, by synthesising the core silica nanoparticles in the presence of a surfactant or a rod-like structure, it is possible to create porous particles, with a larger surface area, thus expanding their potential applications.[15] It is the diverse nature of silica nanoparticles which makes them an ideal model nanoparticle system to further investigate the effects of different polymer coatings on their diffusion through different systems, hence why they were chosen in this study.

Core-shell silica nanoparticles, made-up of an amorphous silica core and polymer shell, are gaining concomitant popularity in the literature, as they allow for additional surface properties not shown by the core particle alone. With the addition of a polymer corona to a nanoparticle, it is possible to manipulate their properties, allowing for controlled/modified release of a substance, increased biocompatibility, greater biodistribution, and/or targeted delivery.[22,23] These functionalisations can make the particle more versatile by enhancing specific surface properties, and/or providing molecules for interactions with protein receptors and antibodies. For drug delivery purposes, the addition of a polymer corona

around a particle is very interesting as it allows for increased biocompatibility and reduced toxicity, selected interactions with specific cellular targets, and controlled release of a formulation encapsulated inside the particle itself.[24]

This chapter focuses on the synthesis of the core silica nanoparticles, and their further functionalisation with three polymers; poly(ethylene glycol), poly(2-oxazolines), and poly(N-isopropyl acrylamide). In addition, information on their full characterisation is provided which was used for later experiments concerning their diffusion in different media, and penetration through biological barriers.

## 2.2 Materials and methods

### 2.2.1 Materials

(3-Mercaptopropyl)trimethoxysilane (MPTS), 95% purity, alkyne terminated poly(2-ethyl-2-oxazoline) (POZ), average molecular weight 5 kDa, maleimide terminated poly(ethylene glycol) (PEG) average molecular weight 5 kDa, and maleimide terminated poly(N-isopropyl acrylamide) (PNIPAM) average molecular weight 5 kDa were purchased from Sigma-Aldrich (Gillingham, UK). Dimethyl sulphoxide (DMSO) was purchased from Fisher Scientific (UK). All other chemicals and reagents (including solvents) used were of analytical grade or higher and were purchased from Sigma-Aldrich unless otherwise stated. All water used in this study was ultrapure water generated from a PureLab UHQ water purification system (18 MΩ), unless otherwise stated.

Part of this project involved collaboration with Prof Richard Hoogenboom from the University of Ghent. In this study, Prof Hoogenboom provided three different variations of poly(2-oxazolines), namely; poly(2-methyl-2-oxazoline) (PMOZ), poly(2-ethyl-2-oxazoline) (PEOZ), and poly(2-n-propyl-2-oxazoline) (PNPOZ). All three polymers were alkyne terminated and had a molecular weight of 5 kDa.

## 2.2.2 Synthesis of thiolated amorphous silica nanoparticles

Thiolated silica nanoparticles were synthesised by self-condensation of MPTS according to previously published methods, with no further modification.[21,25]   0.75 mL MPTS was added to 20 mL DMSO, and reacted with 0.5 mL NaOH (0.5 mol/L).  The reaction mixture was left stirring at room temperature for 24 hours, whilst being continuously bubbled through with air.  The formation of nanoparticles could be observed by the formation of a translucent, white suspension.

Following synthesis, the nanoparticles were purified by dialysis using a cellulose membrane with a molecular-weight cut-off of 12-14 kDa (Medicell International Ltd, UK). Particles were sealed inside the tubing and dialysed against 4 L deionised water, over a 48 hour period.  A minimum of 8 water changes were carried out.  Following dialysis, 3x1 mL aliquots were removed and frozen for lyophilisation.  The remainder were stored in the fridge at 4 $^{\circ}$C until further use.

## 2.2.3 Determination of reactive thiol content

In order to effectively functionalise the nanoparticles with both polymer and fluorophore, the total concentration of reactive thiol groups present on the nanoparticles needed to be determined.  This was carried out using Ellman's assay,[26] by the method of Bravo-Osuna with minor modifications. [27]

Prior to the assay, a sample of the nanoparticle suspension required freeze-drying.  3x1 mL samples were frozen before being placed in a Heto PowerDry LL3000 freeze drier and left for 48 hours.  Each 1 mL sample was then weighed and the dry weight of the particles recorded, providing an average concentration of particles (mg/mL).  The samples were then pooled together for further solid-state analysis.

For Ellman's assay, 3 mg lyophilised nanoparticles were resuspended in 10 mL phosphate buffer (pH 8, 0.5 mol/L) and left to incubate for 1 hour.  Following this incubation, 10x0.5 mL aliquots were removed and placed in Eppendorf tubes.  The

aliquots were then reacted with 0.5 mL 5,5'-dithiobis-(2-nitrobenzoic acid) (0.3 mg/mL) and left for a further 3 hours in the dark. Samples were then centrifuged for 10 min at 13,000 g to remove any dirt and dust, before the UV/vis absorbance was measured at 420 nm.

In order to quantify the total amount of free thiol groups, a calibration curve of cysteine-HCl was recorded. Cysteine-HCl was dissolved in phosphate buffer and then diluted into the following concentration range; 1.26, 0.63, 0.32, 0.16, 0.08, and 0.04 mmol/L. Each sample was then reacted with 0.5 mL 5,5'-dithiobis-(2-nitrobenzoic acid) (0.3 mg/mL) and left for 3 hours. The absorbance was measured at 420 nm. In all cases, a blank of 0.5 mL phosphate buffer and 0.5 mL 5,5'-dithiobis-(2-nitrobenzoic acid) was used which was subtracted from the absorbance of all other values during calculations..

### 2.2.4 Polymer functionalisation

In this work, the thiolated silica nanoparticles were functionalised with 3 different polymers; PEG, POZ, and PNIPAM. 3 different isomers of POZ were used.

### 2.2.4.1 PEGylation of silica nanoparticles

PEGylated nanoparticles were synthesised according to Mun *et al.*[28] To a 10 mL suspension of nanoparticles (5.5 mg/mL in water), was added 100 mg maleimide terminated PEG (5 kDa). The mixture was reacted under constant stirring for 24 hours at ambient temperature, before being purified by dialysis, using the same procedure as described in section 2.2.2.

### 2.2.4.2 POZylation of silica nanoparticles

In total, 4 different polymers were used; poly(2-ethyl-2-oxazoline), purchased from Sigma-Aldrich (PEOZ Sigma), as well as PMOZ, PEOZ, and PNPOZ, provided by Prof Richard Hoogenboom. All the polymers used were alkyne-terminated.

POZ-functionalised nanoparticles were used in two separate studies in this thesis; one comparing the diffusive capabilities of PEG and PEOZ (Sigma) through gastric mucus,

and the other comparing the diffusive properties of POZ macromolecules with different pendant groups.

For synthesis of the POZylated particles used in the PEG vs POZ study, a 5 mL suspension of nanoparticles (5.5 mg/mL in water), was diluted into 5 mL DMSO, and reacted with 100 mg PEOZ, purchased from Sigma-Aldrich. The reaction was catalysed by the addition of 200 µL triethylamine (TEA) and left for 24 hours. Following completion, the sample was purified by dialysis as described in section 2.2.2.

In a pilot study exploring different reaction times, it was found that leaving the particles reacting for 4 days rather than 1 resulted in a higher degree of polymer loading on the particle surface (assessed by thermal gravimetric analysis (TGA)). Therefore, in the second study, investigating the effect of alkyl chain length on nanoparticle diffusion, reactions were left for 96 hours rather than 24 hours, using the same protocol described above. This second study used the POZ macromolecules obtained from Prof. Hoogenboom.

### 2.2.4.3 PNIPAM functionalised silica

Here, a 5 mL suspension of silica nanoparticles (5.5 mg/mL) was diluted into 5 mL ultrapure water, before the addition of 100 mg PNIPAM. The reaction was left stirring for 24 hours at room temperature and purified by dialysis (as discussed in section 2.2.2).

### 2.2.5 Size characterisation

Two principle sizing techniques were used in this work; Dynamic Light Scattering (DLS) and Nanoparticle Tracking Analysis (NTA).

### 2.2.5.1 DLS

DLS is a light scattering technique which determines a hydrodynamic particle size based on a photon auto-correlation function and the refractive index of the sample. This is used to determine a diffusion coefficient which is then used to calculate the hydrodynamic diameter of the particle using the Stokes-Einstein equation.

DLS measurements were recorded using a Zetasizer NanoZS (Malvern Instruments Ltd., UK). Prior to functionalisation, a pilot study was carried out to determine the optimum dilution of nanoparticles used in this study. The stock solution of silica nanoparticles was serially diluted by a factor of 10 each until readings became nonsensical. It was found that a 1 in 10 dilution (from a 5.5 mg/mL stock solution of particles) provided accurate reproducible data, whereas 1 in 1,000 was the lowest level of detection.

Based on the results of this test, a 1:10 dilution was used for all remaining DLS experiments. Each nanoparticle suspension was diluted by 1:10 using ultrapure water into low-volume cuvettes (Fisher Scientific, UK) and placed in the DLS instrument. All readings were recorded for an average of 12 runs, with 10 seconds per run. This was repeated three times for each measurement. 3 independent samples were measured for each particle type. In all cases, a refractive index of 1.432 was used (based on the works of van der Pol *et al*).[29] The results are presented as the mean ± standard deviation of the determined z-average values for the independent repeats. All experiments were performed at 25 $^{\circ}$C.

In addition to particle size experiments, the Zetasizer NanoZS was also used to determine the ξ-potential of the nanoparticle suspensions. Again, a 1 in 10 dilution was used from stock, and the samples placed in DTS-1070 folded capillary tubes, which were sealed to prevent solvent evaporation. Each measurement was carried out in triplicate over an average of 20 runs, which was repeated for 3 independent samples. The results were processed using the Smoluchowski model (Fκa = 1.50), and presented as the mean ± standard deviation of three independent repeats. Again, all experiments were performed at 25 $^{\circ}$C.

**2.2.5.2 NTA**

In addition to DLS, a complimentary technique, NTA, was used to confirm the particle size. NTA is a relatively new technique which tracks the movement of individual particles by shining a laser through a nanoparticle suspension, causing them to scatter light. This

is then detected by a sCMOS camera attached to a microscope. Video recordings are made of the particles moving under Brownian motion, particles are tracked on a frame by frame basis, with the number of pixels that a particle crosses in a given period of time recorded. This distance is used to determine the mean-squared displacement (MSD) for the particle, which is then used to derive the diffusion coefficient, followed by a particle size (again using the Stokes-Einstein equation).

As NTA requires particles to be tracked individually, the dilution generally needs to be much greater than that of a DLS experiment. As this can vary from sample to sample (depending on initial concentration), the correct dilution was determined on a sample by sample basis. The unfunctionalised thiolated silica and PEGylated silica were diluted 1:50,000 (from a 5.5 mg/mL stock solution of particles), and the POZylated and PNIPAM-silica nanoparticles were diluted 1:10,000; so around 20-40 particles were detected on the screen at any given time. All samples were diluted in ultrapure water.

NTA experiments were carried out using a NanoSightLM10 system (Malvern Instruments Ltd., UK), with an LM14 laser module, metal top-plate, green 532 nm laser, syringe pump, and sCMOS camera. 1 mL of diluted nanoparticle suspension was injected into the NTA system using a plastic syringe, before inserting the syringe into the syringe pump. For each sample, 6 x 60 second videos were recorded whilst under a constant flow of 30 AU. Each video was then analysed using the NTA software (v3.0 or 3.1) to determine a modal particle size. In addition to size, the diffusion coefficient for the nanoparticles was determined. Data are presented as mean ± standard deviation of three independent repeats (using the modal particle size and diffusion coefficient generated in the report summary). All experiments were performed at 25 $^{\circ}$C.

### 2.2.6 Surface functionality

To confirm the presence of polymer in a sample of lyophilised nanoparticles, Fourier transformed infrared spectroscopy (FT-IR), and Fourier transformed Raman spectroscopy (FT-Raman) were used. In addition, TGA was used to estimate the degree of polymer

loading, and used as further confirmation of polymer presence, by assessing the degree of thermal decomposition compared to that of unfunctionalised silica and free polymer.

### 2.2.6.1 FT-IR

FT-IR experiments were performed on a Spectrum 100 FT-IR spectrometer (Perkin Elmer, UK). A small amount of lyophilised (solid) nanoparticles were placed on the sample holder and spectra were recorded over an average of 32 runs, at a resolution of 4 cm$^{-1}$. Prior to analysis, a background of air was recorded and subtracted from the recorded spectra. Spectra were recorded between 4000 and 550 cm$^{-1}$.

### 2.2.6.2 FT-Raman

FT-Raman experiments were performed on a Nicolet NXR 9650 Raman spectrometer (Thermo Scientific, UK). Prior to analysis, the instrument was calibrated against a sulphur standard until a clear signal was present. For sample analysis, lyophilised nanoparticles were placed in glass HPLC vials, about a quarter full and tapped to remove any air pockets. They were then loaded into the instrument, and spectra recorded over an average of 1000 scans, between 4000 and 10 cm$^{-1}$, at a resolution of 4 cm$^{-1}$.

### 2.2.6.3 TGA

TGA experiments were performed on a Q500 instrument (TA Instruments, UK) using nitrogen as an inlet gas. Before analysis, the instrument was calibrated against an empty platinum TGA pan, loaded with an empty Tzero aluminium DSC pan. Lyophilised nanoparticles were then placed into the empty DSC pan, ensuring even coverage of the bottom of the pan. This was then loaded back into the TGA pan, and loaded into the instrument. Thermal decomposition was measured by a temperature ramp between 35 and 500 °C at 10 °C/min. In addition to lyophilised nanoparticles, samples of the polymer alone were measured to identify the point of thermal decomposition.

Polymer loading was determined by subtracting the weight loss observed for the unfunctionalised silica nanoparticles from the weight loss seen for the functionalised silica nanoparticles. This was then expressed as a percentage of total mass.

### 2.2.6.4 Solid-state NMR

In addition to the characterisation experiments already discussed, solid-state NMR experiments were carried out to determine how the POZ macromolecules were bound to the silica core. Given that a new chemistry was developed for POZ-functionalisation, this technique acts as an extra level of proof, confirming the binding of the macromolecule to the particle. This study used freeze-dried thiolated silica and POZ-silica nanoparticles, and was compared to a kaolinite standard. $^{29}$Si solid state NMR spectra were recorded using a Bruker 500 MHz Avance III spectrometer at a Larmor frequency of 99.35 MHz (11.75 T), that of $^{29}$Si.

Single pulse magic angle spinning (SPMAS) spectra were recorded, where the standard bore 4 mm MAS probe was spun at 10 kHz. The $^{29}$Si 90° pulse length was 6.25 µs (at the power level of 67.86 W) and the relaxation delay time was 150 s. In addition, cross-polarisation magic angle spinning (CPMAS) measurements were performed, where the 1H 90° pulse length was 3.7 µs (at the power level of 38 W). The CP contact time was 3 ms and the relaxation delay time was 5 s. Between 500 and 4096 signal transients were accumulated, averaged into a single spectrum and analysed using the TopSpin software. All spectra were referenced to external kaolinite signals as a secondary reference (well resolved peaks at -90.0 ppm and -91.4 ppm with respect to TMS).

## 2.3 Results and discussion

### 2.3.1 Functionalisation and reaction mechanisms

Amorphous thiolated silica nanoparticles were chosen as a model nanoparticle, due to ease and cost effective synthesis, as well as containing a high concentration of reactive

thiol groups for further functionalisation with different polymers. Two different synthetic pathways were utilised in the functionalisation reactions; maleimide-thiol conjugation (for PEG and PNIPAM), and alkyne-thiol conjugation (for POZ).

The maleimide-thiol conjugation is a very well characterised reaction which produces high yields in short periods of time.[30,31] The mechanism of the thiol-maleimide reaction is shown in Fig 2.1.
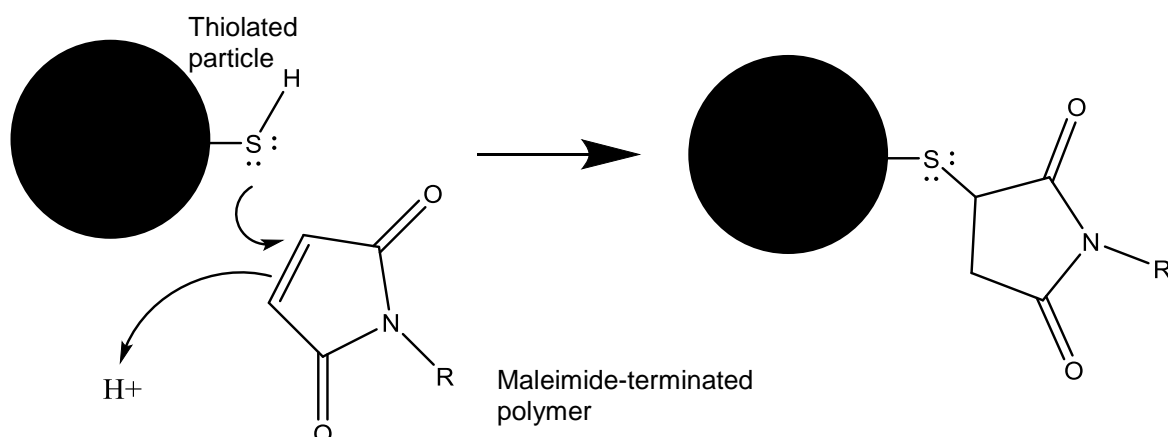


**Fig 2.1 Reaction mechanism for the maleimide-thiol addition.  T**he carbon double bond in the aromatic ring is attacked by the thiol group, causing a covalent interaction between the sulphur atom and the maleimide ring.

The reaction is a Michael addition, where the highly reactive carbon double bond in the aromatic ring is attacked by the thiol nucleophile, causing a covalent interaction between the sulphur atom and the maleimide ring.  This reaction is widely used in click-chemistry applications due to the high speed and good favourability resulting in high yields. [30,32]

In addition to the maleimide-thiol reaction, a less common synthetic pathway was used in the conjugation of alkyne-terminated POZ's to the thiolated silica nanoparticles.  Here, the thiol group is activated by the TEA molecule via hydrogen bonding which causes the thiol to become a stronger nucleophile, which then reacts with the alkyne forming a covalent bond.  Simultaneously the alkyne dissociates the thiol-TEA bond, releasing the catalyst (summarised in Fig 2.2).  It is possible (dependent on the proximity of the thiol groups to each other) that the resulting alkene formed in the reaction can further react with a thiol

group, eliminating all double bonds in the system. However, this secondary reaction is highly dependent on the proximity of the thiol groups. Given that the length of a carbon-sulphur bond is 1.82 Å, this pathway is highly unlikely.[33] This reaction has previously been used in the literature by Ganivada *et al*,[34] who created 3D gel networks using an thiol-alkyne reaction catalysed by TEA.
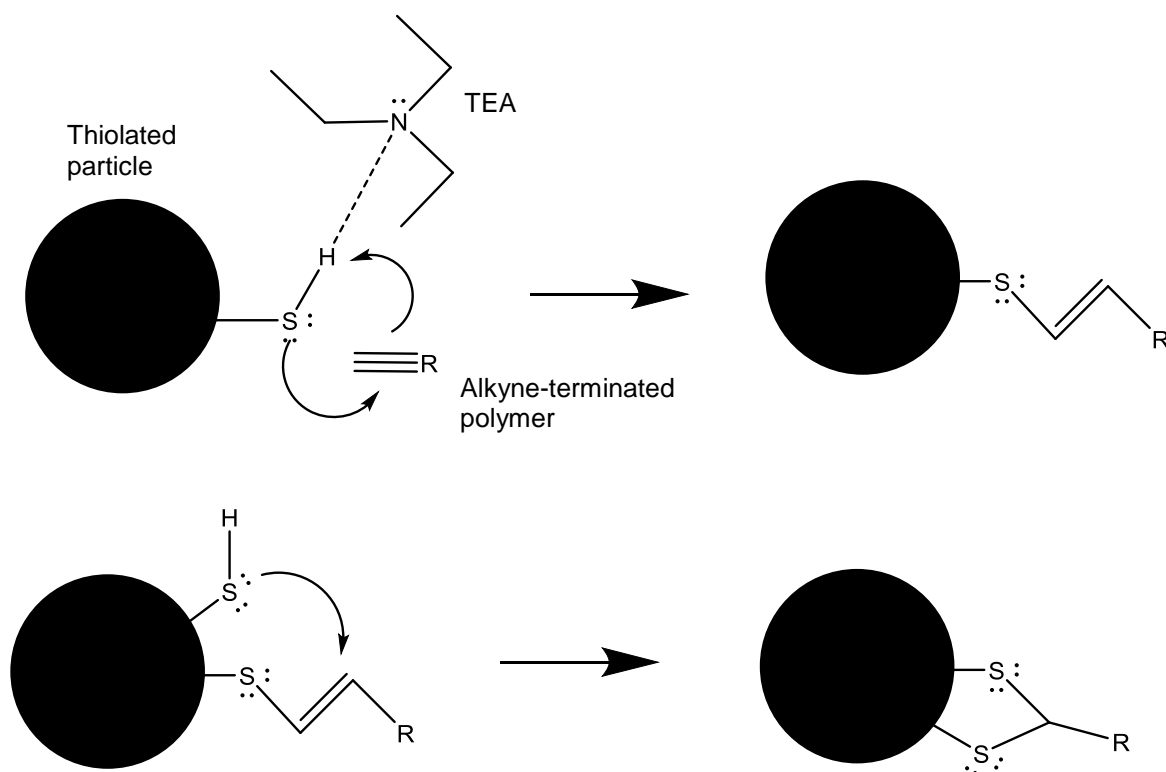


**Fig 2.2 Reaction mechanisms for the alkyne-thiol reaction catalysed by TEA.** The thiol group is activated by the TEA molecule via hydrogen bonding which causes the thiol to become a stronger nucleophile. This reacts with the alkyne forming a covalent bond. Simultaneously the alkyne dissociates the thiol-TEA bond, releasing the catalyst. A secondary reaction between the formed alkene and an adjacent thiol group could occur, eliminating all double bonds in the system.

## 2.3.2 Polymer loading

To assess the degree of functionalisation of polymer onto nanoparticle surface, two techniques were used; TGA (to measure the amount of polymer present in a pure sample of nanoparticles), and Ellman's assay (to assess the number of free thiol groups before and after functionalisation).

### 2.3.2.1 TGA

TGA was used to estimate the degree of functionalisation based on the thermal decomposition of the unfunctionalised and functionalised nanoparticles.  By comparing the weight loss exhibited by the unfunctionalised silica and the functionalised silica, it is possible to calculate the amount of polymer present in the sample.  Fig 2.3 shows the thermal decomposition of the functionalised and unfunctionalised silica nanoparticles.
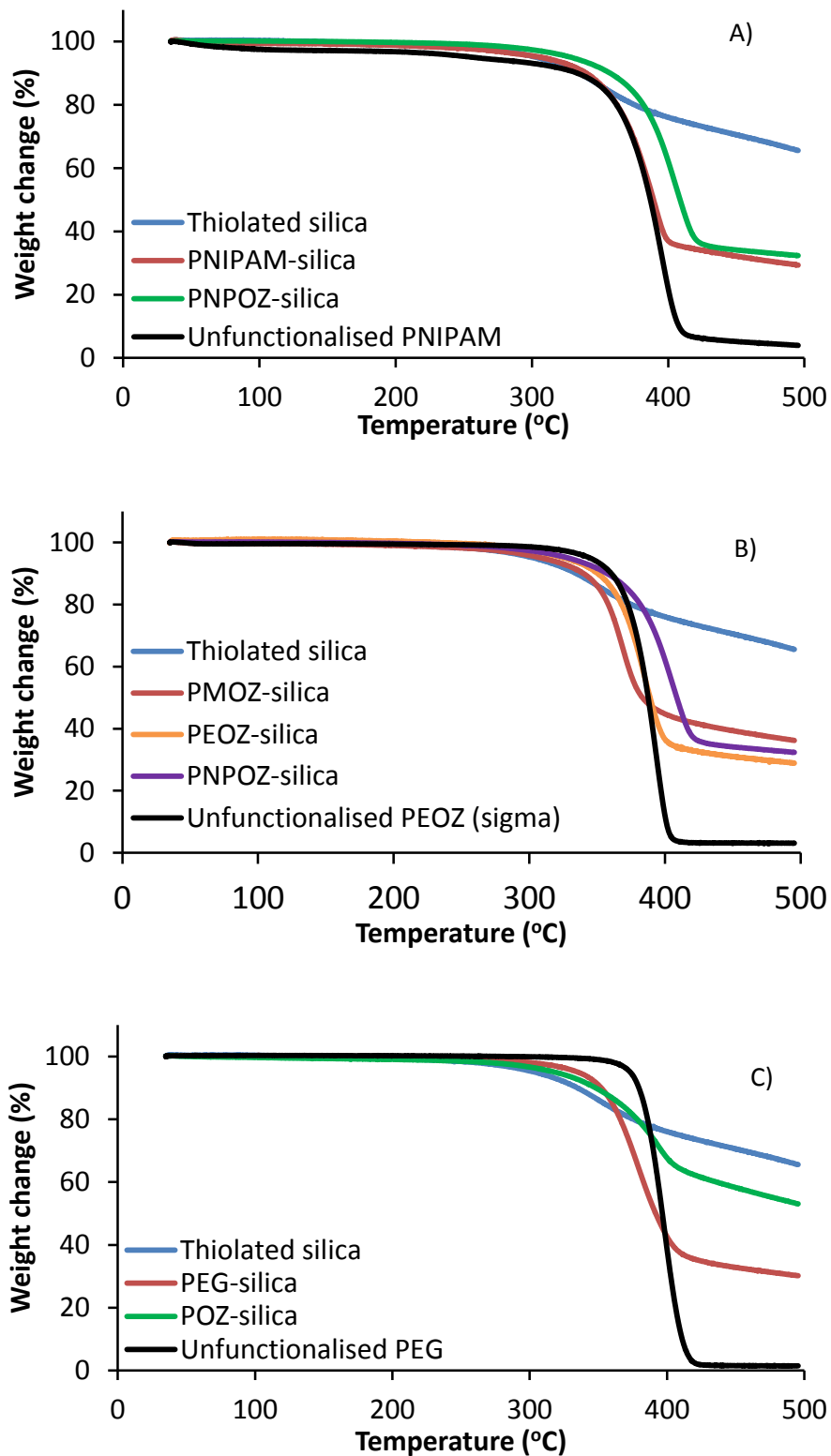
**Fig 2.3 TGA graphs showing the thermal decomposition of functionalised, unfunctionalised nanoparticles, and the free polymer.** A) shows thiolated, PNIPAM, and PNPOZ silica nanoparticles. B) Shows thiolated, PEGylated and POZylated silica nanoparticles. C) shows thiolated, and POZylated silica nanoparticles.

As can be seen, upon functionalisation there are significant differences in the thermal decomposition of the nanoparticles. This suggests the addition of another species, such as a polymer in the system; further confirming the functionalisation of the nanoparticles.

By calculating the % difference between weights before and after decomposition and subtracting the weight loss from thiolated silica alone, it is possible to determine the amount of polymer present on the particle surface. This was carried out using Equation 2.1.

$$\%p = \frac{W_{0(p)} - W_{f(p)}}{100} - \frac{W_{0(s)} - W_{f(s)}}{100}$$
Equation 2.1

Where %p is the amount of polymer present in the sample, Wo(p) is the weight of the polymer functionalised particles at the start before thermal decomposition, Wf(p) is the weight of the polymer functionalised particles after the thermal decomposition, Wo(s) is the weight of the thiolated silica particles at the start before thermal decomposition, and Wf(s) is the weight of the thiolated silica particles after thermal decomposition. Similar calculations have been used in the literature to determine the degree of polymer loading onto functionalised nanomaterials.[41–43]

From this equation, the %-loading of the polymers onto the nanoparticle surface was determined (Table 2.1).

**Table 2.1 Percentage loading of polymers onto the nanoparticle surface based on TGA data**

| Nanoparticle composite | % loading |
|:---:|:---:|
| PEG-silica | 35% |
| POZ-silica | 12% |
| PNIPAM-silica | 36% |
| PMOZ-silica | 29% |
| PEOZ-silica | 37% |
| PNPOZ-silica | 33% |

From the data in Table 2.1, it is clear that the maximum loading onto the nanoparticle surface appears to be between 30-40%, with one exception.  The reason for this cap around 30% could be due to steric hindrance around the particle.  As the particles are very small, only a limited amount of polymer can penetrate through to the particle and react with the thiol groups.

The initial reaction for POZ-grafting onto a nanoparticle surface was 12%, however following some further grafting experiments; it was found that by extending the reaction time, and the degree of polymer loading was increased (from 12 to ca. 35%).  This is why the reaction time changed from 24 hours initially to 96 hours.

TGA analysis was used in this study for two reasons; 1) to act as a further proof for the presence of polymer on the nanoparticle surface, and 2) to quantify the degree of polymer loading onto the nanoparticle surface based on the thermal decomposition of the samples, in relation to the unfunctionalised silica samples.

### 2.3.2.2 Ellman's assay

Ellman's assay can be used to determine the concentration of free thiol groups in a system.  There are many examples in the literature of where this assay has been used in determining the reactive thiol content in polymers,[44] nanoparticles,[45] and proteins.[46]  Here it was used to quantify the reactive thiol content both before and after nanoparticle functionalisation to determine; 1) the reactive thiol content available for functionalisation and fluorescent labelling, and 2) a reduction in reactive thiol content after functionalisation to confirm polymer binding.  Fig 2.4 shows the calibration curve used to determine the total concentration of free thiol groups, and Fig 2.5 shows the reactive thiol content for each particle type used in this study, determined using Ellman's assay.
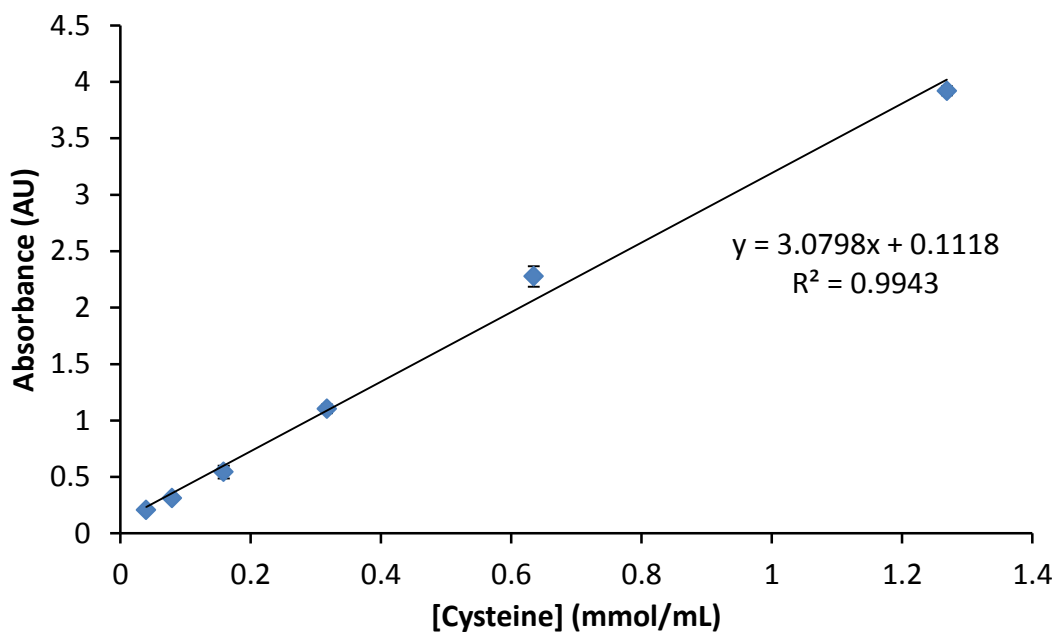
**Fig 2.4 Calibration curve used to determine the concentration of reactive thiol groups.** Mean ± standard deviation, n=3.
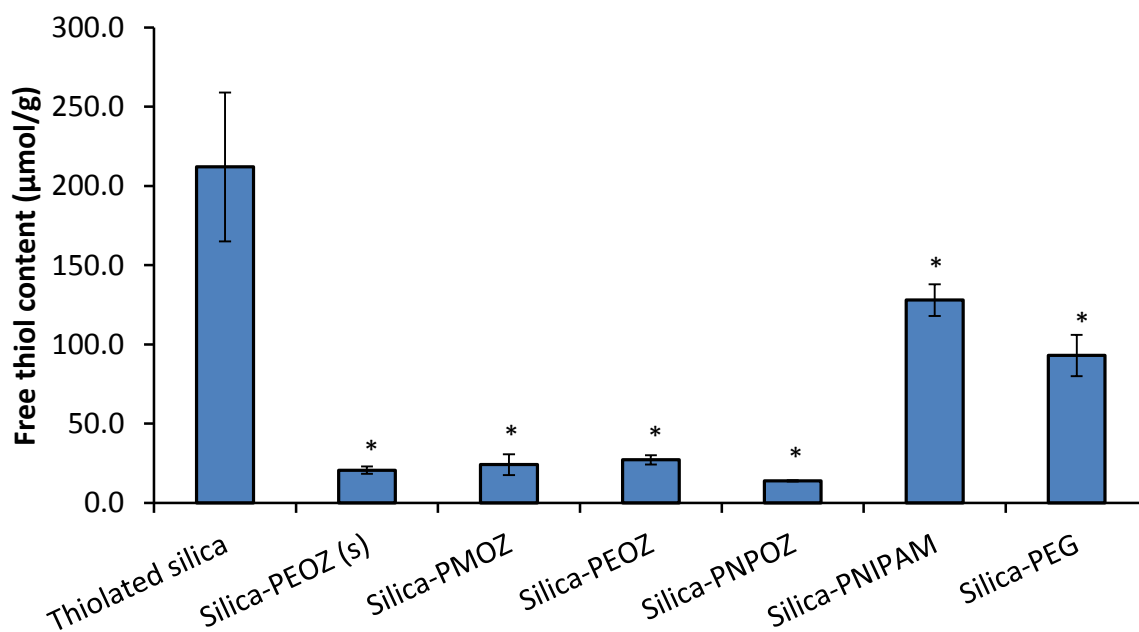


**Fig 2.5 Concentration of reactive thiol groups present on the surface of the functionalised and unfunctionalised silica nanoparticles.** Mean ± standard deviation, n=3 *P<0.05.

As can be seen (Fig 2.5), there is a significant reduction (P<0.05) in reactive thiol content from the unfunctionalised silica (210 ± 47 µmol/g) to the functionalised silica (93 ± 13

µmol/g for PEGylated silica, 128 ± 10 µmol/g for PNIPAMated silica, and ~20 µmol/g for POZylated silica).

Based on these values it is clear there is a reduction in reactive thiol content confirming the binding of polymer to the particles. Despite this, it is interesting to note that there is a clear difference in the amount of reactive thiol groups between the different samples. PEGylated silica has a final reactive thiol content of 93 ± 13 µmol/g, whereas POZylated silica has a final concentration of ~20 µmol/g. The reason for this could be two-fold. Firstly, it is possible that the alkyne group is reacting with two thiol groups (as seen in the second reaction step in Fig 2.2). Upon formation of the initial C-S bond, there is still the presence of a C=C linkage on the end group of the polymer. It is possible that this moiety could further react with another thiol group, theoretically causing two sulphur atoms to bind to a single POZ molecule. However in order for this to be the case, the sulphur atoms would have to be in very close proximity, as C-S typically has a bond length of ~1.7 Å in length,[47,48] depending on the spatial arrangement of the atoms. Although there is a high density of free thiol groups on the particle surface, it is unlikely they are close enough together to form these bonds. The more likely reason is due to the size of the end group. The alkyne moiety is much smaller than the maleimide moiety, so there will be a greater degree of steric hindrance around the particle surface for the PEG and PNIPAM polymers compared to POZ.

### 2.3.3 Particle size

Particle size was determined using both DLS and NTA and compared to gain a comprehensive estimation on the overall particle size.

### 2.3.3.1 DLS

DLS is a light scattering technique where a laser is shone through a suspension of particles which causes the laser light to scatter (Rayleigh scattering). Fluctuations in the scattering, due to particles moving under Brownian motion, are measured at specific time

intervals, which are then fitted to an autocorrelation function. A diffusion coefficient is then determined using Mie theory (based on this autocorrelation function and the refractive index of the sample), followed by a particle size using the Stokes-Einstein equation.

The data in Fig 2.6 shows the particle size distribution of the functionalised nanoparticles used in this study, compared to the unfunctionalised silica nanoparticles (shown in blue in all cases). For comparison, each particle size distribution has been separated into the specific chapter where that particle type will be used. In addition to the size distributions, the z-average values, PDI's and $\xi$-potentials of each sample were also determined using DLS (Table 2.2). The relevant particle size information is provided at the start of the results section in which that population of particles was used.
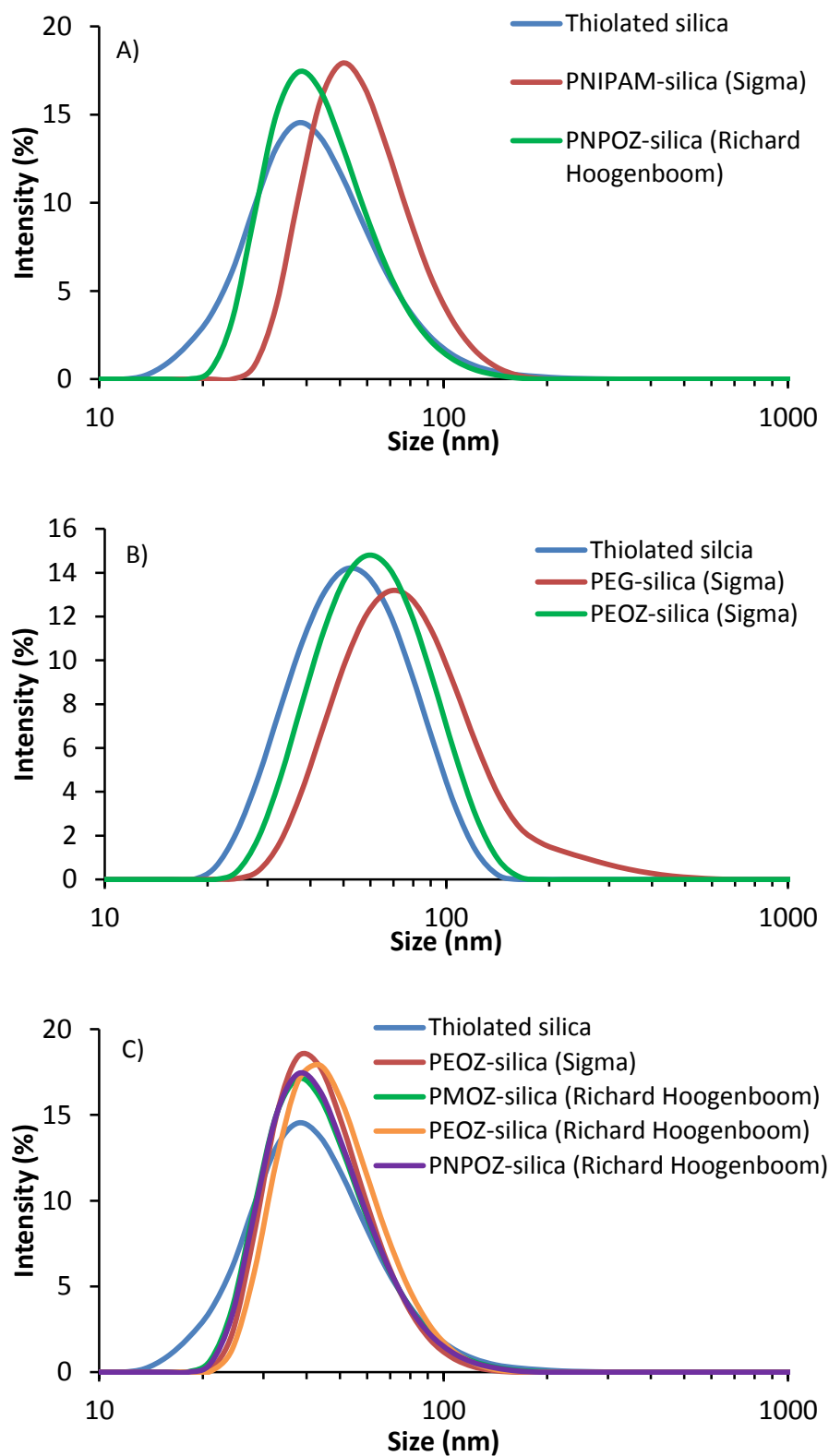
**Fig 2.6 DLS size distributions for unfunctionalised thiolated silica nanoparticles and functionalised nanoparticles.** A) shows the particles used in Chapter 4, B) shows the particles used in Chapter 5, and C) shows the particles used in Chapter 6.  (Mean, n=3)

**Table 2.2 DLS data for both functionalised and unfunctionalised silica nanoparticles.** (Mean ± standard deviation, n=3)

| Nanoparticle | z-average (nm) | PDI | ξ-potential (mV) |
|---|---|---|---|
| Thiolated silica | 52±1 | 0.072±0.003 | -46±2 |
| PNIPAM-silica | 70±1 | 0.111±0.004 | -29±1 |
| PNPOZ-silica | 61±1 | 0.194±0.018 | -21±2 |
| *PEG-silica | 70±1 | 0.175±0.070 | -24±1 |
| PMOZ-silica | 61±4 | 0.188±0.046 | -23±1 |
| *PEOZ-silica (Sigma) | 56±1 | 0.117±0.015 | -22±3 |
| PEOZ-silica | 59±4 | 0.106±0.012 | -20±2 |

*It should be noted that these particles used a separate batch of stock thiolated nanoparticles for synthesis. However no significant difference was noted between the two in all parameters.

As can be seen, upon functionalisation there is a significant ($P<0.05$, Student's T-test) increase in particle size, as is mimicked in the size distributions shown in Fig 2.6. These stats were determined using a standard Student's T-test. The size increase is due to the addition of a polymer onto the particle surface which increases the hydrodynamic radius of the particles. Despite all the polymers being 5 kDa, it would be expected that the final particle sizes be relatively similar. Although this is the case for the PNIPAM and PEG functionalised silica, it varies for the POZ-functionalised silica. This is further explored in chapter 6, and is due to the way the polymer binds to the particle. In the case of PEG and PNIPAM, a brush border is formed, but for POZ, the polymer wraps around the particle.

In addition to the change in size, there are also changes in ξ-potential and PDI. ξ-potential is a measure of particle stability, and is the difference in electric potential of a particle at the interface of the slip plane (the outermost hydration layer of a particle) and that of the bulk solvent (depicted in Fig 2.7).[35]
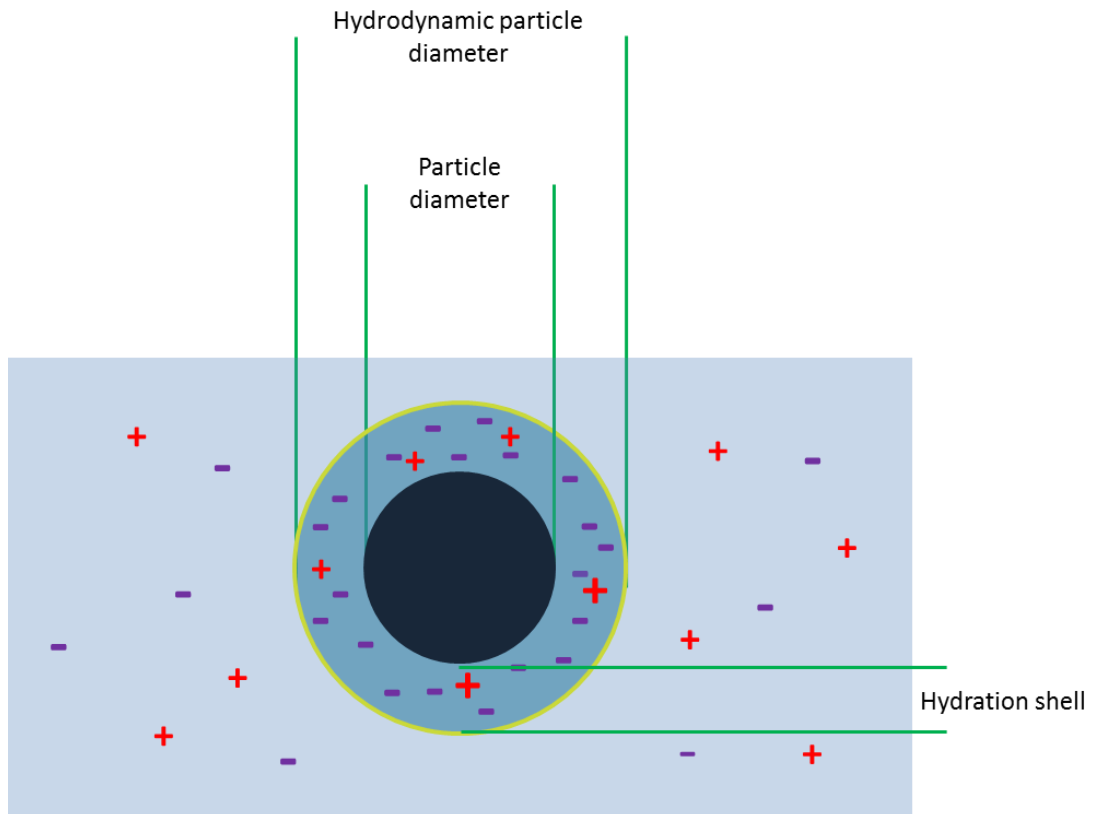
**Fig 2.7 Dynamics of a particle and its solvation shell.** The Difference between the hydrodynamic particle size and the particle diameter, and the location of the slip plane (yellow) surrounding the hydration shell.

The data in Table 2.2 shows a significant change ($P<0.05$,) in $\xi$-potential upon functionalisation (from $-42 \pm 2$ mV to around $-20$ mV). Upon functionalisation the charge around the particle will change, thus causing a change in zeta potential. As the particles synthesised in this study are highly negatively charged (due to the large presence of surface sulphur and Si-O-Si moieties), the overall charge will be reduced after functionalisation as these groups will be masked by the polymer.

Alongside $\xi$-potential, a change in PDI is also observed. PDI (polydispersity index) is a measure of how monodispersed a colloidal suspension is. A sample with a low PDI ($<0.2$) is considered monodisperse in nature, where the particles are of a uniform size and are not aggregated. A larger PDI (between 0.2 and 1) shows that the particles are more

polydisperse, meaning a sample of multiple different sizes, aggregation or contamination, and is based on a fit to the correlation data.[36]

The PDI is calculated based on the mean and standard deviation particle size generated during data processing, and not from the particle distribution. As can be seen in Table 2.2, the unfunctionalised silica particles are highly monodispersed with a PDI of 0.07 ± 0.003. Upon functionalisation, the PDI increases to a maximum of 0.194±0.018, shown for the PNPOZ-silica particles. This increase was unexpected, as by functionalising nanoparticles they are becoming more stable and less likely to aggregate, hence the PDI should decrease. By functionalising a particle, the polymer should act as a protective barrier around the particle, reducing the surface interactions between particles, thus generating a more stable suspension. This is due to a reduction of intermolecular forces existing between individual particles, which would usually cause them to aggregate.

However, upon functionalisation (as has already been discussed), there is a drop in zeta potential suggesting a decrease in stability in the sample, which could encourage aggregation. The particles exist as a highly negative species in suspension (shown by the low ξ-potential), which lessens upon functionalisation. Therefore, this decrease could reduce repulsion, encouraging particle interactions, thus increasing the PDI.

From the DLS data, it is clear that the particles change size following functionalisation, suggesting successful modification. In addition to DLS data, further sizing experiments were carried out using NTA to establish a more robust indication of particle size.

### 2.3.3.2 NTA

NTA is a complimentary particle sizing technique to DLS. Here, a laser is fired through a suspension of particles and the light scattered off them is detected by a camera. This allows videos to be recorded, showing the movement of the particles over a given period of time. During analysis, individual particles are tracked, and from the speed at which the particles are moving, a diffusion coefficient and particle size can be calculated. As the

technique requires individual particles to be tracked, a very low concentration of nanoparticles is required (in these experiments samples were diluted by at least 1:10,000, and then adjusted for optimum concentrations).

Similar to DLS, size distributions can be determined (Fig 2.8), in addition to the mean and modal particle size (Table 2.3), complementing the z-averages form DLS. Along with the particle size, the diffusion coefficient of the particles in an aqueous environment can be determined (Table 2.3). Also shown in Table 2.3, are the calculated diffusion coefficients for the particles in water, based on the particle size determined by NTA. For all sizing experiments, a standard operating procedure (SOP) was written and applied ensuring all data were collected under the same circumstances to minimise error.

**Table 2.3 NTA data for both functionalised and unfunctionalised silica nanoparticles.** Mean ± standard deviation, n=3.

| Nanoparticle | Modal particle size (nm) | Experimental diffusion coefficient (x10$^4$ nm$^2$/s) | Calculated diffusion coefficient (x10$^4$ nm$^2$/s) |
|---|---|---|---|
| Thiolated silica | 54±1 | 788±20 | 908 |
| PNIPAM-silica | 63±3 | 698±29 | 778 |
| PNPOZ-silica | 58±1 | 811±33 | 811 |
| PEG-silica | 62±2 | 687±41 | 791 |
| PMOZ-silica | 61±4 | 798±2 | 817 |
| PEOZ-silica (sigma) | 57±2 | 744±82 | 860 |
| PEOZ-silica | 59±1 | 787±28 | 831 |
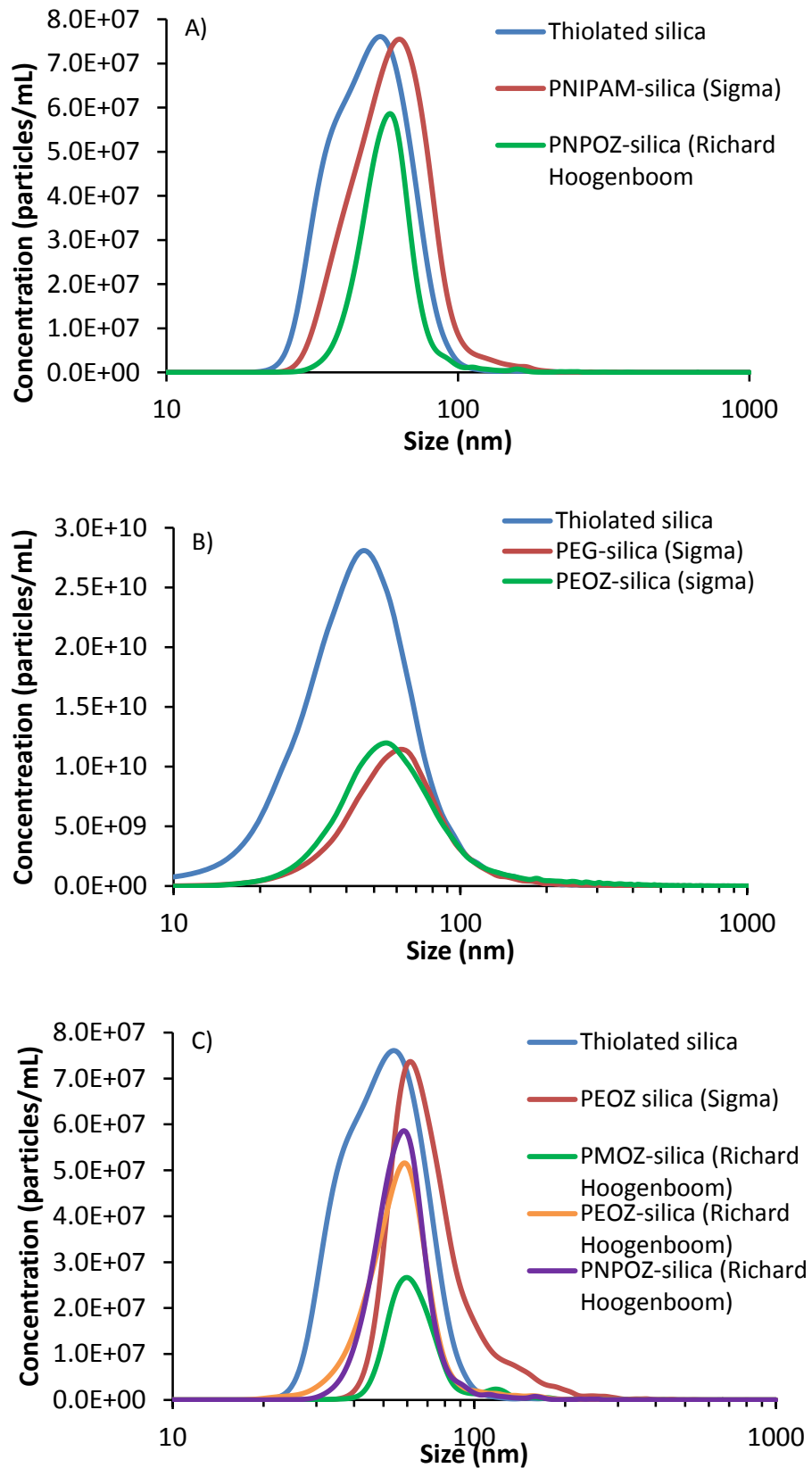
**Fig 2.8 NTA size distributions for unfunctionalised thiolated silica nanoparticles and functionalised nanoparticles.** A) shows the particles used in Chapter 4, B) shows the particles used in Chapter 5, and C) shows the particles used in Chapter 6. Mean n=3.

The PEG-silica and PNIPAM-silica nanoparticles however do show some discrepancy in particle size between the two techniques. The PEGylated silica by DLS has a size of 70±1 nm, whereas by NTA it has a size of 62±2 nm. Likewise, the PNIPAM functionalised silica show sizes of 70±1 and 63±3 for DLS and NTA, respectively. This discrepancy, although only 7 nm, is probably due to the way the data is collected, and was not statistically significant ($P<0.05$, Student's T-test). Both NTA and DLS are light scattering technique, however NTA uses scattered light to track particle movement over a given time period, whereas DLS uses an auto-correlation function to determine particle size. Therefore it is likely that background light is causing the NTA particle sizes to appear lower than DLS. Despite this, the DLS and NTA size data corroborate each other, and provide accurate definitions on the size of the nanoparticles used in this study.

In addition to the values shown in Table 2.3, the size distributions obtained for functionalised and unfunctionalised nanoparticles (blue), show a difference upon functionalisation, corroborating the size distributions obtained for DLS. This further confirms successful conjugation of the polymer to the particle surface. As NTA tracks individual particles, it is possible to obtain a more realistic size distribution compared to DLS.

NTA can also be used to determine the diffusion coefficient of nanoparticles suspended in a given media. Also shown in Table 2.3, are the diffusion coefficients of functionalised and unfunctionalised silica nanoparticles in water. Comparing the experimental and theoretical diffusion coefficients, it is clear that there are discrepancies. It would be expected that as the particle size increases, the diffusion coefficient also decreases, as larger particles move less rapidly under Brownian motion. This can be seen in Fig 2.9, which shows the calculated diffusion coefficient of different sized nanoparticles as determined using the Stokes-Einstein equation. For the calculation, the temperature was assumed to be 25 $^{o}$C, and viscosity was 0.89 cP (that of water at 25 $^{o}$C). An example of how the calculation was carried out can be found in Fig 2.9.
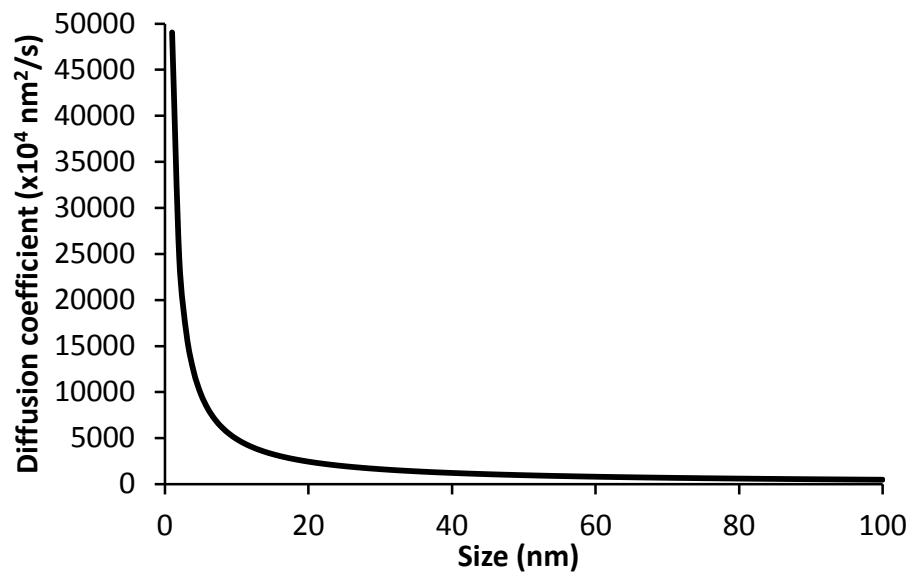
$$Dc = \frac{k_B T}{3\pi \eta d}$$

$$k_B = 1.38 \times 10^{-23} \; m^2 \, \mathrm{kg} \cdot s^{-2} K^{-1}$$

$$Dc = \frac{1.38 \times 10^{-23} \times 298.15}{3\pi \times (8.9 \times 10^{-4}) \times (5 \times 10^{-8})}$$

$$Dc = 9.8 \times 10^{-12} \; m/s$$

$$Dc = 981 \times 10^4 \; nm^2/s$$

**Fig 2.9 Calculation to determine the diffusion coefficient based off the Stokes-Einstein equation, and the diffusion coefficient for particles in water.** The calculation is a step-by-step guide on how the diffusion coefficient was calculated based on 50 nm particles suspended in water (viscosity = 0.89 cP) at 25 $^{\circ}$C (298.15K).

The experimental diffusion coefficients for PMOZ-silica, PEOZ-silica, and PNPOZ-silica are all in good agreement with the calculated diffusion coefficients. However, the diffusion coefficients for thiolated silica, PNIPAM-silica, PEG-silica and PEOZ-silica (Sigma) appear different. Interestingly, in all cases the diffusion coefficient appears to be 100 x10$^4$ nm$^2$/s lower in each case. The likely reason for this is the applicability of the Stokes-Einstein equation. As discussed in Chapter 1 (section 1.2.4), the equation has some limitations i.e. it assumes that all particles are spherical; the same size and are moving under constant

laminar flow.[37]   By deviating from these required conditions, the calculated diffusion coefficient will differ from the experimentally determined one, a phenomenon which has been reported in the literature before.[38,39]   In addition to this, looking at the shape of the bell-curves (Fig 2.8) and the fact that peaks become visible (at ~30 nm for thiolated silica, and >100 nm for the functionalised particles), it is obvious that there are populations of different sized particles in the suspension, likely due to either background noise or vibrations in the environment.   Considering NTA is a particle-tracking technique, any vibrations in the local environment could cause the particles to move unnaturally (i.e. not under Brownian motion).   These vibrations could alter the movement of the particles, causing bias in the data set.   Although the particles would be the same size, the vibrations would make them appear to be different sizes.   This will also change the experimental diffusion coefficients, making them appear different to what they are naturally.   The presence of larger particles (possibly due to aggregation) in the suspension alters the shape of the bell curve, and gives rise to small secondary peaks (Fig 2.8).   It is the presence of these smaller peaks which could also explain the difference in diffusion coefficient between experimental and predicted values.

The NTA size data presented here is in good agreement with the DLS data.   From the size increase between functionalised and unfunctionalised nanoparticles determined by two independent techniques, it is clear that the polymer has successfully been conjugated to the nanoparticle surface.

### 2.3.4 Particle functionality

In order to further probe this particle size increase, and determine the presence of the polymer alongside the amorphous silica nanoparticles, FT-IR and FT-Raman spectroscopy were carried out.

## 2.3.4.1 FT-IR spectroscopy

FT-IR analysis was carried out on lyophilised samples of nanoparticles in order to confirm the presence of the polymer in the sample along with the nanoparticles themselves. The spectra (Figs 2.10, 2.11, and 2.12) were also compared to free polymer (shown in brown in all cases) and the free unfunctionalised nanoparticles (blue).
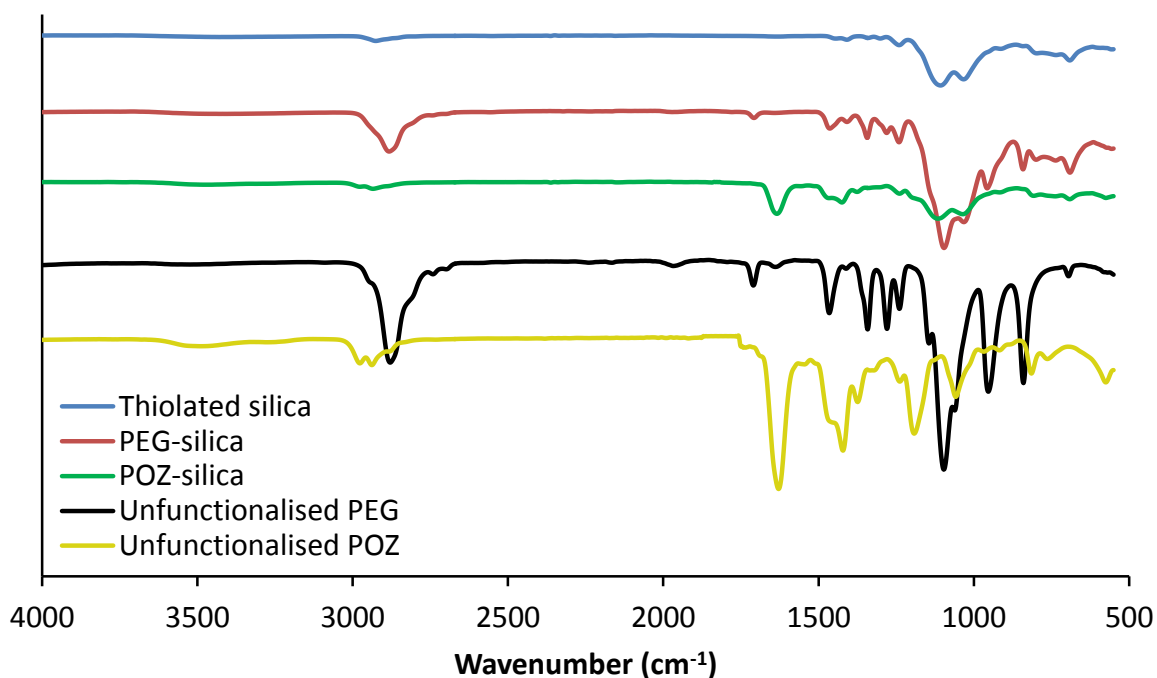


**Fig 2.10 FT-IR spectra for thiolated, PEGylated and POZylated silica nanoparticles.** PEG and POZ were purchased from Sigma-Aldrich.

Fig 2.10 shows the spectra for thiolated, PEGylated and POZylated silica. The spectrum of the thiolated silica (blue) shows two major peaks at 1032 and 1102 cm$^{-1}$; these appear in all spectra for the thiolated silica and represent the Si-O-Si stretches from the disiloxane. Due to the complex nature of the siloxane moiety in the nanoparticles, because of different functionalities attached to the silicon atoms, they exhibit two distinct features between 1300 and 1000 cm$^{-1}$.[40] This agrees well with the nanoparticle structure proposed by Irmukhametova *et al.*[21]

Both of these peaks appear in the other spectra for functionalised particles (red and green) confirming the presence of the silica nanoparticles in these samples. By comparing the peaks that appear in these samples to that of the free polymer (shown in brown and grey) it is possible to further identify the polymer presence in the funcitonalised sample.

In the PEGylated silica (red) spectrum, there is the emergence of several peaks, most noticeably; 2876 cm$^{-1}$ (CH2), 1702 cm$^{-1}$ (C=O), 1642 cm$^{-1}$ (aliphatic C-C), 1342 cm$^{-1}$ (C-O-C), and 1242 cm$^{-1}$ (aliphatic C-N). These peaks also appear in the spectrum for unfunctionalised polymer. The presence of the C=O stretches (from the ketone in the maleimide) and C-O-C (ether vibrations), along with the peak representing the Si-O-Si bonds in the silica particle, clearly demonstrate the successful functionalisation of the nanoparticles with PEG.

Similarly, for the POZylated silica spectrum (Fig 2.10), the presence of peaks at 2940 cm$^{-1}$(CH2), 1630 cm$^{-1}$ (C=O),1476 cm$^{-1}$ (C-H), 1422 cm$^{-1}$ (CH3),and 1236 cm$^{-1}$ (C-N) demonstrate the presence of POZ in this sample. Once again the presence of the Si-O-Si stretches at 1032 and 1102 cm$^{-1}$ show the presence of the silica nanoparticle. The signal generated by the alkyne end group on the polymer is very weak and not detectable. The peaks present for the POZylated silica (green) also appear in the spectra for unfunctionalised POZ, further illustrating the presence of the polymer in the sample.

The next set of spectra to be analysed are those concerning the POZ macromolecules with different pendent groups (Fig 2.11). In this case, the spectra were compared to the unfunctionalised silica nanoparticles (blue), and also that of the PEOZ (Sigma) sample. PEOZ (Sigma) was chosen as a comparison due to a larger abundance of polymer compared to those obtained from Prof Richard Hoogenboom. As the macromolecules only vary by a single methyl group, the spectra should all be relatively similar.
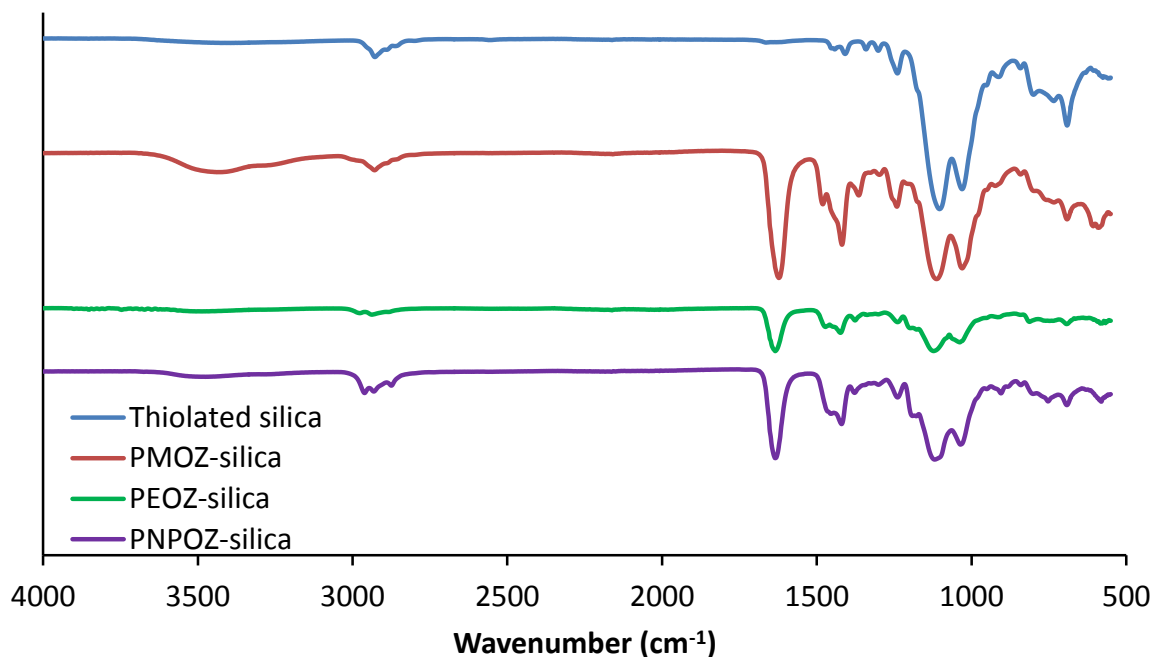
**Fig 2.11 FT-IR spectra for unfunctionalised thiolated silica and POZylated silica nanoparticles.** POZ samples were synthesised by Richard Hoogencoom.

Again, by comparing the spectra obtained for the unfunctionalised silica with those of the functionalised silica, there are clear differences. As with the previous spectra for thiolated silica, there are principle peaks at 1120 and 1089 cm$^{-1}$, representing the Si-O-Si disiloxane moiety. In addition to this, some other smaller peaks appear in the nanoparticle structure at 2923 cm$^{-1}$(C-H), 1237 cm$^{-1}$(C-O), and 687 cm$^{-1}$(Si-S).

As with the spectra for the POZylated nanoparticles (Fig 2.10), upon functionalisation several distinct peaks appear; 2978 cm$^{-1}$(CH2), 1629 cm$^{-1}$ (C=O),1463 cm$^{-1}$ (C-H), 1416 cm$^{-1}$ (CH3),and 1236 cm$^{-1}$ (C-N). Again these peaks are seen in the unfunctionalised polymer itself (black, Fig 2.10). The spectra for the different variations of POZ (PMOZ, PEOZ, and PNPOZ) all have the same peaks, most noticeably the large C=O peak at ~1600 cm$^{-1}$. This again illustrates successful functionalisation of POZ to the silica particle.

The final spectra compare PNIPAM functionalised silica, PNPNOZ functionalised silica and unfunctionalised thiolated silica (Fig 2.12).
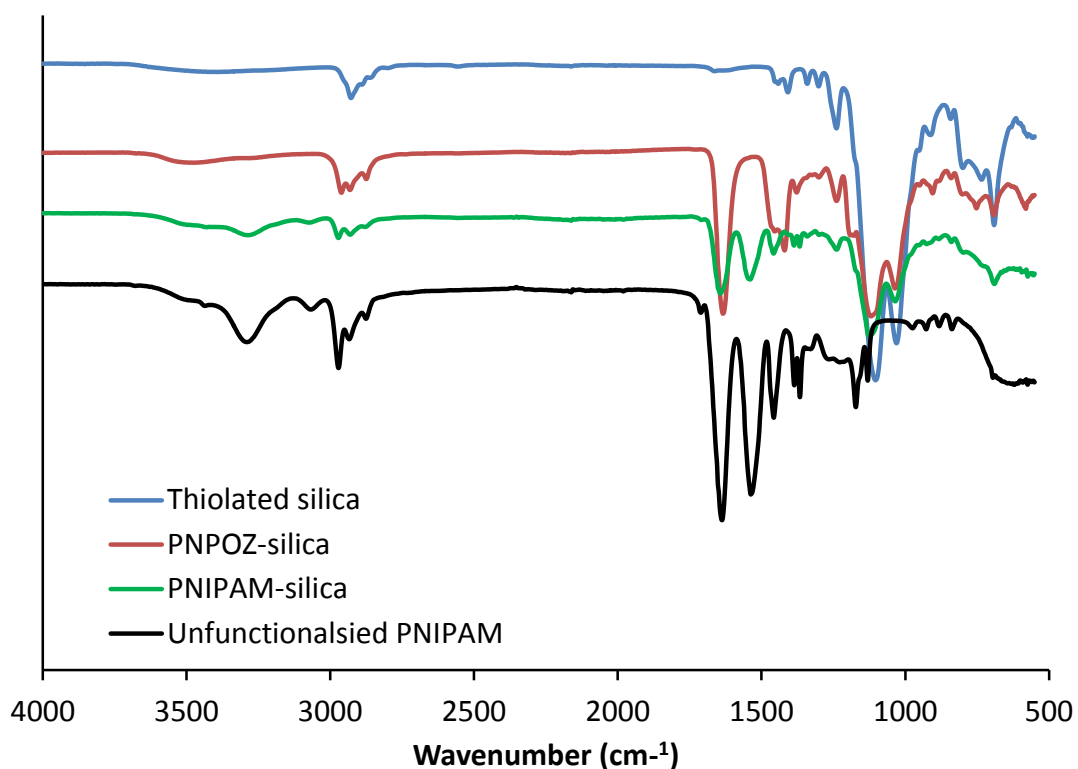
**Fig 2.12 FT-IR spectra for thiolated, PNPOZylated, and PNIPAM silica nanoparticles.** PNPOZ was synthesised by Richard Hoogenboom, and PNIPAM was purchased from Sigma-Aldrich.

The spectrum for PNIPAM functionalised silica nanoparticles (Fig 2.12, green) has predominant peaks at 3298 $cm^{-1}$ (aliphatic C-H), 1632 $cm^{-1}$ (C=O), 1535 $cm^{-1}$ (N-H), and 1459 $cm^{-1}$ (aliphatic C-C). These features are not seen in the spectrum of unfunctionalised silica and therefore demonstrate the presence of PNIPAM bound to the silica particle. In addition, to confirm the presence of the silica, the peaks at 1032, 1102 and 695 $cm^{-1}$ represent the two peaks for Si-O-Si, and one for Si-S, respectively. The peaks representing the bound PNIPAM are also seen in the unfunctionalised PNIPAM (Fig 2.12, black), confirming that the additional peaks are indicative of PNIPAM. The PNPOZ-silica particles used in this study were the same as was discussed for Fig 2.11.

### 2.3.4.2 FT-Raman spectroscopy

FT-Raman is often used as a complementary technique to FT-IR spectroscopy, and allows for the detection of homopolar bonding vibrations such as C=C, and is also more

sensitive to sulphur and silicon based vibrational modes than FT-IR. Fig 2.13 shows the spectra for unfunctionalised silica, PEGylated silica, and POZylated silica along with the spectra for the free polymer.
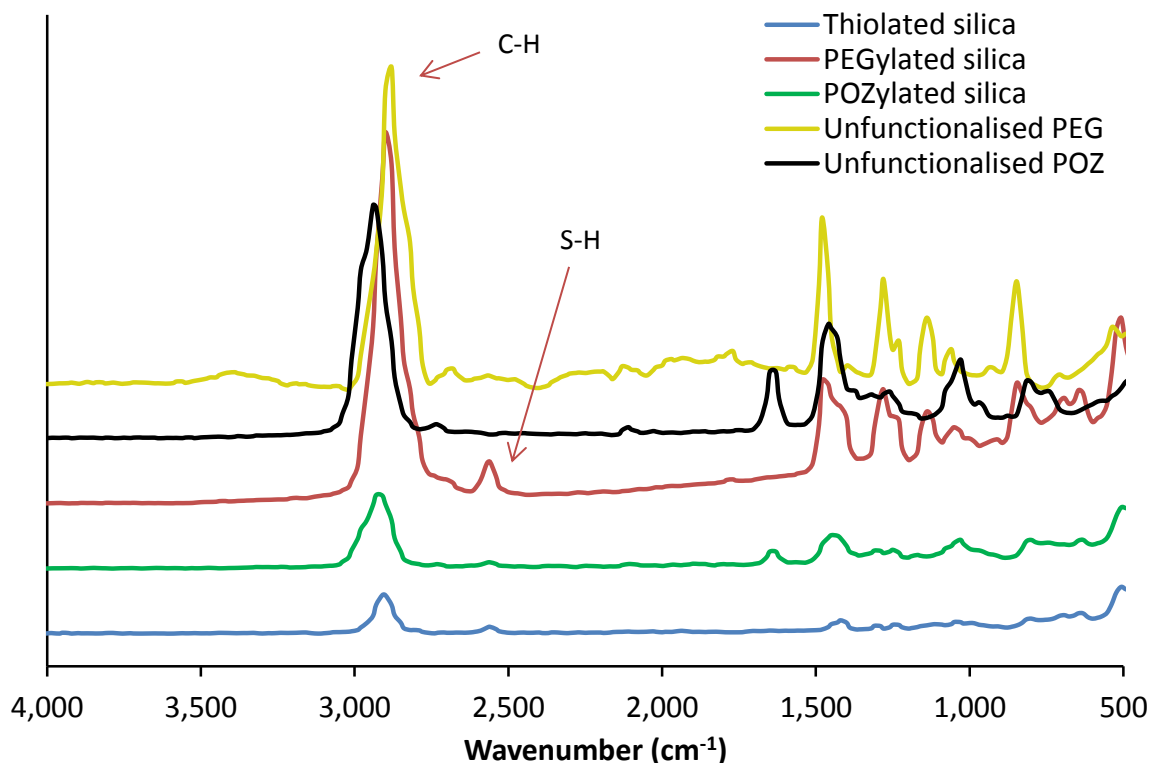


**Fig 2.13 Raman spectra for thiolated (blue), PEGylated (red), and POZylated (green) silica nanoparticles.**

Again there are marked differences between the functionalised and unfunctionalised particles. The emergence of several peaks in the spectra for functionalised particles that are also present in the spectra for unfunctionalised polymer, confirm polymer presence. The spectrum for thiolated silica (blue), shows principle peaks at 2880 cm$^{-1}$ (C-H), 2510 cm$^{-1}$ (S-H), 1400 cm$^{-1}$ (CH2), 1310 cm$^{-1}$ (C-C), 1250 cm$^{-1}$ (C-C), 631 cm$^{-1}$ (C-S), and ~500 cm$^{-1}$ (Si-O-Si and S-S).

As with the spectra for unfunctionalised silica, the spectrum of the PEGylated silica (red), shows the peaks at 2900 cm$^{-1}$ (C-H), 2560 cm$^{-1}$ (S-H), 1480 cm$^{-1}$ (CH2), 1280 cm$^{-1}$ (C-C), 646 cm$^{-1}$ (C-S), and ~500 cm$^{-1}$ (Si-O-Si and S-S) are clearly present, confirming the

presence of the thiolated silica. The minor discrepancies in peak positions for the two spectra could be two-fold; firstly (as the peaks are fairly small in some cases, they were not accurately measured, and secondly that the binding of the polymer has caused a shift in peak position. The latter is especially true as some of the peaks for unfunctionalised nanoparticles and polymer appear in both, namely those representing; C-H, CH2, and C-C groups. In actuality, this discrepancy is likely to be a combination of both these factors.

However there are two additional peaks at 1140 cm$^{-1}$ and 847 cm$^{-1}$, representing the asymmetrical C-O-C and C-O-C stretch respectively. The presence of these two peaks confirms the presence of the ether in PEG, and therefore demonstrates that PEG is present in the sample. Interestingly the peak representing the thiol groups in this spectra appear larger than in the unfunctionalised silica nanoparticles. This is unexpected as there should be a reduction in the number of free thiol groups due to polymer binding (demonstrated by Ellman's assay, and increase in particle size). This change is down to intensity from the sample, which was greater in PEGylated silica than in the unfunctionalised silica.

Similarly for the spectrum of POZylated particles (green), as with the PEGylated and thiolated silica spectra, there are peaks at 2900 cm$^{-1}$ (C-H), 2530 cm$^{-1}$ (S-H), 1420 cm$^{-1}$ (CH2), 1250 cm$^{-1}$ (C-C), 646 cm$^{-1}$ (C-S), and ~500 cm$^{-1}$ (Si-O-Si and S-S). As before these are from the silica particle. The addition of the peak at 1620 cm$^{-1}$ (C=O) confirms the presence the amide group in POZ.

The Raman spectra in Fig 2.14 are from the different variations of POZ functionalised to the silica particles.
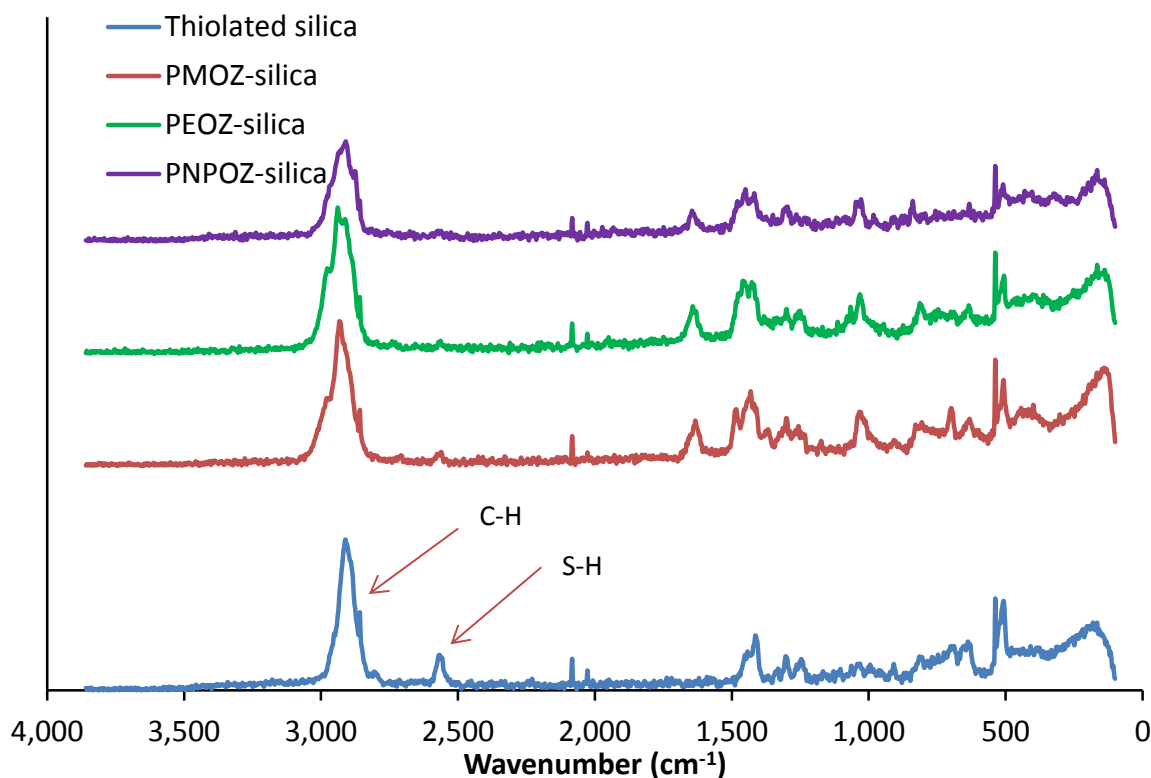
**Fig 2.14 Raman spectra for thiolated and POZylated silica nanoparticles.**

For the thiolated silica (blue), as before there are several distinct peaks; 2898 cm$^{-1}$ (C-H), 2555 cm$^{-1}$ (S-H), 1406 cm$^{-1}$ (CH2), 1294 cm$^{-1}$ (C-C), 1242 cm$^{-1}$ (C-C), 627 cm$^{-1}$ (C-S), and ~500 cm$^{-1}$ (Si-O-Si and S-S). After functionalisation with PMOZ, PEOZ, and PNPOZ it is possible to see two distinct changes; firstly a decrease in the size of the peak at 2555 cm$^{-1}$ (S-H), suggesting a decrease in the number of reactive thiol groups (confirmed with Ellman's assay, section 2.3.2), and secondly the emergence of two new peaks; 1631 cm$^{-1}$ (C=O), and 1024 cm$^{-1}$ (C-C vibrations). These peaks also appear in the spectra for unfunctionalised polymer itself (Fig 2.13, black). The combination of decrease in reactive thiol group and also presence of peaks representing that of POZ further confirms the binding of the POZ macromolecules to the surface of the thiolated silica.

The final spectra (Fig 2.15) are that of PNIPAM-silica, PNPOZ-silica and unfunctionalised silica.
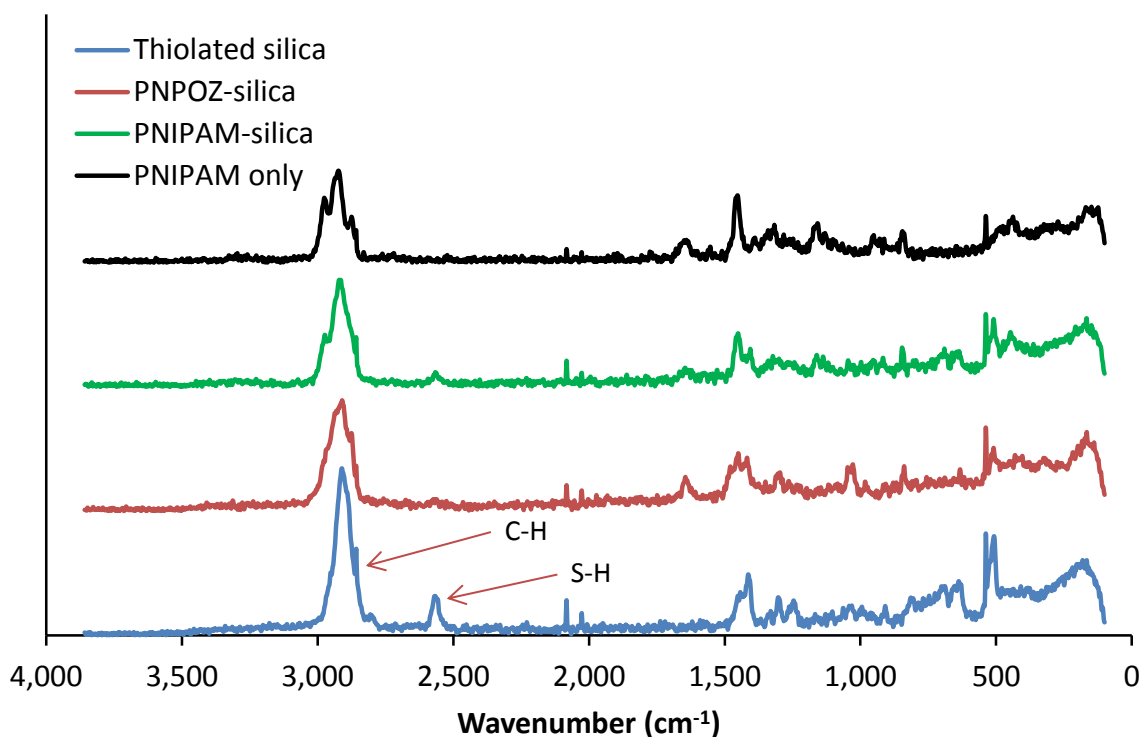
**Fig 2.15 Raman spectra for thiolated, POZylated, and PNIPAM-silica nanoparticles.**

Again, the spectrum for thiolated silica (blue), has several distinct peaks; 2898 cm$^{-1}$ (C-H), 2555 cm$^{-1}$ (S-H), 1406 cm$^{-1}$ (CH2), 1294 cm$^{-1}$ (C-C), 1242 cm$^{-1}$ (C-C), 627 cm$^{-1}$ (C-S), and ~500 cm$^{-1}$ (Si-O-Si and S-S), and PNPOZ has peaks at 1631 cm$^{-1}$ (C=O), and 1024 cm$^{-1}$ (C-C vibrations). Following PNIPAM functionalisation, new peaks arise at; 1628, and 837 cm$^{-1}$ again representing the C=O stretch and C-C vibrations in PNIPAM. These peaks can also be found in the spectra for unfunctionalised PNIPAM (shown in brown).

In order to compare the size of the SH peaks accurately, the ratio of SH intensity to Si-O-Si intensity was calculated (Table 2.4). Given that the Si-O-Si peak will not change following functionalisation (as these moieties do not exist in the polymers being studied), it can be used as an internal standard in the sample.

**Table 2.4 Ratio of intensity for functionalised and unfunctionalised silica nanoparticles**

| Nanoparticle | Si-O-Si intensity | SH intensity | Ratio |
|---|---|---|---|
| Thiolated silica | 1.18 | 0.6 | 1:0.5 |
| PNIPAM-silica | 0.51 | 0.06 | 1:0.1 |
| PNPOZ-silica | 0.44 | 0.04 | 1:0.1 |
| PEG-silica | 3.35 | 1.14 | 1:0.3 |
| PMOZ-silica | 0.76 | 0.06 | 1:0.1 |
| PEOZ-silica (sigma) | 0.28 | 0.06 | 1:0.2 |
| PEOZ-silica | 0.7 | 0.04 | 1:0.1 |

Looking at these values, it is clear that the proportional intensity of SH groups reduced upon functionalisation, suggesting a decrease in the number of reactive thiol groups in the sample.

From the Raman data, it is clear that the particles have successfully been functionalised with the polymers, and corroborates the FT-IR data.

### 2.3.5 Solid-state silicon NMR

In addition previous characterisation experiments, NMR studies were undertaken to further confirm successful surface modification and that the modification process had no adverse effects on the silica core dimensions.

Fig 2.16 shows the CPMAS NMR spectrum of the silica precursor, highlighting two peaks at -57.9 ppm and -67.8 ppm. These resonances are attributed to the $^{29}$Si nuclei at three and two silicon-oxygen-silicon bridge coordination (so called T3 and T2 species), respectively.[49] The SPMAS and CPMAS spectra do not show any significant differences and yield similar intensity ratios $I_{T3}/I_{T2}$ of ca. 8.6.

Figure 2.17 compares CPMAS spectra of the thiolated silica nanoparticles and POZ functionalised silica nanoparticles. The resonance at -67.8 ppm remains

unchanged whereas the peak at -57.9 ppm shifts upfield to -58.9 ppm after functionalisation. The intensity ratio $I_{T3}/I_{T2}$ decreases from ca. 8.6 for the SPMAS experiment, to ca. 7.6 for the CPMAS experiment. The increase in the T2 intensity suggests the proximity of additional protons which will cause enhancement of the signal in the CPMAS experiment.[50]  Both the upfield shift and increase in the intensity of the T2 signal are consistent with the presence of the POZ molecules (the additional source of protons) on the nanoparticle surface.
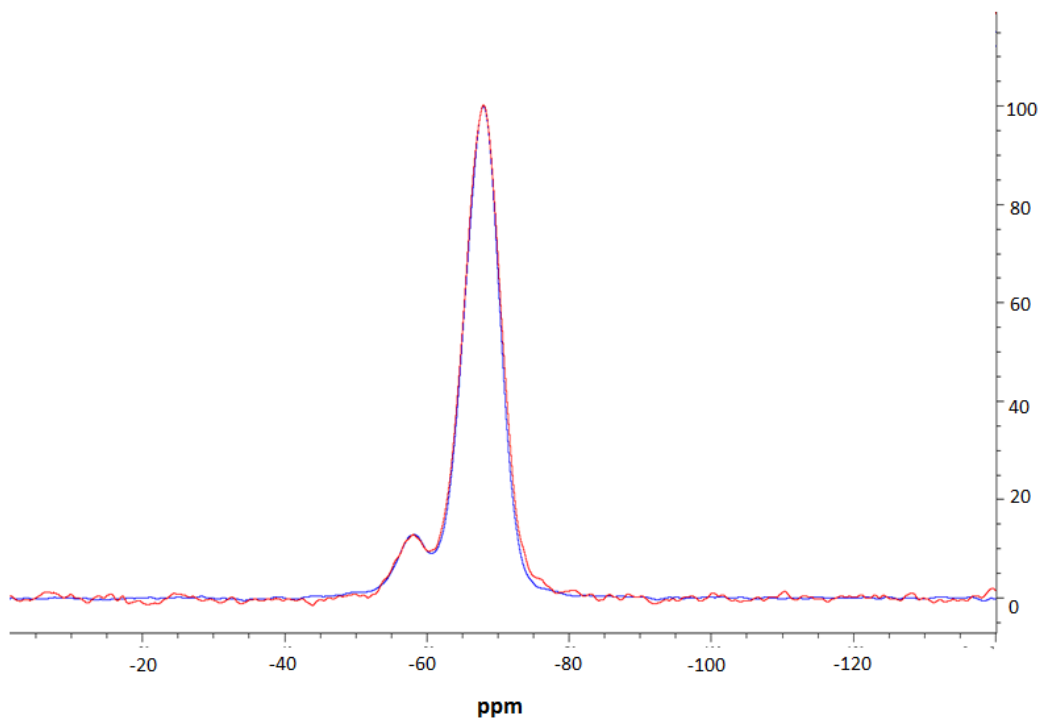
**Fig 2.16 MAS NMR spectra of thiolated silica; SPMAS spectrum is shown in red, CPMAS spectrum is shown in blue.**
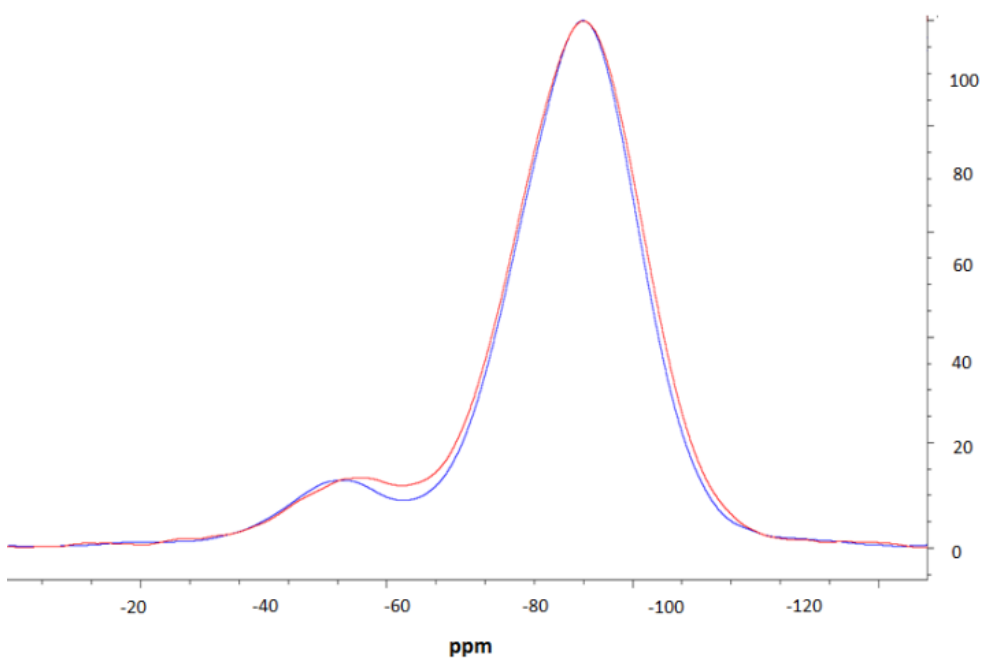


**Fig 2.17 CPMAS NMR spectra of thiolated silica (blue) and PEOZylated silica (red).**

The changes to the T2 resonance suggest that Si-O-Si bridges are predominantly present on the surface of the nanoparticle and thus more sensitive to its modification. Assuming that the nanoparticles are spherical (as shown by Transition Electron Microscopy- TEM) and that T2 species are present only on the surface, the radius of the nanoparticle can be estimated. The intensity ratio $I_{T3}/I_{T2}$ (core vs surface silica) can provide a crude estimate of the size, because the ratio of volume to surface area of the spherical particle changes as the function of its radius. Therefore, both the unfunctionalised thiolated silica nanoparticles and the POZ-silica nanoparticles show a radius estimated to be ~26 nm (both from SPMAS and CPMAS experiments). Both particle sizes appear the same because there are no changes to the number of silicon moieties on the surface with the addition of POZ, and the single pulse experiment does not rely on signal enhancement (proton-carbon cross-polarisation transfer). With the CPMAS experiment, the estimated size is smaller ca. 23 nm, as expected for the enhanced T2 signal intensity.

Although these sizes are in good agreement with the DLS data, it is important to note that the DLS shows that the $R_h$ of the particles is 52 nm. As the size determined by NMR is carried out using solid-state (and therefore not in the presence of water), it would be expected that the size would be smaller (i.e. around 30 nm as depicted by TEM). However, this is not the case. It is likely that the freeze-drying process causes this discrepancy. As water diffusing into the core of the nanoparticle freezes, forming ice crystals, it would expand, thus warp the internal structure of the particle. This would create pockets of empty space inside the particle, making them appear larger. A similar result was reported by Sameti *et al.*, and Abdelwahed, *et al.*,[51,52] who found that the size of silica nanoparticles suspended was larger than the original particle size, without the presence of any cryprotectants.

## 2.4 Conclusions

This study focuses on the synthesis, functionalisation and characterisation of the principle nanoparticles used in this study. Core amorphous silica nanoparticles were synthesised

by the self-condensation of MPTS, resulting in a hydrodynamic diameter of 52 nm core thiolated silica nanoparticles. These particles were then functionalised with three polymers; PEG, POZ, and PNIPAM. Characterisation studies demonstrated successful functionalisation of the particles, and thermal analysis revealed the level of loading exhibited onto the particles.

Previously these nanoparticles have been functionalised with PEG, yielding similar results to those presented here (no significant difference ($P < 0.05$, Student's t-test) was observed. However this is the first time PNIPAM and POZ have been grafted to these specific MPTS-synthesised nanoparticles. In addition, a novel grafting technique was developed, in which alkyne terminated polymers can be grafted onto the surface of thiolated silica using a one-pot method, without any detriment to the particle itself.

Each particle type was used in later experiments to assess their diffusion in various different media.

## 2.5 References

(1)     Steenland, K.; Ward, E. Silica: A Lung Carcinogen. *CA. Cancer J. Clin. 64* (1), 63–69.

(2)     Sellamuthu, R.; Umbright, C.; Roberts, J. R.; Cumpston, A.; McKinney, W.; Chen, B. T.; Frazer, D.; Li, S.; Kashon, M.; Joseph, P. Molecular Insights into the Progression of Crystalline Silica-Induced Pulmonary Toxicity in Rats. *J. Appl. Toxicol.* **2013**, *33* (4), 301–312.

(3)     Kachuri, L.; Villeneuve, P. J.; Parent, M.-É.; Johnson, K. C.; Harris, S. A. Occupational Exposure to Crystalline Silica and the Risk of Lung Cancer in Canadian Men. *Int. J. Cancer* **2014**, *135* (1), 138–148.

(4)     Liu, Y.; Steenland, K.; Rong, Y.; Hnizdo, E.; Huang, X.; Zhang, H.; Shi, T.; Sun, Y.; Wu, T.; Chen, W. Exposure-Response Analysis and Risk Assessment for Lung Cancer in Relationship to Silica Exposure: A 44-Year Cohort Study of 34,018 Workers. *Am. J. Epidemiol.* **2013**, *178* (9), 1424–1433.

(5)     Satpathy, S. R.; Jala, V. R.; Bodduluri, S. R.; Krishnan, E.; Hegde, B.; Hoyle, G. W.; Fraig, M.; Luster, A. D.; Haribabu, B. Crystalline Silica-Induced Leukotriene B4-Dependent Inflammation Promotes Lung Tumour Growth. *Nat. Commun.* **2015**, *6*, 7064.

(6)     Mossman, B. T.; Glenn, R. E. Bioreactivity of the Crystalline Silica Polymorphs, Quartz and Cristobalite, and Implications for Occupational Exposure Limits (OELs). *Crit. Rev. Toxicol.* **2013**.

(7)     Fubini, B.; Zanetti, G.; Altilia, S.; Tiozzo, R.; Lison, D.; Saffiotti, U. Relationship between Surface Properties and Cellular Responses to Crystalline Silica: Studies

with Heat-Treated Cristobalite. *Chem. Res. Toxicol.* **1999**, *12* (8), 737–745.

(8)     Horwell, C. J.; Williamson, B. J.; Donaldson, K.; Le Blond, J. S.; Damby, D. E.; Bowen, L. The Structure of Volcanic Cristobalite in Relation to Its Toxicity; Relevance for the Variable Crystalline Silica Hazard. *Part. Fibre Toxicol.* **2012**, *9* (1), 44.

(9)     Dekkers, S.; Krystek, P.; Peters, R. J. B.; Lankveld, D. P. K.; Bokkers, B. G. H.; van Hoeven-Arentzen, P. H.; Bouwmeester, H.; Oomen, A. G. Presence and Risks of Nanosilica in Food Products. *Nanotoxicology* **2011**, *5* (3), 393–405.

(10)    Slowing, I. I.; Trewyn, B. G.; Giri, S.; Lin, V. S.-Y. Mesoporous Silica Nanoparticles for Drug Delivery and Biosensing Applications. *Adv. Funct. Mater.* **2007**, *17* (8), 1225–1236.

(11)    Charles C. Payne. *The Colloid Chemistry of Silica*; Bergna, H. E., Ed.; Advances in Chemistry; American Chemical Society: Washington DC, 1994; Vol. 234.

(12)    Nakamura, M.; Ishimura, K. One-Pot Synthesis and Characterization of Three Kinds of Thiol-Organosilica Nanoparticles. *Langmuir* **2008**, *24* (9), 5099–5108.

(13)    *Colloidal Silica: Fundamentals and Applications*; CRC Press, 2005.

(14)    Stöber, W.; Fink, A.; Bohn, E. Controlled Growth of Monodisperse Silica Spheres in the Micron Size Range. *J. Colloid Interface Sci.* **1968**, *26* (1), 62–69.

(15)    Wu, S.-H.; Mou, C.-Y.; Lin, H.-P. Synthesis of Mesoporous Silica Nanoparticles. *Chem. Soc. Rev.* **2013**, *42* (9), 3862–3875.

(16)    Rao, K. S.; El-Hami, K.; Kodaki, T.; Matsushige, K.; Makino, K. A Novel Method for Synthesis of Silica Nanoparticles. *J. Colloid Interface Sci.* **2005**, *289* (1), 125–131.

(17)    Li, Z.; Barnes, J. C.; Bosoy, A.; Stoddart, J. F.; Zink, J. I. Mesoporous Silica Nanoparticles in Biomedical Applications. *Chem. Soc. Rev.* **2012**, *41* (7), 2590–2605.

(18)    Rahman, I. A.; Padavettan, V. Synthesis of Silica Nanoparticles by Sol-Gel: Size-Dependent Properties, Surface Modification, and Applications in Silica-Polymer Nanocomposites—A Review. *J. Nanomater.* **2012**, *2012*, 1–15.

(19)    Du, X.; He, J. Amino-Functionalized Silica Nanoparticles with Center-Radially Hierarchical Mesopores as Ideal Catalyst Carriers. *Nanoscale* **2012**, *4* (3), 852–859.

(20)    Cash, B. M.; Wang, L.; Benicewicz, B. C. The Preparation and Characterization of Carboxylic Acid-Coated Silica Nanoparticles. *J. Polym. Sci. Part A Polym. Chem.* **2012**, *50* (13), 2533–2540.

(21)    Irmukhametova, G. S.; Mun, G. A.; Khutoryanskiy, V. V. Thiolated Mucoadhesive and PEGylated Nonmucoadhesive Organosilica Nanoparticles from 3-Mercaptopropyltrimethoxysilane. *Langmuir* **2011**, *27* (15), 9551–9556.

(22)    Wang, Y.; Zhao, Q.; Han, N.; Bai, L.; Li, J.; Liu, J.; Che, E.; Hu, L.; Zhang, Q.; Jiang, T.; et al. Mesoporous Silica Nanoparticles in Drug Delivery and Biomedical Applications. *Nanomedicine Nanotechnology, Biol. Med.* **2015**, *11* (2), 313–327.

(23)    Yang, Y.; Yu, C. Advances in Silica Based Nanoparticles for Targeted Cancer Therapy. *Nanomedicine Nanotechnology, Biol. Med.* **2015**.

(24)    Tanaka, K.; Chujo, Y. Design of Functionalized Nanoparticles for the Applications in Nanobiotechnology. *Adv. Powder Technol.* **2014**, *25* (1), 101–113.

(25)    Irmukhametova, G.; Fraser, B.; Keddie, J.; Mun, G.; Khutoryanskiy, V. V. Hydrogen-Bonding-Driven Self-Assembly of PEGylated Organosilica Nanoparticles

with Poly(acrylic Acid) in Aqueous Solutions and in Layer-by-Layer Deposition at Solid Surfaces. *Langmuir*. American Chemical Society January 12, 2012.

(26)　Ellman, G. L. Tissue Sulfhydryl Groups. *Arch. Biochem. Biophys.* **1959**, *82* (1), 70–77.

(27)　Bravo-Osuna, I.; Teutonico, D.; Arpicco, S.; Vauthier, C.; Ponchel, G. Characterization of Chitosan Thiolation and Application to Thiol Quantification onto Nanoparticle Surface. *Int. J. Pharm.* **2007**, *340* (1–2), 173–181.

(28)　Mun, E. A.; Hannell, C.; Rogers, S. E.; Hole, P.; Williams, A. C.; Khutoryanskiy, V. V. On the Role of Specific Interactions in the Diffusion of Nanoparticles in Aqueous Polymer Solutions. *Langmuir* **2014**, *30* (1), 308–317.

(29)　van der Pol, E.; Coumans, F. A. W.; Sturk, A.; Nieuwland, R.; van Leeuwen, T. G. Refractive Index Determination of Nanoparticles in Suspension Using Nanoparticle Tracking Analysis. *Nano Lett.* **2014**, *14* (11), 6195–6201.

(30)　Hoyle, C. E.; Lowe, A. B.; Bowman, C. N. Thiol-Click Chemistry: A Multifaceted Toolbox for Small Molecule and Polymer Synthesis. *Chem. Soc. Rev.* **2010**, *39* (4), 1355–1387.

(31)　Oria, L.; Aguado, R.; Pomposo, J. A.; Colmenero, J. A Versatile "click" chemistry Precursor of Functional Polystyrene Nanoparticles. *Adv. Mater.* **2010**, *22* (28), 3038–3041.

(32)　Hoyle, C. E.; Bowman, C. N. Thiol-Ene Click Chemistry. *Angew. Chem. Int. Ed. Engl.* **2010**, *49* (9), 1540–1573.

(33)　Trinajstić, N. Calculation of Carbon-Sulphur Bond Lengths. *Tetrahedron Lett.* **1968**, *9* (12), 1529–1532.

(34)　Ganivada, M. N.; Kumar, P.; Shunmugam, R. A Unique Polymeric Gel by Thiol–alkyne Click Chemistry. *RSC Adv.* **2015**, *5* (62), 50001–50004.

(35)　Clogston, J. D.; Patri, A. K. Zeta Potential Measurement. *Methods Mol. Biol.* **2011**, *697*, 63–70.

(36)　Kaszuba, M.; McKnight, D.; Connah, M. T.; McNeil-Watson, F. K.; Nobbmann, U. Measuring Sub Nanometre Sizes Using Dynamic Light Scattering. *J. Nanoparticle Res.* **2007**, *10* (5), 823–829.

(37)　Edward, J. T. Molecular Volumes and the Stokes-Einstein Equation. *J. Chem. Educ.* **1970**, *47* (4), 261.

(38)　Tuteja, A.; Mackay, M. E.; Narayanan, S.; Asokan, S.; Wong, M. S. Breakdown of the Continuum Stokes-Einstein Relation for Nanoparticle Diffusion. *Nano Lett.* **2007**, *7* (5), 1276–1281.

(39)　Kumar, S. K.; Szamel, G.; Douglas, J. F. Nature of the Breakdown in the Stokes-Einstein Relationship in a Hard Sphere Fluid. *J. Chem. Phys.* **2006**, *124* (21), 214501.

(40)　Smith, A. L. Infrared Spectra-Structure Correlations for Organosilicon Compounds. *Spectrochim. Acta* **1960**, *16* (1–2), 87–105.

(41)　Layek, R. K.; Nandi, A. K. A Review on Synthesis and Properties of Polymer Functionalized Graphene. *Polymer (Guildf).* **2013**, *54* (19), 5087–5103.

(42)　Fang, M.; Wang, K.; Lu, H.; Yang, Y.; Nutt, S. Covalent Polymer Functionalization of Graphene Nanosheets and Mechanical Properties of Composites. *J. Mater. Chem.* **2009**, *19* (38), 7098.

(43)　Yang, Y.; Wang, J.; Zhang, J.; Liu, J.; Yang, X.; Zhao, H. Exfoliated Graphite Oxide

Decorated by PDMAEMA Chains and Polymer Particles. *Langmuir* **2009**, *25* (19), 11808–11814.

(44) Langford, C. R.; Johnson, D. W.; Cameron, N. R. Chemical Functionalization of Emulsion-Templated Porous Polymers by Thiol–ene "click" Chemistry. *Polym. Chem.* **2014**, *5* (21), 6200–6206.

(45) Moser, M.; Behnke, T.; Hamers-Allin, C.; Klein-Hartwig, K.; Falkenhagen, J.; Resch-Genger, U. Quantification of PEG-Maleimide Ligands and Coupling Efficiencies on Nanoparticles with Ellman's Reagent. *Anal. Chem.* **2015**, *87* (18), 9376–9383.

(46) Erel, O.; Neselioglu, S. A Novel and Automated Assay for Thiol/disulphide Homeostasis. *Clin. Biochem.* **2014**, *47* (18), 326–332.

(47) Grochowski, M. R.; Li, T.; Brennessel, W. W.; Jones, W. D. Competitive Carbon-Sulfur vs Carbon-Carbon Bond Activation of 2-Cyanothiophene with [Ni(dippe)H]2. *J. Am. Chem. Soc.* **2010**, *132* (35), 12412–12421.

(48) Downard, K. M.; Sheldon, J. C.; Bowie, J. H.; Lewis, D. E.; Hayes, R. N. Are the Elusive Ions Mercaptomethyl(-CH2SH), Hydroxymethyl(-CH2OH), and Aminomethyl(-CH2NH2) Detectable in the Gas Phase? A Joint Ab Initio/experimental Approach. *J. Am. Chem. Soc.* **1989**, *111* (21), 8112–8115.

(49) Sen, T.; Bruce, I. J. Surface Engineering of Nanoparticles in Suspension for Particle Based Bio-Sensing. *Sci. Rep.* **2012**, *2*, 564.

(50) Faulkner, R.; DiVerdi, J.; Yang, Y.; Kobayashi, T.; Maciel, G. The Surface of Nanoparticle Silicon as Studied by Solid-State NMR. *Materials (Basel).* **2012**, *6* (1), 18–46.

(51) Sameti, M.; Bohr, G.; Ravi Kumar, M. N. V.; Kneuer, C.; Bakowsky, U.; Nacken, M.; Schmidt, H.; Lehr, C.-M. Stabilisation by Freeze-Drying of Cationically Modified Silica Nanoparticles for Gene Delivery. *Int. J. Pharm.* **2003**, *266* (1–2), 51–60.

(52) Abdelwahed, W.; Degobert, G.; Stainmesse, S.; Fessi, H. Freeze-Drying of Nanoparticles: Formulation, Process and Storage Considerations. *Adv. Drug Deliv. Rev.* **2006**, *58* (15), 1688–1713.

# Chapter 3

# Diffusion of gold nanoparticles in solutions of Pluronic F-127 at different concentrations

## 3.1 Introduction

Colloidal gold nanoparticles (AuNPs) are one of the most widely studied nanostructures in the literature, mainly due to their unique optical properties, ease and versatility of synthesis, and good biocompatibility. They have applications in a wide array of scientific disciplines, including; drug delivery,[1] cancer detection,[2] bioimaging,[3] and catalysis.[4] This breadth stems from their ease in synthesis, diversity in surface functionality, and also varying morphologies allowing them to be tailor made for bespoke applications.[5–7] There are many reported strategies in the literature on how AuNPs can be synthesised, however a select number are used more often than others. These will briefly be discussed below.

The Frens-Turkevich method is one of the most widely used techniques for synthesizing AuNP's, in part due to its simplistic one-pot method.[8,9] The reaction involves boiling a solution of aqueous gold tetrachloride, followed by the addition of sodium citrate. The addition of sodium citrate (a reducing agent) forms a gold seed around which the particles grow. By adding larger volumes of reducing agent, more seeds are formed, which results in smaller particles (due to smaller amounts of gold precursor available to build the particle), as opposed to smaller volumes of reducing agent which produces fewer seeds resulting in larger particles.[5] This technique allows the synthesis of particles ranging from 15 nm to 150 nm, however larger particles tend to be less monodisperse than smaller ones.

Another popular synthetic strategy is the Brust-Schiffrin technique.[10] Here, the clusters are made by reduction of gold salt in an organic solvent, such as toluene, with sodium borohydride and a thiolated molecule. By taking advantage of the strong Au-S bond, it is possible to create highly monodisperse particles at ambient temperatures. There are several examples in the literature of authors using different thiol ligands; such as benzylthiol and 1,4-benzenedimethanethiol,[11] dodecanethiol,[10] hexanethiolate[12] and phenylethanethiol.[13] The particles, traditionally between 2 and 10 nm, and can be easily modified by taking advantage of the thiol moiety on the particle surface.

In addition to the use of reducing agents to synthesise AuNP's, some more interesting and novel techniques of gold nanoparticle synthesis include using liposomes, micelles/surfactants, and bacteria. This includes various Pluronic functionalised AuNP's,[14–16] and also nanoparticles synthesized in the presence of Pluronic.[17–19] Based on their increased use, a study on the diffusive properties of AuNP's in Pluronics is needed to further understand how they behave in dispersion with the polymers at different temperatures and concentrations.

Poloxamers (also known by their trade-name of Pluronics) are block-co-polymers consisting of a central hydrophobic block of poly(propylene oxide) (PPO), surrounded by two hydrophilic blocks of poly(ethylene oxide) (PEO). In commercial Pluronics, their name is followed by a number classification which represents the molecular-weight of the polymer. Pluronics are used in the drug delivery field due to their unique self-assembling ability to form micelles, and eventually gel upon heating, a process which is reversible by cooling.[20] Due to this ability to gel *in situ* and their good biocompatibility/low toxicity,[21] Pluronics can be loaded with a drug for controlled release. This has been demonstrated for ocular drug delivery,[22] subcutaneous administration,[23] and for use as implants.[24] In addition to a dosage form, there are several examples of nanoparticles loaded into Pluronics and nanoparticles functionalised with Pluronics, in order to provide a network of thermally cross-linked nanoparticles.[25–27]

The aim of this study was to investigate how the diffusion of different sized AuNP's varies depending on both the temperature and state of a complex polymeric system. By studying how the particles diffuse in a gel, and whether increasing particle size hinders their diffusion, it may be possible to determine a pore-size and gain other insights into molecular mobility of nanoparticles in a confined polymer solution, and how this could be translated to a complex biological system.

## 3.2 Materials and methods

### 3.2.1 Materials

$HAuCl_4$, Pluronic F-127, and sodium citrate were purchased from Sigma-Aldrich (Gillingham, UK) and used without any further purification. All water used in this work was ultra-pure obtained from a PureLab UHQ water filtration system (18 MΩ). In addition to the synthesised nanoparticles, 80 nm gold nanoparticles were purchased from Sigma-Aldrich. The reason for this was 2-fold; to serve as a standard of known size and PDI, and also to establish which method was more cost-effective (synthesis or direct purchase).

### 3.2.2 Gold nanoparticle synthesis

Gold nanoparticles were synthesized according to the Frens-Turkevich method.[8,9] An aqueous stock solution of gold tetrachloride was made up to 10 mM, along with a 1% w/v solution of sodium citrate. Following this, the gold tetrachloride solution was diluted to a working concentration of 0.1 mM in 10 mL water, and placed in a round-bottom flask. This was heated in a paraffin bath to 80 ºC under constant stirring. Temperature was measured using an alcohol thermometer. Once the solution had reached temperature, 1% w/v sodium citrate was added at the following volumes; 0.009, 0.016 0.032 0.06 and 0.15 mL. These values were chosen based on the literature describing how different volumes of sodium citrate affect particle size.[28] Each volume of sodium citrate added was added to a separate solution of gold tetrachloride, creating a total of 5 different particle types. Soon after the addition of the sodium citrate, a colour change was observed, the

colour depending on the size of particles produced (see Table 3.1). The particles were left for a further 10 mins to ensure the reaction completed, before being removed from the heat and left to cool to room temperature.

Once at room temperature, the samples were purified by dialysis, using dialysis tubing with a molecular weight cut-off of 12-14 kDa (Medicell International Ltd, UK). They were purified against 4 L deionized water for 48 hours, where the water was changed for a minimum of 8 times. All samples were stored at 4 ºC until further use.

**Table 3.1 Volume of sodium citrate needed for synthesis of gold nanoparticles.**

| Sample name | Vol sodium citrate (mL) | Colour |
|:---:|:---:|:---:|
| Au1 | 0.15 | Red |
| Au2 | 0.06 | Red |
| Au3 | 0.032 | Purple |
| Au4 | 0.016 | Blue |
| Au5* (Sigma) | - | Pink |
| Au6 | 0.009 | Grey |

### 3.2.3 Particle characterisation

Following synthesis, all the particles (including the 80 nm standard particles), were characterised for size using Dynamic Light Scattering (DLS), Nanoparticle Tracking Analysis (NTA), and Transmission Electron Microscopy (TEM).

DLS measurements were performed on a Zetasizer NanoZS system (Malvern Instruments, UK). A refractive index of 0.2 was used for all measurements, which were carried out in disposable 1 mL plastic cuvettes (Fisher Scientific, UK), at 25 ºC. To prepare the samples, the stock solution of particles was diluted 1:100 into ultrapure water, and placed into the cuvettes for analysis. Individual readings of 10 seconds were recorded for a total of 12 runs, which was repeated 3 times per cuvette. Each sample was

measured independently 3 times and the size presented as mean ± standard deviation of these three repeats.

NTA measurements were performed on an LM10 system with an LM14 laser module and metal top-plate, syringe pump, green 532 nm laser, and sCOMS camera (Malvern Instruments, UK). Prior to analysis, samples were diluted 1:10,000 into ultrapure water producing a 1 mL suspension for analysis. 6x60 second videos were recorded for each measurement, and each sample was measured a total of 3 times each. Samples were measured under a continuous flow rate of 30 AU at 25 °C to maximise the number of particles tracked. Analysis was carried out using NTA v3.1 software, and the data presented represents the mean ± standard deviation of the three separate experiments.

Transmission electron microscopy experiments were performed on a JOEM-2010 microscope (JOEL, USA) at an accelerating voltage of 200 kV. Sample preparation was carried out by placing a drop of sample onto parafilm before placing holey carbon film 300 copper mesh grids (HC300Cu, EMresolutions, UK), carbon side down, onto the drop. This was left for 1 minute, before being air-dried and placed in the instrument.

### 3.2.4 Diffusion studies

Diffusion experiments were performed using the NanoSight LM10 system, LM14 laser module with attached LM14 top plate, green 532 nm laser, and syringe pump. Prior to performing the experiments, 4 different solutions of Pluronic F-127 were made in triplicate; 1% w/v, 5% w/v, 10% w/v, and 18% w/v by mixing the appropriate mass of Pluronic F-127 with 30 mL ultrapure water. Each separate concentration sample was freshly prepared to avoid bacterial degradation and contamination. Three solutions of each concentration were made, and each was measured 3 times for each particle type, resulting in a total of 9 measurements for each concentration. Particles were again diluted by 1:10,000 into 1 mL Pluronic solution. A control of particles suspended in water (0% w/v) was also measured under the same conditions as was used for the Pluronic F-127 experiments.

Each measurement consisted of taking a 60 second video at 2 $^0$C intervals between 24 $^0$C and 38 $^0$C, repeated 3 times per sample. Recordings were made whilst the syringe pump was in static mode to ensure the same population of particles was being measured throughout the whole series. Following each temperature ramp series, the syringe pump was advanced (flow rate 500 AU for 5 seconds) in order to measure a different population of particles. The full script can be seen in Fig 3.1.

```
REPEATSTART
SYRINGELOAD 500
DELAY 5
SYRINGESTOP
SETTEMP 24.0
DELAY 20
CAPTURE 60
DELAY 3
SETTEMP 26.0
DELAY 20
CAPTURE 60
DELAY 3
SETTEMP 28.0
DELAY 20
CAPTURE 60
DELAY 3
SETTEMP 30.0
DELAY 20
CAPTURE 60
DELAY 3
SETTEMP 32.0
DELAY 20
CAPTURE 60
DELAY 3
SETTEMP 34.0
DELAY 20
CAPTURE 60
DELAY 3
SETTEMP 36.0
DELAY 20
CAPTURE 60
DELAY 3
SETTEMP 38.0
DELAY 20
CAPTURE 60
DELAY 3
SETTEMP 22.0
DELAY 90
REPEAT 2
```

**Fig 3.1 Script employed to measure diffusion in the Pluronic system**

Following collection, the data was analysed using NTA v3.1.  In all cases the viscosity was set as that of water.  By doing so it is possible to measure the diffusion coefficient of the

particles when exposed to the viscosity of the "local environment bulk viscosity" of the system (as described by Lai *et al*. for a mucus network).[29] Following analysis, several different data files were be exported; "summary," which provided a breakdown of the results obtained from each video, "all tracks," which provided data on the x and y coordinates for each individual particle, and "intensity," which provided the size and diffusion coefficient for each individual particle tracked.

After analysis, both the "summary" and "all tracks" file were exported. Data in the summary file was used to calculate the mean diffusion coefficients ± standard deviation of each separate sample at each temperature. The "all tracks" file was used for calculation of heat maps, the distance each particle moved, and the area that each particle had moved in.

It is important to note that this series of experiments did not use NTA in the flow mode. This is because the diffusion of particles was assessed in a single local environment rather than a continuous system.

### 3.2.5 Application of a python script to calculate heat maps, distance, and area of particle movement

In order to provide more information than just the diffusion coefficient from the exported data files, a python script was written by Dr Mark Spillman (University of Reading), to generate a heat-map of the particles moving, as well as information on how far each individual particle moved, and the area each particle moved in.

A bespoke script written in the Python programming language was used to automate the procedure of trajectory analysis and plotting. The total distance travelled by a particle on a given trajectory was obtained via simple addition of the distance travelled in each step, calculated using Pythagoras' theorem. Particle trajectories were automatically fitted with an ellipse using an implementation[30] of the method described by Fitzgibbon *et al*.[31] The area of the ellipse was calculated to provide the "area of particle movement" metric seen

whilst the coordinates of the centres of the ellipses were used in conjunction with a Gaussian convolution procedure to produce the "heat-maps."

### 3.2.6 Pluronic F-127 characterisation

In order to characterise the Pluronic F-127 solutions, each concentration was subjected to a temperature ramp study using DLS. In each case, 1 mL of the Pluronic F-127 solution was placed in a low-volume 1 mL plastic cuvette (with care taken to avoid air bubbles), before being placed into the Zetasizer NanoZS instrument. In this experiment, the sample was subjected to a temperature ramp, where the temperature was raised by 1 ⁰C, left to equilibrate for 2 mins, and the size recorded. The range studied was between 20 and 40 ⁰C. A refractive index of 1.47 was used in all cases, and the solvent was assumed to be water. Each sample was measured for 10 seconds, for a total of 12 runs, with 3 repeats. This was repeated 3 times for every solution of Pluronic F-127 used. Data are presented as the mean ± standard deviation of the three independent recordings.

## 3.3 Results and discussion

### 3.3.1 Synthesis and characterisation

In the present study, AuNP's were synthesised using the Frens-Turkevich method whereby the addition of different volumes of sodium citrate resulted in the formation of particles of different sizes.[8,9] The particles produced different colours due to surface-plasmon resonance effects on the particle surface. Different sized particles cause the electron clouds to resonate at different frequencies, thus producing suspensions with different colours.[32] Again, this is reflected in this study as the different sized particles show different colours, and are similar to those already reported in the literature. Kimling *et al.* reported how the size of nanoparticles can range from 9 nm up to 120 nm depending on the concentration of $HAuCL_4$ in the starting solution, and the volume of sodium citrate added, initiating the reaction.[28] Following synthesis, all particles were characterised for size using three independent techniques (DLS, NTA, and TEM).

Table 3.2 shows the size of nanoparticles synthesised, and Fig 3.2 shows TEM images of the particles. In addition to the synthesized particles, a standard of 80 nm (Au5) was purchased from Sigma-Aldrich in order to provide a sample of known size with low PDI to act as a comparison. This sample is also included in the table. In addition, we wished to determine which method was more cost-effective. Synthesising the particles was found to be the cheaper option.

**Table 3.2 Size of gold nanoparticles, as determined by dynamic light scattering, and nanoparticle tracking analysis.** Au5[#] was purchased from Sigma-Aldrich. (n=3, mean ±standard deviation)

| Sample name | Size, nm (DLS) | PDI (DLS) | Size, nm (NTA) | Vol sodium citrate (mL) |
|---|---|---|---|---|
| Au1 | 22±1 | 0.376 ± 0.015 | 21 ± 2 | 0.15 |
| Au2 | 27±1 | 0.117 ± 0.028 | 22 ± 2 | 0.06 |
| Au3 | 38±1 | 0.362 ± 0.087 | 52 ± 13 | 0.032 |
| Au4 | 50±1 | 0.353 ± 0.114 | 71 ± 4 | 0.016 |
| Au5[#] | 77±2 | 0.114 ± 0.025 | 79 ± 3 | - |
| Au6 | 95±2 | 0.268 ± 0.038 | 77 ± 7 | 0.009 |
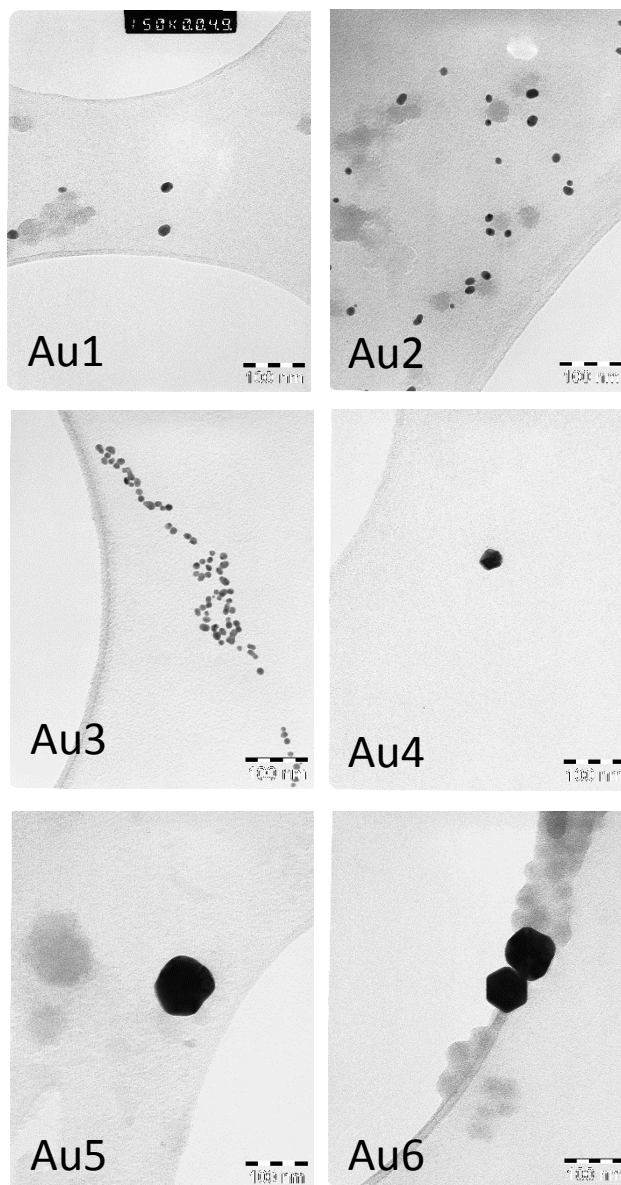
**Fig 3.2 TEM images showing gold nanoparticles Au1-6.** The scale bar represents 100 nm in each image.

From the values for each particle size assessed using each technique, it is clear there are some discrepancies. The likely reason for this is due to variation between data collection as already discussed (Chapter 2.3.2.2). In addition, aggregates cannot be distinguished when using DLS and NTA (dependent on aggregate size), however they can using TEM. The limitation to using TEM is the amount of particles assessed, as well as the size of particle (TEM does not measure Rh like DLS and NTA). DLS and NTA measures a much higher concentration of particle sizes and therefore a more representative data set can be

obtained. The formation of aggregates could also explain the large PDI values shown by some of the particle sizes. Despite this, the TEM data do complement the DLS data.

The data presented show that increasing the volume of sodium citrate results in smaller particles, as demonstrated in the literature.[28]

### 3.3.2 Pluronic characterisation

4 different concentrations of Pluronic F-127 were used in this study; 1% w/v, 5% w/v, 10% w/v, and 18% w/v. Preliminary experiments using 20% w/v Pluronic F-127 revealed that the gelation temperature was too low (~ 24 °C), and the NTA system had a tendency to over-heat, thus altering the phase transition of the polymer. Because of this, a maximum concentration of 18% w/v was chosen which did not cause over-heating whilst still forming a gel at the desired temperature range (around 34 ºC).

Each system was characterised using DLS in order to identify the temperature at which the polymers undergo a transition and form either micelles or gels. From this it was possible to determine the critical micellation temperature (CMT), or Krafft point, and also determine the point at which the bulk solution changed, which could be used to explain some of the diffusion coefficients determined. A graph showing the size of the polymers/micellar structures as a function of temperature can be seen in Fig 3.3.
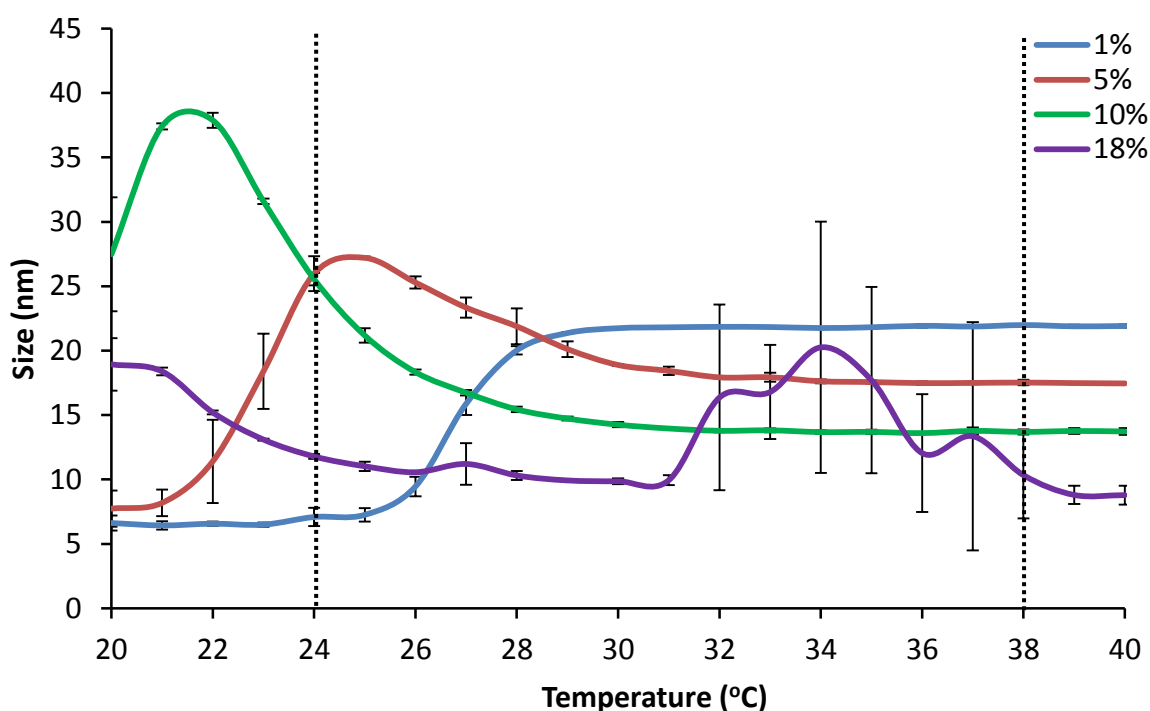
**Fig 3.3 Size changes of Pluronic F-127 at different temperatures obtained using DLS.** Data show the mean of 3 independent repeats ± standard deviation, for different concentrations of Pluronic F-127 in water; 1% w/v (blue), 5% w/v (red), 10% w/v (green), and 18% w/v (purple). The dotted lines show the region in which diffusion experiments were carried out.

Given that the critical micelle concentration (CMC) for Pluronic F-127 is noted to be 0.26-0.8% w/v,[33] the data presented shows that the particles are likely to have formed micelles. Therefore, as temperature increases there is a change from small micelles (6 ± 1 nm), to 22 ± 1 nm micelles (and therefore the CMT) in the 1% w/v solution, similar to the values recorded by other authors.[34] Similarly, the 5% w/v solution also shows a transition from 7 ± 1 nm at 20 °C to 27 ± 1 nm at 25 °C, before dropping down to an average size of 18 ± 1 nm at >30 °C. The size discrepancy between the micelles of 1% and 5% w/v can be due to the concentration of polymer. A higher concentration of polymer results in smaller micelles, due to their special positioning similar to the effect seen in AuNP synthesis where higher concentrations of sodium citrate result in smaller nanoparticles. At higher concentrations stable clusters of polymer aggregate more rapidly than in lower concentrations, leading to more rapid formation of clusters, causing smaller micelles.

116

The size increase observed between 21 and 25 $^{\circ}$C (for 5% w/v), and <20 and 22 for (10% w/v) is likely due to the formation of aggregates. It is well known that during the formation of micelles, the solution becomes unstable, thus increasing the chance of aggregates forming. This is demonstrated here by the initial size increase followed by a decrease and restabilisation represented by the data plateauing.[35]

The 10% w/v solution acts in a similar manner to the 5% w/v solution, with an increase in size up to 38 ± 1 nm as temperature rises to 22 $^{\circ}$C, followed by a decrease until the micelles have reached a steady size of 13 ± 1 nm. The 18% w/v solution shows a steady decrease in size with increasing temperature, to 10 ± 1 nm by 31 $^{\circ}$C, likely caused by the micelles becoming more compact prior to gel formation. After this point, the solution undergoes phase transition and becomes a gel (at >32 $^{\circ}$C). Similar values are reported in the literature.[36] This explains why the scattering at this point becomes more sporadic, and the error increases.

The purpose of the DLS experiments was to identify regions in the polymers/micelles undergoing conformational change, identified by a change in size. This could help explain the data obtained for diffusion experiments (section 3.3.3). Consequently, diffusion experiments were carried out between 24 and 38 $^{\circ}$C (marked in Fig 3.3 by dotted lines), the range where polymer behaviour was well characterised by DLS.

### 3.3.3 Gold nanoparticle diffusion

NTA was used to evaluate the diffusion of various sizes of gold nanoparticles in suspension in differing concentrations of Pluronic F-127 over a range of temperatures, in order to assess how particles behave in a temperature responsive environment. In this study the temperature range started at 24 $^{\circ}$C to avoid the system overheating.

Pluronic F-127 is well known to have unique gelation properties, where (depending on the formulation of the block co-polymer and concentration) it forms micelles followed by gels upon heating.[37] With the increased use of combining Pluronics with nanoparticles

(including gold,[16] silver,[38] and magnetic iron oxide nanoparticles)[39] it is important to understand how these particles behave, with regard to their diffusive properties, in solutions of varying concentrations of Pluronic F-127 at different temperatures.  The concentrations (1, 5, 10, and 18% w/v) were chosen as they provide solutions whereby the polymer is in different states (free polymer->micelles->gel).   Fig 3.4. summarises the data on diffusion coefficients of the different sized gold particles in the various polymer solutions as temperature varies.
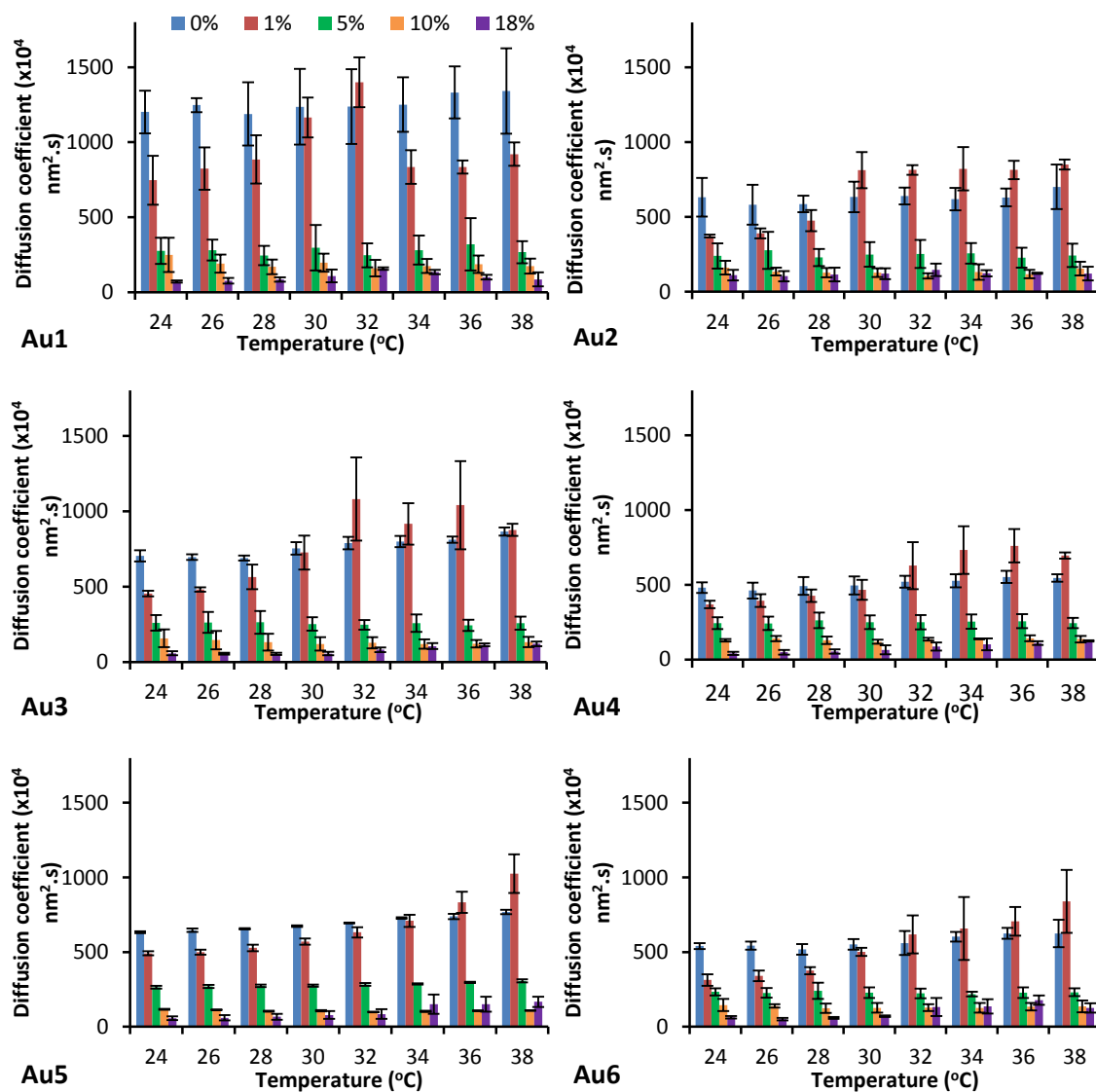
**Fig 3.4 Diffusion coefficients for gold nanoparticles varying in size, through different concentrations of Pluronic F-127, at increasing temperatures.** Mean ± SD, n=3

In order to explain the results, the discussion will firstly consider gold nanoparticle diffusion with differing poloxamer concentrations, and secondly the effects of nanoparticle size. In addition to measuring the particles in Pluronics, the diffusion of AuNP's in water subjected to the same temperature ramp was assessed and served as a control.

### 3.3.3.1 Effect of Pluronic concentration on AuNP diffusion

From the general trend in diffusion coefficients exhibited by the particles, it is clear there are big differences depending on Pluronic concentration. The general decrease in diffusion coefficient seen between each concentration can be ascribed to differences in bulk viscosity of the Pluronic solutions; the higher the concentration, the higher the bulk viscosity, thus more constraint is placed on the particles inhibiting their ability to diffuse.

As can be seen in Fig 3.4; the diffusion coefficient for the particles in water increases with temperature. This is to be expected, as there is a decrease in viscosity as temperature increases, due to a weakening of intermolecular bonds. This causes the particles to move more rapidly, thus allowing them to diffuse faster.[40] Wong *et al.*[41] reported on the diffusion of AuNP's in water and toluene and also found that increasing the temperature also increased the diffusion coefficient of the particles. Further, this trend is predicted by calculating the diffusion coefficient using the Stokes-Einstein equation.

Considering the 1% w/v solution, the diffusion coefficient also shows an initial steady increase as temperature rises. However, the diffusion coefficient jumps at around 30-32 $^{o}$C and the particles become much more diffusive, even more so than their counterpart particle size in water. This can be explained by considering how the Pluronic F-127 molecules behave in solution, from the earlier DLS results. As can be seen in Fig 3.3, there is a change in particle size at the same temperature, caused by the formation of micelles.[42]

With the formation of micelles, the localised viscosity of the solution decreases (as there is more free water rather than polymer networks), which could explain the elevation in

nanoparticle diffusion.  However, the increased diffusivity is much larger than would be expected, and it appears to be higher than the same nanoparticles diffusing in water.  The most likely reason for this is that, as the micelles are being formed, they are moving around under Brownian motion similar to the particles.  With the increase in temperature, the micelles have an increased kinetic energy causing them to move faster, and thus the number of collisions with the gold nanoparticles will increase.  Given that the micelles are much smaller than the AuNP's, they will move faster as predicted by the Stokes-Einstein equation.  Islam *et al*[43] provides a potential explanation for this. Based on the theory of Brownian motion and the Einstein-Smoluchowski relation (Equation 3.1) there will be an increase in the friction coefficient placed on the particle (from Stokes law) which causes the "mobility" of the particle to increase, thus increasing the diffusion coefficient. However, this will eventually normalise (or decrease) back to a steady state (that of a more viscous environment), which is shown in the data presented here at temperatures >34 $^{\circ}$C.

$$D = \mu k_B T \hspace{4cm} \text{Equation 3.1}$$

Where D is the diffusion coefficient, μ is the mobility (ratio of the terminal drift velocity to an applied force) of the particle, $k_B$ is the Boltzmann constant, and T is the temperature.

This explanation is supported considering the three other concentrations studied and comparing them to the DLS data (Fig 3.3).  Both the 5% and 10 % w/v solutions show little change in diffusion coefficient.  As the temperature increases, it is likely a change in viscosity will occur which could further lead to a change in diffusion coefficient.  However, looking at the DLS results, there is no change to the system between the temperatures studied i.e. the particles have already formed into micelles and no further transition is occurring.

Similar to the 1% w/v solution, the 18% w/v solution is also undergoing a transition and again shows a similar increase in diffusion coefficient as seen in the 1% w/v solution.  This is very unusual, as it would be expected that as the system gels, the particles stop moving

and thus no longer diffuse. However, it is likely, as this is a dynamic system, that as the gel is forming, the micelle network is becoming more constraint. As the particles are still moving under Brownian motion, it is possible that they are forming unnatural defects in the gel which could lead to an artificial increase in diffusion coefficient. Fig 3.5 provides scheme of how the gold nanoparticles are behaving as the solution forms micelles followed by a gel which helps in explaining the above description.



Polymer /water     Micelles     Gel
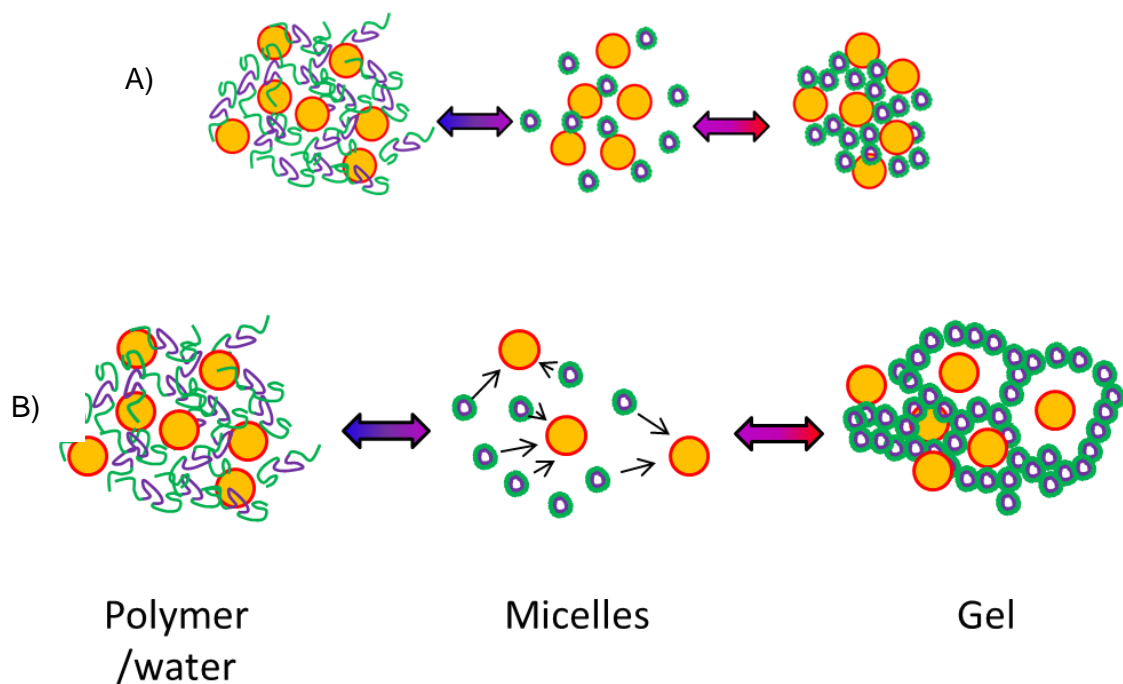
**Fig 3.5 How the gold nanoparticles are behaving in the solution of Pluronics at different temperatures, and how this could effectively alter their diffusive properties.** A) represents the predicted movement of particles, whereas B) shows how the particles are actually moving.

It should be noted that during diffusion experiments, to ensure gold nanoparticles were being measured instead of micelles; the camera level was set to 5. Given that gold nanoparticles are much more effective at reflecting light (due to their metallic nature), this ensures them to be visible in the suspension.

### 3.3.3.2 Effect of particle size on diffusion

In addition to looking at the effects of polymer concentration on the diffusion coefficient, the effect of particle size was also studied. From Fig 3.4, in general, as the particle size increases the diffusion coefficient decreases. This is to be expected from the predicted diffusion coefficients calculated using the Stokes-Einstein equation (Fig 3.6). In this example, the particle size used was that as obtained by the DLS. As can be seen, as particle size decreases, the diffusion coefficient increases. In addition, as temperature increases the diffusion coefficient increases as discussed above.
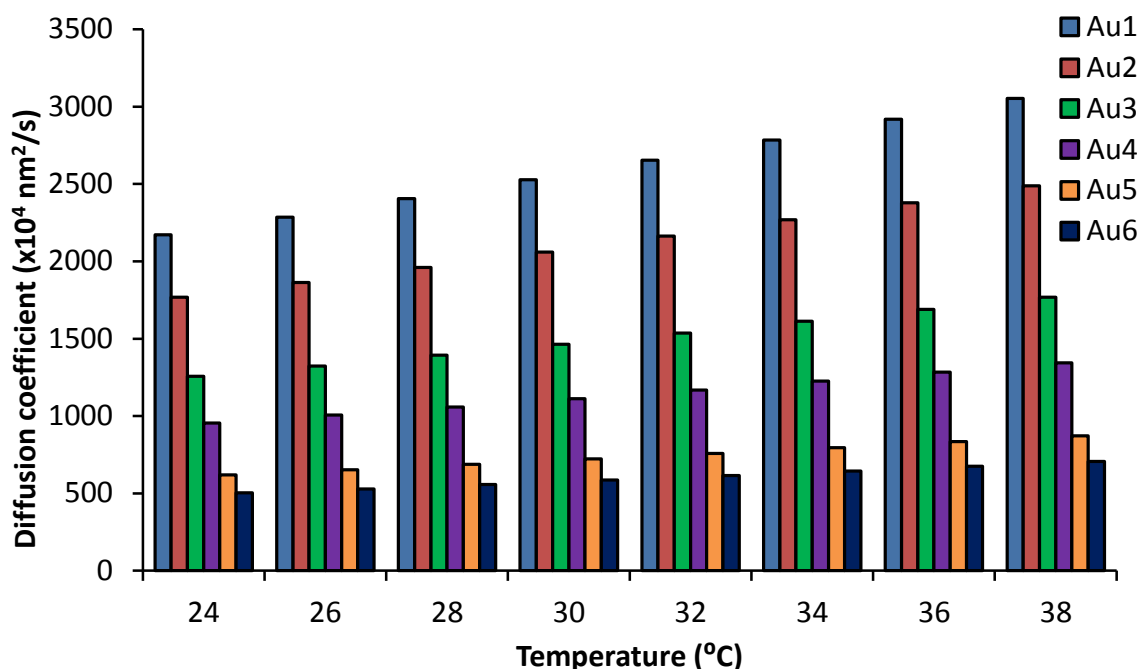


**Fig 3.6.  Calculated diffusion coefficient for AuNP's in water, determined using the Stokes-Einstein equation and the mean dimeter from DLS (taken from Table 3.2).**

In general, as predicted by the Stokes-Einstein equation, the diffusion coefficients for all sample sizes at all concentrations increases as temperature increases. However, there are two main discrepancies in the data. The first is that the predicted diffusion coefficients (Fig 3.6) are for that of the gold particles in water, and should therefore match the diffusion coefficient for the gold particles determined experimentally in water. Although

the largest particle size (Au6) does match that with the predicted diffusion coefficient, there is some discrepancy observed for the others.

The Stokes-Einstein equation assumes several parameters about the sample, namely; spherical, 100% monodisperse particles which move under slip boundary conditions by laminar flow.  If these conditions are not met then the equation is not reliable.[44,45]  The latter are shown in water (i.e. the particles will move under laminar flow), the presence of aggregates in the sample, shown by the large PDI's, and TEM images, will change both the shape of the particles (i.e. they will not be spherical), and also cause a disruption to the nanofluidics.  As the diffusion coefficient presented by NTA is the mean for all the particles measured, the presence of a large number of aggregates will cause larger particle sizes and thus a reduced diffusion coefficient.  This will also explain the large error bars observed on some of the samples (and the large PDI's seen in Table 3.2).

The second discrepancy refers to the apparent difference in diffusion coefficient based on particle size i.e. Au2 has a smaller experimentally diffusion coefficient to Au3 and Au4 (Fig 3.4).   This pattern appears across the whole temperature range studied at all concentrations, suggesting that the aggregates in this sample are much larger than in the other samples, which will cause a shift in diffusion coefficient as described above.

Despite these discrepancies, the general trend in diffusion coefficient matches the calculated values.

### 3.3.4 Particle mapping and local environment

To understand how the particles move in the local environment and track their locations, a python script was written in order to produce a heat-map of particle movement.  Fig 3.7 shows exemplar heat-maps produced for each particle type at the temperature range studied, recorded for the 1%, 5%, 10%, and 18% w/v solution, respectively, and is explained by Fig 3.8.
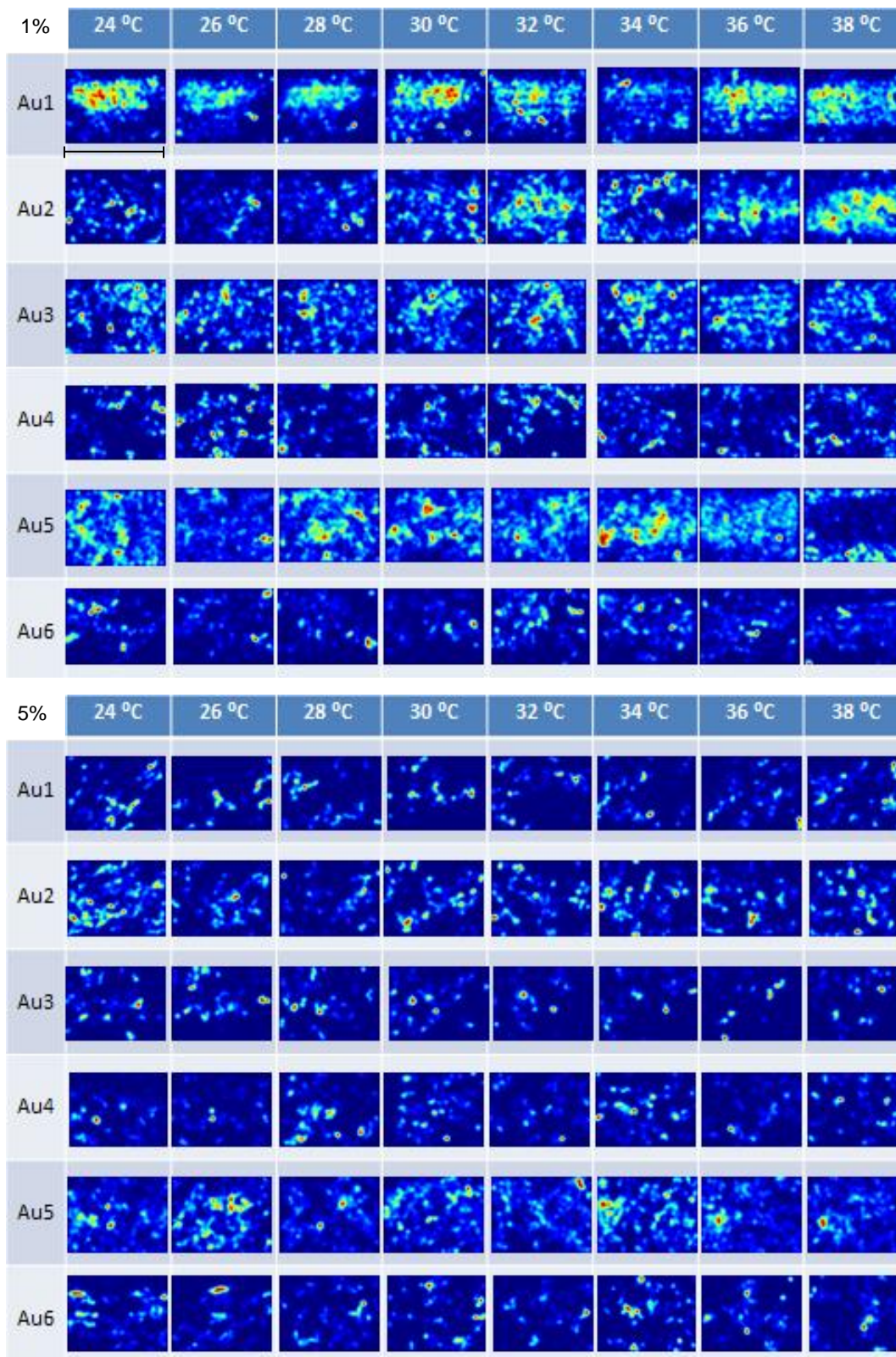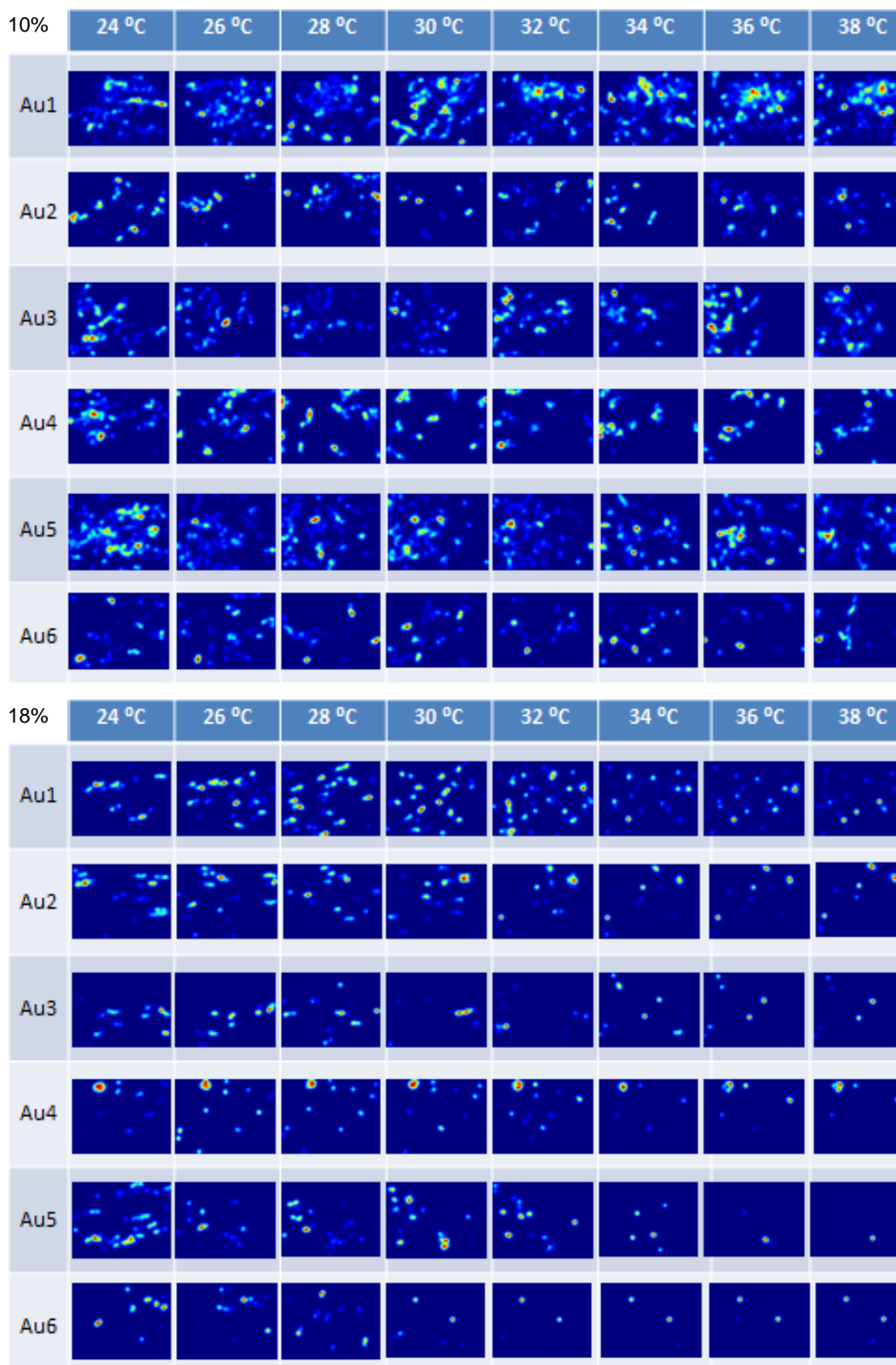
**Fig 3.7 Heat-maps showing the movement of different sized gold nanoparticles at different temperatures recorded over 60 seconds.** The polymer concentration is denoted in the top left corner of each graphic. The scale bar (shown in 1%, Au1, 20 °C) represents 200 μm. A description of intensity of the heat-map can be found in Fig 3.8.
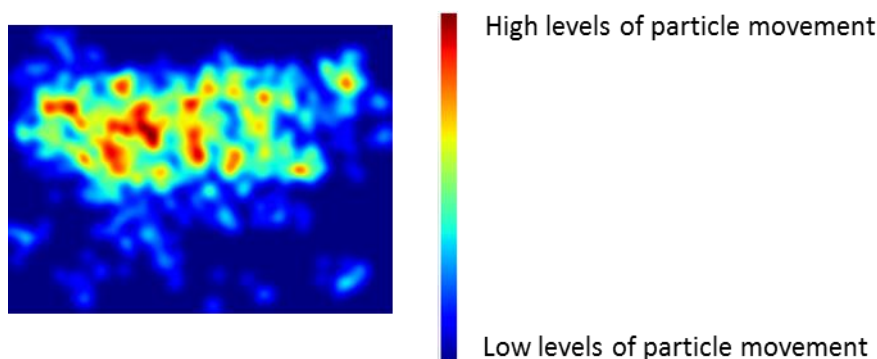
**Fig 3.8 Intensity scale for the heat-maps depicted in Fig 3.7.** Regions in red show regions where there is a large amount of particle movement detected, whereas blue represents regions of little/no particle movement.

As can be seen, the larger particles (Au4, 5, and 6) mostly show very little movement in the 18% w/v solution at higher temperatures (>34 $^{\circ}$C). This is due to the formation of the gel and the particles becoming trapped, unable to move. However, there are some regions of high particle movement further suggesting the formation of a deformed gel, caused by particles undergoing Brownian motion.

It is well known that Pluronic F-127 forms a gel at temperatures above 34 $^{\circ}$C in concentrations above 18% w/v,[46] and is confirmed by the DLS data (Fig 3.3), where the scattering caused by these temperatures becomes very incoherent (>34 $^{\circ}$C). However, the smaller particle sizes (specifically Au1 and Au2) still show general particle movement, suggesting that particles are moving through the gelled state. This is likely due to the particles moving more rapidly due to their smaller size (due to the large degree of movement caused by Brownian motion of sub 25 nm particles), causing the gel to become warped much more readily than with the larger particles. This could mean that the particles are forming an artificial cave in the gel structure, encouraging particle movement. As larger particles tend to move much slower under Brownian motion[47] the gel could be forming more naturally, thus forming fewer artefacts.

This is further demonstrated by the diffusion coefficients shown for these particles in an 18% w/v solution (Fig 3.4). The smaller particles (Au1-3) have steadily increasing

diffusion coefficients, suggesting they are not trapped or demonstrate limited movement due to the formation of the gel, however the diffusion coefficient for larger particles (Au4-6) starts to decline after 34 ºC (the point at which the solution gels), suggesting hindered particle movement (as illustrated by the heat maps).  However, there is still some degree of particle movement, although this could be due to external vibrations.

### 3.3.5 Distance and area of particle movement

In addition to generating a heat-map, the code also allowed for the calculation of the distance travelled by each particle, and the area of the space it was moving in.  The code used the x and y coordinates provided during analysis, and calculated these values based on the number of pixels the particle was crossing.  NTA calculates sizes based on the number of pixels a particle crosses, where 1 pixel equates to 188 nm.  Using this information, the code can calculate the distance travelled by each particle and also the special area it is moving in.  A chart showing the mean distance travelled by each particle can be found in Fig 3.9, and a chart showing the mean area of particle movement can be found in Fig 3.10.
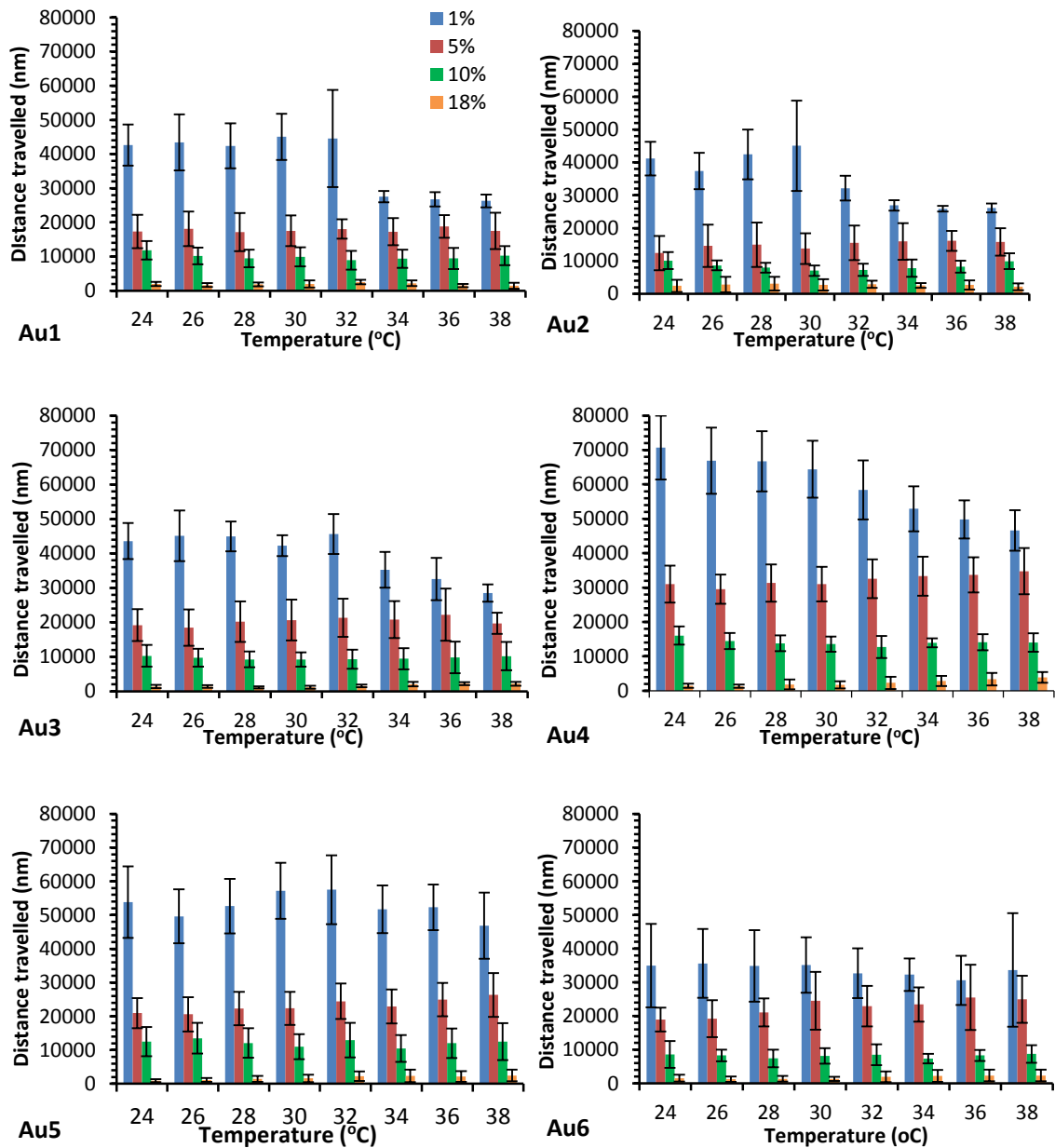
**Fig 3.9 Mean distance travelled by different sized gold nanoparticles in different concentrations of Pluronic F-127, as temperature ramps.** Data represent the mean of 3 repeats.
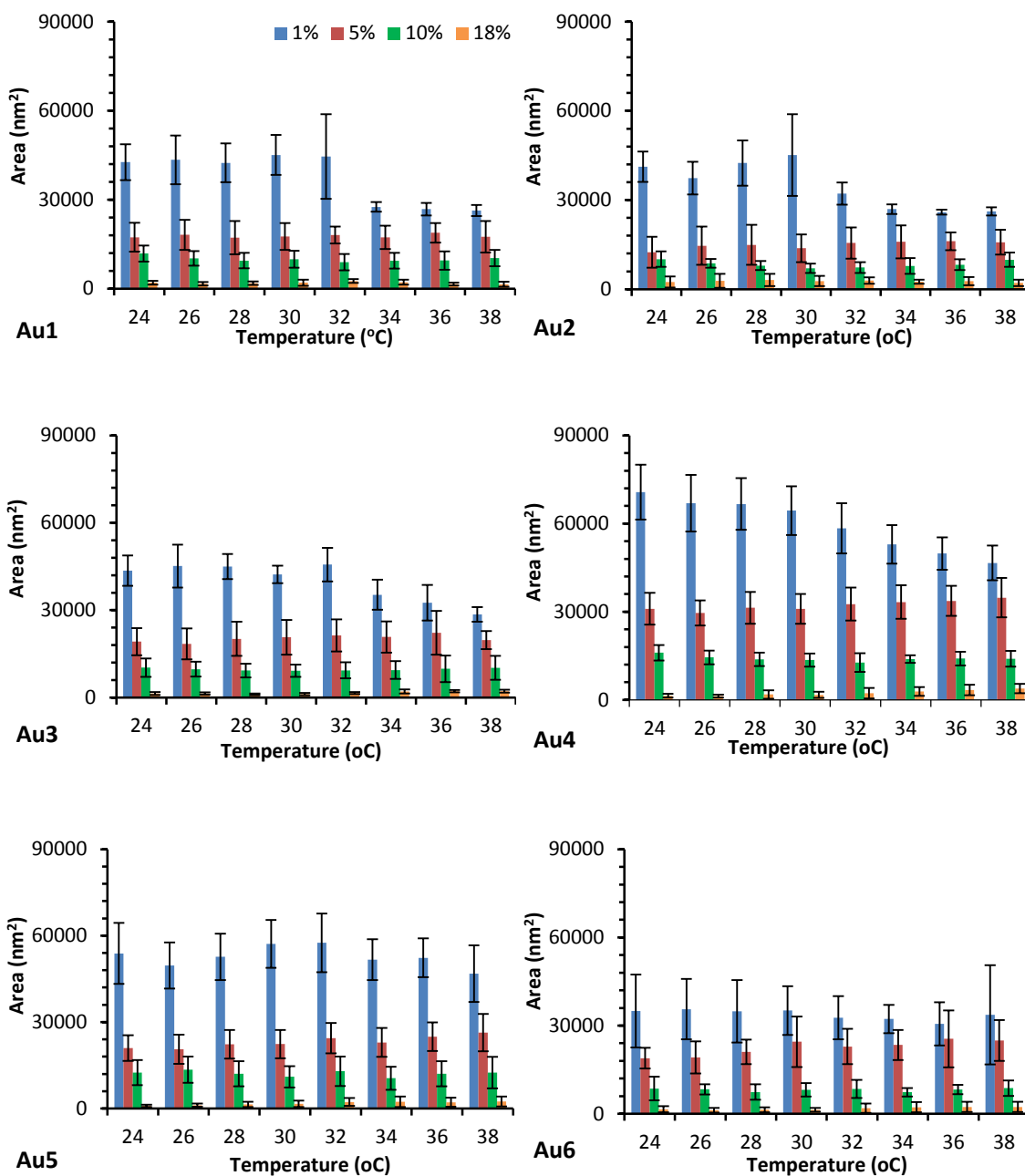
**Fig 3.10 Mean area in which different sized gold nanoparticles are moving in increasing concentrations of Pluronic F-127, as temperature ramps.** Data represent the mean of 3 repeats.

Looking at both the area and distances moved by AuNP's in a 10% w/v solution, there is little change in the value obtained (shown in green), and the particles appear to move at a similar rate; a similar trend was seen in the diffusion coefficients. Similarly, in the 5% w/v solution the mean distance appears to be similar in all the sizes studied, apart from Au6, where the distance decreases. However, the area of movement appears to increase as the particles get larger, except for the largest particle size (Au6). Given that these

particles are larger than the Au5 particles (95 nm compared to 77 nm), it could be that their movement is much more hindered, resulting in a decreased area of movement. A similar trend can be seen in the Au6 particles in the 18% w/v poloxamer system.

The 1% w/v samples have very interesting results, and it appears as through as temperature increases, the distance travelled and area of movement for each particle decreases - an opposite trend to that seen in the diffusion coefficients. As with the diffusion coefficients, they remain relatively constant until ~34 $^{o}$C, when they start to decrease, which (as previously discussed) will be due to phase changes within the solution. The decrease in both distance travelled and area could be due to steric hindrance in the system. With the formation of micelles, the particles have a smaller amount of space to move around in. So despite the fact that they diffuse faster (as seen in Fig 3.4), they have less space to move in as shown by the distance and area graphs shown here (Fig 3.9 and 3.10, respectively). Due to this confined space, there are greater odds of the micelles bombarding into the particles, which could cause them to diffuse faster (as discussed in 3.3.1).

This information potentially allows several additional features about the particle to be understood, including the speed of the particles. In addition, the "area of particle movement" values could potentially be used to determine a pore size of a gel. It also helps explain the trends observed for the diffusion coefficients for each particle. This approach adds extra levels of understanding to how nanoparticles behave in different environments.

## 3.4 Conclusions

The initial concept of this study was to measure the pore size of a gel which contained a suspension of nanoparticles. However, by measuring the diffusion coefficients of gold nanoparticles in different environments allowed investigation of how the conformation and state of the polymer solution affected nanoparticle diffusion.

It would be expected that as the temperature increased, the diffusion coefficient would increase linearly.  This was true for 3 of the samples; the control (0%), 5%, and 10% w/v solutions.  However, the diffusion coefficient for particles suspended in a 1% w/v, and 18% w/v Pluronic solution, appear to not show this pattern.  Based on this, the phase of the solution (solution, micelle suspension, or gel) has been shown to play a major role in diffusion coefficient, and the addition of micelles into a system can significantly affect nanoparticle diffusion coefficients.  This was confirmed by the heat-maps showing the localisation of nanoparticle movement, the values calculated for the average distance travelled by the nanoparticles, and also the size of the area they are moving in.

## 3.5 References

(1)     Ghosh, P.; Han, G.; De, M.; Kim, C. K.; Rotello, V. M. Gold Nanoparticles in Delivery Applications. *Adv. Drug Deliv. Rev.* **2008**, *60* (11), 1307–1315.

(2)     Huang, X.; Jain, P. K.; El-Sayed, I. H.; El-Sayed, M. A. Gold Nanoparticles: Interesting Optical Properties and Recent Applications in Cancer Diagnostics and Therapy. *Nanomedicine (Lond).* **2007**, *2* (5), 681–693.

(3)     Sharma, P.; Brown, S.; Walter, G.; Santra, S.; Moudgil, B. Nanoparticles for Bioimaging. *Adv. Colloid Interface Sci.* **2006**, *123–126*, 471–485.

(4)     Mikami, Y.; Dhakshinamoorthy, A.; Alvaro, M.; García, H. Catalytic Activity of Unsupported Gold Nanoparticles. *Catal. Sci. Technol.* **2013**, *3* (1), 58–69.

(5)     Zhao, P.; Li, N.; Astruc, D. State of the Art in Gold Nanoparticle Synthesis. *Coord. Chem. Rev.* **2013**, *257* (3), 638–665.

(6)     Grzelczak, M.; Pérez-Juste, J.; Mulvaney, P.; Liz-Marzán, L. M. Shape Control in Gold Nanoparticle Synthesis. *Chem. Soc. Rev.* **2008**, *37* (9), 1783–1791.

(7)     Sun, Y.; Xia, Y. Shape-Controlled Synthesis of Gold and Silver Nanoparticles. *Science* **2002**, *298* (5601), 2176–2179.

(8)     Frens, G. Controlled Nucleation for the Regulation of the Particle Size in Monodisperse Gold Suspensions. *Nature* **1973**, *241* (105), 20–22.

(9)     Turkevich, J.; Stevenson, P. C.; Hillier, J. A Study of the Nucleation and Growth Processes in the Synthesis of Colloidal Gold. *Discuss. Faraday Soc.* **1951**, *11*, 55.

(10)    Brust, M.; Walker, M.; Bethell, D.; Schiffrin, D. J.; Whyman, R. Synthesis of Thiol-Derivatised Gold Nanoparticles in a Two-Phase Liquid?Liquid System. *J. Chem. Soc. Chem. Commun.* **1994**, No. 7, 801.

(11)    Vitale, F.; Fratoddi, I.; Battocchio, C.; Piscopiello, E.; Tapfer, L.; Russo, M. V.; Polzonetti, G.; Giannini, C. Mono- and Bi-Functional Arenethiols as Surfactants for Gold Nanoparticles: Synthesis and Characterization. *Nanoscale Res. Lett.* **2011**, *6* (1), 103.

(12)    Toikkanen, O.; Ruiz, V.; Rönnholm, G.; Kalkkinen, N.; Liljeroth, P.; Quinn, B. M. Synthesis and Stability of Monolayer-Protected Au38 Clusters. *J. Am. Chem. Soc.*

**2008**, *130* (33), 11049–11055.

(13)  Meng, X.; Liu, Z.; Zhu, M.; Jin, R. Controlled Reduction for Size Selective Synthesis of Thiolate-Protected Gold Nanoclusters Aun(n = 20, 24, 39, 40). *Nanoscale Res. Lett.* **2012**, *7* (1), 277.

(14)  Rahme, K.; Oberdisse, J.; Schweins, R.; Gaillard, C.; Marty, J.-D.; Mingotaud, C.; Gauffre, F. Pluronics-Stabilized Gold Nanoparticles: Investigation of the Structure of the Polymer-Particle Hybrid. *Chemphyschem* **2008**, *9* (15), 2230–2236.

(15)  Tao, Y.; Han, J.; Ye, C.; Thomas, T.; Dou, H. Reduction-Responsive Gold-Nanoparticle-Conjugated Pluronic Micelles: An Effective Anti-Cancer Drug Delivery System. *J. Mater. Chem.* **2012**, *22* (36), 18864.

(16)  Bae, K. H.; Choi, S. H.; Park, S. Y.; Lee, Y.; Park, T. G. Thermosensitive Pluronic Micelles Stabilized by Shell Cross-Linking with Gold Nanoparticles. *Langmuir* **2006**, *22* (14), 6380–6384.

(17)  Alexandridis, P. Gold Nanoparticle Synthesis, Morphology Control, and Stabilization Facilitated by Functional Polymers. *Chem. Eng. Technol.* **2011**, *34* (1), 15–28.

(18)  Iqbal, M.; Chung, Y.-I.; Tae, G. An Enhanced Synthesis of Gold Nanorods by the Addition of Pluronic (F-127) via a Seed Mediated Growth Process. *J. Mater. Chem.* **2007**, *17* (4), 335–342.

(19)  Sakai, T.; Alexandridis, P. Size- and Shape-Controlled Synthesis of Colloidal Gold through Autoreduction of the Auric Cation by Poly(ethylene Oxide)-Poly(propylene Oxide) Block Copolymers in Aqueous Solutions at Ambient Conditions. *Nanotechnology* **2005**, *16* (7), S344-53.

(20)  Escobar-Chávez, J. J.; López-Cervantes, M.; Naik, A.; Kalia, Y.; Quintanar-Guerrero, D.; Ganem-Quintanar, A. Applications of Thermo-Reversible Pluronic F-127 Gels in Pharmaceutical Formulations. *J. Pharm. Pharm. Sci.* **2006**, *9* (3), 339–358.

(21)  Shachaf, Y.; Gonen-Wadmany, M.; Seliktar, D. The Biocompatibility of PluronicF127 Fibrinogen-Based Hydrogels. *Biomaterials* **2010**, *31* (10), 2836–2847.

(22)  El-Kamel, A. . In Vitro and in Vivo Evaluation of Pluronic F127-Based Ocular Delivery System for Timolol Maleate. *Int. J. Pharm.* **2002**, *241* (1), 47–55.

(23)  Liu, Y.; Lu, W.-L.; Wang, J.-C.; Zhang, X.; Zhang, H.; Wang, X.-Q.; Zhou, T.-Y.; Zhang, Q. Controlled Delivery of Recombinant Hirudin Based on Thermo-Sensitive Pluronic F127 Hydrogel for Subcutaneous Administration: In Vitro and in Vivo Characterization. *J. Control. Release* **2007**, *117* (3), 387–395.

(24)  Qin, J.; Asempah, I.; Laurent, S.; Fornara, A.; Muller, R. N.; Muhammed, M. Injectable Superparamagnetic Ferrogels for Controlled Release of Hydrophobic Drugs. *Advanced Materials*. 2009, pp 1354–1357.

(25)  Barichello, J. Absorption of Insulin from Pluronic F-127 Gels Following Subcutaneous Administration in Rats. *Int. J. Pharm.* **1999**, *184* (2), 189–198.

(26)  Gou, M.; Li, X.; Dai, M.; Gong, C.; Wang, X.; Xie, Y.; Deng, H.; Chen, L.; Zhao, X.; Qian, Z.; et al. A Novel Injectable Local Hydrophobic Drug Delivery System: Biodegradable Nanoparticles in Thermo-Sensitive Hydrogel. *Int. J. Pharm.* **2008**, *359* (1–2), 228–233.

(27)  Oh, K. S.; Song, J. Y.; Yoon, S. J.; Park, Y.; Kim, D.; Yuk, S. H. Temperature-Induced Gel Formation of Core/shell Nanoparticles for the Regeneration of Ischemic Heart. *J. Control. Release* **2010**, *146* (2), 207–211.

(28)  Kimling, J.; Maier, M.; Okenve, B.; Kotaidis, V.; Ballot, H.; Plech, A. Turkevich

Method for Gold Nanoparticle Synthesis Revisited. *J. Phys. Chem. B* **2006**, *110* (32), 15700–15707.

(29)   Lai, S. K.; Wang, Y.-Y.; Wirtz, D.; Hanes, J. Micro- and Macrorheology of Mucus. *Adv. Drug Deliv. Rev.* **2009**, *61* (2), 86–100.

(30)   Nicky van Foreest. http://nicky.vanforeest.com/misc/fitEllipse/fitEllipse.html http://nicky.vanforeest.com/misc/fitEllipse/fitEllipse.html.

(31)   Fitzgibbon, A.W., Pilu, M., and F. R. . Direct Least Squares Fitting of Ellipseesle. *Proc. 13th Int. Conf. Pattern Recognit.* **1996**, 253–257.

(32)   Eustis, S.; el-Sayed, M. A. Why Gold Nanoparticles Are More Precious than Pretty Gold: Noble Metal Surface Plasmon Resonance and Its Enhancement of the Radiative and Nonradiative Properties of Nanocrystals of Different Shapes. *Chem. Soc. Rev.* **2006**, *35* (3), 209–217.

(33)   Gao, Q.; Liang, Q.; Yu, F.; Xu, J.; Zhao, Q.; Sun, B. Synthesis and Characterization of Novel Amphiphilic Copolymer Stearic Acid-Coupled F127 Nanoparticles for Nano-Technology Based Drug Delivery System. *Colloids Surfaces B Biointerfaces* **2011**, *88* (2), 741–748.

(34)   Lin, Y.; Alexandridis, P. Temperature-Dependent Adsorption of Pluronic F127 Block Copolymers onto Carbon Black Particles Dispersed in Aqueous Media. *J. Phys. Chem. B* **2002**, *106* (42), 10834–10844.

(35)   Kabanov, A. V; Batrakova, E. V; Alakhov, V. Y. Pluronic® Block Copolymers as Novel Polymer Therapeutics for Drug and Gene Delivery. *J. Control. Release* **2002**, *82* (2–3), 189–212.

(36)   Nie, S.; Hsiao, W. W.; Pan, W.; Yang, Z. Thermoreversible Pluronic® F127-Based Hydrogel Containing Liposomes for the Controlled Delivery of Paclitaxel: In Vitro Drug Release, Cell Cytotoxicity, and Uptake Studies. *Int. J. Nanomedicine* **2011**, *6*, 151.

(37)   Schmaljohann, D. Thermo- and pH-Responsive Polymers in Drug Delivery. *Adv. Drug Deliv. Rev.* **2006**, *58* (15), 1655–1670.

(38)   Angelescu, D. G.; Vasilescu, M.; Anastasescu, M.; Baratoiu, R.; Donescu, D.; Teodorescu, V. S. Synthesis and Association of Ag(0) Nanoparticles in Aqueous Pluronic F127 Triblock Copolymer Solutions. *Colloids Surfaces A Physicochem. Eng. Asp.* **2012**, *394*, 57–66.

(39)   Jain, T. K.; Morales, M. A.; Sahoo, S. K.; Leslie-Pelecky, D. L.; Labhasetwar, V. Iron Oxide Nanoparticles for Sustained Delivery of Anticancer Agents. *Mol. Pharm.* **2005**, *2* (3), 194–205.

(40)   Chamieh, J.; Davanier, F.; Jannin, V.; Demarne, F.; Cottet, H. Size Characterization of Commercial Micelles and Microemulsions by Taylor Dispersion Analysis. *Int. J. Pharm.* **2015**, *492* (1–2), 46–54.

(41)   Wong, K.; Chen, C.; Wei, K.; Roy, V. A. L.; Chathoth, S. M. Diffusion of Gold Nanoparticles in Toluene and Water as Seen by Dynamic Light Scattering. *J. Nanoparticle Res.* **2015**, *17* (3), 153.

(42)   Bohorquez, M.; Koch, C.; Trygstad, T.; Pandit, N. A Study of the Temperature-Dependent Micellization of Pluronic F127. *J. Colloid Interface Sci.* **1999**, *216* (1), 34–40.

(43)   Islam, M. A. Einstein–Smoluchowski Diffusion Equation: A Discussion. *Phys. Scr.* **2004**, *70* (2–3), 120–125.

(44)   Squires, T. M.; Mason, T. G. Fluid Mechanics of Microrheology. **2009**.

(45)   Kumar, S. K.; Szamel, G.; Douglas, J. F. Nature of the Breakdown in the Stokes-Einstein Relationship in a Hard Sphere Fluid. *J. Chem. Phys.* **2006**, *124* (21), 214501.

(46)   Jeong, B.; Kim, S. W.; Bae, Y. H. Thermosensitive Sol–gel Reversible Hydrogels. *Adv. Drug Deliv. Rev.* **2002**, *54* (1), 37–51.

(47)   Chung, H. S.; Hogg, R. The Effect of Brownian Motion on Particle Size Analysis by Sedimentation. *Powder Technol.* **1985**, *41* (3), 211–216.

# Chapter 4

## Temperature responsive silica nanoparticles – particle solvation and diffusion

### 4.1 Introduction

This chapter describes studies using two temperature responsive polymers (TRP's), poly(N-isopropyl acrylamide) (PNIPAM) and its structural isomer poly(2-n-propyl-oxazoline) (PNPOZ), assessing how their structures change with temperature and consequential effects on their diffusion coefficients in a series of organic solvents with different polarities.

TRP's exist in many forms, and can change properties depending on temperature. There are many examples of TRP's in the literature including poloxamers, poly(n-isopropyl acrylamide), and poly(2-oxazolines). Indeed, most polymers will have either a lower critical solution temperature (LCST), or upper critical solution temperature (UCST), however these are often at either very high or very low temperatures, and so will not be relevant for most pharmaceutical applications.[1]

When a polymer exhibits a response to a temperature its conformational and physical properties will change. The LCST is the critical temperature above which a polymer becomes immiscible with a solvent (e.g. water). At temperatures below the LCST, it is hydrophilic in nature and above the LCST it becomes hydrophobic. Likewise, UCST is the critical temperature below which a polymer becomes immiscible with a solvent. If the temperature of a system is below the LCST of a polymer, then the Gibbs free energy will

be negative, and the polymer will dissolve in solution. However, if the temperature changes and increases to above the LCST, the Gibbs free energy will change from negative to positive, thus causing the polymer to become immiscible.[2] Summarily, the Gibbs free energy goes from positive to negative as temperature rises for the UCST.

By functionalising nanoparticle surfaces with TRP's both the LCST and UCST of a polymer changes due to steric hindrance, caused by the dense packing on the surface.[3] This is an important factor to consider when combining TRP's with nanoparticle formulations (especially for pharmaceutical applications), as the properties of the modified particle can be different than predicted compared to free polymer.

PNIPAM is a widely studied temperature responsive polymer, with a reported LCST of 32 $^o$C. There have been many reported applications for PNIPAM functionalised onto the surface of different nanoparticles, ranging from "smart-glass,"[4] photo-thermal therapy,[5,6] remote-controlled triggered drug release,[7] and bioimaging.[8] By taking advantage of the LCST and combining with the unique properties of nanoparticles, it is possible to design highly versatile systems with very tuneable properties, ideal for the pharmaceutical industry. PNPOZ on the other hand is not as extensively studied as PNIPAM, and very little experimental data exists looking at the size changes occurring around this polymer when grafted to nanoparticles. With an LCST of 25 $^o$C, and good biocompatibility, this polymer is growing in popularity for drug delivery systems.

One of the most beneficial techniques to measure the change in structure of polymers/nanoparticle composites in response to an external stimulus is to use scattering techniques, such as Small Angle Neutron (SANS) or Small Angle X-ray Scattering (SAXS). Both SANS and SAXS provide similar data, and are often used as complementary techniques.

In a SANS experiment, a collimated neutron beam is fired through a sample, which then scatters off any molecules/particles in said sample, which can then be detected by a $^3$He detector. As SANS employs elastic scattering, there is no measurement of energy

transfer between the incident neutron beam and the sample, as they will be the same (inelastic scattering causes a difference in energy transfer). Only scattered neutrons are measured, and therefore a high flux is needed. To perform a SANS experiment, samples need to be suspended in $D_2O$, as deuterium provides greater contrast to neutrons compared to hydrogen and reduces the incoherent background from the solvent. The data generated from a SANS experiment is expressed as value of Q, which is defined in Equation 4.1.

$$Q = \frac{4\pi \sin\frac{\theta}{2}}{\lambda}$$
Equation 4.1

Where θ is the incidence angle of the neutron beam, and λ is the wavelength. Q represents the scattering in reciprocal space, and is the Fourier transformation of scattering in real, or D, space. By plotting the intensity, the "I(Q)", against Q, it is possible to establish structural features and size dimensions existing in the system, such as shape, $R_g$, protein structure, and general morphology.[9] From these data it is possible to assess any interactions the sample may be exhibiting. Scattering at low Q values gives information on large structural features within the sample, and scattering at high Q values gives information on smaller structural features.

One of the main advantages SANS has over similar techniques (such as SAXS), is the ability to perform contrast variation experiments. This is carried out by placing a sample in different ratios of $D_2O$ and $H_2O$, allowing the neutron beam to mask out specific areas of the sample (Fig 4.1).[10]
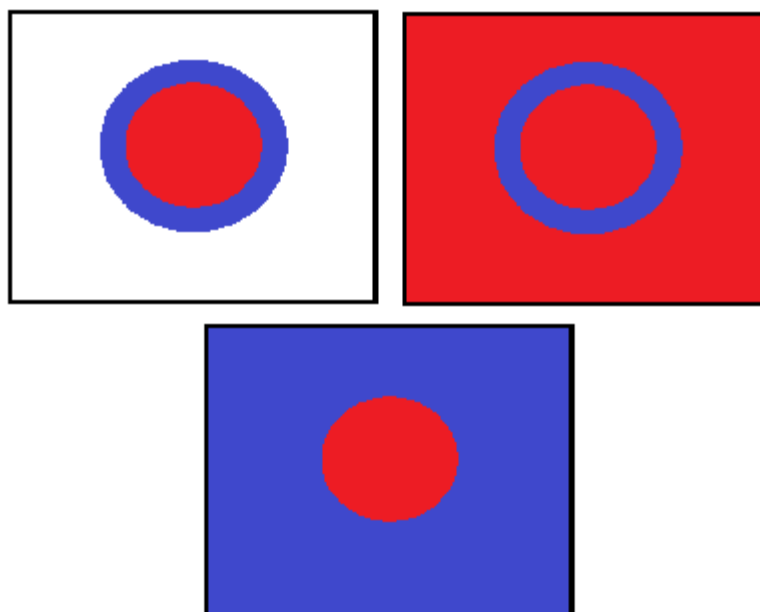
**Fig 4.1 The principle of contrast matching.** By placing a sample in 100% $D_2O$ (top left), it is possible to analyse the whole particle such as the core (red) and shell (blue) structure. By placing the sample in a matched solvent system (made-up of different $D_2O:H_2O$ ratios), it is possible to mask out different parts of the system, allowing for direct measurement of either the core or shell.

Using contrast variation, it is possible to assess any structural changes occurring in different locations on the particle, i.e. changes in the core, or shell of the particle.

The aim of this study was to investigate temperature effects on the size and structure of TRP-functionalised nanoparticles using a variety of techniques including DLS, NTA and SANS, and critically assess how these properties affect nanoparticle diffusion through a variety of solvents varying in polarity.

## 4.2 Materials and methods

### 4.2.1 Materials

The nanoparticles used in this study were the PNIPAM functionalised silica and the PNPOZ functionalised silica nanoparticles synthesised in Chapter 2. In addition to the particles, $D_2O$ (VWR International, UK), DMSO (Fisher, UK), ethanol, and methanol (Sigma-Aldrich, UK) were used.

**4.2.2 DLS**

In addition to the characterisation carried out on these particles in Chapter 2, further DLS experiments were performed to assess the particles temperature responsive nature. Samples were diluted 1:10 into either ultrapure water or methanol, placed in low volume cuvettes (Fisher, UK), and sealed with a stopper and parafilm to avoid solvent evaporation. A temperature ramp- study was then carried out using the Zetasizer NanoZS (Malvern Instruments Ltd, UK) between 20 and 50 $^{o}$C. The SOP allowed 10 minutes equilibration before each measurement was carried out to ensure an even distribution of temperature.

Each recording consisted of 12 runs of 10 seconds, which was repeated three times. Three independent recordings were made, and the data presented as mean ± standard deviation.

In addition to particle size experiments, ξ-potential experiments were also performed in DTS-1070 folded capillary tubes (Malvern Instruments Ltd, UK). Samples were again diluted by 1:10 into ultrapure water, placed into the cuvettes and sealed with PTFE stoppers and parafilm. The samples were then measured using the same temperature ramp and equilibration time as described above. A Smoluchowski model (Fκa = 1.50) was used in all cases and values were recorded over 20 runs, in triplicate.

In all cases, data are presented as mean size (from 3 repeats) as a function of temperature.

**4.2.3 Small Angle Neutron Scattering**

**4.2.3.1 Sample preparation**

Small angle neutron scattering (SANS) was used to measure the structure and interactions of the particles at different temperatures. One day of beam-time was obtained on the D11 instrument at the Institut Laue-Langevin (ILL, proposal number 9-12-

422) with the aim of using contrast matching to observe changes in the polymer corona independent of the core silica particle.

Prior to the experiment, samples were dialysed into $D_2O$ using a 7 kDa molecular-weight cut-off membrane (Medicell International, UK). A 1 mL aqueous suspension of particles was placed into the membrane and sealed, before being placed into a vial containing ~30 mL $D_2O$. $D_2O$ was replaced every 6 hours for a total of 3 changes. Following dialysis, samples were stored in glass vials, sealed with parafilm at 4 $^oC$.

### 4.2.3.2 Contrast match experiments

In order to obtain the contrast match point for the unfunctionalised thiolated silica nanoparticles, a stock solution of particles in 100% $D_2O$ (5.5 mg/mL) was diluted 1:10 into a series of different ratios of $D_2O$:$H_2O$. The volumes chosen were 100% $D_2O$, 75% $D_2O$, 50% $D_2O$, 35% $D_2O$, and 20% $D_2O$. The scattering profiles were obtained and normalised to the same I(Q) values (Fig 4.2) by subtracting the incoherent background.

From this, a single value in Q was taken for each ratio, and the square root of the intensity at that point was plotted against the volume fraction of $H_2O$ (Fig 4.3). The point at which this line crossed the x-axis was taken as the contrast match point. In this experiment it was found to be 20%. In all cases, the incoherent background was subtracted for $D_2O$/$H_2O$ mixture scattering profile.
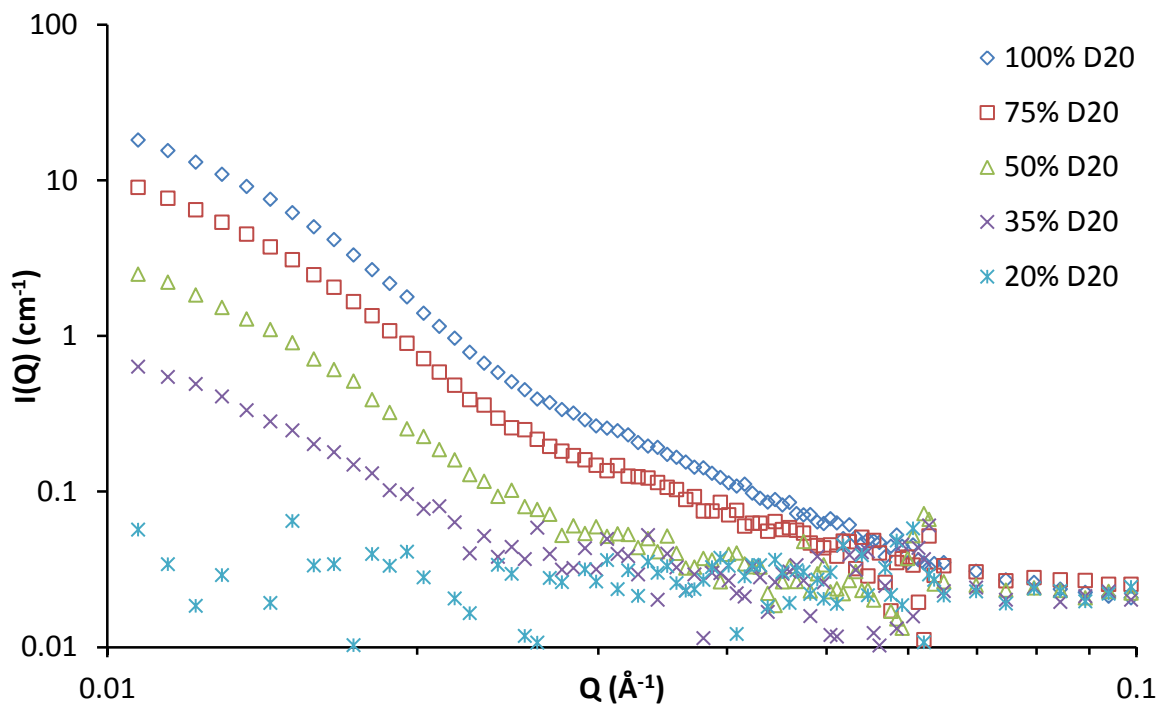
**Fig 4.2 SANS profile for thiolated silica diluted in different volumes of D$_2$O and H$_2$O, normalised against the incoherent background.**
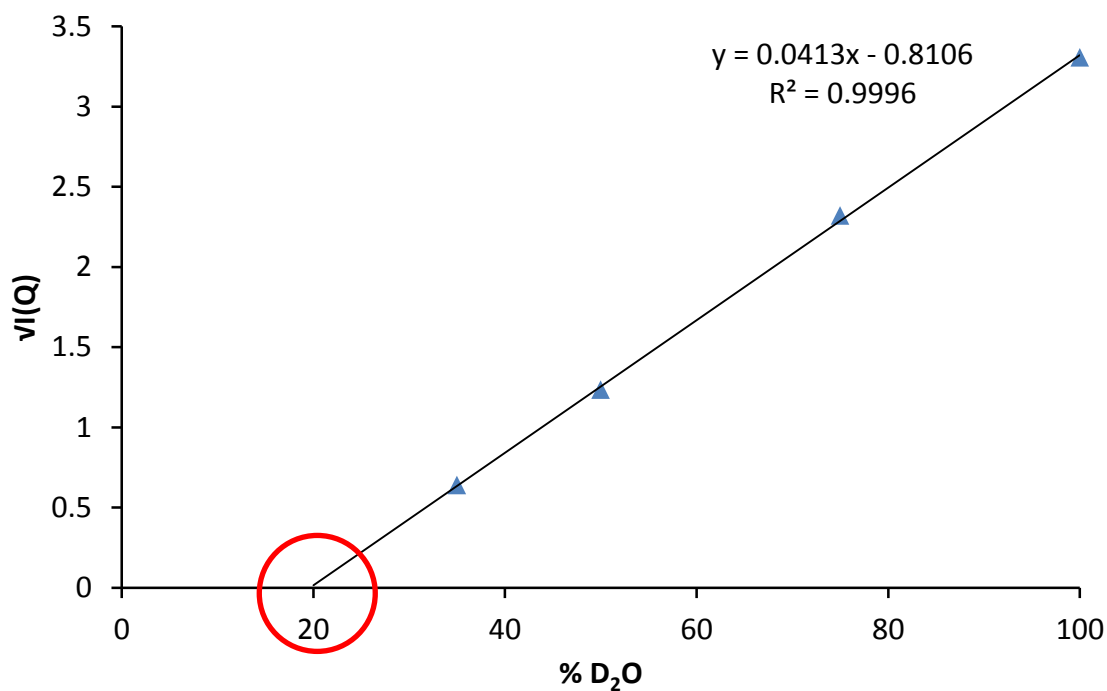


**Fig 4.3 Contrast match point as determined by taking the square root for I(Q) values as a function of D$_2$O concentration.** The circled area represents the contrast-match point

### 4.2.3.3 SANS experiments

From the above, the PNIPAM functionalised silica nanoparticles and the PNPOZ functionalised silica nanoparticles (5.5 mg/mL) were diluted 1:10 into 20% $D_2O$. In addition, PNIPAM-silica, PNPOZ-silica and unfunctionalised silica nanoparticles in 100% $D_2O$, again diluted by a factor of 1:10, were assessed. Samples were placed in 700 μL Hellma cuvettes sealed with a PTFE stopper, and placed in the beam-line. An incident wavelength of 8 Å at 3 detector distances of 1.2 m, 8 m and 28 m were used to cover a large Q-range from 2 x10$^{-3}$ to 0.3 Å$^{-1}$. All samples were measured at 25, 30, 34, and 40 ˚C, where the temperature was controlled by an external water circulation system. The data were then merged over all the detector distances, and the incoherent background subtracted.

Data fitting used the SASview programme (http://www.sasview.org/), using DLS and TEM data to provide the parameters. Various models were used depending on the sample and temperature and are discussed in further detail in section 4.3.4.

### 4.2.4 Nanoparticle diffusion

NTA was used to measure the diffusion coefficient for functionalised and unfunctionalised nanoparticles suspended in different solvents at different temperatures. Solvents were chosen based on their polarity and compatibility with the system. Based on these parameters, the solvents were water, ethanol and DMSO. Preliminary experiments with chloroform found the solvent to be unsuitable with the system and causing expansion of the rubber O-ring, and the samples to leak.

All measurements were performed using the NanoSight LM10 system, with LM14 metal top plate, green 532 nm laser, SCMOS camera, and syringe pump. Before videos were recorded, the stock solution of nanoparticles was diluted down to a working concentration of 1:10,000 by serial dilutions into the appropriate solvent. The final 1 mL suspension was then injected into the NanoSight system and the syringe placed in the syringe pump. For

all experiments, the flow-rate was set at 30 AU.  6×60 second videos were recorded at 25, 30, 35 and 40 $^0$C.  Each particle type was measured in triplicate.  For analyses, viscosity values (shown in Table 4.1, Fig 4.4) were taken from the literature.[11–13]

**Table 4.1 Reported viscosities of different solvents at 25, 30, 35, and 40 $^o$C.[11–13]**

| Solvent | Viscosity at 25 $^o$C (cP) | Viscosity at 30 $^o$C (cP) | Viscosity at 35 $^o$C (cP) | Viscosity at 40 $^o$C (cP) |
|---|---|---|---|---|
| Water | 0.89 | 0.737 | 0.713 | 0.658 |
| Ethanol | 1.04 | 0.983 | 0.895 | 0.818 |
| DMSO | 1.99 | 1.81 | 1.683 | 1.504 |
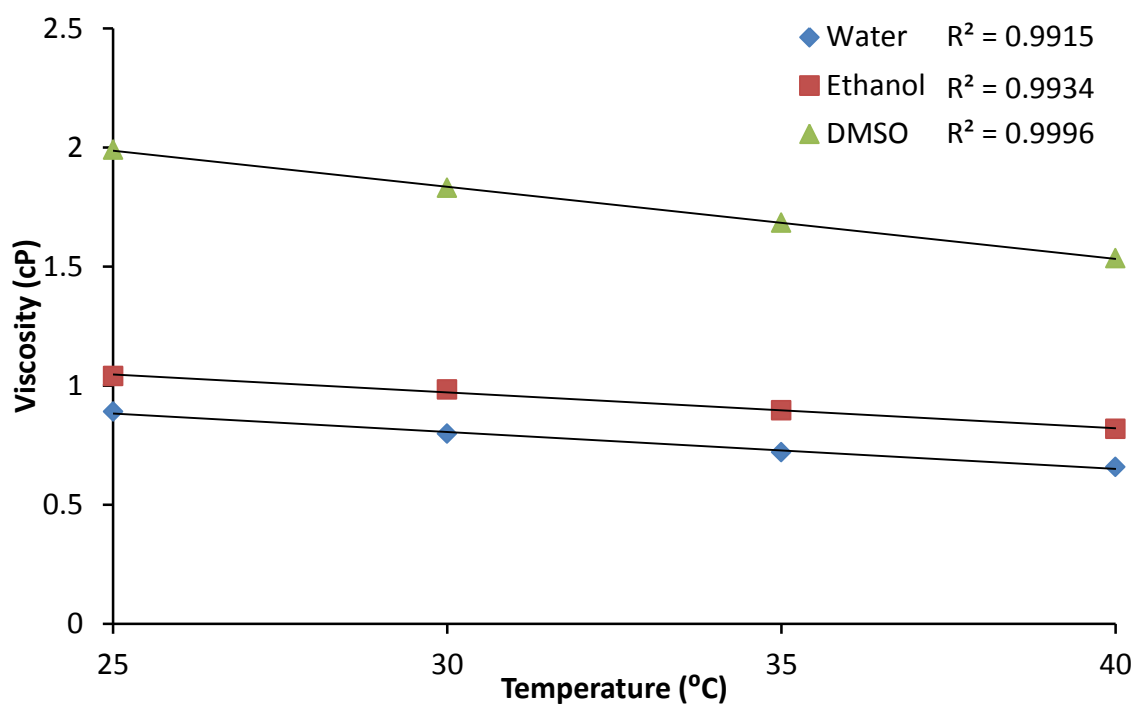


**Fig 4.4 Viscosity of different solvents as a function of temperature.**

### 4.2.5 Statistics

Data are presented as the means of 3 repeats ± standard deviation.  For comparison of diffusion coefficients, a 2-way ANOVA was carried out using a Bonferroni post-hoc test (p<0.05).

## 4.3 Results and discussion

### 4.3.1 Nanoparticle characterisation

The nanoparticles used in this study were the PNIPAM functionalised silica, and PNPOZ-functionalised silica synthesised in Chapter 2. These polymers are reported to have LCST's of 32 and 25 $^{\circ}$C, respectively. A summary of the size data (from Chapter 2, section 2.3.2) can be in Table 4.2.

**Table 4.2 Size and PDI of functionalised and unfunctionalised silica, determined using DLS (a) and NTA (b)**

| Sample | Z-average (nm)[a] | PDI [a] | Modal particle size (nm)[b] |
|---|---|---|---|
| **Thiolated silica** | 52±1 | 0.072±0.003 | 54±1 |
| **PNIPAM-silica** | 70±1 | 0.111±0.004 | 63±3 |
| **PNPOZ-silica** | 61±1 | 0.194±0.018 | 58±1 |

### 4.3.2 DLS

In addition to using DLS to determine the initial particle size following functionalisation, a temperature ramp study was used to assess how the particle diameter, PDI and ζ-potential changed with temperature. The temperature range chosen (20-50 $^{\circ}$C) provided information above and below the reported LCST of both polymers. The unfunctionalised thiolated silica particles were also subjected to the same temperature ramp studies to verify that the changes observed were due to the presence of the polymer and not a trait exhibited by the unfunctionalised particles. Fig's 4.5, 4.6, and 4.7 shows how the size, PDI, and ζ-potential values change as a function of temperature.
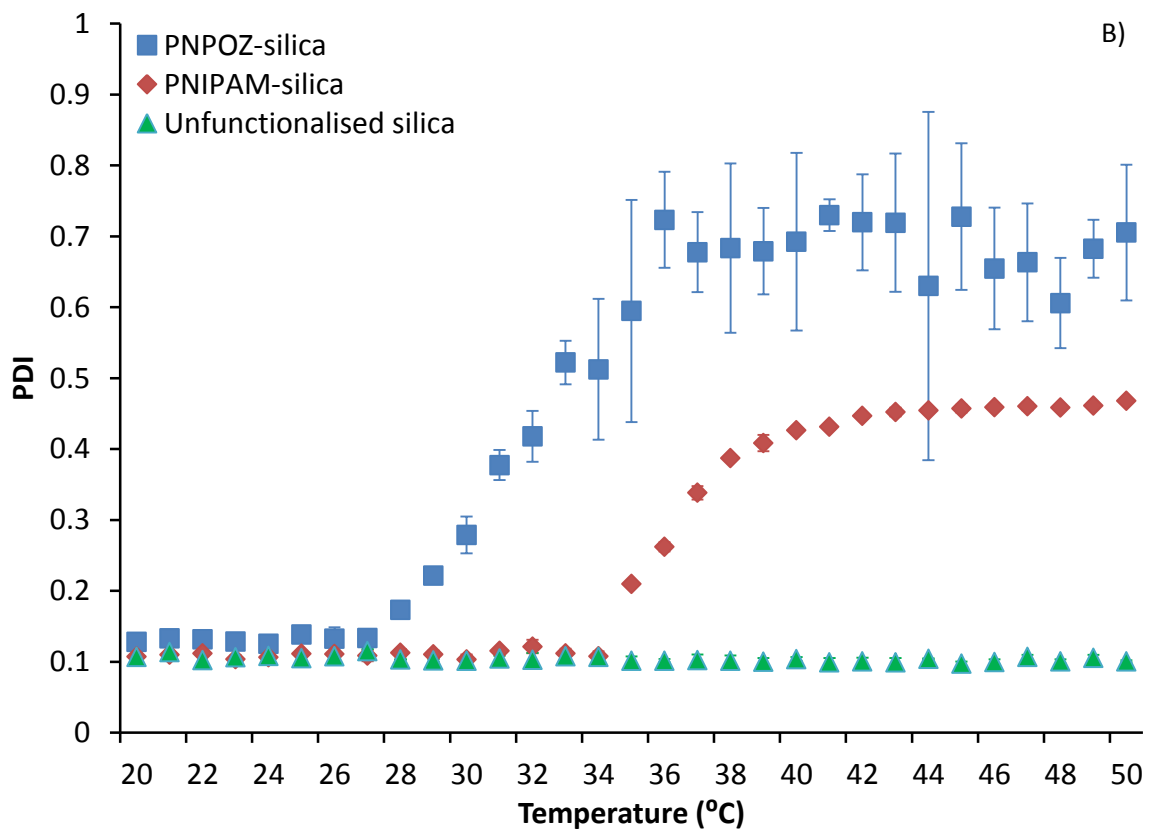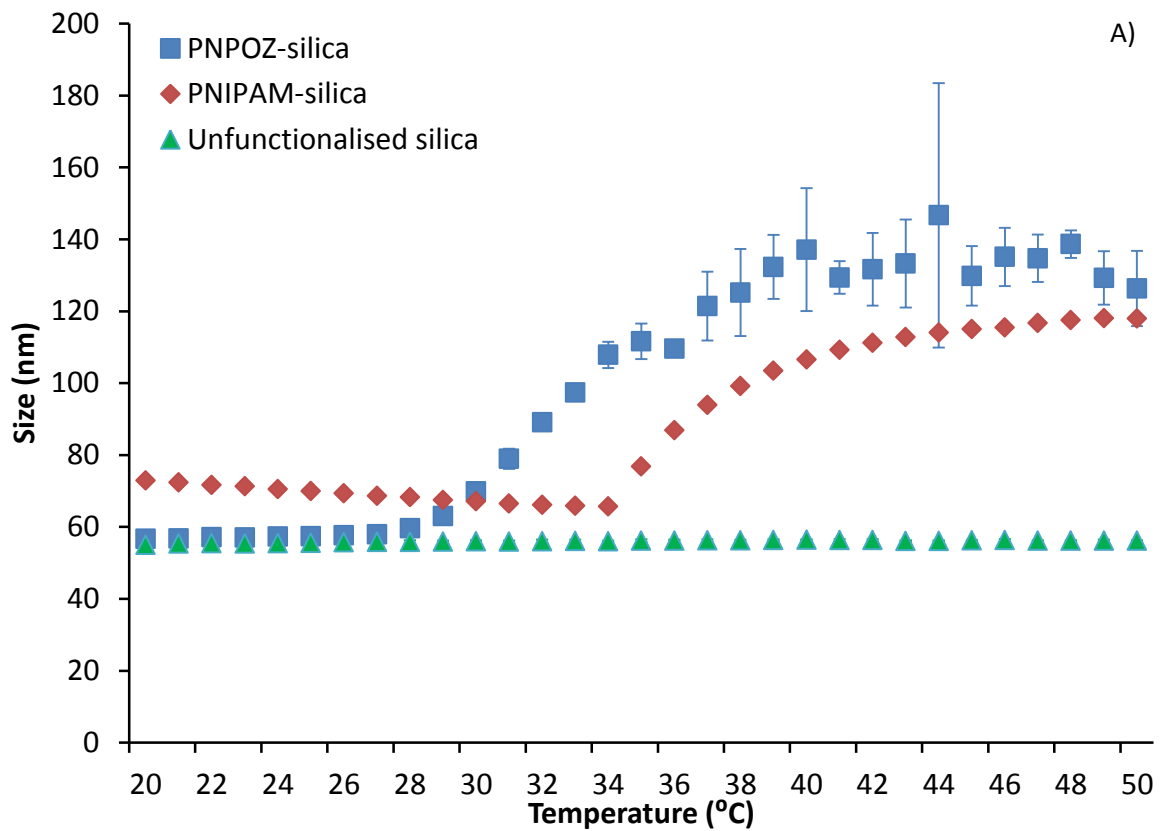
**Fig 4.5 Size (A) and PDI (B) values for functionalised and unfunctionalised nanoparticles as a function of temperature.** Means ± standard deviation, n=3.
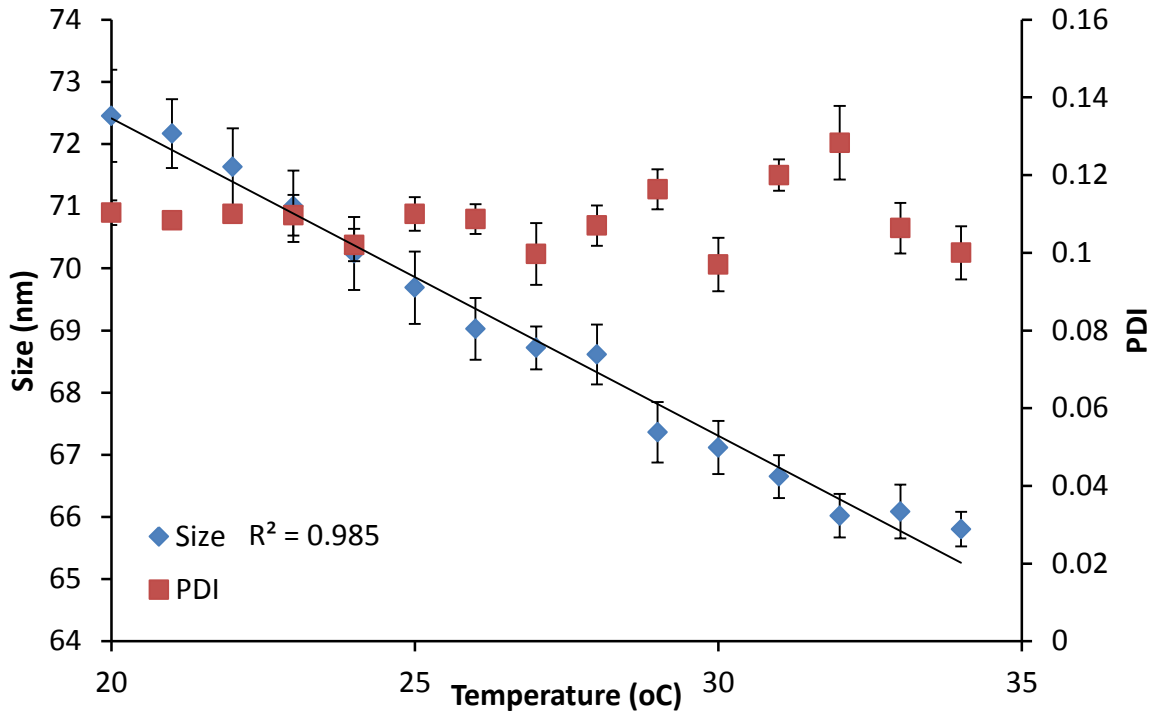
**Fig 4.6 Size and PDI of PNIPAM functionalised silica nanoparticles between 20 and 34 °C.**
Means ± standard deviation, n=3.
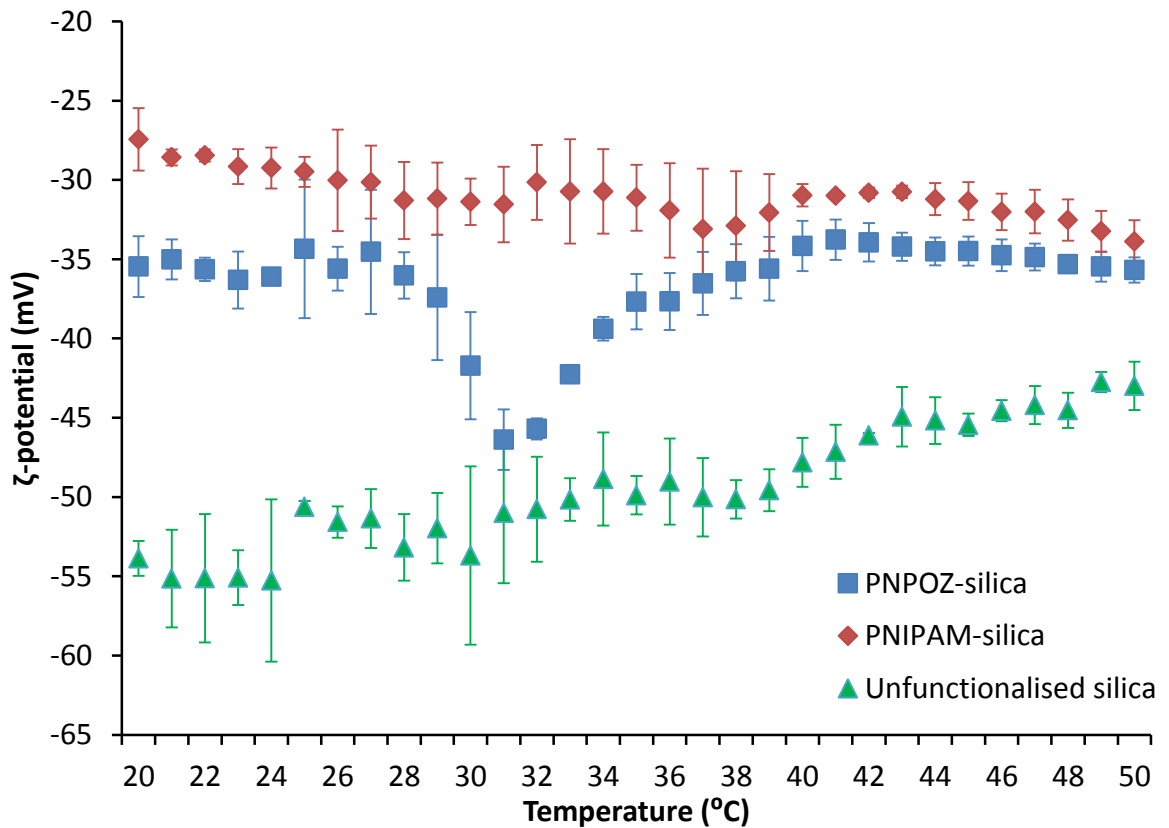


**Fig 4.7 ζ-potential of functionalised and unfunctionalised nanoparticles as a function of temperature.** Means ± standard deviation, n=3.

From the size of the nanoparticles (Fig 4.5A), it is clear that as temperature increases the size of the functionalised nanoparticles also changes significantly. The PNIPAM-silica nanoparticles show a steady decrease in size up to 34 $^{o}$C, followed by an increase between 34 and 40 $^{o}$C, before it plateaus. The slow size decrease was found to be linear with an $R^2$ of 0.98 (Fig 4.6). A similar trend is shown with the PDI values (Fig 4.5B) suggesting that the particles are forming aggregates as the temperature increases above 34 $^{o}$C, although was not found to be linear. Interestingly, the PDI values remains essentially constant between the 3 independent repeats, with very small error bars shown.

From Fig 4.6, it is clear that the size decrease occurs independently of any change in PDI. This particle size decrease has been noted by other authors,[14,15] although there is little explanation for this. It is feasible that the polymer is undergoing phase-transition prematurely, however if this were the case, one would expect the PDI to change in a similar manner as the size. In addition, the size changes would be sudden, occurring at a specific temperature rather than the subtle linear decrease as is shown here. It is more likely that this change is due to changes occurring in the hydration shell around the particle, where interactions between water and the polymer are becoming weaker, thus forcing water into the surrounding media, leading to shrinkage of the hydration shell. This size decrease would cause the PDI values to remain relatively constant, as is the case here. If the polymer was undergoing premature LCST, it would be expected that the PDI values change accordingly.

Following the decrease, a size increase can be noted at 34 $^{o}$C. Given that the LCST of free PNIPAM is 32 $^{o}$C,[16] this alteration is probably due to the brush conformation adopted by the polymer around the particle. Due to the dense polymer packing, the LCST will shift to a higher temperature, due to steric hindrance around the particle, a change noted in the literature.[3] As the temperature continues to ramp, the particle size eventually plateaus (>40 $^{o}$C). This trend is mimicked by the PDI values which also increase, followed by a plateau, confirming that the particles are aggregating. It is interesting to note that the

error bars for the sizes and PDI's are very small, which would not be expected if the particles were strongly aggregating with each other in a random manner. This suggests that the particles are aggregating in a controlled fashion, which is unreported in the literature. Due to the similarity between the PDI and size data, it is most likely that, as the particles are interacting with each other and approach equilibrium, clusters of several nanoparticles are formed. With the steady increase in particle size (and PDI) between 34 and 40 $^{\circ}$C, it is likely that one particle is interacting with another particle, then as temperature ramps these small clusters are further interacting to form a small cluster of nanoparticles. However, once equilibrium has reached these clusters cease to interact any further. This is further described in the context of the SANS data in section 4.3.3.

As with the PNIPAM-silica nanoparticles, the PNPOZ-silica nanoparticles also undergo a phase transition, which causes changes in particle size. The reported LCST of PNPOZ is 25 $^{\circ}$C,[17] which here shifts to ~28 $^{\circ}$C due to steric hindrance around the particles. However, the particles do not show the size decrease shown by PNIPAM, and the size remains relatively stable up to 28 $^{\circ}$C, when the size starts to increase and the particles aggregate. Again, the particle size increases steadily, followed by a plateau which is reached at 37 $^{\circ}$C. Once the particle size has plateaued >37 $^{\circ}$C, the error bars become very large, as would be expected for a truly aggregated system. However, between 28 and 37 $^{\circ}$C, when the particle size is increasing exponentially, the error bars remain small, suggesting weak but uniform aggregates are forming. These trends are also mimicked in the PDI values for the particles over the same temperature range, confirming this interpretation. The unfunctionalised silica nanoparticles show no change in size or PDI across the temperature range studied, as would be expected.

In addition to the size and PDI of the particles, their $\zeta$-potential was also measured across the same temperature range (Fig 4.7). From the data, it is clear that there are changes in $\xi$-potential as temperature increases across all samples. For unfunctionalised silica (Fig 4.7; green), there is a clear decrease in the negative $\xi$-potential as the temperature

149

increases and there is a significant difference between the ξ-potential at 20 °C (-54±1 mV) and that at 50 °C (-43±2 mV) (p>0.05, Student's t-test). Though only a few studies describe the effect of temperature on the ξ-potential of silica nanoparticles, this phenomenon has been noted by other authors and is a property of the silica nanoparticles itself. Several papers report on a decreasing ξ-potential as the temperature increases,[18–20] thought to be due to the dissolution of surface sialic moieties as the temperature changes.[21]

For the PNIPAM functionalised nanoparticles, although there is apparently a slight increase in ξ-potential across the temperature range, the change is not significant (p<0.05). These data suggest that the particles remain stable in suspension, confirming the earlier findings from size and PDI data: the ξ-potentials remain low enough so there will be minimal interactions between the particles. This effect on ξ-potential has been reported by other authors[22] although again there is very little literature data on this.

The changes in ξ-potential occurring for PNPOZ are the most interesting. The ξ-potential remains relatively constant until 27 °C, when it changes significantly (p<0.05) and becomes more negative up to 31 °C (from -31 to -46 mV), followed by a steady decrease between 32 and 40 °C (from -46 to -34 mV) when it remains essentially constant up to 50 °C. Although no significant difference can be observed between the initial ξ-potential and the final ξ-potential (p<0.05), there is a significant difference when the ξ-potential drops to its lowest value; -46 mV (p<0.05). Considering this inflection alongside the size and PDI data (Fig 4.5/4.6), this change occurs as the particles undergo the phase-transition i.e. on the slope as the particles are aggregating. The point at which the ξ-potential starts to increase (27 °C) is the point at which the size and PDI also start to increase. Likewise, once the ξ-potential has "recovered", the particle size and PDI has plateaued. Based on these observations, it is possible to conclude that as the particles are aggregating they are

becoming more stable; however this is only an intermediate step before the particles become fully aggregated, when the $\xi$-potential starts to decrease again.

Considering all the DLS data, some very interesting phenomena are occurring. The PNIPAM-silica nanoparticles show changes in hydration shell thickness below the LCST followed by an equilibrated aggregation, a trend not mimicked in PNPOZ-silica nanoparticles. No changes occur in the unfunctionalised silica nanoparticles, confirming that the presence of the polymer is causing these thermal events. To confirm these finding, SANS experiments were employed.

### 4.3.3 Small Angle Neutron Scattering

### 4.3.3.1 Silica-matched SANS

The initial proposal to measure the structural changes observed by DLS was to use contrast variation to assess changes occurring in the shell around the silica nanoparticle at different temperatures. Initially the silica was matched out by placing particles in a solvent mixture of 80% $H_2O$ and 20% $D_2O$ (as discussed in 4.2.4), and then placed in the beam-line at temperatures chosen based on the DLS data. Following data collection however, no contrast was observed from polymer shell (Fig 4.8) and so unfortunately the data could not be used.
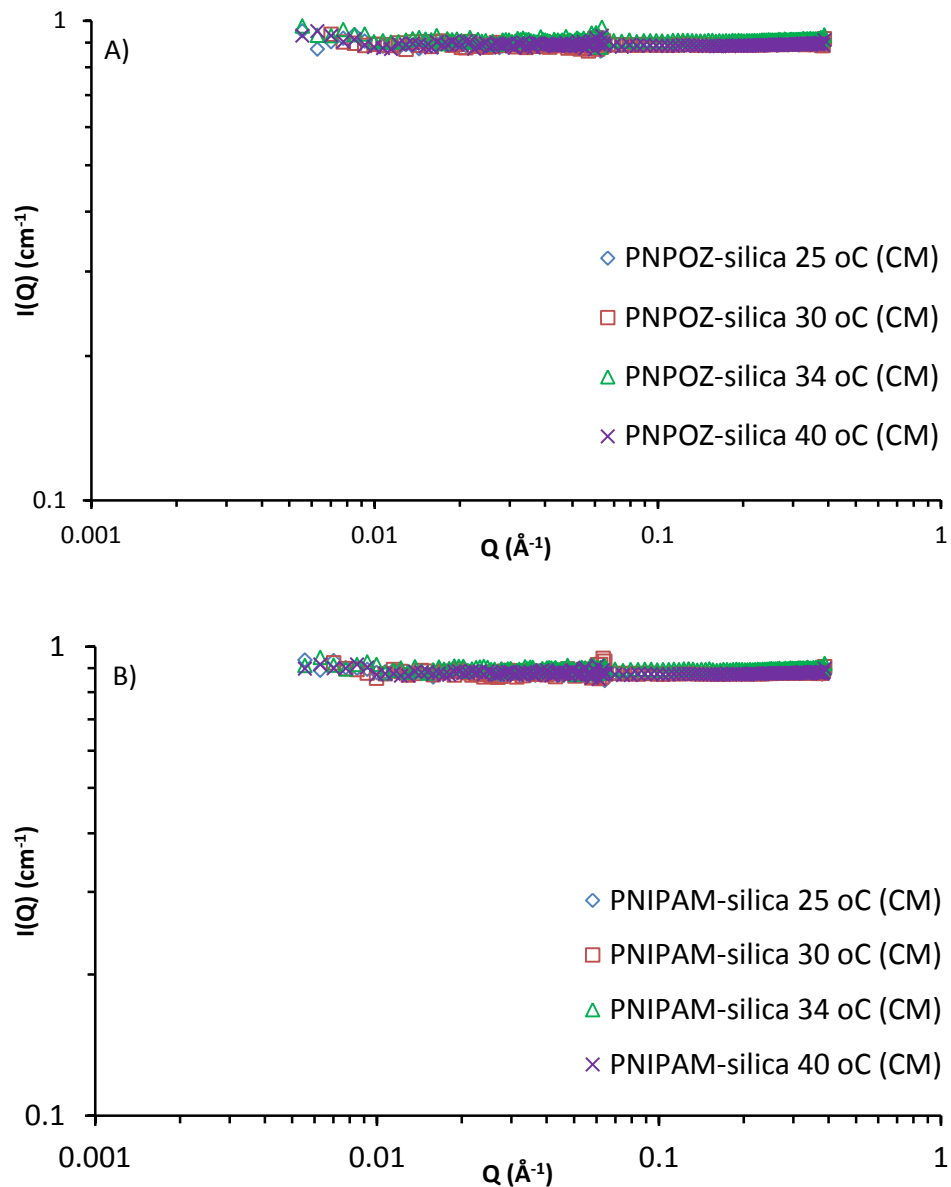
**Fig 4.1 Contrast matched silica nanoparticles functionalised with PNPOZ (A) or PNIPAM (B).**
Data is the reduced scattering data for the shell only at different temperatures.

From the data, it is clear that no structural features can be determined based on the scattering. As the I(Q) is a flat line, it suggests no contrast meaning no structural information can be assessed. The reason for this could be 2-fold; time, and match-point. The strongest limitation to the study was time, and the matched sample could not be detected above the background due to lack of time on the beam-line. Given more time, it could be possible to draw-out some structural information by minimising the background

scattering and improving the statistics. The other limitation is the match-point itself. It is well known that $D_2O$ is much better at scattering neutrons than $H_2O$, hence why it is used in scattering experiments. As the sample is 80% $H_2O$ and only 20% $D_2O$, it means there will be a very high background due to a large amount of incoherent scattering, and any information on the sample will be lost.

Despite the disappointing lack of results, when placed in a non-matched system (i.e. in 100% $D_2O$) the spectra did show some structural features that were possible to analyse.

**4.3.3.2 Scattering in 100% $D_2O$**

The reduced scattering data for PNIPAM and PNPOZ functionalised silica can be found in Fig 4.9, with the incoherent background subtracted.
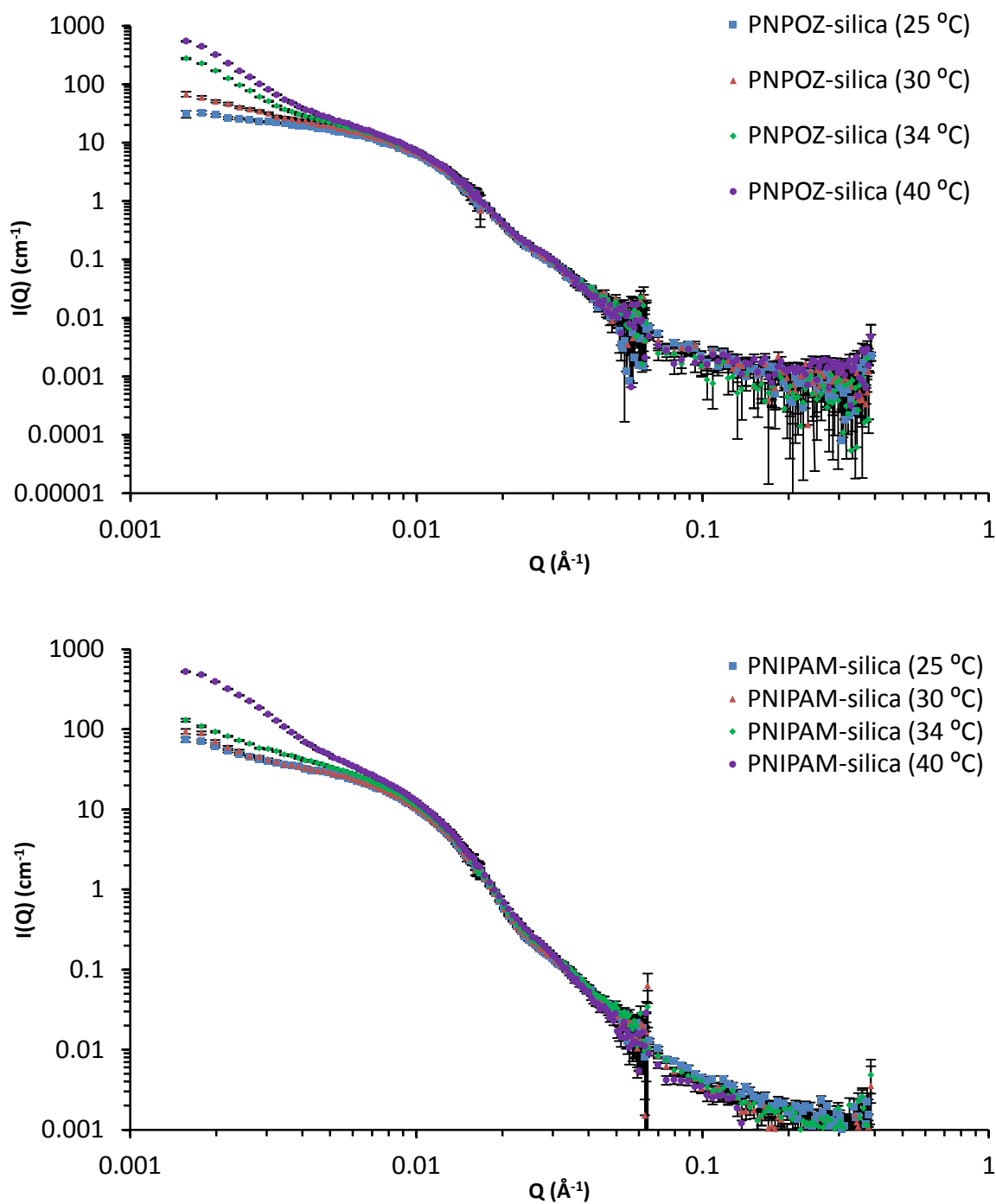
**Fig 4.2 Raw scattering data for PNIPAM-silica and PNPOZ-silica nanoparticles at 25, 30, 35, and 40 °C obtained on the D11 instrument at the ILL.**

Looking at these data, it is clear that the samples change upon heating. PNPOZ has a lower LCST than PNIPAM, and this is reflected in the scattering data. Nothing appears to be changing in the particles at high Q values (known as the Porod region), however at low

Q values (the Guinier region) the scattering patterns start to separate to higher I(Q) values as temperature increases, indicating the presence of a large structure. A definition of these regions can be found in Fig 4.10.
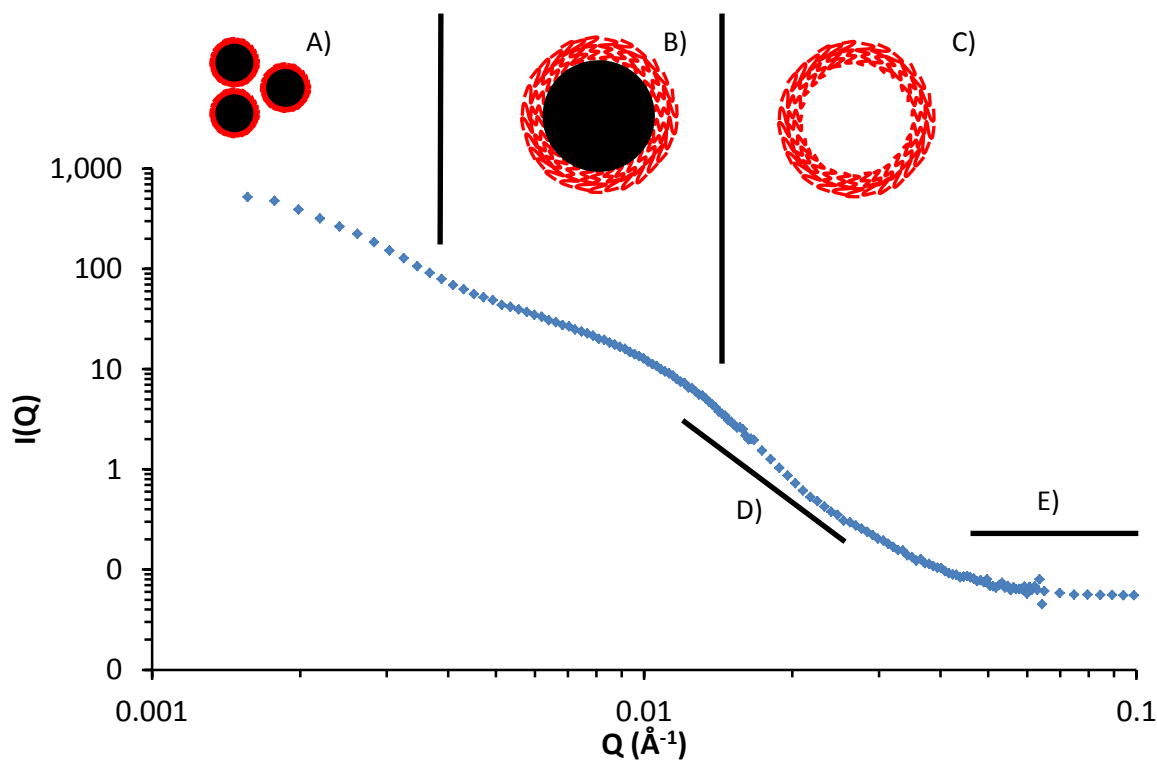


**Fig 4.3 SANS scattering profile for PNIPAM functionalised silica nanoparticles at 40 °C, indicating particle-particle interactions (A), the Guinier region (B), the Porod region (C), the Debye region (D), and (E) incoherent background (subtracted from final results).**

Regions of low Q values (shown in Fig 4.10A) define the bulk-structure of the particles, and are used to assess particle-particle interactions. By fitting this region to a specific model it is possible to generate information on particle aggregates, and interactions. This region is of great interest in the determination of quaternary protein structure.[23] The Guinier region (Fig 4.10B) defines the size of particles, which is dependent on intensity, I(Q). In a monodisperse system, the Guinier region will be flat, indicating a purely monodisperse system of a given size. Here, the Guinier region starts to level off, but the intensity increases again, indicating aggregation amongst the samples. The Porod region (Fig 4.10C) defines the surface of the particle, and (in the case of functionalised

155

nanoparticles) will provide information on the shell-structure. At larger Q values (>1), it is possible to determine the molecular structure of a crystalline material. It is this region where Bragg peaks exist, and as such typically no Bragg peaks occur in a SANS experiment. The Debye region (Fig 4.10D) defines the shape of a particle. By fitting the spectra obtained from a neutron scattering experiment to a defined model, it is possible to provide information on the particle. If this information is then applied to another model, it is possible to establish interactions between the particles, and how they are aggregating. Finally, Fig 4.10E shows the incoherent background, which was removed from the final data series.

One of the key parameters needed in SANS fitting is the scattering length density (SLD) for the particles, polymer and background solvent. This value is based on the sum of individual neutron scattering lengths for atoms making up the unit cell. Each element, and isotope of said element, has a specific scattering length i.e. depending on the nuclear make-up of the element, spin properties and energy levels; neutrons will scatter at a specific wavelength. The scattering length density, defined by Equation 4.2, represents the scattering power from a given system, or unit cell.

$$SLD = \frac{\sum_{i=1}^{N} b_i}{V_m}$$  Equation 4.2,

where N is the number of atoms in a unit cell, $b_i$ is the scattering length contribution from each individual atom and $V_m$ is the volume of the unit cell. It is the SLD that makes it possible to carry out contrast-matching experiments. Given the large differences in SLD between $H_2O$ (-5.61 $\times 10^{-7}$ 1/Å$^2$) and $D_2O$ (6.35 $\times 10^{-6}$ 1/Å$^2$), it is possible to mix the two solvents together in different ratios to match the SLD of a system. For example, the SLD of $SiO_2$ nanoparticles is 3.48 $\times 10^{-6}$,[24] so with a mixture of 35% $D_2O$ and 65% $H_2O$, it is possible to match-out the silica, essentially making it invisible to the neutrons. However, in 100% $D_2O$, as shown here, all the particles (core and shell) are visible to the neutron beam.

**4.3.3.2.1 PNIPAM-silica**

For PNIPAM-silica nanoparticles, the fitting parameters were first established using the scattering profile for unfunctionalised silica alone fitted to a sphere model. Data were fitted to pre-defined form factors built into the SASview software, which define the model being studied. To fit the data accurately, several parameters need to be known, shown in Table 4.3.

**Table 4.3 List of parameters used to fit SANS data to a sphere model, and the definitions of each parameter.** Fitting is for thiolated silica nanoparticles.

| Parameter | Value | Definition |
|-----------|-------|------------|
| Background | 0.05 | The baseline at high Q |
| Scale factor | 0.001 | Volume fraction |
| Radius | 137.2 Å | Particle radius |
| SLD(solvent) | $6.35 \times 10^{-6}$ $1/\text{Å}^2$ | Scattering length density of $D_2O$ |
| SLD(core) | $3.2 \times 10^{-6}$ $1/\text{Å}^2$ | Scattering length density of silica |
| PDI | 0.35 | Polydispersity |

By placing constraints into the model using known experimental values (for example the volume fraction, size and PDI), it is possible to determine the shape and size of the particles. Here, the Q range was shortened to between 0.007 and 0.1 $\text{Å}^{-1}$, removing the large background from the sample, as no change in scattering occurred at values above 0.1 $\text{Å}^{-1}$, as well as the particle interactions shown at low Q, which will be separately studied. The fitting profiles can be found in Fig 4.11.
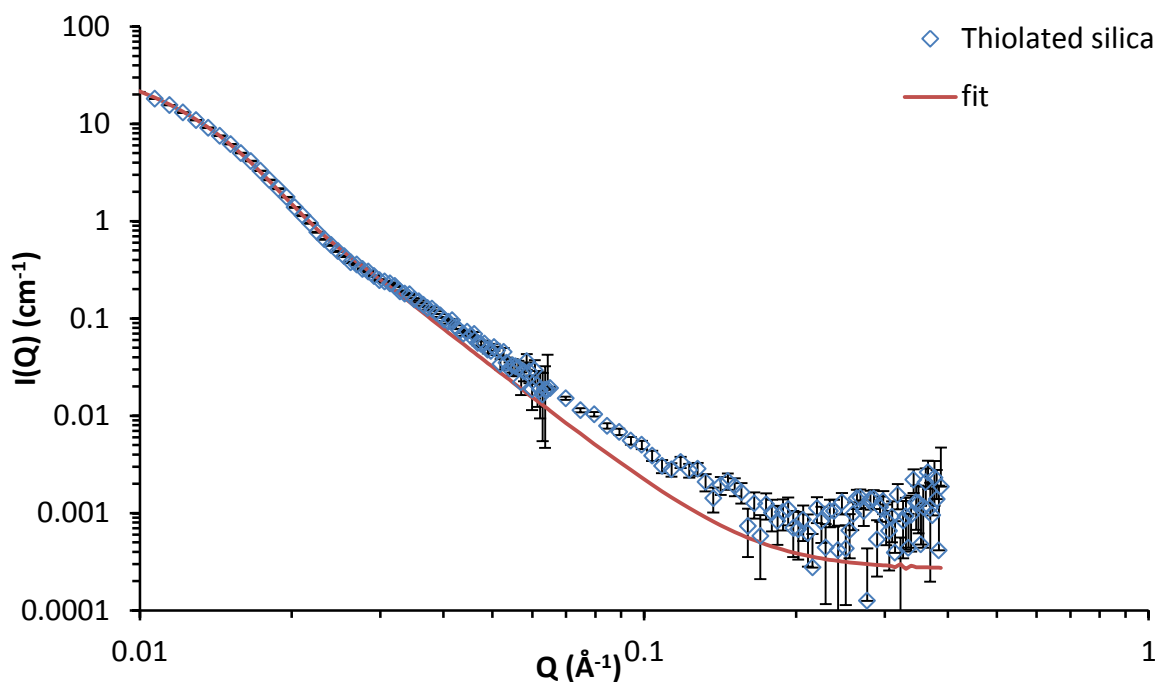
**Fig 4.4 Scattering profile and fit to a sphere molecule for thiolated silica.**

Due to the presence of large error bars at high Q values (~0.06 Å$^{-1}$) it was not possible to gain a more accurate fit (Chi$^2$ = 23).  Despite this, a diameter of 28 nm was obtained, which corroborated with the literature values using SANS on these 50 nm silica nanoparticles,[25] and the TEM data (see Chapter 6 for details).

The values obtained for unfunctionalised silica (namely core radius and PDI) were used as set parameters in further fitting experiments.  PNIPAM-silica and PNPOZ-silica spectra were also fitted to this model, and in all cases a diameter of 28 nm was obtained.

Unfortunately, due to lack of contrast between the polymer and the D$_2$O background it was not possible to obtain any information on the corona around the particle.  Therefore, the data was only fitted to a sphere model.  The scattering profile for PNIPAM-silica nanoparticles at different temperatures can be found in Fig 4.9.

It is clear that at low Q values (due to the increase in intensity in the Guinier region) larger aggregates form even below the LCST.  This can be seen by an increase in intensity rather than a levelling off.  The reason for this could be two-fold; a high concentration of

particles, causing particles to interact more readily in a confined environment, or sample contamination.  General aggregation of the sample is unlikely as (based on the DLS data) the sizes at lower temperatures suggest no aggregation (due to low PDI and particle sizes similar to that of the unfunctionalised silica).  In addition, ξ-potential values are around -30 mV, suggesting that very few particle interactions could occur.  However, it is possible that the dilutions used in DLS experiments may not be best suited for SANS experiments.

From fitting the spectra to a sphere, the inter-particle interactions were determined.  For this, the particles were fitted to either a linear pearls model, or a fractal model depending on the temperature.  These fits can be found in Fig 4.12, and the findings summarised in Table 4.4.
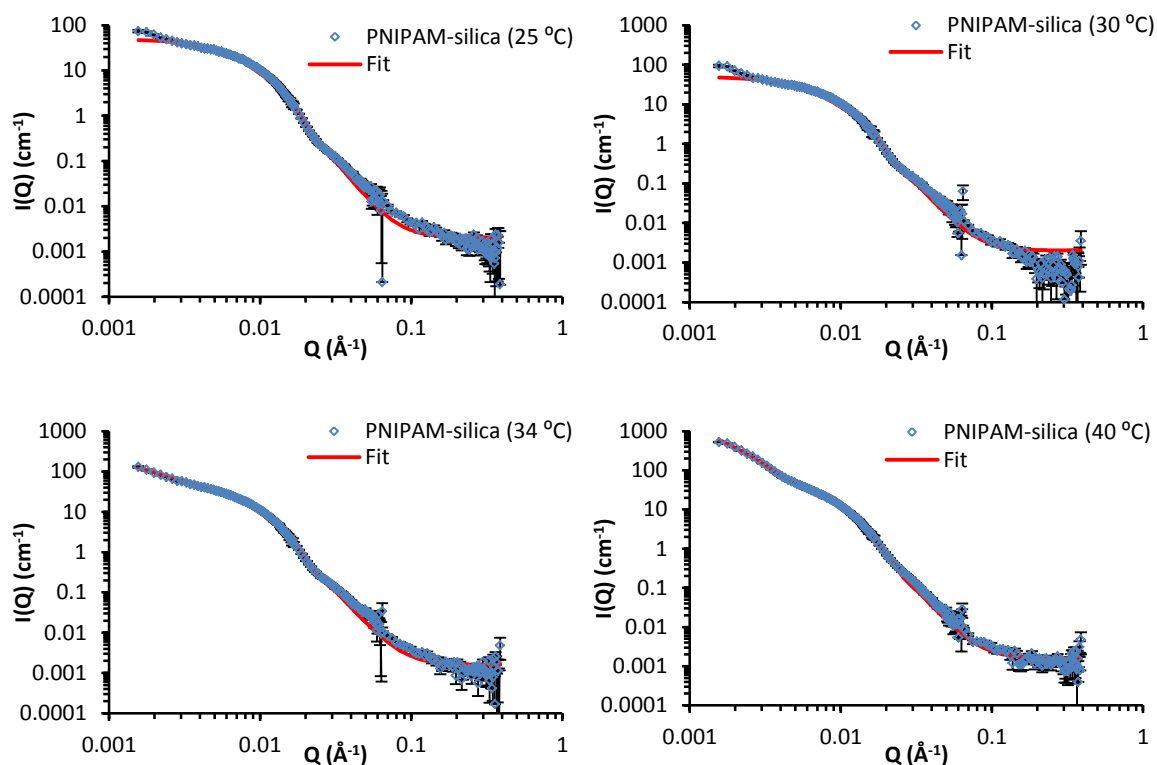


**Fig 4.5 Fitting profile of PNIPAM-silica nanoparticles to a linear-pearls model (at 25, 30, and 34 °C), or a fractal model (40 °C)**

**Table 4.4 Data obtained from the fits of PNIPAM-silica nanoparticles at different temperatures.** Samples at 25, 30, and 34 $^{o}$C were fitted to a linear-pearls model, whereas 40 $^{o}$C was fitted to a fractal model.

| Temperature ($^{o}$C) | Number of pearls | Distance between pearls (nm) | Fractal dimension | Size of aggregate (nm) |
|---|---|---|---|---|
| 25 | 3 | 2.3 x10$^{-8}$ | - | - |
| 30 | 3 | 2.0 x10$^{-8}$ | - | - |
| 34 | 14 | 5.3 x10$^{-7}$ | - | - |
| 40 | - | - | 2.5 | 84 |

From these data, it is possible to conclude that at lower temperatures (i.e. below 30 $^{o}$C) the particles are loosely agglomerated (possibly due to a high concentration). This is represented by a very close proximity of particles to each other. It should be noted that in fitting, the value representing "number of pearls" did not affect the fit, and changing this number resulted in very minor changes to the Chi$^{2}$ of the fit, further suggesting particle agglomeration. However, at 34 $^{o}$C, the point at which the particles undergo phase-transition (shown by DLS), the particles become less tightly aggregated, but the number of particle interactions increases. This time, changing the number of pearls does alter the fit, suggesting only a limited number of particles are interacting with each other, confirming the equilibrium hypothesis discussed earlier. Finally, at 40 $^{o}$C, the particles no longer fitted to a linear-pearl model, and instead were fitted to a fractal model. Here, it is possible to conclude that the final agglomerates have a well-defined structure, with a fractal dimension of 2, with a definitive size, as predicted by DLS. From this, a proposed model for the agglomerates can be deduced (Fig 4.13).
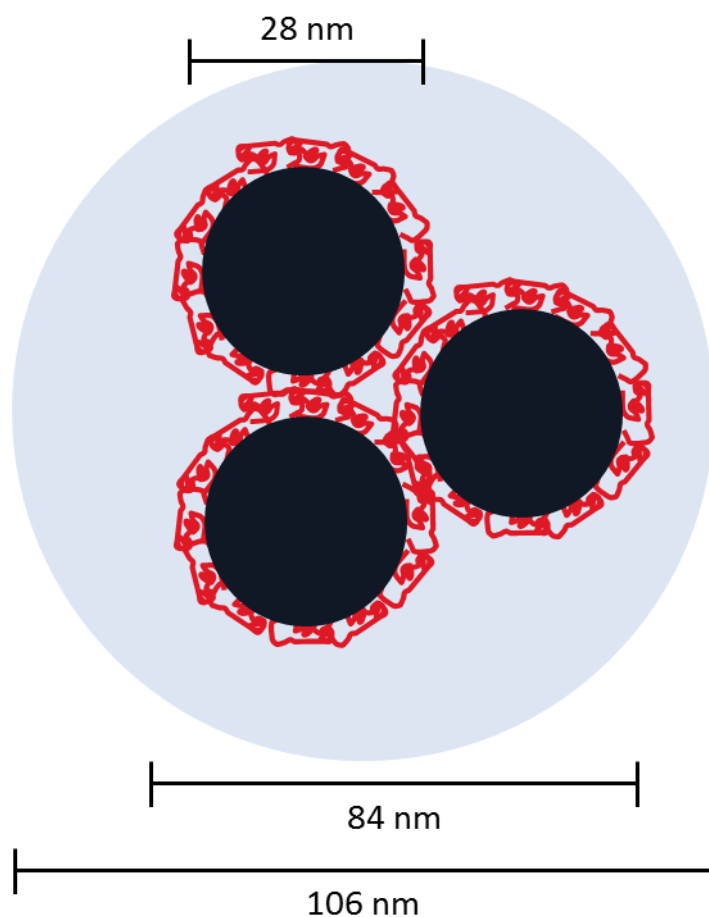
**Fig 4.6 Proposed structure of PNIPAM-silica nanoparticles in an aggregated state at 40 $^{o}$C.**

Given that the silica core has a radius of 14 nm (diameter 28 nm), and the overall size of the aggregate is 84 nm, 3 nanoparticles appear to interact to form this 3D structure. Depending on the spatial orientation of these particles, this data is corroborated by DLS (Chapter 2, and Table 4.2). The 84 nm aggregate size predicted by SANS fits the DLS size of 106 nm at the same temperature (when one takes into consideration the addition of a hydration shell around the aggregate which is not detected by SANS).

The SANS data is in good agreement with the DLS data (Chapter 2, and Table 4.2), and confirms the hypothesis that at higher temperatures (above 34 $^{o}$C), the functionalised nanoparticles form small clusters with a very uniform overall size. It is likely that the temperature will dictate how tight the interactions between the particles are given the

changes observed in DLS: higher temperatures cause tighter interactions. From these data it is not possible to describe the interactions occurring in the particles between 34 and 40 $^o$C (shown in DLS) due to lack of SANS data.

### 4.3.3.2.2 PNPOZ-silica

In addition to PNIPAM-silica, PNPOZ-silica was also measured at the same temperatures. As with the PNIPAM-silica; the particles were first fitted to a sphere model, followed by the fractal model. Due to the high levels of hydration exhibited by the PNPOZ macromolecules, it was not possible to differentiate between the core and the shell of the particle, given that the shell is masked by $D_2O$ surrounding the particle i.e. in the hydration shell. Previous studies looking at POZ macromolecules have shown that they become highly hydrated, explaining the lack of contrast shown here.[26,27] As such, the particles were fitted to a sphere model alone, resulting in a size of 28 nm. Again, all fits were between 0.007 and 0.1 $Å^{-1}$.

From these fits, the particle interactions were again modelled to either a linear-pearls model or fractal model depending on the temperature. These data can be found in Fig 4.14, and summarised in Table 4.5.
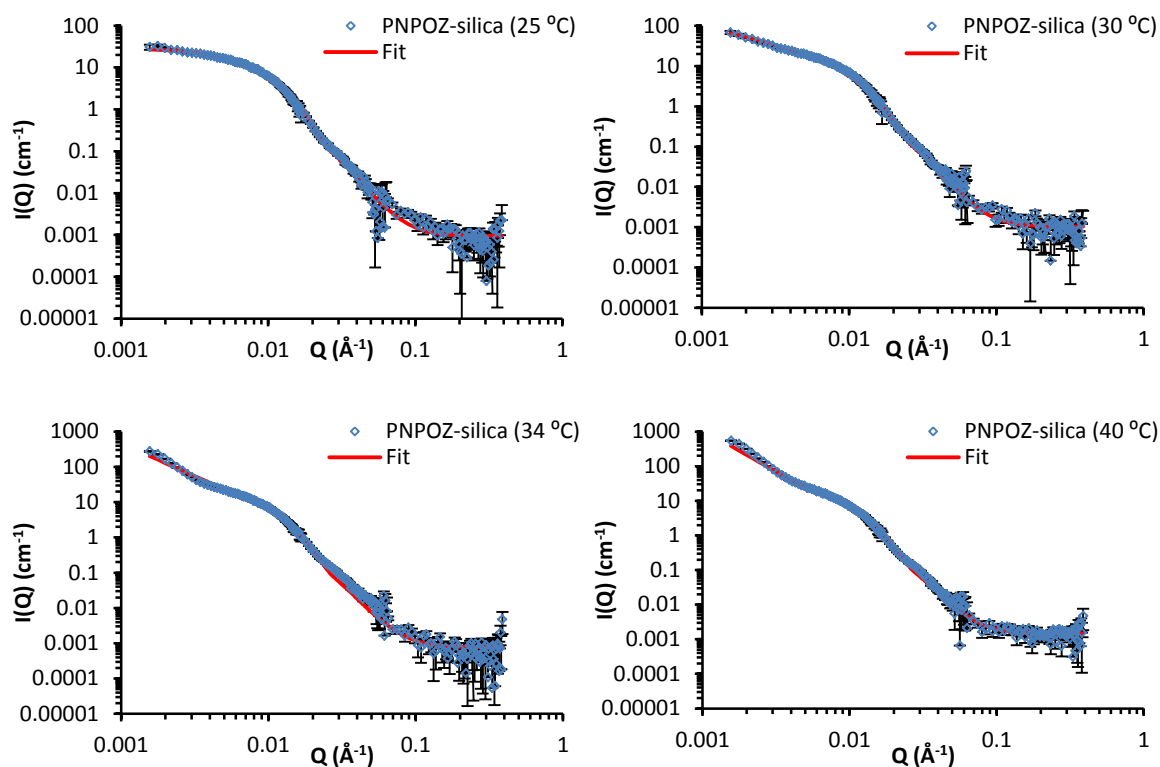
**Fig 4.7 PNPOZ-silica nanoparticles fit to a linear pearls model at 25 and 30 °C, and a fractal model at 34 and 40 °C**

**Table 4.5 Summary of the data obtained from PNPOZ-silica fitting.**

| Temperature (°C) | Number of pearls | Distance between pearls (nm) | Fractal dimension | Size of aggregate (nm) |
|---|---|---|---|---|
| 25 | 2 | 2.8 x10$^{-8}$ | - | - |
| 30 | 3 | 2.8 x10$^{-8}$ | - | - |
| 34 | - | - | 2 | 7854 |
| 40 | - | - | 3 | 237 |

From these data two conclusions can be made. Firstly at 25 and 30 °C, there is some aggregation suggesting a high concentration of particles, as was seen with the PNIPAM-silica particles. At higher temperatures however, there appears to be bulk aggregation of the samples, as shown in the fractal model. Unlike the PNIPAM-silica particles, the aggregate size here is very large, and varies markedly. Indeed, an aggregate size of 7.8

μm (at 34 °C) shows that the particles are simply aggregating randomly together in suspension, unlike the PNIPAM-silica particles. DLS data (Fig 4.5), showed large error bars at higher temperatures (i.e. above 34 °C), along with a large increase in PDI (up to a PDI of 1), confirming the formation of large aggregates. Although both polymers are structural isomers (Fig 4.15), it is problematic to make a direct comparison, as PNIPAM contains an isopropyl group, whereas PNPOZ contains an n-propyl group.
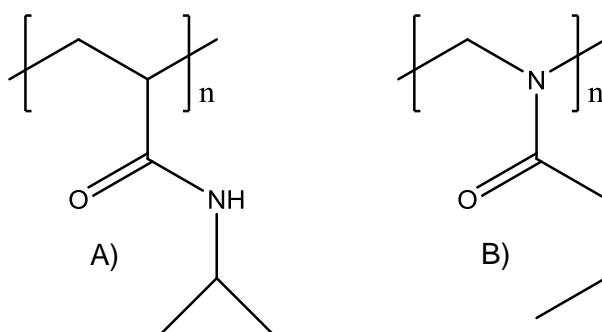


**Fig 4.8 Molecular structure of PNIPAM (A) and PNPOZ (B).**

However, it could be that the position of the nitrogen atom plays a key role in how the particles are aggregating, whether uniformly or randomly. Given that the nitrogen atom in a secondary amide is more accessible, it is able to form stronger hydrogen bonds with water molecules in the surrounding media.[28] A tertiary amide however (as found in PNPOZ) will form fewer hydrogen bonds, thus binding more weakly to water molecules. Assuming this is the case and that PNPOZ is interacting more weakly with water, the hydration shell around the particles will be more unstable (both above and below the LCST), causing a weaker hydration shell. To test this hypothesis, additional SANS and DLS data on poly(2-isopropyl-2-oxazoline) will be required.

Considering the DLS data, as already discussed, it is clear that the hydration shell around PNIPAM plays a strong role in how it behaves at different temperatures (based on the initial size decrease, followed by aggregation). Given that there is no size decrease in the PNPOZ-silica nanoparticles, it suggests that the hydration shell is weaker (as water is

more loosely bound and will not change at lower temperatures), which leads to more random aggregation. This is confirmed using SANS analysis and the inter-particle interactions.

### 4.3.4 Diffusion in organic solvents

Given the structural changes shown by these particles at different temperatures, the diffusion coefficient variation in different solvents with different polarities was studied. Here, the diffusion of functionalised and unfunctionalised nanoparticles was measured in 3 different solvents; water, ethanol and DMSO at different temperatures (Fig 4.16). The temperatures were chosen based on the phase of the polymer-nanoparticle composite, shown by the DLS data (Fig 4.5), and reflect those used in SANS experiments.
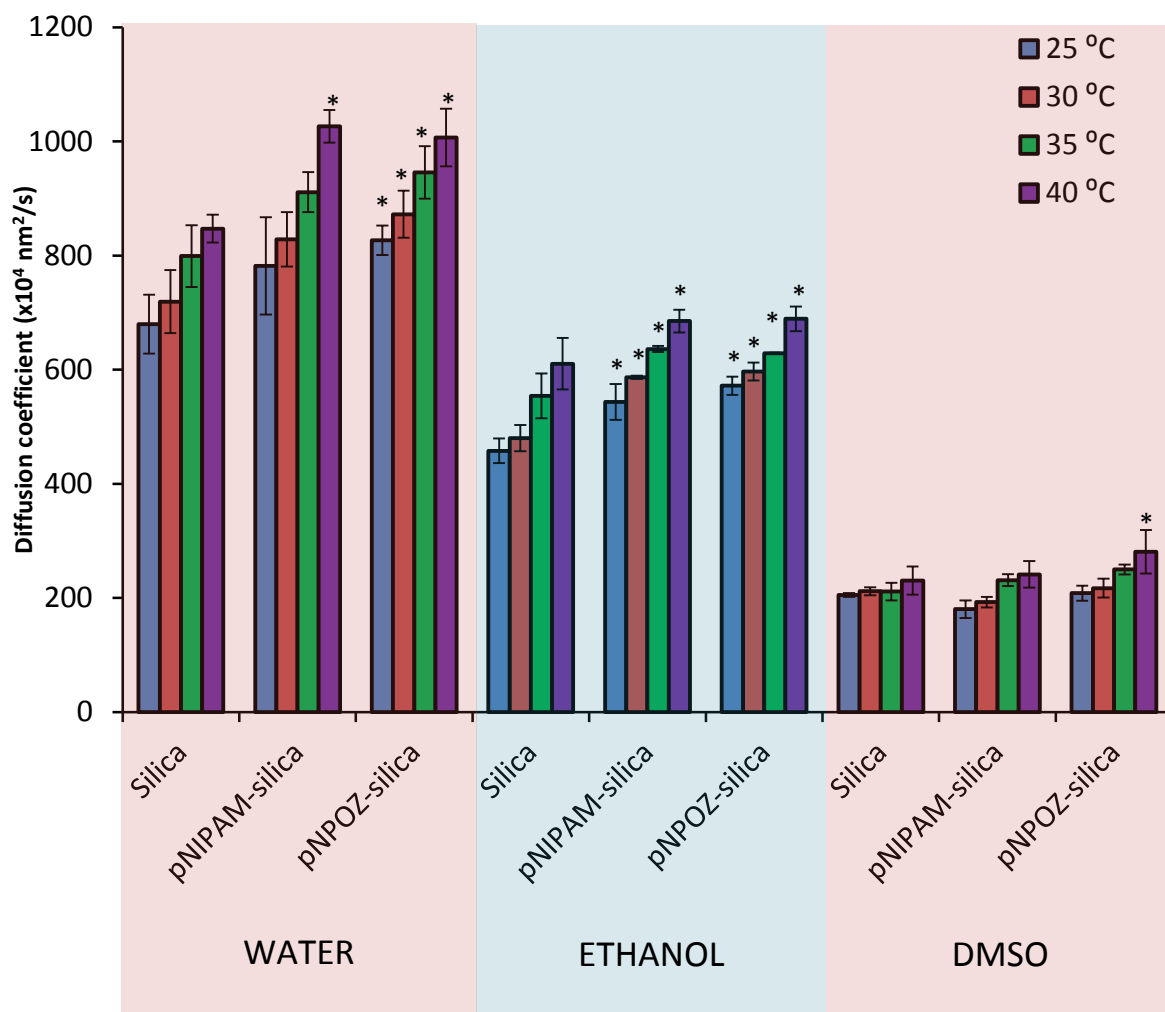
**Fig 4.16 Diffusion coefficients for functionalised and unfunctionalised silica nanoparticles in water, ethanol, and DMSO at different temperatures.** Means ± standard deviation, n=3, *P<0.05 against unfunctionalised silica at the same temperature.

The data show clear differences between the solvents. As would be expected, the particles are most diffusive in water, followed by ethanol, and DMSO. This is due to changes in viscosity between the solvents. Water at 25 °C has a viscosity of 0.89 cP, whereas ethanol has a higher viscosity (1.04 cP) at the same temperature and DMSO higher still (1.99 cP), meaning the particles will diffuse slower.

Similarly, as the temperature increases, the diffusion coefficient also increases. Again, this is to be expected as (by increasing the temperature) the viscosity decreases due to a weakening of the intermolecular interactions between molecules, caused by an increased amount of energy in the system. This causes the particles to diffuse faster because the viscosity is reduced.

Interestingly, it appears as though functionalising the nanoparticles causes them to diffuse significantly faster in ethanol (p<0.05 for both PNIPAM and PNPOZ, Student's t-test), and water (p<0.05 for PNPOZ and PNIPAM at 40 $^o$C, Student's t-test). This phenomenon has been noted before,[25] and is likely due to the "hairy" nature of the particles disrupting the normal laminar flow of the particles, this providing them with extra mobility, causing them to propel through the media faster.

Since both PNIPAM and PNPOZ undergo a coil to globule transition, causing the particles to become more hydrophobic in nature, it would be expected that placing the particles in a more polar environment would alter their diffusive properties. This can be seen from the diffusion coefficient of the particles, compared to the unfunctionalised silica. In DMSO, the least polar of the three solvents, the functionalised particles start to move more rapidly at the higher temperatures compared to the thiolated silica. This difference was found to be significant (p>0.05) at 40 $^o$C for PNPOZ-silica. It should be noted that, as the particles are diluted from their stock-solution in water into the solvent, a co-solvency effect will exist between the water bound to the particles themselves and the solvent in the external environment. This will cause the particles to behave differently depending on the temperature. Indeed, PNIPAM-silica nanoparticles suspended in methanol measured using the same temperature ramp experiments show no phase transition, however they did exhibit the subtle decline in particle size (Fig 4.17).
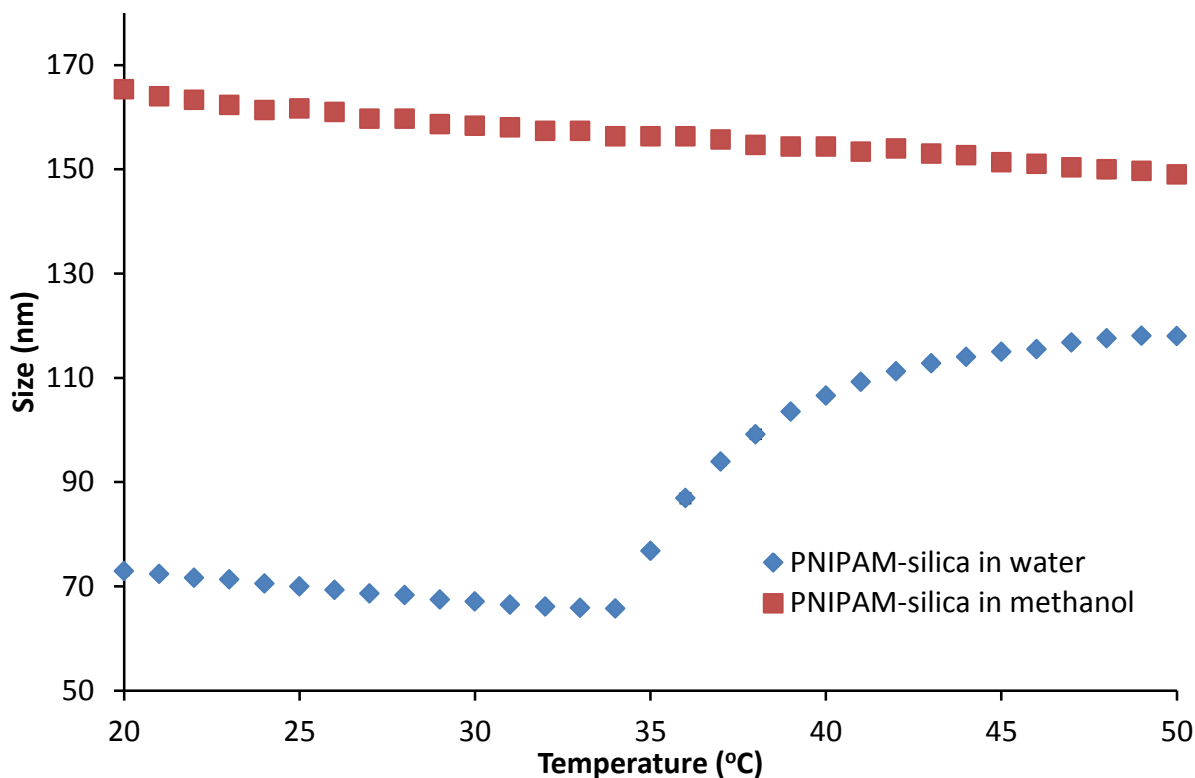
**Fig 4.17 Size of PNIPAM-silica nanoparticles suspended in water (blue) and methanol (red) recorded using DLS.** Means ± standard deviation, n=3

As can be seen, a co-solvency effect between the particles in water and the particles in methanol exists which eliminates the phase-transition. This will affect their diffusion coefficient by minimising the changes caused by the LCST of the polymer, thus explaining the pattern in diffusion coefficients of particles in DMSO. Previous research has suggested that the addition of methanol to PNIPAM-functionalised nanoparticles, leads to a decrease in LCST,[29] which would explain why the size appears much larger than the unfunctionalised particles; they have already undergone phase transition and formed aggregates.

Given that the LCST is dependent on several factors, concentration of solvent, size of PNIPAM chain, and grafting density,[30] the co-solvency effect has a dramatic effect on apparent size and state of the particles (i.e. aggregated vs free) in solution, which would

further affect their diffusion coefficients. This could explain the phenomenon here, and why the effects seen are not as marked as would be expected.

Considering the diffusion coefficients for the more polar solvents (water and ethanol), there is an increase in diffusion coefficient both above and below the LCST for PNIPAM and PNPOZ-silica nanoparticles. It would be expected that the diffusion coefficient would decrease in samples above the LCST, mainly due to the formation of aggregates and the more hydrophobic nature of the polymer shell. However, this does not appear to be the case, and the phase of the shell around the particle does not affect the diffusion coefficient. It is possible to rule out particle aggregation based on the fact that the concentration of particles (as determined by NTA) does not change between samples. It has been suggested in the literature that PNIPAM is not fully hydrophobic both below and above the LCST,[31] meaning that the hydrophobic nature of the shell will be significantly weakened. By relating this to the diffusion coefficients, it means that the particles will not show decreased movement based on hydrophobic interactions. Although there is no research relating the same principle to PNPOZ, given that PNIPAM and PNPOZ are structural isomers of each other (the only difference being the isopropyl group in PNIPAM, and the $1^0/2^0$ structure of the amide), it is possible that a similar phenomenon is occurring and that PNPOZ is also not fully hydrophobic after the LCST. To assess how the diffusion of particles varies at higher concentration in these solvents, additional experiments could be carried out, using DOSY.

Given the LCST of PNIPAM and PNPOZ is 32 and 25 $^o$C respectively, it is possible to conclude that the phase and size of the solvation shell around the particles does not affect the diffusion coefficient. For ethanol, this can be explained by the co-solvency effect described above, and in water systems this is due to the hydrophobic nature of the polymer.

These findings show that the LCST of a polymer can be greatly affected by the physicochemical properties of the surrounding media. This is important in many areas,

including drug delivery given the continuing interest in the development of "smart" nanoparticle systems which are responsive to temperature.

## 4.4 Conclusions

This study investigated the temperature responsive nature of two different polymers (PNIPAM and PNPOZ) grafted to silica cores and how the phase transition affects their diffusion in organic solvents with different polarities. Using a combination of SANS and DLS, it is possible to conclude that the PNIPAM-silica nanoparticles undergo a phase-transition at 34 $^{\circ}$C, after which they form controlled aggregates of similar sizes based on an equilibrium. This effect was not seen in the PNPOZ-silica nanoparticles which form random clusters in solution.

Regarding their diffusion coefficients, it is clear that both the addition of a polymer shell around the particles and the polarity of the solvent play a key role in determining the particles diffusion coefficient. In DMSO, the least polar of the solvents studied, the unfunctionalised particles diffuse at a similar rate regardless of temperature. A similar observation was seen for the functionalised particles below the LCST of the polymer shell, whereas above the LCST the particles are much more diffusive. This is to be expected as the particles are more hydrophobic in nature. In addition, in more polar solvents (namely water and ethanol) the functionalised particles appear to diffuse faster after functionalisation. This is likely due to the polymer shell interacting strongly with the surrounding media, causing the particles to move faster under Brownian motion, and indeed the diffusion coefficients of both types of functionalised particle (PNIPAM-silica and PNPOZ-silica) appear relatively similar. The effect of phase transition shows a continuing increase in diffusion coefficient. This is likely due to the hydrophobic nature of the particles repelling water, causing them to move faster, rather than aggregating and moving slower.

This study is the first to examine the molecular effects of temperature responsive nanoparticles in different polar environments, and shows that functionalised particles will diffuse more rapidly than unfunctionalised particles regardless of environment, and the transition of the polymer has no effect, except in more polar systems. This study is useful for multiple industries, given the wide applications of TRP-functionalised nanomaterials appearing in the literature.

## 4.5 References

(1)     Ougizawa, T.; Inoue, T. UCST and LCST Behavior in Polymer Blends and Its Thermodynamic Interpretation. *Polym. J.* **1986**, *18* (7), 521–527.

(2)     Heyda, J.; Soll, S.; Yuan, J.; Dzubiella, J. Thermodynamic Description of the LCST of Charged Thermoresponsive Copolymers. *Macromolecules* **2014**, *47* (6), 2096–2102.

(3)     Yu, Y.; Kieviet, B. D.; Liu, F.; Siretanu, I.; Kutnyánszky, E.; Vancso, G. J.; de Beer, S. Stretching of Collapsed Polymers Causes an Enhanced Dissipative Response of PNIPAM Brushes near Their LCST. *Soft Matter* **2015**, *11* (43), 8508–8516.

(4)     Zhu, M.-Q.; Wang, L.-Q.; Exarhos, G. J.; Li, A. D. Q. Thermosensitive Gold Nanoparticles. *J. Am. Chem. Soc.* **2004**, *126* (9), 2656–2657.

(5)     Huang, X.; El-Sayed, M. A. Gold Nanoparticles: Optical Properties and Implementations in Cancer Diagnosis and Photothermal Therapy. *J. Adv. Res.* **2010**, *1* (1), 13–28.

(6)     Huang, X.; Jain, P. K.; El-Sayed, I. H.; El-Sayed, M. A. Plasmonic Photothermal Therapy (PPTT) Using Gold Nanoparticles. *Lasers Med. Sci.* **2008**, *23* (3), 217–228.

(7)     Baeza, A.; Guisasola, E.; Ruiz-Hernández, E.; Vallet-Regí, M. Magnetically Triggered Multidrug Release by Hybrid Mesoporous Silica Nanoparticles. *Chem. Mater.* **2012**, *24* (3), 517–524.

(8)     Yoon, T.-J.; Yu, K. N.; Kim, E.; Kim, J. S.; Kim, B. G.; Yun, S.-H.; Sohn, B.-H.; Cho, M.-H.; Lee, J.-K.; Park, S. B. Specific Targeting, Cell Sorting, and Bioimaging with Smart Magnetic Silica Core-Shell Nanomaterials. *Small* **2006**, *2* (2), 209–215.

(9)     Schmatz, W.; Springer, T.; Schelten, J.; Ibel, K. Neutron Small-Angle Scattering: Experimental Techniques and Applications. *J. Appl. Crystallogr.* **1974**, *7* (2), 96–116.

(10)    Paul, A.; Fallis, I.; Cooper, C.; Wess, T.; Thomas, K.; Heenan, R.; King, S.; Griffiths, P. A Contrast Variation Small-Angle Scattering Study of the Microstructure of 2,5-Dimethyl-7-Hydroxy-2,5-Diazaheptadecane–toluene–butanol        Oil-in-Water Metallomicroemulsions. *Soft Matter* **2010**, *6* (11), 2552.

(11)    C. Wohlfarth. Viscosity of Ethanol. Data Extract from Landolt-Börnstein IV/25: Viscosity of Pure Organic Liquids and Binary Liquid Mixtures. In *Landolt-Börnstein - Group IV Physical Chemistry*; 2009; pp 110–120.

(12)    Ciocirlan, O.; Iulian, O. Density, Viscosity and Refractive Index of the Dimethyl

Sulfoxide + O-Xylene System. *J. Serbian Chem. Soc. 74* (3), 317–329.

(13)   Kestin, J.; Sokolov, M.; Wakeham, W. A. Viscosity of Liquid Water in the Range −8 °C to 150 °C. *J. Phys. Chem. Ref. Data* **1978**, *7* (3), 941.

(14)   Shan, J.; Chen, J.; Nuopponen, M.; Tenhu, H. Two Phase Transitions of Poly( N - Isopropylacrylamide) Brushes Bound to Gold Nanoparticles. *Langmuir* **2004**, *20* (11), 4671–4676.

(15)   Tang, H.; Zhang, B.; Wu, P. On the Two-Step Phase Transition Behavior of the Poly(N-Isopropylacrylamide) (PNIPAM) Brush: Different Zones with Different Orders. *Soft Matter* **2014**, *10* (37), 7278–7284.

(16)   Wu, J.; Zhou, B.; Hu, Z. Phase Behavior of Thermally Responsive Microgel Colloids. *Phys. Rev. Lett.* **2003**, *90* (4), 48304.

(17)   Hoogenboom, R.; Thijs, H. M. L.; Jochems, M. J. H. C.; van Lankvelt, B. M.; Fijten, M. W. M.; Schubert, U. S. Tuning the LCST of poly(2-Oxazoline)s by Varying Composition and Molecular Weight: Alternatives to poly(N-Isopropylacrylamide)? *Chem. Commun. (Camb).* **2008**, No. 44, 5758–5760.

(18)   Weihong Jia, S. R.; Hu, B. No Effect of Water Chemistry on Zeta Potential of Air BubblesTitle. *Int. J. Electrochem. Sci* **2013**, *8*, 5828–5837.

(19)   Tauer, K.; Gau, D.; Schulze, S.; Völkel, A.; Dimova, R. Thermal Property Changes of poly(N-Isopropylacrylamide) Microgel Particles and Block Copolymers. *Colloid Polym. Sci.* **2009**, *287* (3), 299–312.

(20)   Evenhuis, C. J.; Guijt, R. M.; Macka, M.; Marriott, P. J.; Haddad, P. R. Variation of Zeta-Potential with Temperature in Fused-Silica Capillaries Used for Capillary Electrophoresis. *Electrophoresis* **2006**, *27* (3), 672–676.

(21)   Ramachandran, R.; Somasundaran, P. Effect of Temperature on the Interfacial Properties of Silicates. *Colloids and Surfaces* **1986**, *21*, 355–369.

(22)   Mori, T.; Maeda, M. Temperature-Responsive Formation of Colloidal Nanoparticles from poly(N-Isopropylacrylamide) Grafted with Single-Stranded DNA. *Langmuir* **2004**, *20* (2), 313–319.

(23)   Triolo, F.; Graziano, V.; Heenan, R. H. Small Angle Neutron Scattering Study of the Quaternary Structure of Haemocyanin of Rapana Thomasiana. *J. Mol. Struct.* **1996**, *383* (1–3), 249–254.

(24)   Moonen, J. A. H. M.; de Kruif, C. G.; Vrij, A.; Bantle, S. Small-Angle Neutron Scattering of Colloidal Silica Dispersions in a Non-Polar Solvent. *Colloid Polym. Sci.* **1988**, *266* (9), 836–848.

(25)   Mun, E. A.; Hannell, C.; Rogers, S. E.; Hole, P.; Williams, A. C.; Khutoryanskiy, V. V. On the Role of Specific Interactions in the Diffusion of Nanoparticles in Aqueous Polymer Solutions. *Langmuir* **2014**, *30* (1), 308–317.

(26)   Rehfeldt, F.; Tanaka, M.; Pagnoni, L.; Jordan, R. Static and Dynamic Swelling of Grafted Poly(2-Alkyl-2-Oxazoline)s. *Langmuir* **2002**, *18* (12), 4908–4914.

(27)   Bissadi, G.; Weberskirch, R. Efficient Synthesis of Polyoxazoline-Silica Hybrid Nanoparticles by Using the "grafting-Onto" Approach. *Polym. Chem.* **2016**, *7* (6), 1271–1280.

(28)   Le Questel, J.-Y.; Laurence, C.; Lachkar, A.; Helbert, M.; Berthelot, M. Hydrogen-Bond Basicity of Secondary and Tertiary Amides, Carbamates, Ureas and Lactams. *J. Chem. Soc. Perkin Trans. 2* **1992**, No. 12, 2091.

(29)   Winnik, F. M.; Ringsdorf, H.; Venzmer, J. Methanol-Water as a Co-Nonsolvent System for poly(N-Isopropylacrylamide). *Macromolecules* **1990**, *23* (8), 2415–2416.

(30)   Plunkett, K. N.; Zhu, X.; Moore, J. S.; Leckband, D. E. PNIPAM Chain Collapse Depends on the Molecular Weight and Grafting Density. *Langmuir* **2006**, *22* (9), 4259–4266.

(31)   Pelton, R. Poly(N-Isopropylacrylamide) (PNIPAM) Is Never Hydrophobic. *J. Colloid Interface Sci.* **2010**, *348* (2), 673–674.

# Chapter 5

## Diffusion and penetration of PEGylated and POZylated nanoparticles through gastric mucus

### 5.1 Introduction

This chapter discusses the diffusive properties of PEGylated and POZylated nanoparticles through mucin dispersions, and assesses their ability to penetrate into gastric mucosa. It has previously been shown that poly(ethylene glycol) (PEG) can enhance nanoparticle diffusion through a mucin network,[1,2] however poly(2-oxazolines) (POZ) have not been studied for this phenomenon.

PEG is an important pharmaceutical polymer, and is used in multiple dosage formulations and marketed drugs. It is a biocompatible, non-toxic polymer which also exhibits "stealth" properties, making it undetectable by the immune system, hence its wide number of applications in the pharmaceutical industry.[3] In addition, it has been shown that by functionalising nanoparticles with PEG it is possible to reduce the surface interactions between the core particles and the external environment, thus enhancing biocompatibility whilst maintaining the unique properties of a nanomaterial.[4] This concept led investigators to study the effects of PEGylated polystyrene nanoparticles on diffusion though mucus barrier.[5,6] It was found that upon functionalisation, the particles were significantly more diffusive through fresh mucosa than the unfunctionalised particles, which became trapped and did not diffuse at all. This finding is of great interest, as it provides the potential for hydrophobic drugs (which would normally be trapped in mucus) to be delivered by less invasive routes, e.g. by the oral route or airways in the form of an aerosol.

POZ macromolecules show similar pharmaceutical properties as PEG in that they are non-toxic, biocompatible polymers which exhibit similar "stealth" properties.[7] However, they carry some significant advantages over PEG which makes them an increasingly popular polymer in both academia and industry, and there are examples of POZ formulations currently undergoing clinical trials, highlighting their importance as the next-generation PEG.[8] Despite this, POZ is not currently FDA approved, although approval is expected within the next few years.[9]

As already stated, POZ has some significant advantages over PEG. Under some conditions, it has been shown that PEG can bioaccumulate and form vacuoles in certain organs. POZ however does not show this effect and is more readily cleared from the body via renal clearance than PEG, with no reported bioaccumulation.[10,11] However, the biggest advantage POZ has over PEG is a functionalisable alkyl side chain, allowing for easy modification such as the binding of a pro-drug,[12,13] or a specific ligand allowing for targeted drug delivery.[14]

POZ is synthesised using a cationic ring-opening polymerisation reaction of 2-oxazolines.[15] This method of synthesis allows highly controllable synthesis, resulting in POZ macromolecules of different molecular weights where the PDI can be kept low. PEG is synthesised by the ring-opening of ethylene oxide, under anionic conditions.[16] As ethylene oxide is more toxic compared to 2-oxazolines, there is reduced risk of adverse effects if the polymer contains any starting material, providing a further advantage of POZ over PEG.

With the known mucus penetrating abilities of PEG, it is valuable to examine whether POZ has the same ability. In this study, the mucus penetrating effects of POZ were assessed by grafting 5 kDa poly(2-ethyl-2-oxazoline) to 50 nm silica nanoparticles. In addition, 5 kDa PEGylated silica was used as a positive control, based on the fact that it has previously shown mucus penetrating abilities.[1,2]

Prior to synthesis and functionalisation (described in Chapter 2), the particles were fluorescently labelled with either BODIPY TMR C5 maleimide, or fluorescein-O-methacrylate. This allowed the particles to be visible over the mucin dispersion, making it possible to measure their diffusion coefficient in a dispersion using Nanoparticle Tracking Analysis (NTA). In addition, a novel technique was developed in order to measure how far the particles could permeate through a fresh gastric mucosa.

## 5.2 Materials and methods

### 5.2.1 Materials

Unfunctionalised thiolated silica, PEGylated silica and POZylated silica nanoparticles were used (see Chapter 2 for details). Here, POZ was purchased from Sigma.

Fluorescein-O-methacrylate, BODIPY TMR C5 maleimide and DMSO were purchased from Fisher (UK). Porcine gastric mucin type II, triethylamine (TEA), and kaolinite were purchased from Sigma-Aldrich (UK). All the water used was ultrapure and particle free (18 $\Omega$M). For the permeation study, a fresh porcine stomach was obtained from a local abattoir (P.C.Turner Abattoirs, Farnborough, UK).

### 5.2.2 Synthesis of fluorescently labelled nanoparticles

Two different fluorophores were used; BODIPY TMR C5 maleimide (excitation 544 nm, emission 570 nm), and fluorescein-O-methacrylate (excitation 490 nm, emission 520 nm).

All particles were fluorescently labelled prior to polymer functionalisation. Based on the results of the Ellman's assay (Chapter 2, 2.3.1), nanoparticles were labelled with fluorophore so that only 5% of the free thiol groups were reacted, leaving 95% free for polymer functionalisation. This loading was selected from an optimisation study wherein a series of increasingly fluorescent nanoparticles were produced and their fluorescence spectra determined, compared to that of a 1% w/v mucus dispersion. Given that mucin has an intrinsic fluorescence, it is important to determine a quantity of fluorophore needed

to make the particles visible.  It was found that 5% labelling was sufficient to ensure that the particles were detectable above the background fluorescence.

380 µL aqueous BODIPY (1.8 mM) was reacted with a 5 mL suspension of nanoparticles (19±3 mg/mL). The fluorophore and nanoparticles were reacted for 24 hours in the dark, and then purified by dialysis in 4 L deionised water (again in the dark), using a 12-14 kDa cut-off membrane.  The water was changed over a 48 hour period with a minimum of 8 changes.

For fluorescein labelling, fluorescein-O-methacrylate was initially dissolved, in a 50:50 % v/v ethanol - deionised water solution, to a final fluorescein concentration of 1.8 mM. Additionally, a 5 mL nanoparticle suspension (19±3 mg/mL) was diluted with 5 mL DMSO. Following this, 0.4 mL of ethanolic fluorescein-O-methacrylate solution was added (so the final concentration of fluorescein in the reaction mixture was 0.066 mM), along with 200 µL TEA (0.033 mM final concentration). The reaction was left to stir in a flask for 24 hours in the dark.  Particles were purified by dialysis once the reaction was complete.

### 5.2.3 Characterisation of mucin dispersion

Prior to the diffusion studies, mucin dispersions were assessed for their rheological properties in order to identify the viscosity of the dispersion.  Three fresh solutions of 1, 2, and 3% w/v porcine gastric mucin type II were prepared in 50 mL miliQ water.

Rheological analysis used an AR 2000ex rheometer (TA Instruments, UK) with a 40 mm parallel plate and solvent trap.  Initially, samples were measured to determine the linear viscoelastic region at 25 $^{\circ}$C.  Two experiments were performed; an amplitude sweep and a frequency sweep, using the 3% dispersion.  Initially, a frequency sweep was performed, scanning between 0.1 and 10 Hz, at set amplitudes of 1 %.  Following this, an amplitude sweep was performed, between 0.1 and 10%, at a fixed frequency of 3 Hz.  All experiments were performed at ambient temperature.  The final optimal parameters

employed were; amplitude 1 % and frequency 3 Hz.  These were applied for all remaining rheological experiments.

After determination of the linear viscoelastic region, samples were subjected to a temperature ramp in order to measure the viscosity of the dispersions.  Here, the instrument was set to increase by 1 $^{0}$C/min, between 20 and 40 $^{0}$C.  Viscosity was then plotted as a function of time, and the line equation used to determine the viscosity the mucin dispersions at 25 and 37 $^{0}$C. Each solution was measured 3 times, for each parameter (amplitude, frequency, and temperature), resulting in a total of 9 readings for each concentration.

### 5.2.4 Nanoparticle diffusion in a mucus dispersion

NTA was used to measure the diffusion coefficients for BODIPY labelled nanoparticles. All measurements were performed using a NanoSight LM10 system, with LM14 laser module and metal top plate, SCOMS camera, green 532 nm (50 mW) laser, and syringe pump. Before any videos were recorded, the stock solution of nanoparticles was diluted down to a working concentration of 1:1,000 by serial dilutions into milliQ water.  10 µL of the final dilution was then added to 990 µL of 1% w/v gastric mucin dispersion, resulting in a final dilution of 1:10,000.

The final 1 mL suspension was then injected into the NanoSight system and the syringe pump, using plastic 1 mL syringes, used to flow the sample.  For all experiments, the flow-rate was set at 70 AU in order to minimise fluorescent bleaching of the nanoparticles during analysis.  All videos were recorded through a long pass filter with a wavelength cut-on of 550 nm (Thorlabs, UK). 6×60 second videos were recorded at both 25 and 37 $^{0}$C. Each independent stock dispersion of mucin was measured three times for each nanoparticle type, resulting in a total of nine 6x60 second videos for each temperature, for each type of nanoparticle.  Following recording, the videos were analysed using NTA v2.3 and the diffusion coefficient of the particles determined.  The viscosity determined from

rheological analyses (20 cP and 23 cP for 25 and 37 $^{o}$C, respectively) was used during analysis.

### 5.2.5 Nanoparticle penetration through a mucosal barrier

The fresh porcine stomach was dissected to remove any connective tissue and muscle, leaving only the mucosa, submucosa, and stomach lining intact. 4×1 cm$^2$ sections were cut and placed on a glass plate, with the mucosal layer facing upward. 200 µL of fluorescein labelled nanoparticles (5 mg/mL) were then pipetted onto the sections and left to incubate over 4 time periods; 0, 15, 30, and 45 minutes at room temperature. Deionised water was used as a blank control. At the end of the incubation period, each section was placed mucus side up into a small (3.5×5.5 cm) weighing boat (Fisher Sceintific, UK), half filled with Optimum Cutting Temperature (OCT) media, a cryoprotective embedding medium, and placed on dry ice, before being completely embedded in OCT to preserve the particle-loaded mucus membrane. Once all sections were embedded, samples were left on dry ice for 3-4 hours, before being transferred to a -80 $^{0}$C freezer for 24 hours.

Following the time-dependent penetration experiment, samples were sectioned for fluorescent microscopy analysis. Here, samples were removed from the -80 $^{0}$C freezer and placed on dry ice before being mounted onto a standard solid object holder, 22 mm in diameter using OCT. This was then left for at least 30 mins in dry ice to ensure the OCT had fully set. 30 µm sections were cut transversely using a standard 189 × 27 × 10 mm microtome blade at 22$^{o}$, placed onto superfrost glass slides (VWR, UK) and left to air dry for 30 minutes before being stored in a slide box. All sections were cut from interior to exterior (i.e. upwards through the mucosal layer) in order to avoid forced penetration of particles into the biological tissue during the cutting process. All sections were cut using a Bright 5040 cryostat in a Bright Model PTF freezing chamber at -20 $^{0}$C (Bright Instrument Co. Ltd, UK). 2 slides were prepared for each sample, each containing 5 tissue sections.

Once all the sections had been collected, the penetration of the nanoparticles could be assessed. This was carried out by placing the slides under a Leica MZ10F stereomicroscope (Leica Microsystems, UK) and recording images through an ET-GFP filter. Exposure times of 0.8 ms and a gamma setting of 1 were used for all experiments. Three images were taken for each section, for both slides.

ImageJ software (National Institute of Health, USA, v1.43, http://imagej.nih.gov/ij/) was used to quantify the degree of penetration for each nanoparticle used in this study. For each image (six for each particle type at each time point); a line was drawn across the mucus barrier, measuring 1.5 mm in length, and the "plot profile" measured. This was repeated 5 times at random locations along the mucus barrier for each image, providing a total of 15 (3×5) profiles for each sample. Each individual profile was then assessed for the degree of penetration. This was done by measuring the width of the predominant peak using Excel, 2010. After each profile had been analysed, the mean distances were calculated. The value obtained for the blank tissue (tissue with water containing no particles) at the appropriate time point was then subtracted from the other values at the same time point in order to determine penetration. Fig 5.1 provides a step-by-step description of this process.

For each image, the background was subtracted off, allowing any background fluorescence to be removed, resulting in measurements being made from the same pixel intensity.
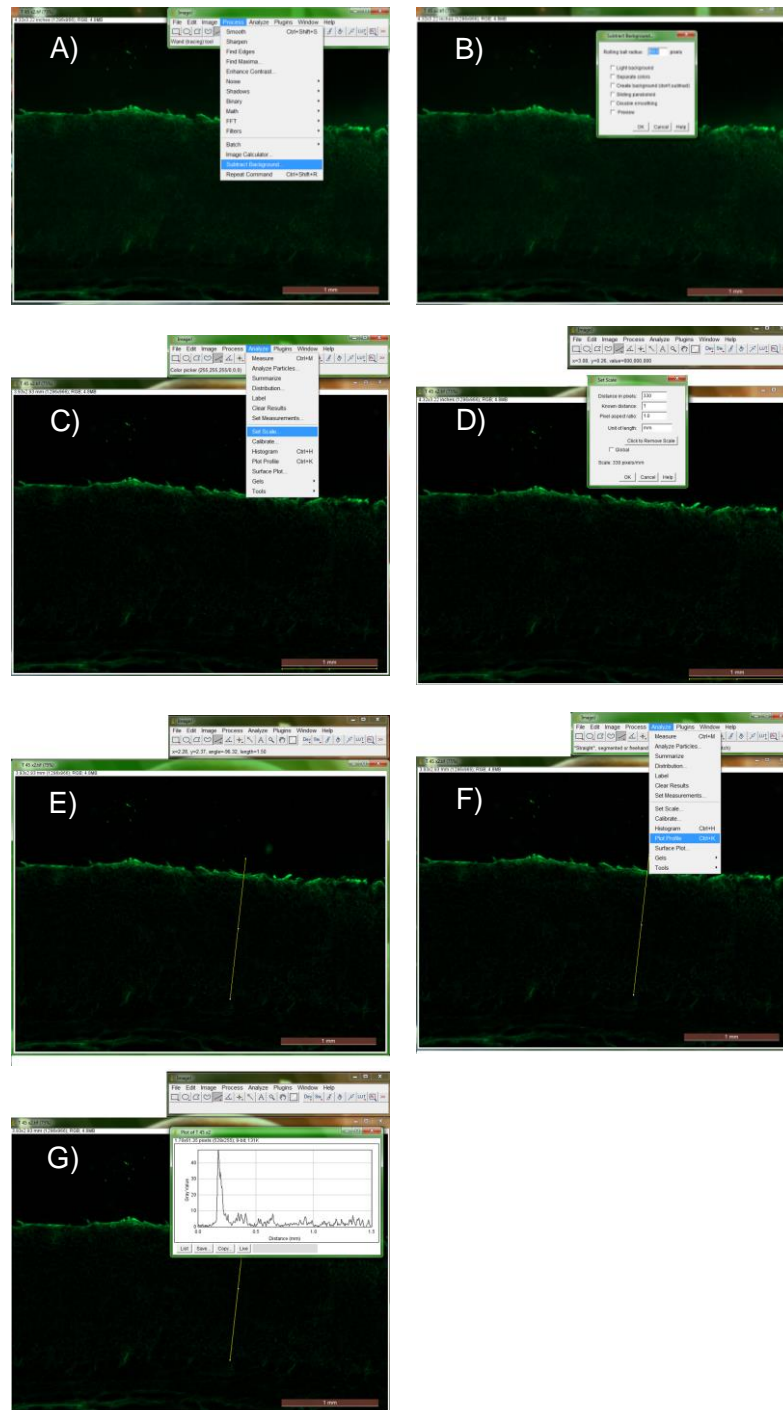
**Fig 5.1. Step by step description (using screen shots) for the method used to measure nanoparticle penetration through a gastric mucosa (section 5.2.5).** A) and B) show subtraction of the background (process>subtract background). C) and D) show how the scale was set. E), F), and G) show the analysis. The profile from g) was exported and plotted in Excel in order to measure the peak width.

181

### 5.2.6 Statistics

Each experiment was repeated 3 times (unless otherwise stated), and the data presented as mean ± standard deviation. Two-way ANOVA statistical analyses were performed on GraphPad Prism v5.0 using Tukey's post hoc test, where *P>0.05* was considered to be statistically insignificant. Tukey's was used to compare the differences between the groups, allowing for the identification of significant differences between the functionalised and unfunctionalised particles at different temperatures/time points.

## 5.3 Results and discussion

### 5.3.1 Nanoparticle characterisation, and fluorescence

The nanoparticles used in this study were previously characterised as described in Chapter 2. Table 5.1 shows the DLS and NTA data for the specific particles used in this study.

**Table 5.1. The size and of the functionalised and unfunctionalised nanoparticles as determined by DLS (a) and NTA (b) (see Chapter 2 for details).** All values show the mean ± standard deviation of three independent repeats

| Sample | Z-average (nm)[a] | PDI[a] | Modal particle size (nm)[b] |
|---|---|---|---|
| Thiolated silica | 48±1 | 0.137±0.050 | 47±3 |
| PEGylated silica | 70±1 | 0.175±0.070 | 63±2 |
| POZylated silica | 56±2 | 0.130±0.010 | 57±2 |

Fluorescent labelling was carried out before functionalisation. In order to determine the minimum level of fluorescence labelling required to allow the particles to be visible above the background fluorescence of the mucin, a pilot study was carried out whereby the fluorescence of 1% w/v gastric mucin dispersions were compared to particles labelled with an increased concentration of fluorophore (Fig 5.2)
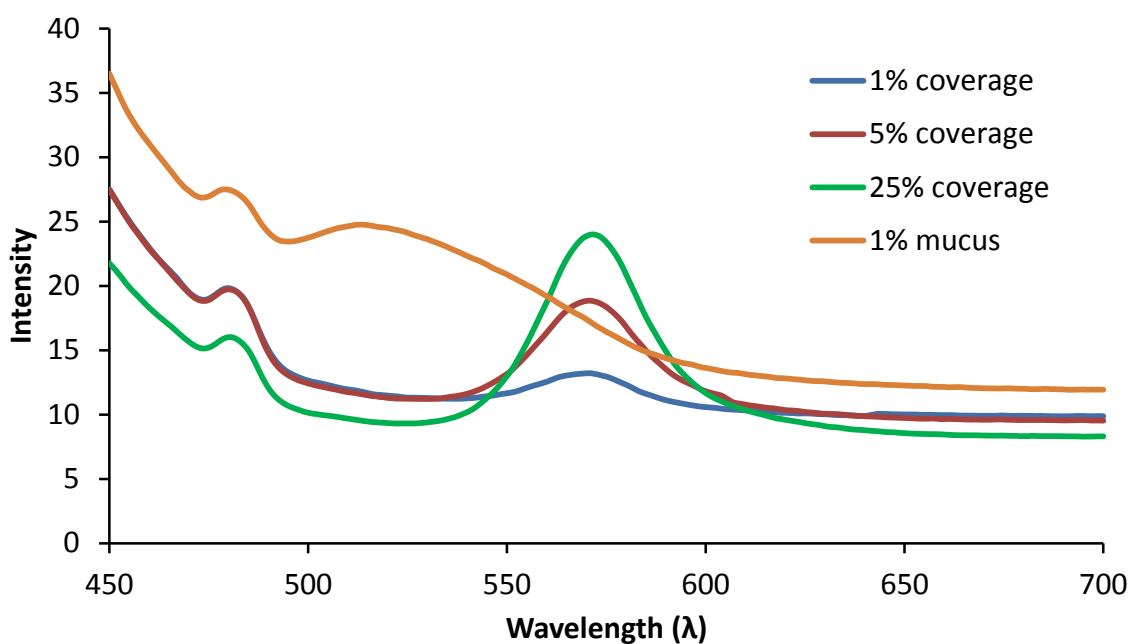
**Fig 5.2. Fluorescence spectrum for a 1% w/v gastric mucin dispersion, and thiolated silica nanoparticles labelled with different degrees of BODIPY TMR C5 maleimide.**

From this pilot study, 5% coverage of fluorophore was sufficient to make the particles visible above the background fluorescence of the mucin dispersion. Therefore, 5% of the reactive thiol groups were covalently bound to fluorophore by calculating the molar equivalent of fluorophore needed to bind to 1.8 mM free thiol groups on the nanoparticle surface. These particles were then used for polymer functionalisation.

### 5.3.2 Characterisation of the mucin dispersion

As shown by the Stokes-Einstein equation, viscosity is a key parameter when calculating the diffusion coefficient for nanoparticles in suspension. Therefore prior to any diffusion experiments, the mucin dispersions needed to be fully characterised. In this study, three mucin dispersions were made; 1%, 2%, and 3% w/v. Physiological mucus contains between 2 and 5% w/v of mucins,[17] depending on the disease state of the organism. NTA has optimum working viscosities of 0 to 10 cP, therefore an optimum concentration needs to be determined that is both close to physiological relevance, and also fulfils the criteria allowing it to be used in NTA. Although a small sheer will exist when the dispersion is passing through the syringe pump, this will only be small, and NTA effectively works as a

183

zero-sheer system.  It is important to note however, that given the flow set-up utilised in these experiments, there could be potential disruption of mucin fibres.  However, given that the dispersion is being uniformly moved through the system, it is unlikely this will alter the results to much.

Rheology is the study of the flow conditions of a liquid system.  By applying a fixed force and amplitude, it is possible to determine the viscosity of a system based on the amount of friction exerted on the liquid.  Prior to measuring the viscosity, experiments need to be performed ensuring the mucin remains in the linear viscoelastic region.  These experiments were performed on the 3% w/v dispersion only, as the rheological properties of a high concentration polymer will be the same as a lower concentration of the same polymer (excluding the viscosity).[18]  Initially a frequency sweep experiment was performed to understand how the storage and loss moduli change as a function of oscillation frequency.  The data shows the angular frequency (rad/s), which was converted to frequency (Hz) using Equation 5.1, where $\nu$ is the frequency (Hz), and $\omega$ is the angular frequency (rad/s).

$$\nu = 2\pi \times \omega$$
<div align="right">Equation 5.1</div>

From this, the frequency distribution could be plotted (Fig 5.3).
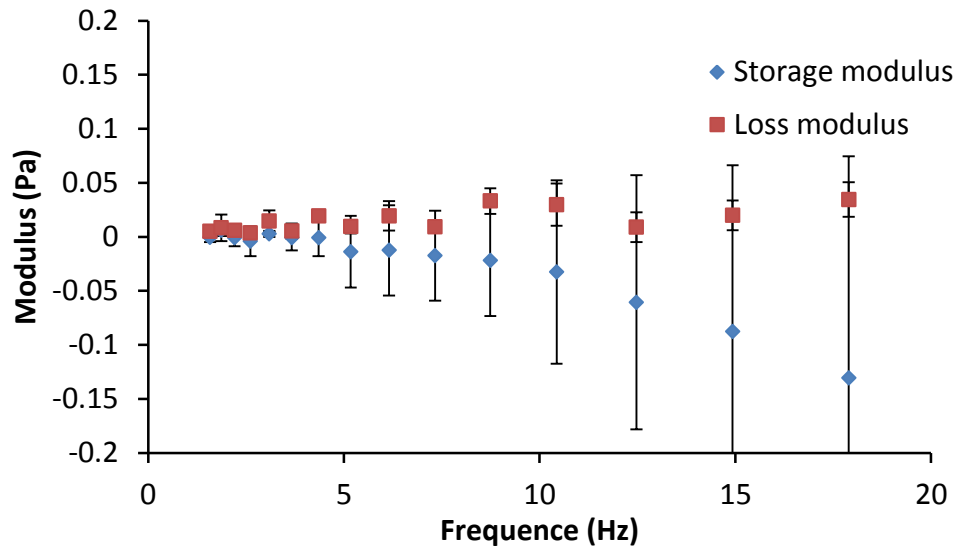
**Fig 5.3 Frequency sweep showing the storage and loss modulus of a 3% w/v mucin dispersion.** Values represent the means of 3 repeats.

From Fig 5.3, it is clear that the storage modulus changes as a higher frequency is applied.  The frequency chosen for future experiments was 3 Hz, as both the storage and loss moduli are linear at this frequency.  Following the frequency sweep, a strain sweep experiment was performed where the frequency was set at 3 Hz, and the strain was measured between 0.5 and 10%.  These data can be found in Fig 5.4.
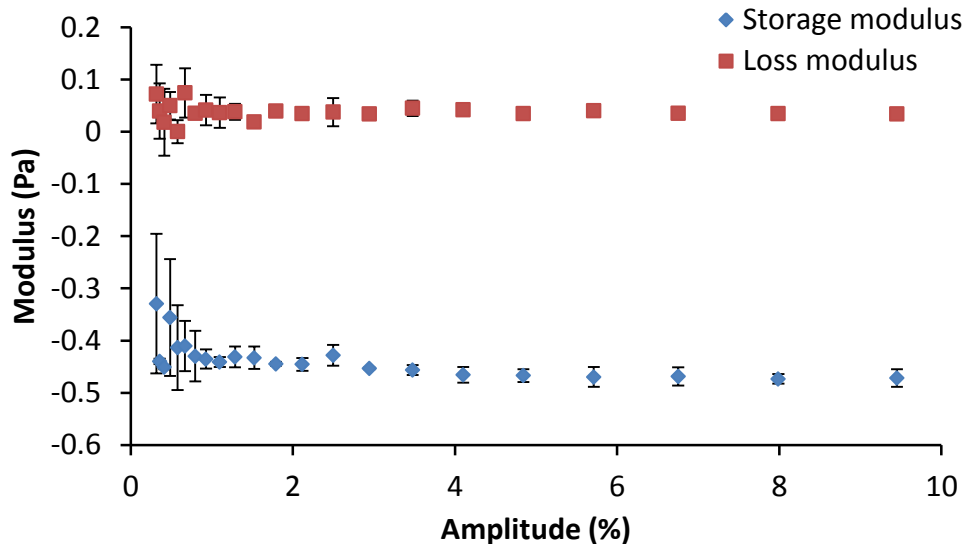


**Fig 5.4 Strain sweep showing the storage and loss modulus of a 3% w/v mucin dispersion.**
Values represent the means of 3 repeats.

As with the frequency sweep, a point needs to be selected where both the storage and loss moduli are linear. Based on this, 1% amplitude was chosen to perform the temperature ramp study. It should be noted that the mucin dispersions presented here are not a gelled system, unlike physiological mucus, as the storage modulus is below the loss modulus. Physiological mucus exists as a gel. This is known for powdered mucin dispersions.[19]

After determining the above parameters, the viscosity of the dispersions was measured as a function of temperature. This was carried out on 1, 2, and 3 % w/v gastric mucin dispersions. The results are in Fig 5.5.
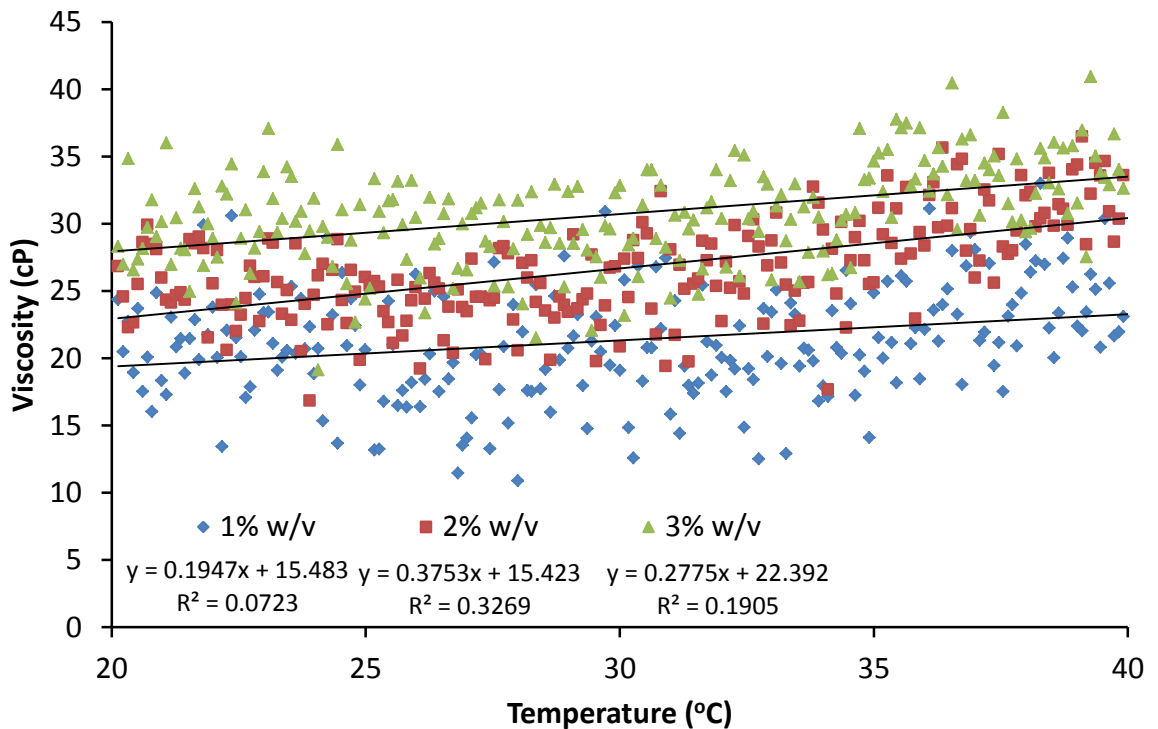


**Fig 5.5 Viscosity of 1, 2, and 3% w/v gastric mucin dispersions as a function of temperature.**
Mean ± standard deviation, n=3.

Using the equation for each line (shown in Fig 5.5), it is possible to calculate the viscosity of the dispersions at 25 and 37 $^{o}$C, the temperatures at which the diffusion experiment will be performed (Table 5.2)

**Table 5.2 Viscosity of mucin dispersions at 25 and 37 $^{o}$C as calculated from the rheology data.**

| [Mucin dispersion] (w/v) | Viscosity at 25 $^{o}$C (cP) | Viscosity at 37 $^{o}$C (cP) |
|---|---|---|
| 1% | 20.3 | 22.6 |
| 2% | 24.8 | 29.3 |
| 3% | 29.2 | 32.5 |

Considering the data as a whole, 1% w/v mucin dispersions were chosen for diffusion experiments, as the particles are visible at this concentration and the mucin dispersion has the lowest viscosity for NTA analysis. During preliminary experiments it was found that the particles were not visible in the 2 and 3% w/v dispersions, due to the consistency of the dispersion.

### 5.3.3 Diffusion and penetration of nanoparticles through a gastric mucosa

### 5.3.3.1 Nanoparticle diffusion in a gastric mucus dispersion

NTA has previously been used to study the diffusion of nanoparticles through solutions of different polymers, namely poly(acrylic acid), poly(N-vinylpyrrolidone), poly(ethylene oxide), and hydroxyethylcellulose.[4] This study was the first to use NTA to measure the diffusion of nanoparticles through a biological dispersion.[20] Previous studies looking at the diffusion of nanoparticles through mucus dispersions and gels used a technique called multiple particle tracking (MPT). Similar to NTA, this technique measures the movement of individual particles over a given period of time, and maps their trajectories. Based on their movement over a given time-scale, it is possible to calculate the mean-squared displacement followed by a diffusion coefficient.[21] This technique has been used to track the movement of nanoparticles,[22] proteins,[23] and vesicles[24] inside living cells and other biological milieu, and allows the calculation of the micro-rheology of a given environment.[22]

Based on the results from rheology experiments, a 1% w/v solution was chosen to measure diffusion coefficients, due to the working viscosity limits of the system. The mean diffusion coefficient were then calculated at two temperatures; 25 and 37 $^{o}$C, room and physiological temperature. The results are shown in Fig 5.6, and the distribution of diffusion coefficients can be found in Fig 5.7 for the functionalised and unfunctionalised nanoparticles in mucin dispersions.
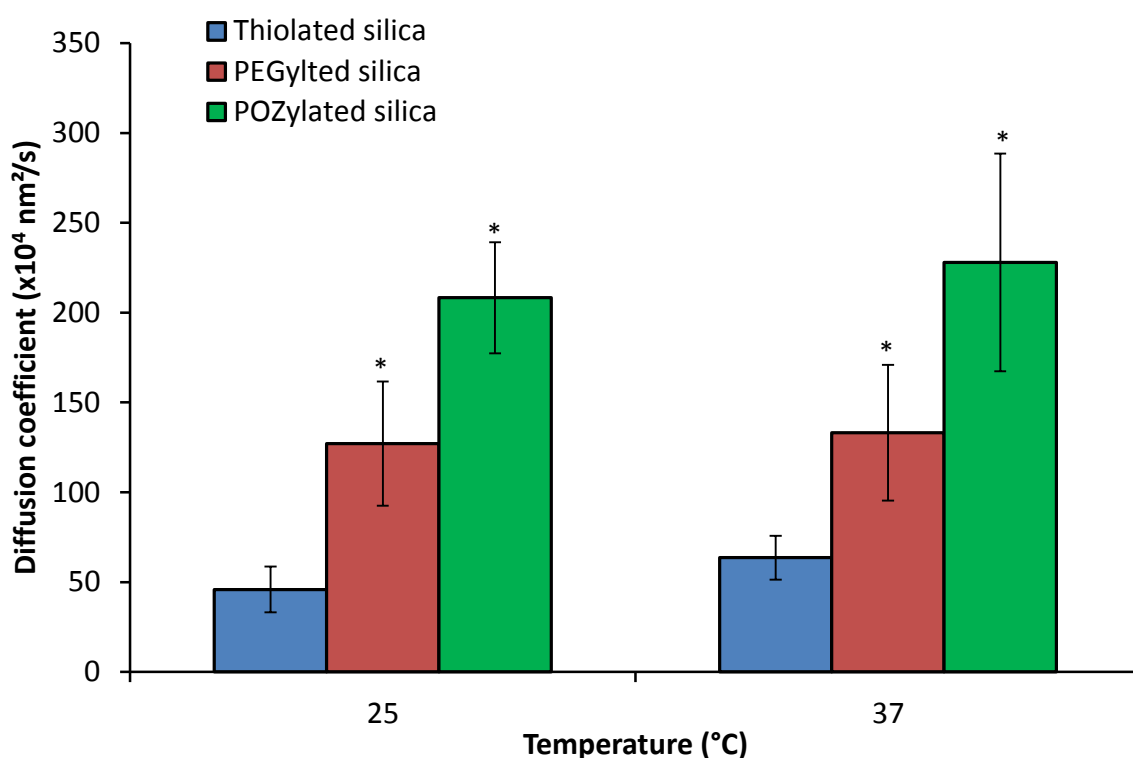


**Fig 5.6 Diffusion coefficient for thiolated (blue), PEGylated (red), and POZylated (green) nanoparticles in a gastric mucin dispersion, measured using NTA.** Mean ± standard deviation, n=3. Values marked * show significant differences compared to thiolated silica nanoparticles (p<0.05). No significant difference exists between the diffusion coefficients determined at 25 $^{o}$C and those at 37 $^{o}$C, or between PEG and POZ (p>0.05).
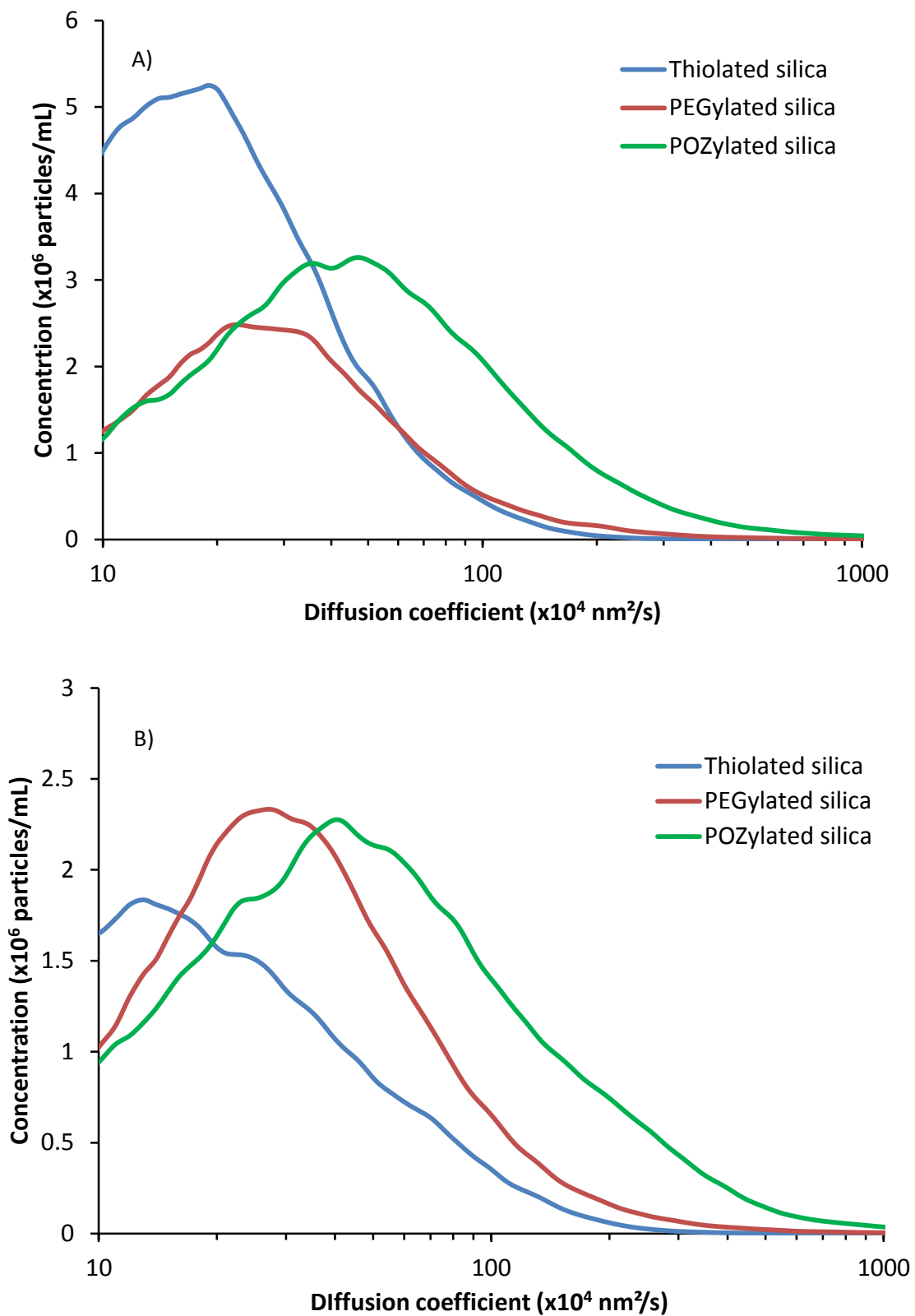
**Fig 5.7 Distribution of diffusion coefficients for thiolated, PEGylated, and POZylated silica nanoparticles in 1% w/v gastric mucus at 25 $^{\circ}$C (A) and 37 $^{\circ}$C (B).** Mean distributions, n=3.

From Fig 5.6 and 5.7, it is clear that upon functionalisation their diffusion coefficient is significantly higher. Thiolated species are well known to be mucoadhesive,[25–28] and so the particles used in this study will inevitably demonstrate the same mucoadhesive interactions. Indeed, the thiolated silica used in this study has previously been studied for retention on bovine cornea[29] and bladder mucosa,[30] confirming this hypothesis. The particles have a very small diffusion coefficient, $46\pm12 \times 10^4$ nm$^2$/s (as seen in Fig 5.6) compared to the particles in water ($788\pm20 \times 10^4$ nm$^2$/s). It is likely that, due to their small size, they diffuse around the mucus network and so do not contact the protein, thus not adhering to them; the reported diameter for a mucus network is 200-300 nm.[31] As the mucus dispersion used here was prepared from freeze-dried processed mucus and not fresh mucus, it is also likely that during the processing procedure many of the cysteine residues have been lost, thus allowing fewer mucoadhesive interactions.

By functionalising nanoparticles (or even proteins) it is possible to reduce their surface interactions with the surrounding medium, thus minimising the mucoadhesive effects. It has previously been reported by several authors that by functionalising polystyrene nanoparticles with PEG it is possible to enhance their diffusion through a mucosal barrier[1,32]. The data presented in Fig 5.6 confirms this, as the PEGylated nanoparticles are significantly more diffusive than the unfunctionalised silica nanoparticles, where the diffusion coefficients were $127\pm34 \times 10^4$ nm$^2$/s for PEGylated silica, compared to $46\pm12 \times 10^4$ nm$^2$/s for thiolated silica at 25 $^{\circ}$C. This is mimicked in the distribution for diffusion coefficients (Fig 5.7), where there is a clear shift to the right after functionalisation.

In addition, this study also looked at the addition to POZ to a particle surface and whether this polymer-nanoparticle composite shows similar enhanced diffusion coefficients as exhibited by PEG. As Fig 5.6 shows, there is a statistically significant increase in diffusion coefficient with POZylation, where the diffusion coefficient increases from $46\pm12 \times 10^4$ nm$^2$/s (unfunctionalised silica) to $208 \pm31 \times 10^4$ nm$^2$/s (POZylated silica). Again, this is further illustrated by the distribution of diffusion coefficients (Fig 5.7), where there is a

clear shift to the right upon functionalisation. No statistically significant difference was noted between PEG and POZ (p>0.05). It should be noted that as the mucin dispersions are under flow, there could be a disruption of the fibrous network. By forcing the dispersion through the syringe pump, a sheer will be placed on the mucin which will break-up the mesh-like structure the protein exhibits, reducing the diffusion coefficients determined less physiologically relevant.

Based on these data, it is clear that the addition of either PEG or POZ to the surface of the nanoparticles significantly increased their diffusion coefficient through the mucin dispersion compared to the functionalised silica. Limitations to the Stokes-Einstein equation were described in Chapter 1, section 1.2.4; here, diffusion coefficients for the functionalised and unfunctionalised nanoparticles in mucus were calculated using the equation (Fig 5.8).
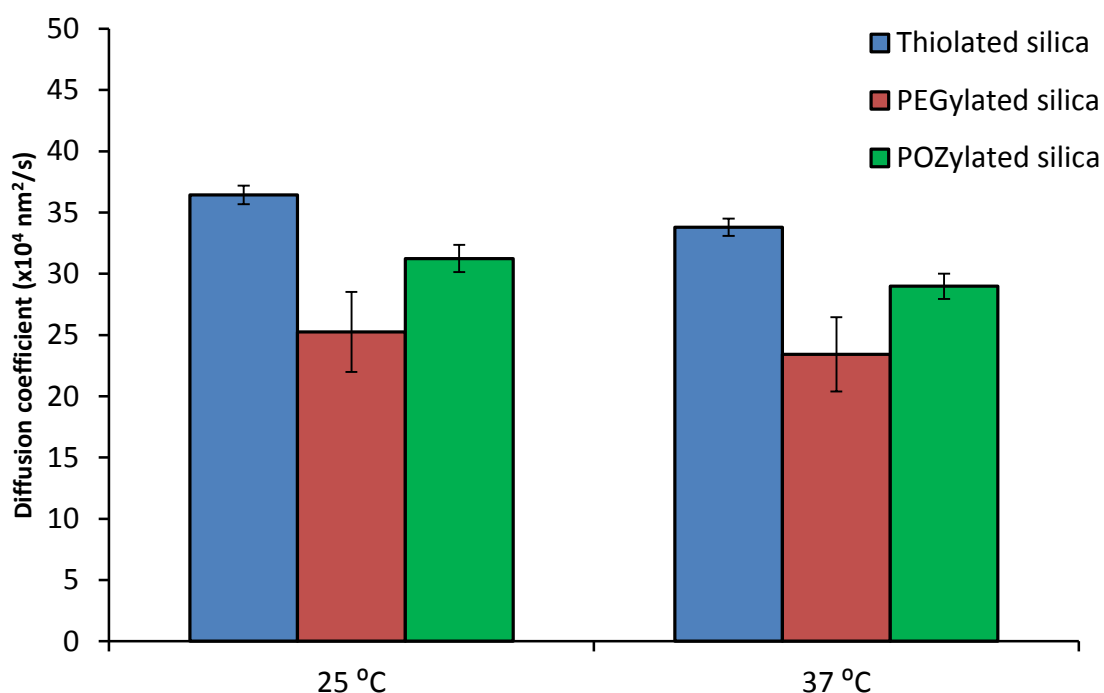


**Fig 5.8 Calculated diffusion coefficients for functionalised and unfunctionalised silica nanoparticles in mucus at 25 and 37 $^{\circ}$C.** Data are based on the nanoparticle size obtained by DLS ± SD.

As can be seen, based on the calculated diffusion coefficients it would be expected that the unfunctionalised silica nanoparticles diffuse the fastest, as they are the smallest in size, followed by POZylated nanoparticles and PEGylated nanoparticles respectively. However that is not the case. When looking at the experimentally determined diffusion coefficients (Fig 5.6), there are clear discrepancies between the two data sets. The calculated and experimentally determined diffusion coefficients for thiolated silica at 37 $^{o}$C (blue), $34 \pm 1$ x$10^4$ nm$^2$/s and $46 \pm 12$ x$10^4$ nm$^2$/s respectively, are relatively similar, and within the standard deviation of each-other (i.e. not significant, P<0.05, Student's t-test). However, the calculated diffusion coefficients for PEGylated silica ($23 \pm 3$ x$10^4$ nm$^2$/s) and POZylated silica ($29 \pm 1$ x$10^4$ nm$^2$/s), are clearly different from the experimentally determined diffusion coefficients ($127 \pm 36$ x$10^4$ nm$^2$/s and $208 \pm 31$ x$10^4$ nm$^2$/s for PEG and POZylated silica respectively.

As expected, the calculated diffusion coefficients for both PEGylated and POZylated nanoparticle is smaller than that of the thiolated silica, as the particle size is larger, and will therefore diffuse slower under Brownian motion. However, when considering the experimentally determined diffusion coefficient for these particles, there is a clear difference to those calculated. The reason for this could be two-fold; the functionalised surface of the particles is causing the particles to diffuse faster (a factor not considered in the Stokes-Einstein equation), and/or a deviation from the Stokes-Einstein equation due to the presence of non-spherical particles with a "hairy" surface, a widely studied limitation of this equation,[33,34] as confirmed by TEM and TGA analysis (Chapter 2, Section 2.3.2).

Despite differences between the two sets of data, it is clear that experimentally, functionalisation causes the nanoparticles to diffuse more rapidly through a mucus dispersion compared to unfunctionalised particles. To corroborate these data, further experiments were carried out designed to investigate the penetration of a nanoparticle suspension though a fresh gastric mucosa.

## 5.3.3.2 Nanoparticle penetration through a gastric mucosa

Although NTA has been shown to be a useful technique in the assessment of nanoparticle diffusion, it does not necessarily provide a real-life description of how the particles are behaving. Therefore, a new technique was developed to measure nanoparticle penetration through a mucosal barrier using fluorescence microscopy.

In this methodology, fluorescent particles were placed directly onto the surface of a mucosa and left to penetrate through the barrier. By taking 30 µm sections of the tissue and assessing the band of fluorescence, it is possible to establish the degree of penetration, whilst keeping the mucus layer intact. It would be expected that the thickness of this band increases depending on the functionality of the particle, and as time progresses. The images obtained can be found in Fig 5.9.

Although they provide good qualitative data, the images themselves show no quantitative data. Therefore ImageJ was used, a piece of software which is regularly used to obtain quantitative information from qualitative data such as images,[35] to measure the thickness of the band and establish the degree of penetration (Fig 5.9).
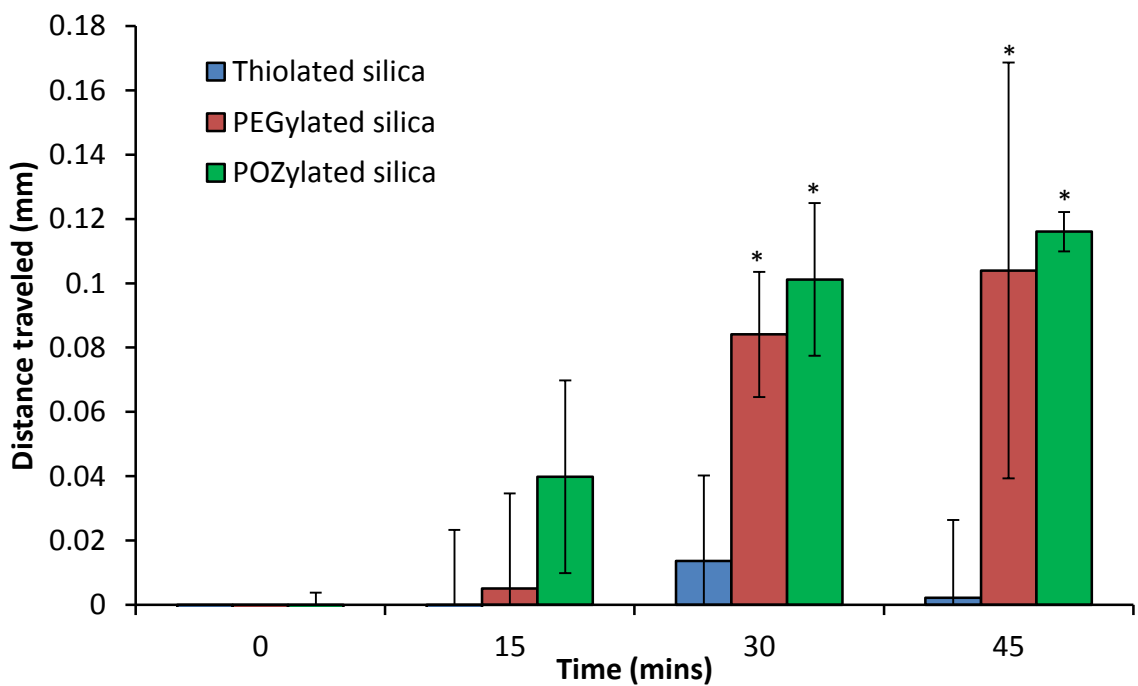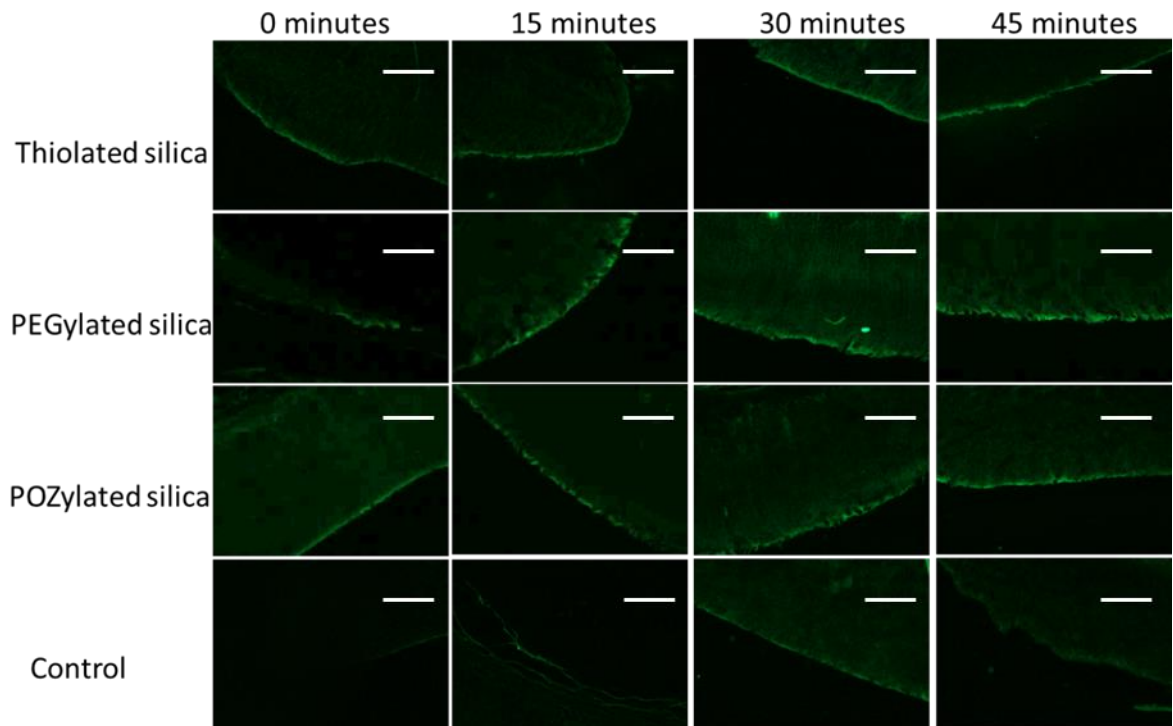
**Fig 5.9 Penetration of fluorescently labelled fluorescent nanoparticles through a porcine gastric mucosa.** Images shown are exemplar at magnification x4; scale bar = 1 mm. The green line represents the surface of the mucosa. Graph shows the distance of nanoparticle permeation as determined by ImageJ analysis on the images (means ± standard deviation, n=3). All values were subtracted from values obtained for control sections with no particles. * represents significant differences ($p<0.05$) compared to thiolated silica at the same time point.

From simple observation of the images obtained, it is hard to quantify any information, and there is little clear difference between the particle types. However following ImageJ analysis, it was possible to determine that the functionalised nanoparticles were more penetrative than the unfunctionalised nanoparticles, thus complementing the NTA data.

The thiolated nanoparticles show very little penetration into the gastric mucosa, even following 45 minutes of treatment, whereas PEGylated and POZylated particles have greater penetration into the biological tissue. Given the large error bars, it is likely that some degree of penetration of the thiolated material is occurring in the tissue, albeit very limited due to the mucoadhesive nature of the particles. The enhanced penetration of PEG and POZylated nanoparticles into the gastric mucosa, compared to their thiolated counterpart, are in agreement with the data of their diffusivity in mucin dispersions, demonstrated using NTA.

This finding is notable on two counts; 1) it confirms the reliability of NTA to measure nanoparticle diffusion through mucin dispersions, and 2) it confirms that POZylated nanoparticles enhance nanoparticle permeation and diffusion to a similar degree as PEGylated silica. Due to the advantages that POZ has over PEG (Chapter 5, section 5.1), this information provides impetus for the use of this polymer in the future design of orally administered nanoparticle formulations, once FDA approval is granted.

Based on the data here, it is not possible to elucidate a mechanism for the enhanced penetration. Despite this, it is possible to speculate that the enhanced penetration is due to two main factors. Firstly, the presence of the polymer on the nanoparticle surface masks the strong negative charge of the particle, and also the free thiol groups. Both of these factors encourage mucoadhesion by the formation of disulphide bonds with free cysteine residues, or by forming electrostatic interactions with the glycoprotein. Secondly, the polymers (both hydrophilic in nature) provide a more hydrophilic environment around the particle (due to entrapment of water molecules), thus encouraging their diffusion through the mucus.

## 5.4 Conclusions

The above data explored enhancement of thiolated silica nanoparticle diffusion through a mucosal barrier. The nanoparticles were functionalised with either PEG or POZ, fully characterised, and their diffusion through mucin dispersion measured using NTA. In addition, a novel method was developed to assess the penetration of nanoparticles through an *ex vivo* mucosa, attempting to mimic how the particles would behave in a biological setting. It was found that, upon functionalisation, the nanoparticles were significantly more diffusive than the unfunctionalised nanoparticles, thus confirming their ability to rapidly penetrate though a mucosal barrier. It has previously been shown that the addition of PEG to a particle surface encourages mucus penetration; however this is the first time POZ has been used in a similar application. Given the advantages POZ has over PEG, this finding may allow the development of novel biologically compatible nanomedicines which can be delivered by the oral route.

## 5.5 References

(1)    Lai, S. K.; O'Hanlon, D. E.; Harrold, S.; Man, S. T.; Wang, Y.-Y.; Cone, R.; Hanes, J. Rapid Transport of Large Polymeric Nanoparticles in Fresh Undiluted Human Mucus. *Proc. Natl. Acad. Sci. U. S. A.* **2007**, *104* (5), 1482–1487.

(2)    Lai, S. K.; Wang, Y.-Y.; Hanes, J. Mucus-Penetrating Nanoparticles for Drug and Gene Delivery to Mucosal Tissues. *Adv. Drug Deliv. Rev.* **2009**, *61* (2), 158–171.

(3)    Rowe, R. C.; Sheskey, P. J.; Quinn, M. E. Handbook of Pharmaceutical Excipients. Pharmaceutical Press 2009.

(4)    Mun, E. A.; Hannell, C.; Rogers, S. E.; Hole, P.; Williams, A. C.; Khutoryanskiy, V. V. On the Role of Specific Interactions in the Diffusion of Nanoparticles in Aqueous Polymer Solutions. *Langmuir* **2014**, *30* (1), 308–317.

(5)    Lai, S. K.; Wang, Y.-Y.; Hanes, J. Mucus-Penetrating Nanoparticles for Drug and Gene Delivery to Mucosal Tissues. *Adv. Drug Deliv. Rev.* **2009**, *61* (2), 158–171.

(6)    Lai, S. K.; O'Hanlon, D. E.; Harrold, S.; Man, S. T.; Wang, Y.-Y.; Cone, R.; Hanes, J. Rapid Transport of Large Polymeric Nanoparticles in Fresh Undiluted Human Mucus. *Proc. Natl. Acad. Sci. U. S. A.* **2007**, *104* (5), 1482–1487.

(7)    Viegas, T. X.; Bentley, M. D.; Harris, J. M.; Fang, Z.; Yoon, K.; Dizman, B.; Weimer, R.; Mero, A.; Pasut, G.; Veronese, F. M. Polyoxazoline: Chemistry, Properties, and Applications in Drug Delivery. *Bioconjug. Chem.* **2011**, *22* (5), 976–986.

(8)    Serina Therapeutics. A Study of Weekly Subcutaneous Injections of SER-214 in Subjects With Parkinson's Disease (PD), to Determine the Safety, Tolerability and Pharmacokinetic (PK) Profile of SER-214. NCT02579473, 2015.

(9)     Macgregor-Ramiasa, M. N.; Cavallaro, A. A.; Vasilev, K. Properties and Reactivity of Polyoxazoline Plasma Polymer Films. *J. Mater. Chem. B* **2015**, *3* (30), 6327–6337.

(10)    Gaertner, F. C.; Luxenhofer, R.; Blechert, B.; Jordan, R.; Essler, M. Synthesis, Biodistribution and Excretion of Radiolabeled poly(2-Alkyl-2-Oxazoline)s. *J. Control. Release* **2007**, *119* (3), 291–300.

(11)    Verbrugghen, T.; Wyffels, L.; Monnery, B.; Hoogenboom, R.; Staelens, S. In Vivo Imaging of 89Zr-Labeled poly(2-Ethyl-2-Oxazoline)s and Poly(ethylene Glycol)s. *Nucl. Med. Biol.* **2014**, *41* (7), 645.

(12)    Wei, H.; Yu, C. Cyclodextrin-Functionalized Polymers as Drug Carriers for Cancer Therapy. *Biomater. Sci.* **2015**, *3* (7), 1050–1060.

(13)    Sehlinger, A.; Verbraeken, B.; Meier, M. A. R.; Hoogenboom, R. Versatile Side Chain Modification via Isocyanide-Based Multicomponent Reactions: Tuning the LCST of poly(2-Oxazoline)s. *Polym. Chem.* **2015**, *6* (20), 3828–3836.

(14)    Qiu, L.-Y.; Yan, L.; Zhang, L.; Jin, Y.-M.; Zhao, Q.-H. Folate-Modified poly(2-Ethyl-2-Oxazoline) as Hydrophilic Corona in Polymeric Micelles for Enhanced Intracellular Doxorubicin Delivery. *Int. J. Pharm.* **2013**, *456* (2), 315–324.

(15)    Hoogenboom, R. Poly(2-Oxazoline)s: A Polymer Class with Numerous Potential Applications. *Angew. Chem. Int. Ed. Engl.* **2009**, *48* (43), 7978–7994.

(16)    Roberts, M. J.; Bentley, M. D.; Harris, J. M. Chemistry for Peptide and Protein PEGylation. *Adv. Drug Deliv. Rev.* **2012**, *64*, 116–127.

(17)    Cone, R. A. Barrier Properties of Mucus. *Adv. Drug Deliv. Rev.* **2009**, *61* (2), 75–85.

(18)    Uneyama, T.; Suzuki, S.; Watanabe, H. Concentration Dependence of Rheological Properties of Telechelic Associative Polymer Solutions. *Phys. Rev. E. Stat. Nonlin. Soft Matter Phys.* **2012**, *86* (3 Pt 1), 31802.

(19)    Kočevar-Nared, J.; Kristl, J.; Šmid-Korbar, J. Comparative Rheological Investigation of Crude Gastric Mucin and Natural Gastric Mucus. *Biomaterials* **1997**, *18* (9), 677–681.

(20)    Mansfield, E. D. H.; Sillence, K.; Hole, P.; Williams, A. C.; Khutoryanskiy, V. V. POZylation: A New Approach to Enhance Nanoparticle Diffusion through Mucosal Barriers. *Nanoscale* **2015**, *7* (32), 13671–13679.

(21)    SUH, J. Real-Time Multiple-Particle Tracking: Applications to Drug and Gene Delivery. *Adv. Drug Deliv. Rev.* **2005**, *57* (1), 63–78.

(22)    Tseng, Y.; Kole, T. P.; Wirtz, D. Micromechanical Mapping of Live Cells by Multiple-Particle-Tracking Microrheology. *Biophys. J.* **2002**, *83* (6), 3162–3176.

(23)    Apgar, J.; Tseng, Y.; Fedorov, E.; Herwig, M. B.; Almo, S. C.; Wirtz, D. Multiple-Particle Tracking Measurements of Heterogeneities in Solutions of Actin Filaments and Actin Bundles. *Biophys. J.* **2000**, *79* (2), 1095–1106.

(24)    Genovesio, A.; Liedl, T.; Emiliani, V.; Parak, W. J.; Coppey-Moisan, M.; Olivo-Marin, J.-C. Multiple Particle Tracking in 3-D+t Microscopy: Method and Application to the Tracking of Endocytosed Quantum Dots. *IEEE Trans. Image Process.* **2006**, *15* (5), 1062–1070.

(25)    Davidovich-Pinhas, M.; Bianco-Peled, H. Mucoadhesion: A Review of Characterization Techniques. *Expert Opin. Drug Deliv.* **2010**.

(26)    Dufresne, M.-H.; Gauthier, M. A.; Leroux, J.-C. Thiol-Functionalized Polymeric Micelles: From Molecular Recognition to Improved Mucoadhesion. *Bioconjug. Chem.* **2005**, *16* (4), 1027–1033.

(27)    Sreenivas, S.; Pai, K. Thiolated Chitosans: Novel Polymers for Mucoadhesive Drug Delivery – A Review. *Trop. J. Pharm. Res.* **2008**, *7* (3), 1077–1088.

(28)    Bernkop-Schnürch, A. Thiomers: A New Generation of Mucoadhesive Polymers. *Adv. Drug Deliv. Rev.* **2005**, *57* (11), 1569–1582.

(29)    Mun, E. A.; Morrison, P. W. J.; Williams, A. C.; Khutoryanskiy, V. V. On the Barrier Properties of the Cornea: A Microscopy Study of the Penetration of Fluorescently Labeled Nanoparticles, Polymers, and Sodium Fluorescein. *Mol. Pharm.* **2014**, *11* (10), 3556–3564.

(30)    Irmukhametova, G. S.; Mun, G. A.; Khutoryanskiy, V. V. Thiolated Mucoadhesive and PEGylated Nonmucoadhesive Organosilica Nanoparticles from 3-Mercaptopropyltrimethoxysilane. *Langmuir* **2011**, *27* (15), 9551–9556.

(31)    Lai, S. K.; Wang, Y.-Y.; Wirtz, D.; Hanes, J. Micro- and Macrorheology of Mucus. *Adv. Drug Deliv. Rev.* **2009**, *61* (2), 86–100.

(32)    Yang, M.; Lai, S. K.; Yu, T.; Wang, Y.-Y.; Happe, C.; Zhong, W.; Zhang, M.; Anonuevo, A.; Fridley, C.; Hung, A.; et al. Nanoparticle Penetration of Human Cervicovaginal Mucus: The Effect of Polyvinyl Alcohol. *J. Control. Release* **2014**, *192*, 202–208.

(33)    Tuteja, A.; Mackay, M. E.; Narayanan, S.; Asokan, S.; Wong, M. S. Breakdown of the Continuum Stokes-Einstein Relation for Nanoparticle Diffusion. *Nano Lett.* **2007**, *7* (5), 1276–1281.

(34)    Mauro, J. C.; Ellison, A. J. Breakdown of the Fractional Stokes–Einstein Relation in Silicate Liquids. *J. Non. Cryst. Solids* **2011**, *357* (24), 3924–3927.

(35)    Collins, T. J. ImageJ for Microscopy. *Biotechniques* **2007**, *43* (1 Suppl), 25–30.

# Chapter 6

# Effects of alkyl length on the penetration of poly(2-oxazoline) functionalised silica nanoparticles through mucus

## 6.1 Introduction

This chapter describes investigations of alkyl chain length effects on nanoparticle diffusion through a gastric mucosa. As previously discussed, poly(2-oxazolines) (POZ) are synthesised by a living polymerisation cationic ring-opening reaction (CROP) (Fig 6.1).



Poly(2-methyl-2-oxazoline       Poly(2-ethyl-2-oxazoline       Poly(2-methyl-2-oxazoline
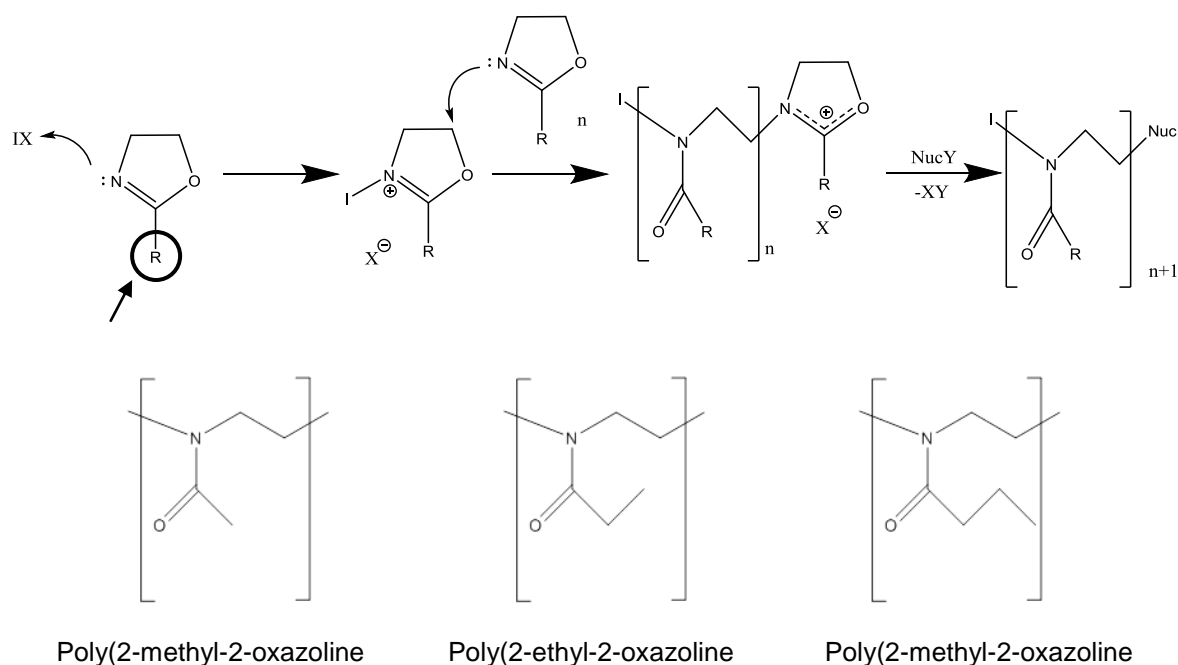
**Fig 6.1 Reaction mechanism for the synthesis of poly(2-oxazolines) by a cationic ring-opening polymerisation, and the chemical structure of the polymers used in this study.** The interchangeable R-group has been circled and highlighted.

CROP reactions proceed by forming a chain with a cationic centre, through which additional monomeric units can be added.[1,2] The reaction proceeds through the $S_N1$ route allowing the synthesis of well-defined polymers.

During the initiation step, the ring is activated by either a Brönsted acid, carbonium ion, onium ions, or a photo/covalent initiator. This generates a cationic intermediate, centred on the nitrogen atom (Fig 6.1). The reaction can then propagate by further addition of a monomer via the nitrogen atom which attacks the intermediate, causing the ring to open and the polymer to form. This causes the new monomer to become charged, allowing the next monomer to react and add to the polymer chain. The reaction is terminated by the addition of a nucleophile, which attacks the positive cationic intermediate, stabilising the complex and inhibiting the binding of any further monomers. This causes the initiating molecule to reform and the reaction ceases.

As shown in Fig 6.1, oxazolines contain an R group (circled) which allows further modifications to the monomer, coupling different moieties and so modifying the physicochemical properties of the polymer after synthesis. There have been many types of POZ synthesised in the literature with functional side chains tailored to specific applications. It is well known that by attaching an aliphatic chain onto this pendent group, it is possible to change the polymers response to external stimuli, such as temperature, by changing its lower critical solution temperature (LCST).[3,4] However, there are examples of other chemistries in the literature, attaching more complex molecules onto the pendent group of the POZ molecule.

Cesans *et al.* (2006)[5] synthesised POZ macromolecules with functional amino side chains by attaching a Boc-protected amino group onto the oxazoline monomer. This was then polymerised into the functional polymer using the CROP method described above. This demonstrates that it is possible to attach biologically active molecules, such as proteins, receptor ligands,[6] and siRNA.[7] Given the good biocompatibility of POZ (discussed in

Chapter 5), this makes POZ attractive to the pharmaceutical industry especially in controlled and targeted drug delivery. There are other examples in the literature of POZ molecules with a wide variety of pendent groups including thiols, carboxylic acids, alcohols, and maleimides.[8] These provide more targets for the attachment of further functional molecules and more complex systems.

This chapter focuses on poly(-2-methyl-2-oxazoline) (PMOZ), poly(2-ethyl-2-oxazoline) (PEOZ), and poly(2-n-propyl-2-oxazoline) (PNPOZ), the structures of which can be found in Fig 6.1. Through this series, the role of different alkyl chain lengths in the polymer on diffusion was examined. It is well known that by changing the side-group on a polymer it is possible to change and tailor its fundamental physicochemical properties. Factors such as viscosity, degree of swelling, and response to certain stimuli (such as temperature) can be readily changed using this method. A study by Farhangi *et al.* described the chain dynamics of poly(alkyl methacrylate) in solution.[9] By binding fluorophores to poly(alkyl methacrylate) molecules with different chain lengths they were able to probe the polymer chain dynamics, and their ability to form excimers. They found that excimer formation decreased with increasing alkyl chain lengths, and polymers that were more flexible (based on their $T_G$ values) further increased excimer formation. By translating this into functionalised nanomaterials, these minor modifications may cause dramatic changes to a nanoparticle's diffusive properties.

Based on the proposed mechanisms of mucus penetration, the increased alkyl chain length should cause the particles to diffuse slower, due to the relative hydrophobicity and hydration of the molecule. Considering mucus from a chemical stand-point, the primary mechanism by which it entraps foreign objects is via strong adhesive interactions such as hydrogen bonding and Van der Waals forces.[10] By minimising the points of contact between a nanoparticle and the mucus fibres, by coating with a hydrophilic, inert polymer, it is possible to generate mucus penetrating nanoparticles.[11] Based on the principle that a longer alkyl chain (composed of repeat methyl groups) is generally more hydrophobic than

a short chain polymer,[12,13] the aim of this study was to determine the extent of which hydrophobicity/alkyl chain length has on the rate of a polymer/nanoparticle complex diffusion through gastric mucin.  This provided; 1) some insights into the mechanism by which mucus penetration occurs, and 2) a good benchmark in the future design of mucus-penetrating nanomaterials.

## 6.2 Materials and methods

### 6.2.1 Materials

The particles used were the amorphous silica nanoparticles functionalised with different variations of POZ, provided by Prof Richard Hoogenboom (see Chapter 2 for details).  In addition, fluorescein-o-methacrylate, Alexa 546 C5 maleimide, and DMSO were purchased from Fisher (UK), and porcine gastric mucin type II and TEA was purchased from Sigma-Aldrich (UK).  All the water used was ultrapure (18 MΩ).  Haematoxylin and eosin were purchased from Brunel Microscopes Ltd (UK).  All other chemicals were of analytical grade purchased from Sigma-Aldrich (UK) unless otherwise stated.

### 6.2.2 Synthesis of fluorescently labelled nanoparticles

Previous studies showed that 5% of the nanoparticles free thiol groups needed to be functionalised to allow them to be visible above the background fluorescence of mucin.  Fluorescein-O-methacrylate nanoparticles were synthesised according to the protocol described in Chapter 5.

For Alexa 546 labelled nanoparticles, 1 mg of dye was dissolved in 5 mL water.  From this, 200 µL of aqueous fluorophore was added to a 2 mL aqueous suspension of nanoparticles (5 mg/mL).   The suspension was left stirring overnight, and purified by dialysis, as described in Chapter 2.

### 6.2.3 TEM

TEM images were recorded on a Phillips CM20 analytical TEM using a 4 megapixel AMT camera. An accelerating voltage of 200 kV was used. Samples were prepared by placing a drop of nanoparticle suspension in aqueous dispersion onto a section of parafilm. A Holey Carbon film 300 mesh copper grid (HC300Cu, EMResolutions, UK) was then placed onto the drop and left for 1 minute. The grid was left to air dry before being placed in the instrument.

### 6.2.4 Small Angle Neutron Scattering

Small angle neutron scattering (SANS) experiments were performed on the D11 instrument at the Institute Laue-Langevin (Grenoble, France). Experimental set-up utilised the same procedure as discussed in Chapter 3, at 25 $^{o}$C only. Fitting used the SASview programme, using DLS and TEM data to fir the spectra to a sphere and core-shell model, using the same SLD parameters as discussed in Chapter 4.

### 6.2.5 Nanoparticle diffusion

Diffusion experiments were carried out using the NTA LM10 system with LM14 metal top-plate, sCMOS camera, green 532 nm laser and syringe pump. Prior to analysis, 3x25 mL gastric mucin type II dispersions (1% w/v) in ultrapure water were made, and left to stir overnight to ensure complete hydration. Alexa 546 labelled nanoparticles were diluted by a factor of 1:100 in water to form a stock solution. 10 µL of these particles was then spiked into 1 mL mucin dispersions (1% w/v) for analysis, resulting in a total dilution of 1:10,000.

Samples were injected into the NanoSight system and the flow-rate set at 50 AU in order to minimise fluorescent bleaching of the nanoparticles during analysis. All videos were recorded through a 565 nm cut-on filter. 6×60 second videos were recorded at 25 and 37 $^{0}$C. Each independent dispersion of mucin was analysed three times with each

nanoparticle type, resulting in a total of 9×6, 60 second videos for each temperature. Analysis was carried out using NTA v3.1 software.

## 6.2.6 Mucus penetration study

The mucus penetration study was carried out according to the protocol used in Chapter 5, with minor modifications.

A fresh porcine stomach was obtained from a local abattoir (P.C.Turner Abattoirs, Farnborough, UK), and dissected to remove any connective tissue and muscle, leaving only the mucosa, submucosa, and stomach lining intact.  4×1 cm$^2$ sections were cut and placed on a glass plate, with the mucosal layer facing upward.  200 µL of fluorescein labelled nanoparticles were pipetted onto the sections. Deionised water was also administered as a blank control.  Samples were left to incubate for 0, 15, 30, 45, and 60 minutes, in a temperature controlled environment, at 37 $^o$C.  Following each time point, tissue sections were placed mucus side up into a small (3.5×5.5 cm) weighing boat (Fisher, UK), half filled with OCT.  They were then placed on dry ice, before being completely embedded in OCT to preserve the particle-loaded mucus membrane.  Once all sections were embedded, samples were left on dry ice for 3-4 hours, before being transferred to a -80 $^o$C freezer for 24 hours until processing.

For sectioning, samples were removed from the -80 $^o$C freezer and placed on dry ice. Each sample was mounted onto a standard solid object holder, 22 mm in diameter using OCT, and placed on dry ice for 30 mins until completely frozen. 20 µm sections were cryosectioned transversely using a standard 189 × 27 × 10 mm blade at 22$^o$, placed onto superfrost charged slides (Life Technologies, UK) and left to dry in air for 30 minutes before being stored in a slide box.  All sections were cut from interior to exterior (i.e. upwards through the mucosal layer) in order to avoid carriage of particles into the biological tissue during the cutting process. All sections were cut using a Bright 5040

cryostat in a Bright Model PTF freezing chamber at -20 $^0$C (Bright Instrument Co. Ltd, UK).

Sections were placed under a Leica MZ10F stereomicroscope (Leica Microsystems, UK) and images taken using an exposure time of 0.8 ms. All images were recorded through an ET-GFP filter (Leica Microsystems, UK), enabling the particles to be detectible on the tissue, due to their fluorescent labelling. Three images were taken for each section.

ImageJ software (National Institute of Health, USA, v1.43, https://imagej.nih.gov/ij/) was used to quantify penetration of the nanoparticles. For each image (10 for each particle type at each time point, from a different tissue section), the background was subtracted, a line drawn across the mucus barrier, and the "plot profile" measured. This was repeated 5 times at random locations along the mucus barrier for each image, providing a total of 50 (10×5) profiles for each sample. Each individual profile was then assessed for the degree of penetration. This was done by measuring the width of the predominant peak using Microsoft Excel 2010. After each profile had been analysed, the mean values were calculated. The value obtained for the blank tissue at the appropriate time point was then subtracted from the other values at the same time point in order to determine penetration.

**6.2.7 Histological analysis**

In addition to fluorescent analysis, some sections were used for histological analyses. For staining, sections were initially immersed in a 1% v/v haematoxylin solution, and left for 5 minutes. The samples were then washed using deionised water to remove any excess solution, followed by another wash with 0.1 M ethanolic HCl for 10 seconds and a final wash with deionised water. The section was then counterstained with eosin for 2 minutes before a final washing step in deionised water.

The sections were examined under a light microscope (Leica DM2500 M, Leica, UK), and images obtained using an Infinity 1-1C camera (Lumenera, UK).

### 6.2.8 Statistics

Statistical analysis was carried out using GraphPad Prism, v5.0. Means ± standard deviations were determined and assessed for significance using 2-way ANOVA with a Bonferoni post hoc test. Values of $p < 0.05$ were considered to be significant. Bonferroni was used to compare the differences between the groups, allowing for the identification of significant differences between the functionalised and unfucntionalised particles at different temperatures/time points.

## 6.3 Results and discussion

### 3.1 Nanoparticle characterisation

The nanoparticles used in this study were characterised previously (Chapter 2). Table 6.1 shows the size and PDI as determined by Nanoparticle Tracking Analysis (NTA) and Dynamic Light Scattering (DLS). All POZ macromolecules used in this study were synthesised by Richard Hoogenboom. It should be noted that during synthesis the PEOZ-silica synthesised by Richard Hoogenboom was compared to the PEOZ-silica purchased from Sigma (Chapter 2). No significant differences were found between the two so the later was not used in this study.

**Table 6.1 The size, and PDI of the functionalised and unfunctionalised nanoparticles used in this study, determined by DLS (a) and NTA (b) (see Chapter 2 for details).** Mean ± standard deviation, n=3

| Nanoparticle | z-average (nm)[a] | PDI[a] | Mode diameter (nm)[b] |
|---|---|---|---|
| Thiolated silica | 52±1 | 0.072 | 54±1 |
| PMOZ-silica | 61±4 | 0.188 | 61±4 |
| PEOZ-silica | 59±1 | 0.106 | 59±1 |
| PNPOZ-silica | 61±1 | 0.194 | 63±3 |

In addition to the characterisation carried out in Chapter 2, TEM images were also recorded for unfunctionalised silica. No images were recorded for the functionalised silica, as it was not possible to identify the polymer corona around the particles (due to lack of contrast). TEM images can be found in Fig 6.2.
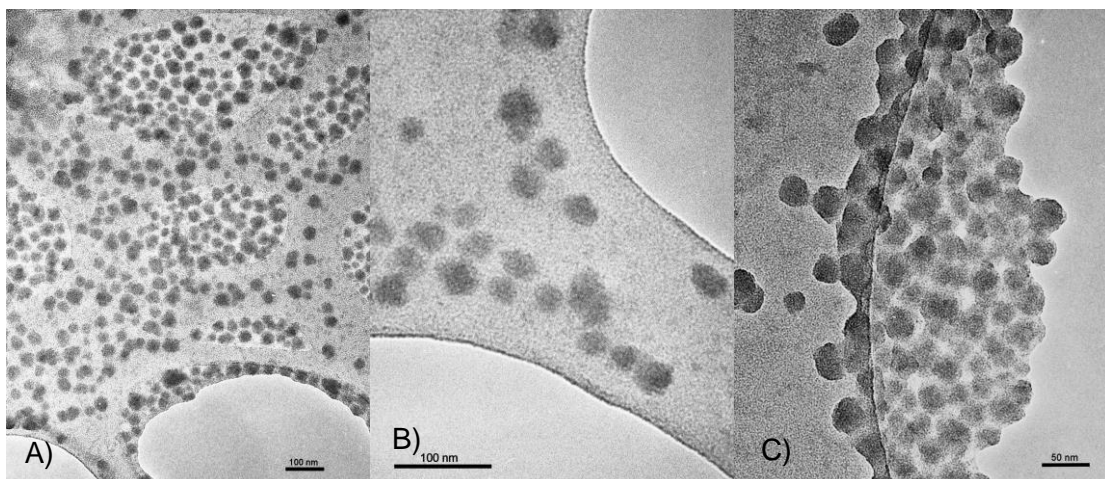


**Fig 6.2 TEM images recorded for unfunctionalised silica nanoparticles.** The scale bar in A) and B) represents 100 nm, and the scale bar in C) represents 50 nm.

From the TEM images, the particle size 28±2 nm (i.e. particles without the hydration shell) and they are approximately spherical.

**6.3.2 SANS**

SANS can probe both the external and internal structure of nanoparticles. Here, SANS was used to determine the structure of functionalised silica nanoparticles and to confirm that decorating the particle surface with POZ has no detrimental effects to the core particle itself.

The scattering profiles for these particles are shown in Fig 6.3; fitting to a sphere model for each particle type is given in Fig 6.4. The scattering profile for thiolated silica was initially fitted to a spherical form factor, using DLS and TEM data as a guide. The particle was found to have a radius of 137 Å, resulting in a diameter of 28 nm, which is

significantly (P<0.05) smaller than the size determined by DLS (52 nm) but corroborates the size established by TEM.
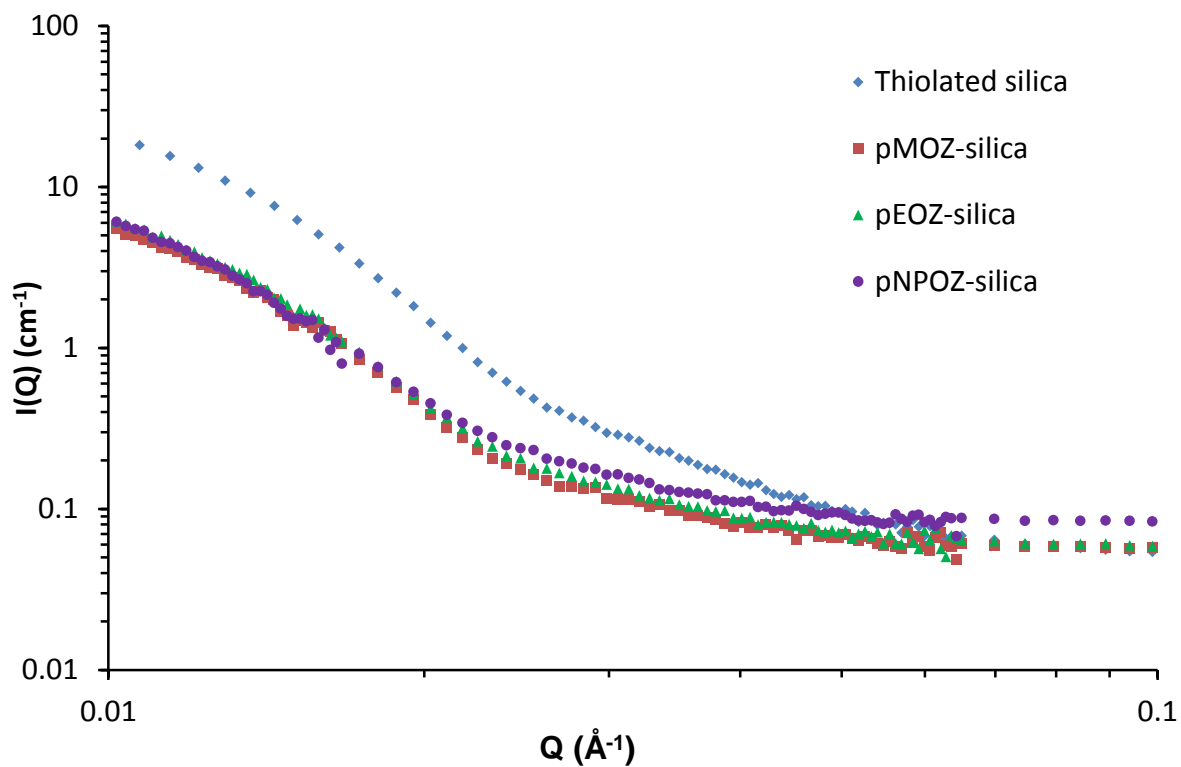
**Fig 6.3 SANS profiles for thiolated silica (blue), pMOZ-silica (red), pEOZ-silica (green), and pNPOZ-silica (purple) nanoparticles.** Scattering profiles were recorded on D11 at 25 °C.
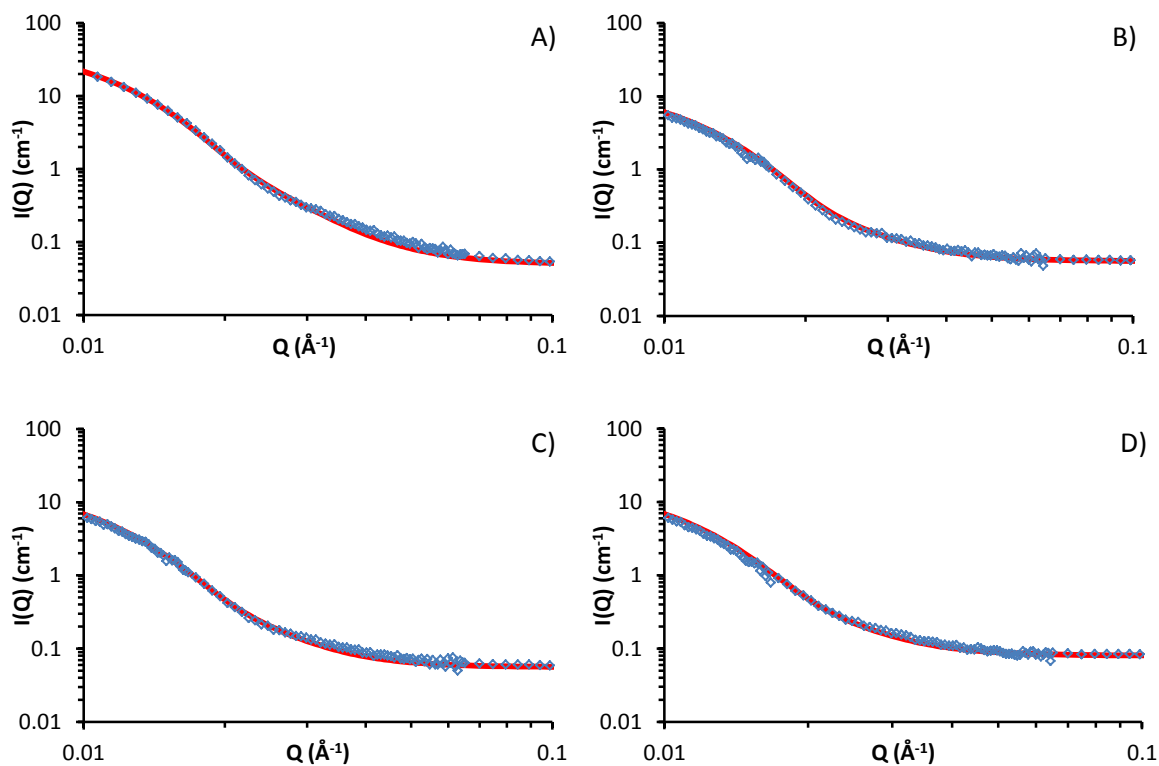


**Fig 6.4 Raw scattering data (blue) and fits (red) for functionalised and unfunctionalised silica nanoparticles.** A) Thiolated silica, B) PMOZ-silica, C) PEOZ-silica, and D) PNPOZ-silica

Previous studies by Mun *et al.*[14] (who studied the core-shell structure of PEGylated MPTS silica nanoparticles) showed sizes of 30 nm for these particles using SANS. The discrepancy between the sizes determined by SANS analysis with that from DLS is due to the presence of a solvation shell around the particle. The solvation shell is detected by DLS (shown by the $r_h$), however is not shown in SANS. The large 20 nm hydration shell around the particle is due to a large abundance of surface -SH and -Si-O$^-$ groups, leading to strong interactions between water molecules and the nanoparticle surface.

Upon functionalisation, only minor changes in the scattering pattern arise (at high Q values ~0.03 Å$^{-1}$). A study of the swelling behaviour of PMOZ and PEOZ showed that POZ macromolecules are highly hydrated and bind tightly to water, and that PMOZ is significantly more hydrated than PEOZ.[15] This phenomenon explains why the shell is barely visible using SANS; it is highly hydrated and offers no contrast to the $D_2O$ background, and so cannot be seen. It was found during curve fitting that changing the size of the shell (in a core-shell model) did not affect the curve. Based on this, the particles were fitted to a spherical form-factor only, and displayed a size of 28 nm for all particles. With no significant change in size or scattering observed, it can be concluded that the addition of the polymer shell does not change the nanoparticles core architecture during the functionalisation reaction.

Although the SANS data could not be fitted to a core-shell model, the size of the hydrated polymer shell can be estimated. From the SANS/TEM data, the core diameter is 28 nm. Light scattering sizes include the hydration shell and provide a diameter of 52 nm for the thiolated particles; from this, a hydration layer of ~13 nm for the non-polymer coated particles can be postulated. The particle diameters from DLS data in Table 1 for the functionalised nanoparticles then indicate shell thicknesses of 4, 3, and 5 nm for PMOZ, PEOZ, and PNPOZ, respectively. Similar values have been reported in the literature for PMOZ functionalised silica.[16] It should be noted that these sizes are estimates based on

the difference in hydration shell thickness. Clearly it is feasible that some polymer is present within the hydration shell, which would suggest a larger shell thickness.

### 6.3.3 Diffusion through a mucus dispersion

Fig 6.5 shows the mean diffusion coefficients of the thiolated and POZylated nanoparticles in a gastric mucin dispersion.
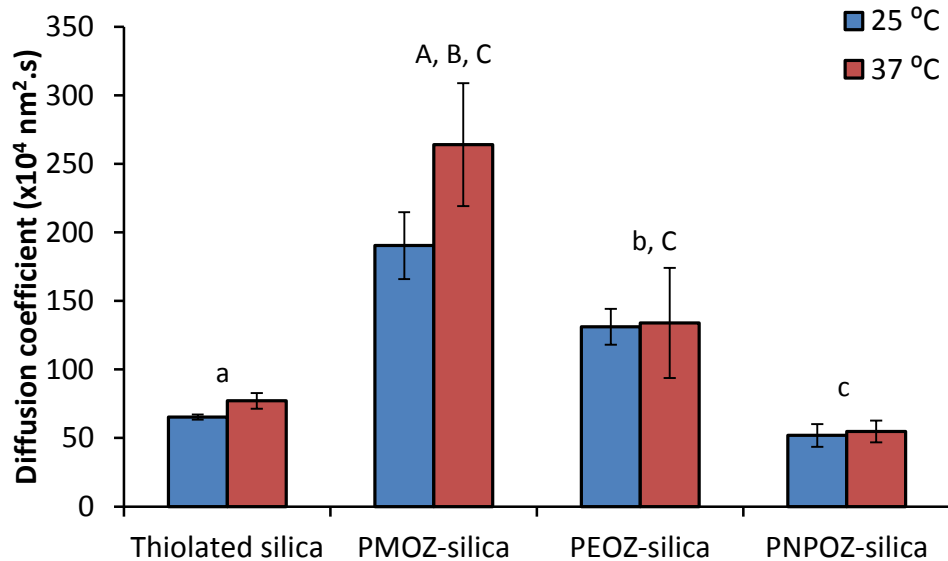


**Fig 6.5 Mean diffusion coefficients of thiolated and POZylated nanoparticles in gastric mucin dispersions.** Mean ± standard deviation, n=3. Columns noted with capital letters are significantly different from their lower case counterparts (P<0.05).

Figure 6.5 clearly shows that the diffusion coefficient changes as the particle becomes functionalised. Although the diffusion coefficient at 37 $^{o}$C is greater than the diffusion coefficient at 25 $^{o}$C, no significant difference was noted. This is to be expected, as an increase in temperature causes a change in viscosity, and also an increase in energy in the system, thus allowing the particles to diffuse more rapidly, as predicted by the Stokes-Einstein equation.

As previously shown, the thiolated silica has a diffusion coefficient of ~60 x10$^{4}$ nm$^{2}$·s. Following POZylation, the diffusion coefficient drastically increases to ~200 x10$^{4}$ nm$^{2}$·s for

PMOZ, and ~130 x10$^4$ nm$^2$·s for PEOZ. It was found that by varying the alkyl chain length on the functionalised POZ macromolecules drastic changes to the diffusion coefficient were found. PMOZ was significantly more diffusive than PEOZ and PNPOZ; and PEOZ was significantly more diffusive than PNPOZ.

PNPOZ-silica nanoparticles shows similar diffusion coefficients to the unfunctionalised silica, with no significant differences noted between the two. This is likely due to the increasing hydrophobicity of the particles. As the chain length increases, the hydrophobicity of the polymer chain also increases, thus causing the particles to become more immobile though mucus. Although mucus is a complex mixture of proteins, carbohydrates and salts, the primary solvent is still water, so an increased hydrophobicity will cause more immobile particles.

These results provide insights into factors that could govern mucus penetration. Previously it has been hypothesised that it was the masking of the surface properties of the core nanoparticle itself that caused the increased mucopenetration,[11,17,18] however this study shows that the hydrophobicity/hydration of the shell also plays an important role. The masking of the surface properties on the particle (i.e. high surface charge and free thiol groups) is of fundamental importance when looking at a mucus penetrating system. However this study suggests that hydrophobicity and degree of polymer hydration can also play a key role in determine the rate of mucus penetration.

To corroborate the diffusion data established by NTA and confirm the influence of hydrophobicity, nanoparticle penetration across a gastric mucosa was measured.

### 6.3.4 Penetration through a gastric mucosa and histology

In order to assess penetration of the functionalised nanoparticles into gastric mucosa, fluorescence microscopy was employed. Fig 6.6 shows the penetration of nanoparticles into a gastric mucosa, as measured by fluorescence microscopy and ImageJ analysis, and provides exemplar microscopy images taken using the stereo microscope.
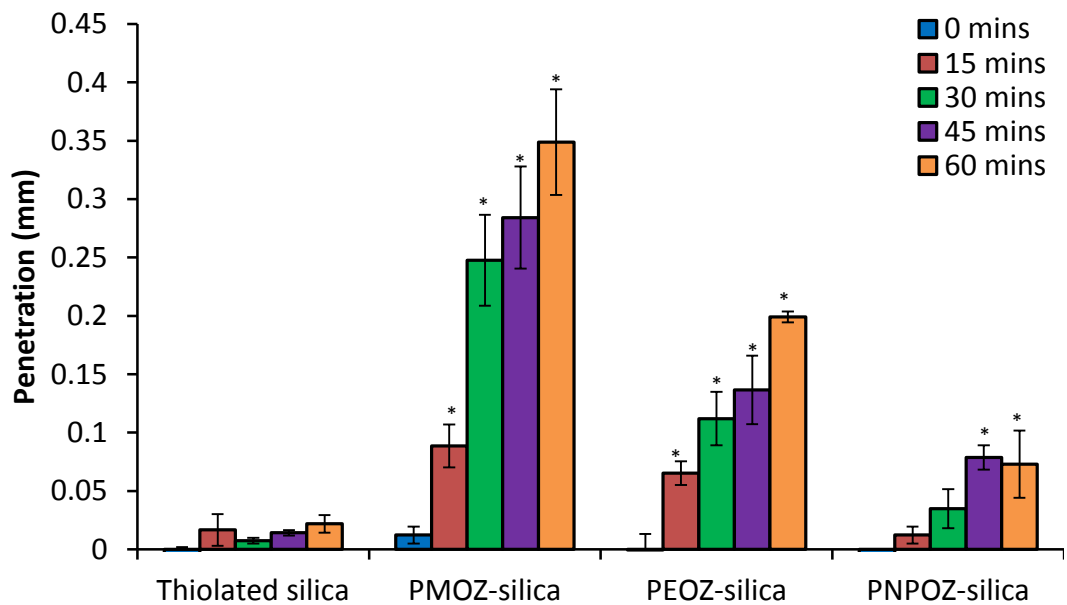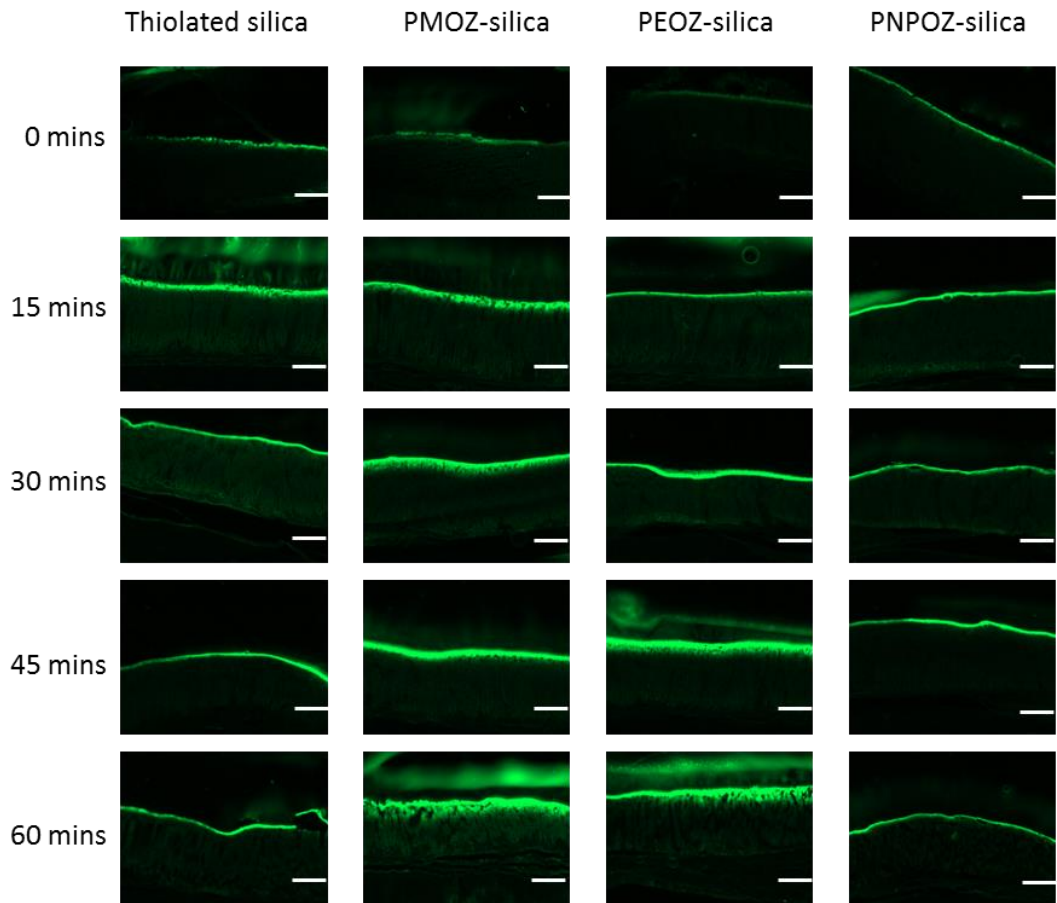
**Fig 6.6 Penetration of thiolated and POZylated silica nanoparticles across a mucosa.**
Images are exemplar images, with at a magnification of x4.  The scale bar represents 1
mm.  Chart shows permeation across 10 different sections, ± standard deviation.
\* significant differences (p>0.05) compared to thiolated silica at the same time point.  The
green represents the surface of the mucosa, with the mucus layer above it.

From Fig 6.6, it is clear that PMOZ-silica nanoparticles are significantly more penetrating than both PEOZ, and PNPOZ (p>0.05), in accord with the diffusion coefficients for the particles in Fig 6.5. Data on the penetrative abilities of nanoparticles is strongly corroborated by the diffusion coefficients measured by NTA i.e., that functionalisation increased penetration, and PMOZ appears more penetrating than PEOZ and PNPOZ. Considering the fluorescent images generated (Fig 6.6), a relatively thick green band can be seen for PMOZ and PEOZylated silica as time progresses compared to the unfunctionalised thiolated silica.

For PNPOZ-silica nanoparticles, there is no significant increase in diffusion coefficient compared to the thiolated parent particles. However there is a significant difference observed in their penetration into a mucosa at the longer time periods, also evident in the images. This is due to the interactions between the mucus and the particles. Although the diffusion coefficients of the nanoparticles are similar ($77\pm6$ or $51\pm8$ $x10^4$ $nm^2\cdot s$ for silica and PNPOZ-silica, respectively), the thiolated silica is mucoadhesive in nature and will therefore stick to the surface of the mucosa and not penetrate through (Fig 6.6). It is unlikely that PNPOZ is mucoadhesive, as the polymer remains water-soluble. As such, the particles will permeate through the mucus, just at a reduced rate compared to the shorter aliphatic chained-polymers.

Further, penetration of the particles was linear with time, with $R^2$ values of 0.95, 0.98, and 0.92 for PMOZ, PEOZ, and PNPOZ, respectively (Fig 6.7).
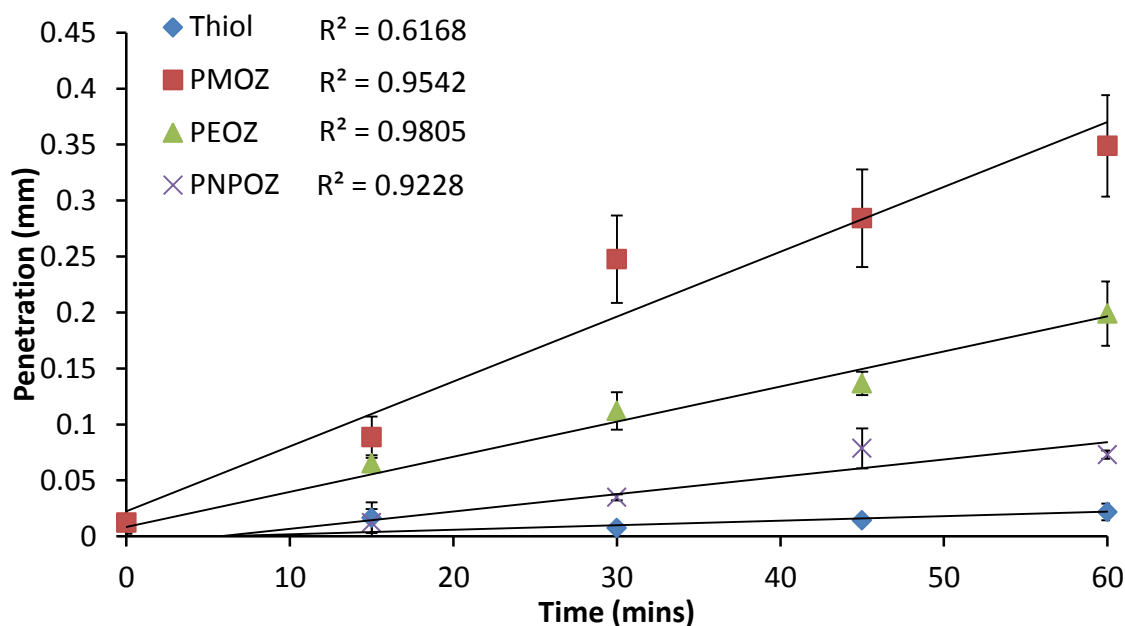
**Fig 6.7 The linear nature of nanoparticle penetration with time for thiolated, PMOZ, PEOZ, and PNPOZ-silica nanoparticles as a function of time.** Data represent the means of 3 repeats ± standard deviation

Based on the SANS data and previous reports, the difference in diffusion coefficient and permeation is likely due to the hydration of the polymer. PMOZ is significantly more hydrated than PEOZ, which explains this trend and, although not reported elsewhere, it is logical to conclude that PNPOZ will be less hydrated than the other polymers. This shows that the hydrophobicity of polymer grafted onto the surface of a nanoparticle plays a key role in the degree of penetration for nanoparticles through mucus barriers, and minor alterations can lead to large changes. It is well known that hydrophobic molecules are poorly penetrating through mucus barriers,[19] in agreement with these results, as methylated polymers are more hydrophilic than propylated polymers. Based on the data presented here and the findings of the data presented in Chapter 5 and subsequent publication,[20] it is possible to conclude that PMOZ may be better at enhancing diffusion compared to PEG and PEOZ.

The variance in rates of penetration accords with the diffusion coefficients for the particles in the mucin dispersion (Fig 6.6). As the alkyl chain length increases (from methyl to

propyl) there is a significant (P<0.05) change in both penetration and diffusion coefficient for PMOZ and PEOZ-silica nanoparticles, again a trend which was found to be linear when plotted against number of methyl groups.   This was found for both the penetration and diffusion coefficients (Fig 6.8).
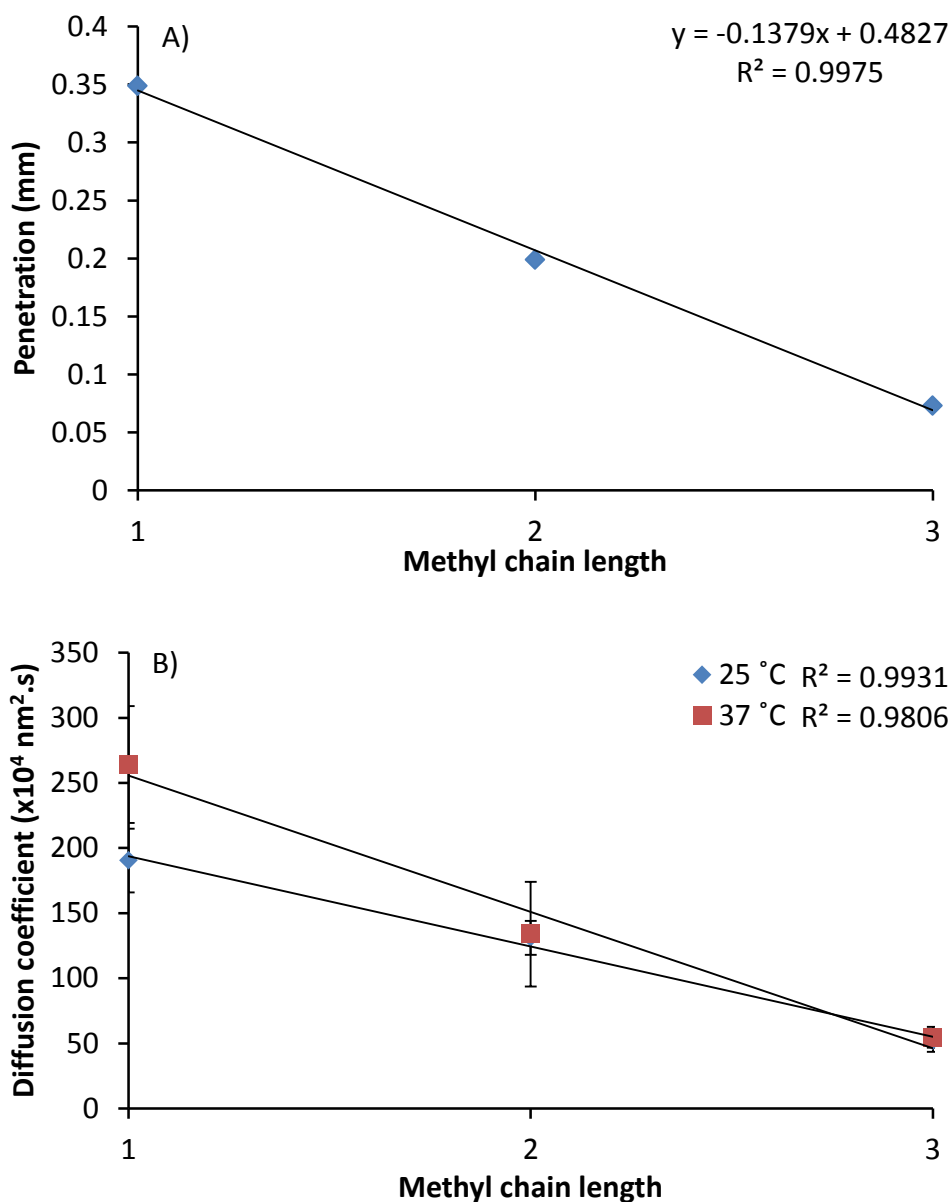


**Fig 6.8 The penetration at 60 mins (A) and diffusion coefficient (B) of nanoparticles functionalised with POZ as a function of alkyl chain length.** Values represent the mean of 3 repeats ± standard deviation.

These results show that the length of the alkyl chain of a polymer grafted onto the surface of a nanoparticle can have a significant effect on their ability to diffuse through a gastric mucosa.  Using the equation generated by Fig 6.8A, it could be possible to design polymers with the specific intention of acting as enhancers of mucus penetration. However, it is clear that the linear relationships above may only apply to aliphatic pendent groups and further work would need to be carried out to determine if the same trend is true for aromatic pendent groups, and other more complex models (such as amino acids, sugar residues, or drugs).

Previous mechanisms of how polymer-functionalised nanoparticles diffuse through a mucus barrier suggest that the main reason for the enhanced penetration is due to a masking of the nanoparticles surface properties.  However, the above results suggests that if a polymer is designed to be highly hydrophilic as well as containing these "stealth" properties, the diffusion of the particles will be significantly enhanced. The thiolated silica nanoparticles do not show any mucopenetrating abilities, and are well known to be mucoadhesive.[21,22]

In addition to fluorescence microscopy, some sections (chosen at random) were used for histological analysis.  Fig 6.9 shows sections of a porcine stomach stained with hematoxylin and eosin. Hematoxylin and eosin are commonly used to assess the pathology of a section, to determine disease states and toxicity.  In this study, histology was used to assess the structure and integrity of the porcine stomach.
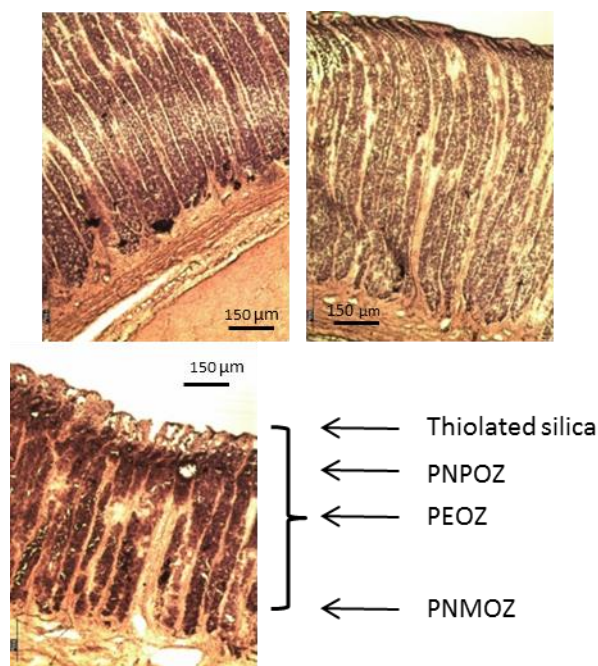
**Fig 6.9 Histology sections of a porcine mucosa, stained with haematoxylin and eosin.** The section clearly shows the mucosa and gastric pits in the stomach. Also included is an image showing how par the particles are permeating into the tissue.

Fig 6.9, shows the histology of a porcine stomach lining, clearly showing the gastric pits and underlying muscle tissue. Comparing these sections to the fluorescent images in Fig 6.6, it is possible to conclude that the PMOZ and PEOZ functionalised nanoparticles are beginning to diffuse into the gastric pits. This shows they have successfully and rapidly crossed the mucosal barrier and have reached the underlying cells. Based on this evidence, either PMOZ or PEOZ could be used in the development of a formulation which could enhance the delivery of a drug into the gastric pits, where it can then either enter into systemic circulation or have a local effect, for example against cancer.

The evidence presented here clearly shows that the length of the alkyl chain has a significant effect on both the diffusion coefficient and degree of penetration of nanoparticles through a mucosal barrier. Given this, it is also possible to conclude that the hydrophobicity/hydration of the nanoparticle surface plays an important role in this diffusion phenomenon.

## 6.4 Conclusions

The effects of the *alkyl* chain length of poly(2-oxazolines) on nanoparticle diffusion and permeation into a gastric mucosa were investigated. Chapter 2 shows that by functionalising with PEOZ, there is a significant enhancement in nanoparticle diffusion coefficient, similar to that of PEG. This study extends this work by showing that by decreasing the length of the alkyl pendant group on the poly(2-oxazoline) macromolecule the particles will diffuse significantly quicker through a mucus dispersion, and as a result penetrate further through a mucosal barrier. This provides a basis for the design of potential mucus penetrating nanoparticles by showing that hydrophobicity plays a key role in determining the penetrative effects of a nanoparticle suspension.

## 6.5 References

(1)     Tauhardt, L.; Kempe, K.; Gottschaldt, M.; Schubert, U. S. Poly(2-Oxazoline) Functionalized Surfaces: From Modification to Application. *Chem. Soc. Rev.* **2013**, *42* (20), 7998–8011.

(2)     Nuyken, O.; Pask, S. Ring-Opening Polymerization—An Introductory Review. *Polymers (Basel).* **2013**, *5* (2), 361–403.

(3)     Schmaljohann, D. Thermo- and pH-Responsive Polymers in Drug Delivery. *Adv. Drug Deliv. Rev.* **2006**, *58* (15), 1655–1670.

(4)     Park, J.-S.; Kataoka, K. Comprehensive and Accurate Control of Thermosensitivity of Poly(2-Alkyl-2-Oxazoline)s via Well-Defined Gradient or Random Copolymerization. *Macromolecules* **2007**, *40* (10), 3599–3609.

(5)     Cesana, S.; Auernheimer, J.; Jordan, R.; Kessler, H.; Nuyken, O. First Poly(2-Oxazoline)s with Pendant Amino Groups. *Macromol. Chem. Phys.* **2006**, *207* (2), 183–192.

(6)     Gussin, H. A.; Tomlinson, I. D.; Little, D. M.; Warnement, M. R.; Qian, H.; Rosenthal, S. J.; Pepperberg, D. R. Binding of Muscimol-Conjugated Quantum Dots to GABAC Receptors. *J. Am. Chem. Soc.* **2006**, *128* (49), 15701–15713.

(7)     Parmar, R. G.; Busuek, M.; Walsh, E. S.; Leander, K. R.; Howell, B. J.; Sepp-Lorenzino, L.; Kemp, E.; Crocker, L. S.; Leone, A.; Kochansky, C. J.; et al. Endosomolytic Bioreducible Poly(amido Amine Disulfide) Polymer Conjugates for the in Vivo Systemic Delivery of siRNA Therapeutics. *Bioconjug. Chem.* **2013**, *24* (4), 640–647.

(8)     Guillerm, B.; Monge, S.; Lapinte, V.; Robin, J.-J. How to Modulate the Chemical Structure of Polyoxazolines by Appropriate Functionalization. *Macromol. Rapid*

*Commun.* **2012**, *33* (19), 1600–1612.

(9) Farhangi, S.; Weiss, H.; Duhamel, J. Effect of Side-Chain Length on the Polymer Chain Dynamics of Poly(alkyl Methacrylate)s in Solution. *Macromolecules* **2013**, *46* (24), 9738–9747.

(10) Cone, R. A. Barrier Properties of Mucus. *Adv. Drug Deliv. Rev.* **2009**, *61* (2), 75–85.

(11) Lai, S. K.; Wang, Y.-Y.; Hanes, J. Mucus-Penetrating Nanoparticles for Drug and Gene Delivery to Mucosal Tissues. *Adv. Drug Deliv. Rev.* **2009**, *61* (2), 158–171.

(12) Cusola, O.; Valls, C.; Vidal, T.; Tzanov, T.; Roncero, M. B. Electrochemical Insights on the Hydrophobicity of Cellulose Substrates Imparted by Enzymatically Oxidized Gallates with Increasing Alkyl Chain Length. *ACS Appl. Mater. Interfaces* **2015**, *7* (25), 13834–13841.

(13) Smith, R.; Tanford, C. Hydrophobicity of Long Chain N-Alkyl Carboxylic Acids, as Measured by Their Distribution Between Heptane and Aqueous Solutions. *Proc. Natl. Acad. Sci. U. S. A.* **1973**, *70* (2), 289–293.

(14) Mun, E. A.; Hannell, C.; Rogers, S. E.; Hole, P.; Williams, A. C.; Khutoryanskiy, V. V. On the Role of Specific Interactions in the Diffusion of Nanoparticles in Aqueous Polymer Solutions. *Langmuir* **2014**, *30* (1), 308–317.

(15) Rehfeldt, F.; Tanaka, M.; Pagnoni, L.; Jordan, R. Static and Dynamic Swelling of Grafted Poly(2-Alkyl-2-Oxazoline)s. *Langmuir* **2002**, *18* (12), 4908–4914.

(16) Bissadi, G.; Weberskirch, R. Efficient Synthesis of Polyoxazoline-Silica Hybrid Nanoparticles by Using the "grafting-Onto" Approach. *Polym. Chem.* **2016**, *7* (6), 1271–1280.

(17) Lai, S. K.; Wang, Y.-Y.; Wirtz, D.; Hanes, J. Micro- and Macrorheology of Mucus. *Adv. Drug Deliv. Rev.* **2009**, *61* (2), 86–100.

(18) Lai, S. K.; O'Hanlon, D. E.; Harrold, S.; Man, S. T.; Wang, Y.-Y.; Cone, R.; Hanes, J. Rapid Transport of Large Polymeric Nanoparticles in Fresh Undiluted Human Mucus. *Proc. Natl. Acad. Sci. U. S. A.* **2007**, *104* (5), 1482–1487.

(19) Cone, R. A. Barrier Properties of Mucus. *Adv. Drug Deliv. Rev.* **2009**, *61* (2), 75–85.

(20) Davidovich-Pinhas, M.; Bianco-Peled, H. Mucoadhesion: A Review of Characterization Techniques. *Expert Opin. Drug Deliv.* **2010**, *7* (2), 259-71

(21) Mun, E. A.; Morrison, P. W. J.; Williams, A. C.; Khutoryanskiy, V. V. On the Barrier Properties of the Cornea: A Microscopy Study of the Penetration of Fluorescently Labeled Nanoparticles, Polymers, and Sodium Fluorescein. *Mol. Pharm.* **2014**, *11* (10), 3556–3564.

(22) Mansfield, E. D. H.; Sillence, K.; Hole, P.; Williams, A. C.; Khutoryanskiy, V. V. POZylation: A New Approach to Enhance Nanoparticle Diffusion through Mucosal Barriers. *Nanoscale* **2015**, *7* (32), 13671–13679.

# Chapter 7

## Concluding remarks and future work

### 7.1 Concluding remarks

Given recent technological development and the increasing popularity of nanoparticles in multiple industries, the need to understand how these particles behave in solution on a molecular level is evident, and in particular their diffusive properties in different environments which is often overlooked. Given the current trend in functionalised nanomaterials, especially as drug delivery systems, there is a growing need to learn more about how they are behaving in specific environments, how they diffuse differently depending on their surface chemistry, and how external factors (such as pH, temperature, or charge) can affect their diffusion.

The aims of this thesis were to synthesise and characterise a series of functionalised nanomaterials, and assess how their diffusion can be manipulated in a variety of different media, primarily focused on the development of novel nanomaterials for enhanced transmucosal delivery by the oral route. This was achieved by focusing on several key areas; how different sized nanoparticles diffuse through a complex viscous environment, mimicking that of a biological system, the effects of structure and aggregation state on diffusion at different temperatures and how this affects diffusion in polar environments, culminating in how the nanoparticles physicochemical properties of functionalised nanomaterials can affect diffusion and permeation through a gastric mucosa.

As has been described throughout the course of this thesis, nanoparticles have been widely studied as drug delivery systems, and there is a large increase in popularity of developing so-called mucus penetrating systems. Functionalising nanoparticles with PEG has been shown to decrease the surface interactions between the particle and the

surrounding mucus environment, thus causing them to diffuse more readily.[1] However, since this initial discovery there have been very few fundamental studies investigating the physical and chemical forces governing mucus penetration. One goal of this research was to understand the fundamental forces governing this process.

The first portion of this study explored the diffusion of different sized gold nanoparticles in suspension with different concentration of Pluronic F-127, a temperature responsive block co-polymer which, depending on the concentration, forms micelles followed by gels upon heating. Here, we wanted to assess how the changing nature of a complex polymer environment affected the diffusion of particles, based on the state of the system (i.e. free polymer to micelles, to gel). The polymeric system chosen (Pluronic F-127) provided a well defined mimic for a complex biolgical medium such as mucus making it possible for the effect of size to be explored. It was found that although the transition between free polymers to micelle to gel can constraint the system causing the particles to travel in a smaller area, however can lead to an increased diffusion coefficient due to changes in the local micro- (or nano-) environment. This was confirmed using a bespoke script which plotted particle movement and calculated the average distance travelled by individual particles and also the total area they moved in.

The next step looked at how a polymer corona around a particle affected diffusion; and whether the physicochemical properties of said shell changed the particles diffusion coefficient. Poly(2-oxazolines) were chosen as model polymers in this regard for several reasons; good biocompatibility and similarity to PEG, ease in synthesis and functionalisation, and finally a functionalisable side chain, making it possible to tune the polymer to have different properties. In addition, POZ macromolecules exhibit a temperature-responsive nature, which can be exploited for pharmaceutical applications.

Continuing on from looking at how particle size affects diffusion, the next step was to assess how structural features of polymer functionalised nanoparticles and how minor changes to the molecular isomeric structure of the polymers can alter the aggregation

state of temperature responsive polymers. By switching between a secondary or tertiary amine, drastic changes in the interactions and aggregation behaviour of PNIPAM-silica and PNPOZ-silica nanoparticles can be seen. However, the influence of the amine has not been definitively proven since it is not only this amine that is changing in our system; PNIPAM has a secondary amine with an isopropyl side chain attached, whereas PNPOZ has a tertiary amine with a linear propyl chain attached. It could be that changing between an isopropyl or n-propyl chain could also be causing this effect. However, the temperature of the system can result in interesting diffusive properties of the particles in different polar environments, ascribed to a co-solvency effect between the hydration shell around the particles (consisting of water), and the solvent environment the particles are suspended in.

Finally, POZ-functionalised nanoparticles were assessed for their ability to permeate through a mucosa. The first study in this regard, directly compared the mucus penetrating abilities of PEG and POZ. It was found that POZylation increased the diffusivity of the nanoparticles just as effectively as PEGylation did. Given the advantages POZ has over PEG, this finding suggests potential future use of POZ in nanoscale drug delivery systems.[2] Subsequently, the role of side-chain dynamics of the polymer shell on nanoparticle mucus permeation was explored. POZ derivatives with 3 different moieties (methyl, ethyl and propyl) were used in this study. In addition to confirming the results of the previous study (that PEOZ-silica allows nanoparticles to diffuse more readily), it was found that the hydration/hydrophilicity of the polymer plays a key role in mucus permeation. PMOZ-nanoparticles were significantly more diffusive than PEOZ and PNPOZ functionalised silica, a trend that was found to be linear. This adds further data on the previous report and looks at the fundamental forces governing mucus penetration, a factor not previously studied.

To draw the research together, this thesis has provided fundamental studies into how nanoparticle diffusion can be manipulated by changing subtle natures of a system, be it a

polymer corona around the particle, or the environment it is moving in. With the surge in popularity of functionalised nanomaterials reaching consumer products, it is clear that much is still unknown about how these particles actually behave in different systems, and how their diffusion can vary with marginal changes to said system. The main findings of this thesis summarise some of these changes and highlight how little is actually known about the nature of nanoparticle diffusion, and how these properties cannot necessarily be easily predicted based on their chemical and physical properties. Despite this, the field of nanoparticle diffusion is expanding rapidly, yet much more work is needed to detail the fundamental science underlying this process, before the development of novel particles with manipulated diffusion coefficients can be designed.

## 7.2 Future work

Given the multidisciplinary nature of this thesis, proposed future works are split into three different areas; mucus-penetration, stimuli-responsive nanomaterials, and physical effects on diffusion.

### 7.2.1 Mucus penetration

The work in this thesis further adds to current scientific understanding of mucus penetrating nanoparticles, by describing how POZ can enhance permeation into a mucosa in addition to PEG. In addition, the work on the effects of alkyl chain-length has further advanced this understanding and provided information on a potential mechanism of action for mucus penetrating nanoparticles. Despite this, there are still several effects to study in this regard; molecular weight of the polymer itself and also size and composition of core particle.

Research into the diffusion of polymer molecular weight (in this case PEG) on modified silica nanoparticles has been carried out by Mun *et al*,[3] in different polymer solutions. However, no work currently exists exploring the effect of polymer molecular weight on nanoparticle diffusion and permeation into a gastric mucosa. By taking the findings of

Mun *et al*, it would be expected that smaller molecular weight polymers would diffuse faster, due to resulting smaller particles. However, this area would need further study to confirm this hypothesis. In addition, by changing the core-silica size one would expect the diffusion coefficient to vary accordingly; larger particles diffusing more slowly.

Given the wide range in nanoparticle size and functionality studied in the literature, drawing on these different parameters, including the findings here where the hydrophobicity of a polymer was found to play an important role on mucus penetration, it could be possible to create a model/computer simulation of how particles could diffuse through a mucosa, and perhaps allow rational design of coatings to enhance diffusion.

### 7.2.2 Diffusion of temperature responsive particles

Continuing the work examining temperature responsive polymers grafted to nanoparticles, and how their aggregation state influences their diffusion has potential.

To corroborate and expand on the diffusion studies carried out using NTA, DOSY would provide information on how the bulk of the particles were behaving in solution, providing further insight into how the particles were behaving in different states in different polar environments. This will provide more insight into the processes discussed, and determine any other effects seen in the diffusion regarding the bulk aggregates.

As discussed in the thesis, one limitation to this study was the use of PNPOZ over poly(2-isopropyl-2-oxazoline) (PIPOZ). Given this, the same series of experiments should investigate the temperature responsive nature of PIPOZ-silica nanoparticles and whether they conform to the same trend as seen in PNIPAM-silica nanoparticles. This will provide a more comprehensive understanding of how the structure of the polymer (i.e. primary, secondary or tertiary amide) can affect both the structure, interactions and diffusive properties of the nanoparticles.

### 7.2.3 Diffusion of nanoparticles in a complex micellar suspension/gel

Given the bespoke application of a novel script designed to capture the distance travelled by nanoparticles and the area they move in, there are numerous possibilities to explore. These include applying this code to the mucus penetrating particle above, to assess how not only diffusion coefficient is affected but also net movement.  The limitation is, however, that for the code to be applied, NTA needs to work in static mode.  Given that the nanoparticles are prone to fluorescent bleaching this may not be possible; however by recording short videos (<10 sec), it may be possible to generate some data though pilot work will need to be carried out to confirm this.

In addition, if a highly porous gel is injected into the NTA system, which contains particles, more detailed information regarding their interactions and net movement could be determined through application of this code, potentially making it very useful in the polymer physics field.

## 7.3 References

(1)     Lai, S. K.; O'Hanlon, D. E.; Harrold, S.; Man, S. T.; Wang, Y.-Y.; Cone, R.; Hanes, J. Rapid Transport of Large Polymeric Nanoparticles in Fresh Undiluted Human Mucus. *Proc. Natl. Acad. Sci. U. S. A.* **2007**, *104* (5), 1482–1487.

(2)     Mansfield, E. D. H.; Sillence, K.; Hole, P.; Williams, A. C.; Khutoryanskiy, V. V. POZylation: A New Approach to Enhance Nanoparticle Diffusion through Mucosal Barriers. *Nanoscale* **2015**, *7* (32), 13671–13679.

(3)     Mun, E. A.; Hannell, C.; Rogers, S. E.; Hole, P.; Williams, A. C.; Khutoryanskiy, V. V. On the Role of Specific Interactions in the Diffusion of Nanoparticles in Aqueous Polymer Solutions. *Langmuir* **2014**, *30* (1), 308–317.